Cranfield University

Jason Shinpei Bennett

Hypersonic Flow Control Using Magneto-Hydrodynamics

School of Engineering

Ph.D. Thesis

CRANFIELD UNIVERSITY

SCHOOL OF ENGINEERING

DEPARTMENT OF AEROSPACE SCIENCES

PH.D. THESIS

SUBMITTED IN ACADEMIC YEAR 2006-2007

BY

Jason Shinpei Bennett

Hypersonic Flow Control Using Magneto-Hydrodynamics

Under the Supervision of Dr. Scott Shaw

January 2008

THIS THESIS IS SUBMITTED IN PARTIAL FULFILMENT OF THE REQUIREMENTS FOR THE DEGREE OF DOCTOR OF PHILOSOPHY.

Abstract

The focus of the present work is on the use of magneto hydrodynamics as a flow control device for supersonic and hypersonic vehicles. A three dimensional parabolized Navier Stokes solver was developed to take into account the effects of magnetic fields , by incorporating two magneto-hydrodynamic models. The modified solver was then used to study the effects of magneto-hydrodynamics on a variety of configurations, one study of which involved surrogate model based optimisation procedures.

The first component of research involved validation of the low magnetic Reynolds number model model against well documented test cases. Good agreement with the numerical test cases for flows past a blunt body and a flat plate boundary layer flow, both in the presence of a magnetic field, was found. A novel application of the method of manufactured solutions to the simplified magneto-hydrodynamic model was made to ensure its accuracy. Assessment of the procedures used for numerical optimisation, were made against known closed-form solutions, and a theoretical axisymmetric body of revolution.

An investigation for an optimal magnetic field configuration, for an over-sped Ramjet intake was made. It was found that for a suitable choice of magnetic field strength, shock on lip could be achieved. Furthermore, for a suitable choice for the position of the magnetic field source, the design condition can also be satisfied using a weaker magnetic field. Finally a study examining the use of magnetic fields for flows past a slender body were was performed. Given a suitably orientated dipole source, it was shown that the magnetic field can introduce asymmetries, for an otherwise symmetric flowfield, and thereby introduce side forces on the missile.

TABLE OF CONTENTS

CHAPTER 1 : INTRODUCTION 17

1.1 Aims and Objectives 19

1.2 Outline of Thesis 20

CHAPTER 2 : THE HYPERSONIC FLOW REGIME 21

2.1 Aerodynamics of the Hypersonic Flow Environment 21

2.2 Conclusions 27

CHAPTER 3 : IMPNS AND THE PNS EQUATIONS 29

3.1 The Parabolised Navier Stokes Equations 29

3.2 IMPNS Flow Solver 33

CHAPTER 4 : REVIEW OF PAST LITERATURE 37

4.1 Introduction 37

4.2 Interest within Aerospace 37

4.3 TPS and Heat Transfer Mitigation 38

4.4 Experimental Investigations 40

4.5 Computational Methods for MHD 41

4.6 Magneto Gasdynamic Models 43

4.6.1 Full Form 43

4.6.2 The Magneto Hydrodynamic Approximation 45

4.6.3 Further Approximations 47

4.7 Numerical Investigations 53

4.8 Conclusions 56

CHAPTER 5 : IMPLEMENTATION OF MHD MODEL 59

5.1 SMHD Model 59

5.2 Magnetic Induction Equation 60

5.3 Additional PNS Terms 66

5.4 Solution Algorithm 67

CHAPTER 6 : VERIFICATION OF THE LOW RE_M MODEL 69

6.1 Uniform Field applied to a Flat Plate 69

6.1.1 Laminar Flow 71

6.1.2 Turbulent Flow 73
6.2 Blunt Body Calculation 75
6.3 Conclusions 86

CHAPTER 7 : VERIFICATION OF SIMPLIFIED MHD FLOW SOLVER 89
7.1 Introduction 89
7.2 Compression Expansion Corner 90
7.3 Problems with MHD Equations 96
7.4 Method of Manufactured Solutions 97
7.5 MHD Verification 99
7.5.1 Test 1: MMS as a Corrective Tool 100
7.5.2 Test 2: Oscillatory Manufactured Solution 108
7.6 Consequences of MMS 111
7.7 Conclusions 113

CHAPTER 8 : NUMERICAL OPTIMISATION 117
8.1 Sampling Procedures 117
8.2 Optimisation Procedures 121
8.3 Surrogate Models 124
8.4 Response Surface Representation 125
8.5 Response Surface Validation 133
8.5.1 Polynomial Surface 133
8.5.2 Power Law Body 135

CHAPTER 9 : SHYFE OPTIMISATION STUDY 141
9.1 Introduction 141
9.2 Intake Aerodynamics 142
9.3 Preliminary Study & Geometry Simplification 144
9.3.1 Grid & Iterative Convergence 147
9.3.2 Optimality Condition 147
9.4 Magnetic Field Effects 151
9.5 Variable Dipole Location 156
9.6 LSQ Fit Method 161
9.7 RBF fit method 164
9.7.1 RBF Tuning Procedure 165
9.8 Conclusions 172

CHAPTER 10 : MHD CONTROL OF SLENDER BODY 175
10.1 Introduction 175
10.2 Slender Body Flow Control 175
10.3 Baseline Case: No Field 178
10.3.1 Grid and Iterative Convergence 179
10.3.2 Comparison with Experiment 181
10.4 Application of Magnetic Field 186
10.4.1 Parameters Under Investigation 189
10.5 Results 190
10.5.1 Zero Incidence 190
10.5.2 Effect of Incidence 196
10.6 Effects on Other Forces 202
10.7 Stability and Comparison to Conventional Devices 206
10.8 Engineering aspects of MHD control 210
10.9 Conclusions 211

CONCLUSIONS AND FUTURE WORK 214

BIBLIOGRAPHY 220

APPENDIX A : COMPONENT TESTING 235

LIST OF FIGURES

1 Supersonic and hypersonic vehicles 22
2 Mean Free Path as a Function of Altitude [3] 26
3 Leading Edge Characteristics of a Flat Plate, in Supersonic Flow 30
4 Staggered Cell V', spanning two cells 63
5 Cell V', used to calculate viscous flux 64
6 Iterative (left) and Grid Convergence (right) of U velocity Profile 71
7 Laminar velocity profiles, single sweep 72
8 Laminar velocity profiles, multi sweep 72
9 Turbulent velocity profiles 74
10 Effect on Skin Friction Coefficient 74
11 2D Axisymmetric Blunt Body Grid, and Magnetic Field Lines 76
12 Iterative (left) and Grid Convergence (right) of Pressure Coefficient Distribution 76
13 Shock standoff Distance as a function of Q_∞ 78
14 Magnitude of Magnetic Field, in Tesla 79
15 Vector Field of Lorentz Force, Dipole Field 80
16 Vector Field of Lorentz Force, Uniform Field 81
17 Density Profiles along Stagnation Line 81
18 Shock Stand-off, Uniform and Dipole Fields 82
19 Shock standoff Distance as a function of M_∞ 83
20 Shock and expansion waves through compression-expansion channel . . . 90
21 Normalised pressure distributions, no magnetic field 91
22 Field Imposed After 2 Sweeps, Pressure Distribution at j=1 92
23 Field Imposed After 2 Sweeps, Pressure Distribution at j=20 93
24 Field Imposed After 2 Sweeps, Pressure Distribution at j=50 93
25 Field Imposed After 2 Sweeps, Pressure Distribution at j=110 94
26 Constant Field Pressure Distributions, j=1 and j=20 94
27 Constant Flow,B_x and B_y Distributions, along j=1 95
28 Manufactured Solution for B_x: Test 1 101
29 B_x,B_y Profiles for Multiple Grid Levels, in x and y 102
30 B_x,B_y Profiles in x and y, Solution a function of x only 104
31 B_x,B_y Profiles in x and y, Source term removed 104
32 B_x,B_y Profiles in x and y, Solution a function of y only 106
33 B_x,B_y Profiles for Multiple Grid Levels, in x and y 107

34 Manufactured Solution for B_x: Test 2 109
35 B_x, Profile for Multiple Grid Levels, in y 110
36 B_y Profiles for Multiple Grid Levels, in x 110
37 L2 Norms of Solution Error, in B_x and B_y 111
38 B_x distributions, along j=1 112
39 B_y distributions, along j=1 112
40 Central Composite Design with n = 3 variables 118
41 Orthogonal Sampling Procedures 119
42 Optimal solution dependency on initial point 122
43 Power Law Body profiles 136
44 Power Law Grid, for n=0.6575 137
45 PNS and Response Surface predictions of Drag Coefficient, M_∞ = 5.0 . . 138
46 Shock Standoff for n=0.625, and n=0.7025 140
47 Ramjet Schematic 142
48 Physical features of the SHyFE intake flowfield 143
49 SHyFE grid, and vicinity of the cowl 144
50 Mach number contours ahead of cowl, velocity vectors over the step . . . 145
51 Geometry after Modifications 146
52 Pressure coefficient profiles for iterative and grid convergence 148
53 Shock front location as a function of Mach number 149
54 Shock Front locations, having added sample data in vicinity of original minimum 151
55 Magnetic Field Line Schematic for SHyFE Geometry 153
56 Objective function, as a function of Magnetic Interaction Parameter . . . 155
57 Objective function, after refinement of Q_∞ range 156
58 $|y_{cowl} - y_{\rho_\infty}|$ as a function of dipole location 157
59 Max Lorentz Force as a function of dipole location 158
60 Lorentz force contours, Domain of influence of dipole at different locations 159
61 Sample point distribution after 1 (left) and 1000 (right) simulations 161
62 Sample Data and 2^{nd} order Polynomial Representation 162
63 Sample Data and 2^{nd} order Polynomial Representation, second iteration . 163
64 RBF function generated using original sample data 167
65 Objective function contours, illustrating multiple local optima 168
66 Contour Profiles near global minimum, after 1 (top) and 5 (bottom) iterations 170
67 Effect of a small change in Q_∞ 171
68 ONERA B1 Slender Body 178

69 Circumferential Pressure Coefficient Distributions, on Three Grids 181
70 Axial Pressure Coefficient Distributions 182
71 Axial Pressure Coefficient Distributions 182
72 Circumferential Pressure Coefficient Distributions, $\alpha = 5°$ 183
73 Circumferential Pressure Coefficient Distributions, $\alpha = 10°$ 184
74 Circumferential Pressure Coefficient Distributions, $\alpha = 15°$ 185
75 Vortex Structures for Flows at Incidence 187
76 Magnetic Field Orientation for Slender Body 188
77 Azimuthal Dipole Locations for each Streamwise Station 189
78 Side Force Coefficient, at Zero Incidence 190
79 Circumferential Pressure Coefficient Distributions, $\alpha = 0°, x = 2.0D$ . . . 192
80 Vorticity Magnitude Contours, $\alpha = 0°, x = 2.0D, \phi = 210°$ 193
81 Vorticity Magnitude Contours, $\alpha = 0°, x = 2.0D, \phi = 330°$ 194
82 Streamlines, $\alpha = 0°, x = 2.0D, \phi = 210°$ 195
83 Streamlines, $\alpha = 0°, x = 2.0D, \phi = 330°$ 195
84 Side Force Coefficient, $\alpha = 5°$ 197
85 Side Force Coefficient, $\alpha = 10°$ 197
86 Side Force Coefficient, $\alpha = 15°$ 197
87 Vorticity Magnitude Contours, $\alpha = 5°, \phi = 330°$ 198
88 Circumferential Pressure Coefficient Distributions, $\alpha = 5°, x = 0.5D, \phi =$ 330° 199
89 Circumferential Pressure Coefficient Distributions, $\alpha = 5°, \phi = 330°, x =$ 7.6D 199
90 Streamlines, $\alpha = 5°, x = 2.0D, \phi = 330°$ 200
91 Vorticity Magnitude Contours, $\alpha = 15°, \phi = 330°$ 201
92 Lorentz Force Vector Field, $\alpha = 15°, x = 2.0D$ 202
93 Lift Coefficient Variation 202
94 Lift Coefficient Variation 203
95 Lorentz Force Vector Field, $\alpha = 15°, x = 2.0D, \phi = 270°$ 203
96 Circumferential Pressure Coefficient, Starboard side. $\alpha = 15°, x = 3.0D$. 204
97 Drag Coefficient Variation 205
98 Skin Friction Distributions for $\alpha = 10°$, Field applied at $\phi = 330°$ 206
99 Pitching Moment Coefficient, as a function of Angle of Incidence 209

LIST OF TABLES

1 Shock Stand-off Distances on Grid Levels 77
2 Grid properties 85
3 Grid Common Ratio Values 85
4 Table of sample data for regression coefficients 127
5 Iterative and Grid Convergence for Power Law Body, n=0.65 138
6 Effect of Mach number on Optimum Parameter 139
7 Shock stand-off positions at different convergence tolerances 147
8 Shock stand-off positions for grid levels 147
9 RBF and PNS predictions to objective function 169
10 Iterative and Grid Convergence $\alpha = 0.0°$ 179
11 Iterative and Grid Convergence $\alpha = 10.0°$ 179
12 C_L Experimental Results for B1, with and without fin, from [1] 207
13 Delta wing Lift Coefficient, from [151] 208
14 Table of sample data for Regression coefficients 236

NOMENCLATURE

Units

The units which are used in the nomenclature have the following meanings:

M	mass
L	length
T	time

Symbols

Symbol	Unit	Quantity
a	L/T	speed of sound
A		area of cell interface; Alfven velocity
$\mathbf{A}$		flux Jacobian
$\mathbf{A}_{u,v,w,E}$		contributions to momentum and energy equations
B		Magnetic Field Vector
c	L/T	speed of light in a vacuum; magnetic field wave speeds
$\mathbf{c}_i$		sample point for radial basis function
c_D		drag coefficient
c_f		skin friction coefficient
c_L		lift coefficient
c_p		pressure coefficient
d,D	L	diameter of body
$d_{i,j}$		Euclidean distance between samples i and j
E	ML^2/T^2	total energy
e_t	ML^2/T^2	total energy
$\mathbf{E}$		electric field vector
$\mathbf{F}_n$		Flux vector normal to a surface
h		grid spacing; shift parameter
$\mathbf{H}$		Volumetric source term
$\hat{\mathbf{i}}, \hat{\mathbf{j}}, \hat{\mathbf{k}}$		unit vectors in i,j,k directions
i		grid node index in the x dimension; multi purpose index
$\mathbf{I}$		Identity matrix
j		grid node index in the y dimension
$\mathbf{J}$		diffusion term for gas species and total energy
$\mathbf{j}$		sum of convection and conduction current
k		grid node index in the z dimension; coefficient of thermal conductivity
Kn		Knudsen number
l		length of body; cell edge length
L		Typical length scale

M		Mach number
$\mathbf{m}$		vector dipole moment
$\hat{\mathbf{m}}$		Local Mach number
n		direction normal to a surface; power law exponent
$\hat{\mathbf{n}}$		unit normal directed into the cell volume
p	ML/T^2	pressure
$\mathbf{Q}$		vector of conserved variables
Q		magnetic interaction parameter
r		body fineness ratio
$\mathbf{r_0}$		dipole centre
R		distance between any point $\mathbf{x}$ and $\mathbf{r_0}$
Re		Reynolds number
Re_m		Magnetic Reynolds number
$\mathbf{R}$		Right Hand Side of conservation equation
δs_{beg}	L	grid spacing at beginning of an edge
δs_{end}	L	grid spacing at end of an edge
S_m, S_∞		Magnetic force number
$\mathbf{s}$		Surface area vector
S		volume surface; source term for manufacture solution
t	T	time
δt	T	simulation time step
T		temperature, in Kelvin
u,v,w	L/T	velocity components of $\mathbf{u}$
$\mathbf{u}$	L/T	flow velocity
V	L^3	volume of a grid
x	L	streamwise position of dipole
x, y, z	L	position components of $\mathbf{x}$
$\mathbf{x}$	L	position vector
y		objective function for optimization
α		angle of incidence
β		shock angle; radial basis function exponent
ϵ_0		permittivity of free space
ζ		variable to denote crossflow (z) direction
η		variable to denote crossflow (y) direction
θ		azimuthal angle on slender body
γ		ratio of the specific heats
δ		boundary layer thickness
λ	L	mean free path; magnetic diffusivity
λ	M/LT	second viscosity
λ		eigenvalues of Jacobian
μ	M/LT	dynamic viscosity
μ_T	M/LT	turbulent viscosity

ξ		variable to denote streamwise direction
$\hat{\xi}$		unit normal in streamwise direction
ρ	M/L^3	density; radial basis function
ρ_c	M/L^3	electric charge density
$\Delta\tau$		Pseudo time step
$\tau_{i,j}$		Shear stress tensor
ϕ		azimuthal position of dipole; normalized radial basis function
ω		Vigneron's parameter; production term for gas species

Superscripts and Subscripts

$(.)_a$	applied component of magnetic field; Alfven wave
$(.)_{AVE}$	cell-averaged quantity
$(.)_{cowl}$	position of SHyFE cowl
$(.)_f$	fast magnetic wave
$(.)_i$	tensor index; cell index; index for gas species
$(.)_{i,j,k}$	denotes anything at grid node i,j,k
$(.)_\infty$	reference quantity
$(.)^{inv}$	inviscid
$(.)_j$	tensor index; cell index
$(.)_k$	cell index
$(.)_{min}$	minimum of a quantity
$(.)_{MMS}$	manufactured solution
$(.)_n$	vector directed normal to a cell interface; iteration number
$(.)_s$	slow magnetic wave
$(.)^T$	transpose
$(.)^{vig}$	denotes Vigneron's approximation
$(.)^{vis}$	viscous
$(.)_\xi$	vector taken in ξ direction
$(.)_{x,y,z}$	x,y,z components of given vector
$(.)_0$	variables on left/bottom of a cell interface
$(.)_1$	variables on right/top of a cell interface
$(.)^*$	non-dimensional variable

CHAPTER 1

Introduction

Interest in hypersonic flows has grown considerably since the end of the Second World War. The Cold War era saw the United States and the Soviet Union injecting a vast amount of funds into what would prove to be the dawn of the hypersonic age.

In 1949, the V-2, which was developed initially in Nazi Germany, and subsequently brought to the United States after the Second World War, was launched from the test grounds on White Sands. This test was one of the first in a series of experiments to assess the usage of multistage rockets to achieve higher altitudes, as attached to the V-2 was another slender body rocket, the WAC Corporal. This combined "Bumper" rocket, reached an altitude of 400km, and achieved a velocity of 8290 km/h, the equivalent of about Mach 7, a record at the time. Just over ten years later, through the use of a multistage rocket, Yuri Gagarin's pioneering manned space mission allowed him to orbit the earth. Upon firing the retro rocket to take him back into the earth's atmosphere, Vostok 1 travelled at speeds up to 25 times the speed of sound. Later that year would see the beginning of series of test flights by the U.S. Air Force, using the X-15, which exceeded velocities of Mach 5.

The above are several examples of historical firsts [8], as far as hypersonic flight is concerned. Following the above, events have been a series of further milestones, Mercury, Gemini and the Space Shuttle program to name but a few. More recently, NASA's X-43A became the first test aircraft to fly at Mach 10, using a SCRAMJET engine.

Through military applications such as Inter-Continental Ballistic Missiles (ICBM's), space exploration, and in the design of next generation civil aircraft, interest in hypersonic aerodynamics has grown considerably over the past half century. Although hypersonic flight has been achieved, research into hypersonic flight technologies still very much continues, in the prospect of hypersonic flight being as common as large commercial aircraft are today. There remain important practical hurdles that need to be overcome in order to make such modes of transport re-usable, and hence economically viable.

One of the major problems encountered by hypersonic vehicles on a ballistic re-entry trajectory is extreme temperatures, as a result of heat conduction and friction, which the body has to endure. Upon atmospheric reentry for example, it is known that body temperatures can extend up to approximately 10,000 degrees Kelvin. Vehicle designers must regard this as a paramount issue, as without necessary precautions the kinetic energy

is large enough to vapourise the body. This has consequences particularly on the shape of the body. In 1958, Allen and Eggers [5] made the crucial discovery that a high drag, blunt body would provide the best geometrical shape for an effective heat protection system. This design has been part of spherical section, and sphere cone bodies, such as that seen on the Apollo or Galileo space capsules. The more recent Shuttle program is based on a delta-wing geometry, but nevertheless it still employed a blunted nose region.

In addition to the blunted geometries, a variety of thermal protection systems (TPS) are used on reentry vehicles to overcome the high temperatures encountered during hypersonic flight. Ablative thermal protections systems work by depositing layers of carbon on the outer layer of the body through pyrolysis, which prevents radiative heat transfer. In addition to this gases are produced, which act to lift the hot gas away from the body surface through blowing. This prevents heat transfer through convection. Thermal soak TPS consists of a set of tiles which form the surface of the body, and are designed to protect against a long duration of heat at a lower intensity, rather than the largest peak heat fluxes. The tiles used can be heated up to 1000K, and still be relatively warm to the touch. However they suffer from the disadvantage that they are brittle, and are easily damaged. Other passive and actively cooled mechanisms are available to supplement these, but the two approaches outlined above are most commonplace for withstanding high temperatures.

The life cycle of such hypersonic vehicles is often given in terms of the cost of the thermal protection system. While it may be difficult to assess exactly the cost of such a system, the fact that we do not yet see hypersonic flight on a commercial scale, suggests that it is currently prohibitively expensive. Indeed, the aforementioned TPS on reentry vehicles undergo rigorous examination before the re-use of the vehicle is even considered, and consequently hypersonic flight on a large scale is somewhat distant. Alternative means of protecting the vehicle need to be considered.

Due to the high temperatures encountered during hypersonic flight, it is not uncommon for the flow to ionise. Under such conditions, ions and electrons are present in the flow, and to a greater or lesser extent, depending on the conductivity of the fluid, the flow is then subject to the effects of electromagnetic forces. It is with this in mind that research into the use of magneto-hydrodynamics (MHD) for hypersonic flows is being considered.

The idea of applying a magnetic field to a hypersonic flow field was in fact considered initially during the 1950's, at the time when interest in hypersonic flight was first spawning. At the time, various theoretical treatises were published outlining the effects of applying a magnetic field to pertinent flow problems. At the time however, the use of magnetic fields was not seen as a viable solution, due to the problems associated with being able to apply strong enough magnetic fields to influence the flow.

Interest in the area has become renewed recently, as the emergence of powerful

electromagnets, and various methods of ionising the flow have rekindled the potential applicability of magneto-hydrodynamics to hypersonic flows. While experimental and computational studies into the effects of magneto hydrodynamics is widespread, currently little has been done to address the issue as what form an optimal magnetic field should take for a given hypersonic vehicle.

1.1 Aims and Objectives

The present work aims to develop a better understanding of the underlying physical phenomena that occur when a magnetic field is applied to an ionised flow field, over supersonic and hypersonic flight vehicles of interest.

Specifically, the work seeks to identify the most suitable magnetic field configuration required for a generic hypersonic vehicle, given a set of design constraints. The Low Magnetic Reynolds number model, and the simplified magneto-hydrodynamic model are developed and integrated into an existing computational fluid dynamics solver, which are subsequently verified and validated.

Initially studies are performed over simpler geometries, that are typical features found within a hypersonic vehicle, to comprehend the effects of a magnetic field in isolation. Later a full study of the flow past more general vehicles is considered to examine the effects in unison.

In order to achieve the aims specified, the following objectives can be established:

- Assess suitability of IMPNS code to solving problems typically encountered in hypersonic flight, in the absence of a magnetic field.
- Set up optimisation tools required to perform a MHD optimisation study. This requires independent testing of the MHD models, to assess the accuracy of the optimisation procedures themselves.
- Investigate several MHD models, and implement them into the IMPNS flow solver. Perform verification studies, as well as validation of models with available test cases.
- Investigate the effects of applying a magnetic field to isolated components of a hypersonic vehicle.
- Optimisation study on a general hypersonic vehicle, which takes into account the effect of the applied magnetic field.
- Identify novel areas of application for magneto-hydrodynamics to aerodynamics.

1.2 Outline of Thesis

The reader should bear in mind that every chapter in this thesis forms part of the foundation that will be used in the optimisation study based on the use of a magnetic field. Every component of the optimisation tool must be tested rigorously. Not only is this necessary to ensure confidence in the methods and models used, but it is also required so that bounds may also be placed on their domains of applicability. With this perspective, every section is verified and/or validated to the greatest extent possible.

The following chapter is a review of the environment in which hypersonic vehicles operate, and provides the context of what aspects ought to be considered in designing such a vehicle. A discussion of several prediction methods is ensued by a description of the parabolized Navier Stokes model, along with a demonstration of the predictive capabilities of the model for the problems of interest.

Next, the phenomenology of magnetic fields applied to ionised flows is discussed, and an introduction as to how magneto-hydrodynamics may alleviate some of the problems encountered is discussed. An overview as to how magnetic fields have been used in practical flow problems is also provided.

Following this, the low magnetic Reynolds number model is developed and validated, and the simplified magneto-hydrodynamic model is introduced. A method of manufactured solutions procedure is applied to the latter, to verify the implementation, and the former model is validated extensively to cover cases that will form building blocks for the final study.

This section is ensued by a description of the optimisation methods used in aerodynamic design, and also a discussion of sampling methods. The methods to be used subsequently are tested in a closed form solution, and a minimal drag body problem which has a theoretical solution.

Chapter 9 conducts a novel optimisation study over a ramjet intake, aimed at analysing the optimal field configuration, given a set of design considerations, and the final chapter considers the effects of applying a magnetic field to a slender body with the aim of generating asymmetric side forces. The thesis concludes with a discussion of the main findings of the study and suggestions for further work.

CHAPTER 2

The Hypersonic Flow Regime

It is instructive at this initial stage to provide an outline as to what the prominent features that characterise the hypersonic flow regime are. Given this, a quantitative description of the problems encountered is discerned, to which ultimately, the application of magnetic fields is hoped to provide a solution.

2.1 Aerodynamics of the Hypersonic Flow Environment

Categorisation of what constitutes the "hypersonic flow regime", is somewhat more intricate, compared to the definition of supersonic flow. The transition from subsonic to supersonic flow is clearly defined as the point at which the flow Mach number exceeds unity, and is characterised physically by the emergence of a shock.

As the following section will demonstrate, there are many discernible characteristics of hypersonic flows that distinguish it from the supersonic regime. However, unlike the appearance of shock waves in the transition to supersonic flow, there is no sudden isolatable feature that changes in the hypersonic regime. Rather there are a series of transitions that occur over a wide range of Mach numbers, typically anything from Mach 3 to about Mach 12.

A qualitative inspection of vehicles designed for the hypersonic flow environment reveals clear distinctions in some of the major characteristics, compared to supersonic and subsonic vehicles. For example, supersonic vehicles have distinctly isolatable features that can be identified as the mechanisms that provide lift, propulsion and storage. Consider the picture below of Mig-29 [1(a)]; lift is provided by its wings, propulsion by gas turbines and storage in its fuselage. In contrast, modern day hypersonic vehicles' components are more closely integrated as the illustration of a NASA Shuttle [1(b)] shows. Its delta wing geometry, and fuselage can be described as being part of a more common unit, and indeed, its engine is located at the rear of the fuselage. The same can be said of the scramjet powered X43 [1(c)], where the propulsion unit is located on the underside of the vehicle, and is designed to ensure the leading edge shock generated from the front of the body impinges on the cowl lip.

Supersonic designs are commonly feature sharp nose regions, a slender fuselage, thin wings and sharp leading edges that are aimed to minimise wave drag at supersonic

(a) Mig 29

(b) Shuttle

(c) X43

Figure 1: Supersonic and hypersonic vehicles

speeds. This is demonstrated in the Mig 29 figure. Hypersonic vehicles are designed with alternative objectives in mind however, and thus applying the same thought process in designing hypersonic vehicles is not entirely straight forward. Consider for example the Shuttle body. Its delta wings are blended with the body, with blunted leading edges, and its nose is also rounded. Furthermore, the underside of the aircraft is flat. These have the objective of generating a shock wave that is detached from the body during atmospheric reentry, thereby reducing the heat transfer to the body surface. The features described above, have all been designed with the hypersonic environment in mind. The following are the key aspects that constitute this flow regime, and hence govern the design of the aforementioned vehicles.

- 1. THIN SHOCK LAYER:

  Conventional oblique shock theory demonstrates that for a given flow deflection angle, the higher the incident Mach number, the lower the wave angle. This consequence of higher Mach number has important repercussions in both vehicle design, and in the computational treatment when trying to simulate such problems. The stronger the incident Mach number, the higher the post shock enthalpy, which culminates in a higher temperature region nearer the surface. Furthermore, since the shock is confined to a thinner region nearer to the body, it experiences higher heat transfer rates. In addition to this, the shock wave can become merged with the viscous boundary layer.

  This results in complications when trying to simulate the problem numerically. A common approach for viscous flows is to use a boundary layer solver, and couple it to an inviscid Euler calculation outside of the boundary layer. The boundary layer equations assume that the normal variation of pressure, in relation to the solid surface is negligible. In other words, $\frac{\partial p}{\partial n} = 0$. If, as in the current case, a shock wave is passing through the boundary layer, then clearly such an approximation is unreasonable. A more sophisticated model, taking into account this variation, is needed.

- 2. ENTROPY LAYER:

  A common feature of many hypersonic vehicles, is the use of a blunt cone in the nose region of the body. In light of the proximity of an oblique shock to the surface of the body, and the high temperatures associated with a thin shock layer, the blunted region serves to detach the shock away from the body surface. This ensures that there is a greater distance between the body surface and the shock, and has beneficial effects on the heat transfer rates.

In the proximity of the tip of the blunt body, the shock can be regarded as a normal shock. As such, the entropy change across the shock in this region is larger than any other parts. This region of high entropy is convected downstream along the body surface, and has the effect of thickening the boundary layer. The region is also associated with larger velocity and thermodynamic gradients as a result of stronger vorticity, and poses similar problems to the thin shock layer when trying to use boundary layer calculations, as the interactions between the inviscid portion and the boundary layer are strongly coupled.

- 3. VISCOUS EFFECTS:

The extreme velocities associated with hypersonic flows means that the flow has a large amount of kinetic energy. In the presence of viscosity, this acts to increase the boundary layer temperature, and consequently the skin friction and heat transfer coefficients. Indeed, it is precisely the large heat transfer rates that govern much of the design of space re-entry vehicles.

Furthermore, conventional boundary layer theory illustrates that boundary layer thickness, δ, scales as $O(M_\infty^2)$. The thickening of the boundary layer with Mach number has effects on the inviscid flow region, which in turn affects the viscous region. This interaction between the flow regions has strong influences upon the lift and drag acting on the body, since the induced pressure acting on a body may change as a result of considerable interaction.

Once again, a standard boundary layer/Euler calculation is ineffective, as it is incapable of resolving the interactions between the two flow regions accurately. This can be accounted for by the effect of the hypersonic viscous interaction parameter, a measure of the degree of interaction between the viscous and inviscid regions.

- 4. HIGH TEMPERATURE EFFECTS:

Within the hypersonic flow regime, the high kinetic energy in the pre-shock region is decelerated into a high enthalpy, high temperature region, downstream of the shock. Typically the post-shock temperature increases as a function of Mach number, and associated with this are various physical phenomena, which play an increasingly important role. In the absence of models that are capable of capturing such activity, there can be severe misrepresentationss in quantities of interest.

To highlight such an error as an example, Anderson [8] considers the post shock temperature behind a normal shock. Assuming a perfect gas law, the post shock temperature is governed by the following shock relation;

$$T_{shock} = T_\infty \left(\frac{2\gamma(\gamma - 1)}{(\gamma + 1)^2} \right) M_\infty^2 sin^2\beta \tag{2.1.1}$$

For an atmospheric re-entry vehicle travelling at Mach 32.5 at an altitude of 35km and a freestream temperature of $283K$, then for a normal shock ($\beta = 90°$), the post shock temperature is $58128K$. Considering that the surface temperature of the sun is approximately $5700K$, it is hard to imagine anything being able to tolerate such extreme temperatures. The true figure is in fact about 11000 K, and this inaccuracy is a direct consequence of using the perfect gas law, as the assumption of a constant ratio of specific heats $\gamma = 1.4$, does not apply. An alternative model, such as chemical equilibrium and non-equilibrium models need to be used instead. Furthermore, constituent relationships for the viscosity and thermodynamic quantities such as thermal conductivity need to be revised.

As the ambient temperature increases, certain processes start to occur which change the chemical composition of the flow. From $800K$ onwards, vibrational excitation of diatomic molecules begins to occur, culminating in O_2 disassociation from around $2500\ K$, and N_2 from $4000K$ onwards, whence the following decompositions take place:

$$\begin{aligned} O_2 &\longrightarrow 2O \\ N_2 &\longrightarrow 2N \end{aligned} \tag{2.1.2}$$

At higher temperatures in excess of $9000K$, the process of ionisation starts to occur, resulting in free electrons within the flow domain;

$$\begin{aligned} O &\longrightarrow O^+ + e^- \\ N &\longrightarrow N^+ + e^- \end{aligned} \tag{2.1.3}$$

It is the presence of these free electrons that results in the communications black-out to the re-entry vehicle upon re-entry. Furthermore, free electrons are a source of electromagnetic forces which are another source of complication, as in itself, not only can it alter the nature of the flow by acting as another body force. The ionisation process can be taken into account using a non-equilibrium model which

incorporates electron production and absorption through the processes described by the above equations. Details of this can be found in [7].

- 5. Low Density/High Altitude Flow

  Given that almost nearly all hypersonic vehicles operate within the upper regions of the atmosphere, it would be ill advised to ignore any changes in flow properties that are due to changes in the operating altitude. The degree of rarefaction, or sparsity of the ambient gas, is commonly measured in terms of the Knudsen number. This is defined as the ratio of the mean free path to a typical length scale of the problem in question;

$$Kn = \lambda / L \tag{2.1.4}$$

The mean free path λ represents the average distance a gas particle has to travel before colliding with another particle, and is clearly an increasing function of altitude. The magnitude of the Knudsen number has consequences on the nature of the physics of the flow field. For example, the mean free path, λ in the above equation is an increasing function with respect to altitude, as the data in graph [2] illustrate.

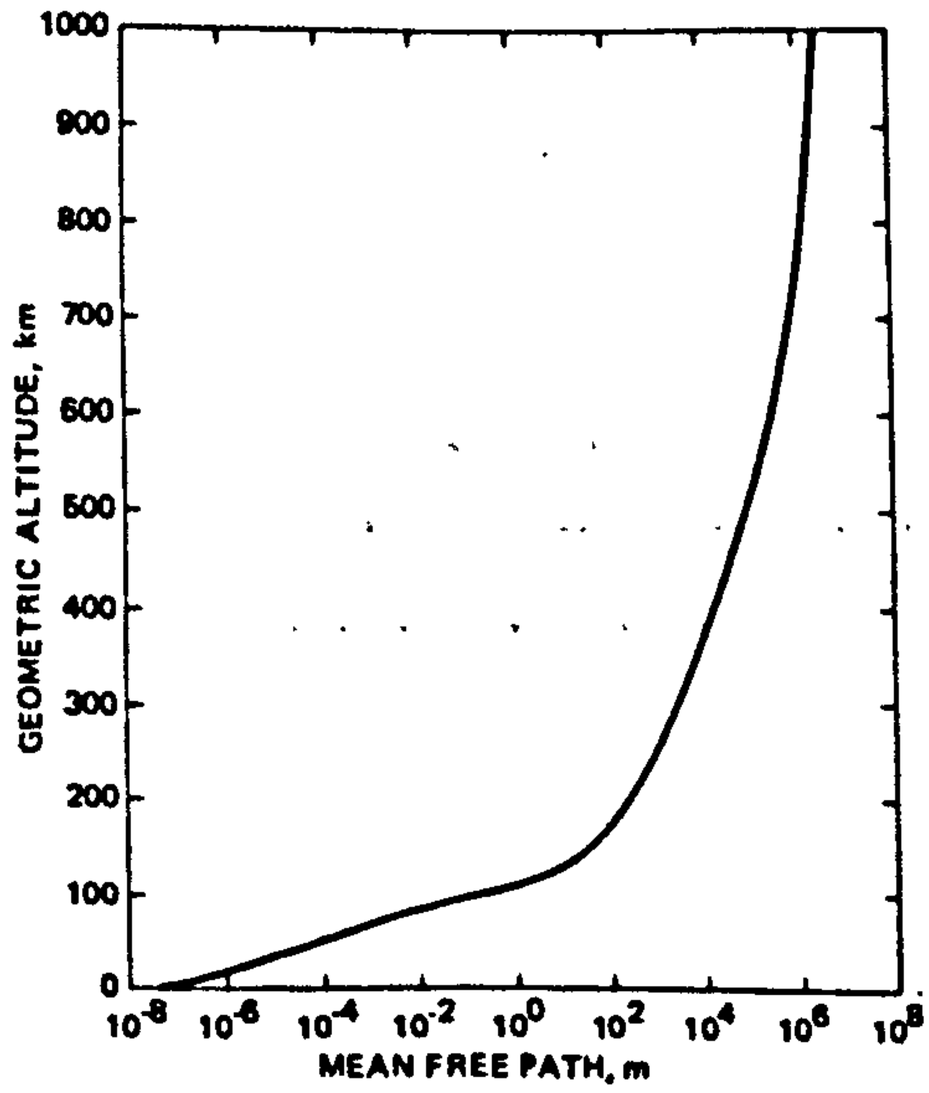

Figure 2: Mean Free Path as a Function of Altitude [3]

As such, since hypersonic vehicles typically operate at higher altitudes than most other aerial vehicles, its Knudsen number is typically greater, and in some instances, the continuum assumption ($Kn \ll 1$) can become violated. Furthermore, it can also

be shown that at higher Knudsen numbers, the zero-slip condition ceases to be a good approximation of behaviour in the vicinity of a solid surface, and that there is in fact a non-zero tangential velocity at the wall.

It is commonplace to utilise a Navier Stokes solver for hypersonic flow problems, but seldom is consideration made for the fact that the vehicle may be operating outside of the range of validity of the model. The following argument based on the Knudsen number is a clear illustration of this.

The Knudsen number provides a qualitative guide as to the type of models that ought to be used for different fluid dynamics problems. Typically, for $Kn \geq 1$, a statistical mechanics formulation is considered to be most suitable, as the mean free path of a molecule is comparable to a length scale of the problem. Conversely, for $Kn \ll 1$, the mean free path is negligibly small compared to the problem length scale, and hence continuum models ought to be considered. Indeed one of the basic assumptions of the Navier Stokes equations is that the fluid can be treated as a continuum, and not a collection of individual flow particles.

For large Knudsen numbers ($\gg 1$), direct simulation Monte Carlo (DSMC) methods [68], [19] are used commonly, and continuum models such as the Navier Stokes equations, or sub-models within, are used for the alternate extreme, $Kn \ll 1$. In addition to this, recently there is an increasing amount of interest in the continuum-transition regime frequently quoted as being in the range $0.1 \leq Kn \leq 1$, akin to the range of Knudsen numbers within which hypersonic vehicles operate. Various solution methods are currently under investigation, including hybrid Navier Stokes-DSMC calculations [29],[27], and 'extended hydrodynamic' models, such as the various forms of the Burnett equations [21],[3] ,[86].

2.2 Conclusions

This section illustrated the operating conditions of many hypersonic vehicles, and the factors that need to be considered when designing vehicles, or in trying to simulate such flows. It highlighted the requirement for models that adequately describing hypersonic flow phenomena in its entirety. Chemistry models to describe the processes of dissociation and ionisation, and extended formulations that capture the effects of increasing Mach number are both areas that ought to be taken into account.

While the current thesis will not go into detail regarding these models, it is nonetheless important to be aware of the limitations of the models being used, when taking into account its accuracy. Despite the fact that not all models may be implemented within

IMPNS, by taking note of this, we are more aware of the fact that certain features may not be captured by the code, due to the lack of certain models.

Without a significantly greater computational capability, it would not make sense to implement all models that take into account chemistry, rarefaction and so on, as computational overheads soon increase very quickly. It is therefore necessary to make a judicious choice as to what models ought to be incorporated into IMPNS. The next section attempts to address this issue, providing an engineering background into the current and future roles of magneto-hydrodynamics.

CHAPTER 3

IMPNS and the PNS Equations

3.1 The Parabolised Navier Stokes Equations

For engineering problems of interest the designer is commonly confronted with the problem of obtaining a reasonable prototype to meet requirements. At the design stages of product development, time and cost constraints may well apply in being able to perform large scale computational calculations. Furthermore, the same argument can be applied to obtaining experimental data such as wind tunnel test data, for stages in the design process where immediate flight test data of prototypes is not immediately available. The user may have simplified empirical methods at his/her disposal, but these can tend to be unreliable for atypical novel designs, as they are inherently dependent on data from existing models.

Restricting attention to problems that require the use of computational fluid dynamics as a design tool, three dimensional solutions to the full Navier Stokes equations require a large amount of CPU time and memory resources. In time dependent computations, there are several different time scales that need to be resolved, requiring small time-stepping. Even steady calculations involve solutions to a four dimensional problem. The advent of multiprocessor machines has reduced the computation time required for such solutions, but the machines too represent an overhead for an organisation. Therefore for large scale problems of practical engineering interest do not necessarily make this model practical for all situations.

Fortunately several simplifications can be made to the Navier Stokes equations, which focus on particular aspects of flow physics. For example the boundary layer equations restrict attention to flows which are in the vicinity of a solid surface, where it is possible to reduce the momentum equation normal to the wall to a simple statement that the pressure variations normal to the wall are equal to zero. This greatly simplifies the system of equations to solve, as one need not solve the full momentum equation normal to the wall. The mathematical nature of the equations also change, from being an elliptic problem to a parabolic one, which lends itself to space marching algorithms that are easier to solve. The Euler equations on the other hand assumes that the flow is inviscid, equivalent to letting the Reynolds number tend to infinity in the Navier Stokes equations.

These models are advantageous as they are more easy to solve than the full governing equations, but at the expense of not being able to capture some of the flow phenomena.

Obviously, viscous interaction is not captured by the Euler equations, and there are several cases were the boundary layer equations are unsuitable. Near the leading edge of a flat plate boundary layer for example, there exists a merged layer region where the shock generated from the leading edge is submerged into the viscous region, and is indistinguishable to the rest of the flow. A schematic of the leading edge region of a flat plate boundary layer is presented in figure [3];

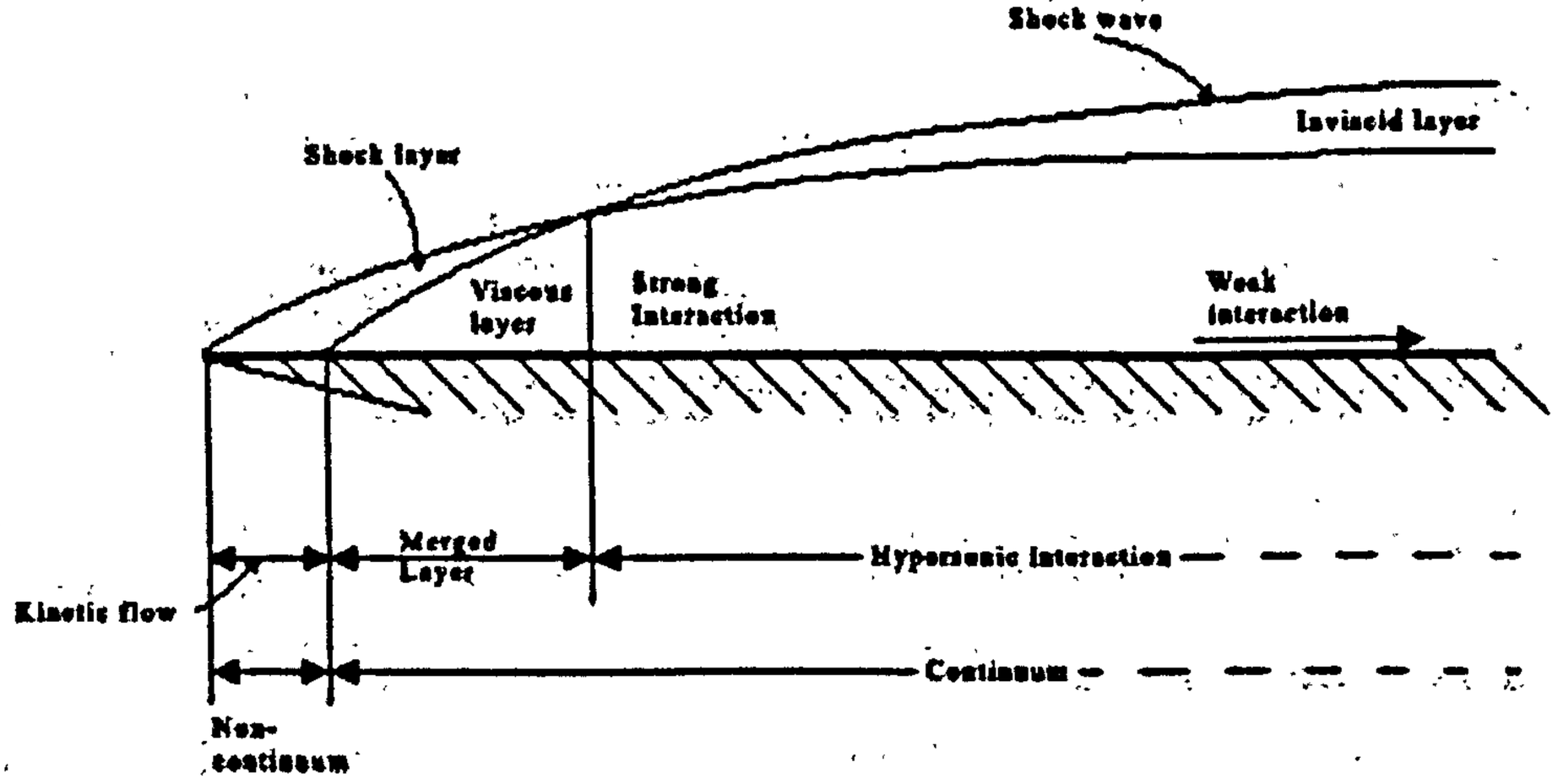

Figure 3: Leading Edge Characteristics of a Flat Plate, in Supersonic Flow

The boundary layer equations are not applicable here, as the model has been formulated to deal with cases where the inviscid and viscous flow regions are essentially decoupled, in other words, in the "weak interaction" region. When a boundary layer solver is coupled to an inviscid solver, the assumption is that the interactions between the viscous and inviscid regions are weak. As the flow evolves downstream, an inviscid region develops between the shock layer, and the viscous part of the flow. Prior to this, in the "strong interaction region" of the boundary layer the viscous and inviscid parts are entwined. To solve for flows in such a region the boundary layer equations may be coupled with an inviscid flow solver, but this method has been found to be inefficient compared to solvers where the governing equations capture both inviscid and viscous phenomena.

The issue of model complexity and computational expense is of great importance when choosing an appropriate model. Combining this requirement with the observation in the previous section that one of the main areas of application is in hypersonic reentry vehicles, the Parabolised Navier Stokes (PNS) equations provide a suitable compromise between the two ends.

To illustrate this point, the PNS equations are able to predict three dimensional steady supersonic flows efficiently. Work by Qin et al [127, 14] and Tannehill [107, 155]

illustrate the accuracy in predicting supersonic flows for slender body vehicles such as missiles, and other supersonic configurations. The computational time required for a characteristic calculation is similar to that needed for the inviscid portion using an Euler solver, or the viscous part using a boundary layer code [6]. However, the advantage in the model is that it is valid in both portions of the flowfield, and is hence valid where there is strong interaction between the boundary layer and inviscid flow regions. The model is restrictive in the fact that the flow in the inviscid portion must be supersonic, but for the purposes of investigating the effect of magneto-hydrodynamics in the areas outlined before, this is no hindrance to the study. Indeed it is particularly suited to supersonic and hypersonic flows, and therefore this model was chosen as the development tool for the current work.

One of the disadvantages of the parabolized Navier Stokes equations is that although it can treat subsonic portions within an attached boundary layer through modifications such as Vigneron's approximation, it is unable to treat flows passed a blunt nosed body, or regions where streamwise separation is present, such as for a compression corner with a large enough wedge angle. To overcome this, one must solve for such probems using a multi-sweep algorithm. The procedure for the multi-sweep algorithm is as follows: an initial space marching sweep is performed, and the algorithm proceeds from the downstream to the upstream boundary of the multi-sweep region, and back again. The calculation continues upstream and downstream until convergence is obtained. The solution is assumed to be converged when the convergence criterion is satisfied for all stations without any further iterations on any station within the multi-sweep region.

The mathematical derivation of the parabolized Navier Stokes model is not as rigorous as the boundary layer equations or the Euler equations, but instead, have been formulated by considering particular flow problems. As a result of this, several different forms of the governing equations have appeared in the literature [26, 139]. Some formulaions neglect the pressure gradient term in the streamwise direction, a matter to be discussed later in this section. All come under the common label of Parabolised Navier Stokes.

A common similarity with all forms however, is that they consist of a simplified form of the steady Navier Stokes equations, with viscous derivatives omitted in the streamwise direction. For supersonic and hypersonic flows where the flow is predominantly in the streamwise direction, such an assumption is usually accurate. The model to be used throughout the thesis is that first proposed by Cheng et al [26], and is given by the following governing equations;

Continuity equation

$$\frac{\partial \rho u}{\partial x} + \frac{\partial \rho v}{\partial y} + \frac{\partial \rho w}{\partial z} = 0 \qquad (3.1.1)$$

X Momentum equation

$$\frac{\partial \rho uu}{\partial x} + \frac{\partial \rho uv}{\partial y} + \frac{\partial \rho uw}{\partial z} = -\frac{\partial p}{\partial x} + \frac{\partial}{\partial y}\left(\mu \frac{\partial u}{\partial y}\right) + \frac{\partial}{\partial z}\left(\mu \frac{\partial u}{\partial z}\right) \qquad (3.1.2)$$

Y Momentum equation

$$\frac{\partial \rho vu}{\partial x} + \frac{\partial \rho vv}{\partial y} + \frac{\partial \rho vw}{\partial z} = -\frac{\partial p}{\partial y} + \frac{\partial}{\partial y}\left((\lambda + 2\mu)\frac{\partial v}{\partial y} + \mu \frac{\partial w}{\partial z}\right) + \frac{\partial}{\partial z}\left(\mu\left[\frac{\partial w}{\partial y} + \frac{\partial v}{\partial z}\right]\right) \qquad (3.1.3)$$

Z Momentum equation

$$\frac{\partial \rho wu}{\partial x} + \frac{\partial \rho wv}{\partial y} + \frac{\partial \rho ww}{\partial z} = -\frac{\partial p}{\partial z} + \frac{\partial}{\partial y}\left(\mu\left[\frac{\partial v}{\partial z} + \frac{\partial w}{\partial y}\right]\right) + \frac{\partial}{\partial z}\left((\lambda + 2\mu)\frac{\partial w}{\partial z} + \mu \frac{\partial v}{\partial y}\right) \qquad (3.1.4)$$

Energy equation

$$\begin{aligned}\frac{\partial \rho uE}{\partial x} + \frac{\partial \rho vE}{\partial y} + \frac{\partial \rho wE}{\partial z} = {} & \rho \dot{q} + \frac{\partial}{\partial y}\left(k\frac{\partial T}{\partial y}\right) + \frac{\partial}{\partial z}\left(k\frac{\partial T}{\partial z}\right) - \left(\frac{\partial pu}{\partial x} + \frac{\partial pv}{\partial y} + \frac{\partial pw}{\partial z}\right) \\ & + \frac{\partial}{\partial y}\left(u\mu\frac{\partial u}{\partial y}\right) + \frac{\partial}{\partial z}\left(u\mu\frac{\partial u}{\partial z}\right) \\ & + \frac{\partial}{\partial y}\left(v\lambda\left[\frac{\partial v}{\partial y} + \frac{\partial w}{\partial z}\right] + 2v\mu\frac{\partial v}{\partial y}\right) + \frac{\partial}{\partial z}\left(v\mu\left[\frac{\partial w}{\partial y} + \frac{\partial v}{\partial z}\right]\right) \\ & + \frac{\partial}{\partial y}\left(w\mu\left[\frac{\partial w}{\partial y} + \frac{\partial v}{\partial z}\right]\right) \\ & + \frac{\partial}{\partial z}\left(w\lambda\left[\frac{\partial v}{\partial y} + \frac{\partial w}{\partial z}\right] + 2w\mu\frac{\partial w}{\partial z}\right)\end{aligned} \qquad (3.1.5)$$

where μ is the dynamic viscosity, and the second viscosity λ is taken to equal $\frac{2}{3}\mu$. The efficiency in solution time is obtained from the fact that the solution procedure reduces from a time-marching based solver commonly used for Navier Stokes calculations to a space marching algorithm. This is a consequence of being able to neglect the streamwise viscous derivatives on the right hand side of the above equations, meaning that the solution

at any one station uses only information from the stations immediately prior to the current one. The solution procedure is therefore more memory efficient than the time marching method commonly used for Navier Stokes equations, as only the grid data for the current station has to be stored. For single sweep cases, the model has thus been found to be computationally faster than the full system of equations.

In light of the applications outlined in the previous section, the PNS equations, using the multi-sweep algorithm described above, are a good choice for developing a magneto-hydrodynamic model. Aerospace applications where magneto-hydrodynamics may be utilised are almost unanimously supersonic or hypersonic, which the PNS equations are particularly suited to.

3.2 IMPNS Flow Solver

It is beneficial at this point to describe the main aspects of the proposed PNS solver, so as to provide a suitable background into the main issues concerning further model implementation. IMPNS (Implicit Multiple Parabolised Navier Stokes) is a space marching CFD solver used to simulate the effects of supersonic and hypersonic flows, by solving the above mentioned PNS equations. In the past it has been used to find flow solutions to various supersonic flow problems of interest. These include predicting flow characteristics over slender bodies [128, 127, 14] and in trying to understand supersonic flows around geometries that exhibit complex shock interaction behaviour [15, 126].

The PNS equations are discretised using a finite volume formulation, as shown:

$$\int_S F_n dS + \int_V H dV = 0 \tag{3.2.1}$$

with the flux $F_n = F_n^{inv} - F_n^{vis}$ and volumetric source terms $H = H^{inv} - H^{vis}$ being decomposed into convective and diffusive contributions. F_n^{inv} is given by $F_n^{inv} = (\hat{n}^T u)\Phi + (p, \hat{n}^T, 0)^T$ where $\hat{n}$ is the face unit normal vector directed into the cell volume, and

$$\Phi = (\rho, \rho u^T, \rho E)^T + p(0, 0, 0, 0, 1)^T \tag{3.2.2}$$

The diffusive flux is defined as

$$F_n^{vis} = \hat{n}^T[\tau(0, \hat{i}, \hat{j}, \hat{k}, u)^T + k(0, 0, 0, 0, \nabla T)^T] \tag{3.2.3}$$

where the components of the shear stress tensor are given by

$$\tau_{ij} = Re^{-1}(\mu + \mu_T) * \left(\frac{\partial u_j}{\partial x_i} + \frac{\partial u_i}{\partial x_j} - \frac{2}{3}\delta_{ij}\nabla^T u \right) \tag{3.2.4}$$

Closure to the above system of equations is provided by the perfect gas law, for the equation of state, and Sutherland's law is used to compute the laminar viscosity. An Euler calculation option is available for flows where viscous effects are negligible, and for turbulent flows, the one equation model of Spallart and Allmaras is available.

On a structured grid, equation [3.2.1] can be recast as

$$[F_\xi^{inv} s_\xi]_{i-1/2}^{i+1/2} + [F_\eta s_\eta]_{i-1/2}^{i+1/2} + [F_\zeta s_\zeta]_{i-1/2}^{i+1/2} = 0 \tag{3.2.5}$$

where s_i represents the surface area of grid cell surface for the co-ordinates. ξ represents the streamwise flow direction, and η and ζ are crossflow directions. Notice that the flux in the streamwise direction only includes an inviscid contribution, consistent with the PNS assumption.

The space marching algorithm proceeds from the most upstream station (i=1), to the most downstream (i=in), one streamwise station at a time. For each station a first order flux is calculated based on values of flow variables immediately upstream. Then for every crossflow plane, a pseudo time term is added to solve for the primitive variables in an iterative manner.The fluxes across cell volumes in the crossflow directions are approximated using either the Flux Vector Differencing scheme of Osher and Solomon [116], the flux vector splitting scheme proposed by Steger and Warming [153] or that of AUSM [89], with spatial resolution being enhanced by MUSCL [160] primitive variable interpolation. Viscous fluxes are calculated on a 'staggered cell', the union of two adjacent halves of grid cells either side of the interface being considered, and are evaluated at the staggered cell centre, based on information on the cell edges.

Close inspection of equation [3.1.2] illustrates the fact that space-marching cannot be applied directly to this equation, due to the $\frac{\partial p}{\partial x}$ pressure gradient term. Indeed, strictly speaking the governing equations lend themselves to space marching algorithms in regions where the local Mach number is greater than one outside of the viscous region. For any station within subsonic parts of the boundary layer, there are upstream influences. A space marching solution is not well posed in such regions, resulting in exponentially growing solutions, that are physically invalid. As mentioned earlier, some PNS models actually remove this term completely to ensure a simple unmodified space-marching

algorithm can be applied.

IMPNS resolves this term using two different methods, depending on the nature of the problem. Firstly, for flows not involving separation in the streamwise direction, a portion of the pressure gradient term is suppressed in the subsonic part of the boundary layer. Vigneron's modification [161] to the pressure gradient term is applied, which removes any elliptic influence of $\frac{\partial p}{\partial x}$, and hence any upstream propagation of information. The inviscid flux in the streamwise direction is replaced by

$$F_{\xi}^{vig} = F_{\xi}^{inv} - [1-\omega]p\begin{pmatrix} 0 \\ \hat{\xi} \\ 0 \end{pmatrix} \tag{3.2.6}$$

$$\omega = MIN\left\{1, \frac{\sigma_{vig}\gamma(\mathbf{m}^T\hat{\xi})^2}{1+(\gamma-1)(\mathbf{m}^T\hat{\xi})^2}\right\} \tag{3.2.7}$$

In the above expression, $\hat{\xi}$ is the unit normal in the streamwise direction, and $\hat{\mathbf{m}}$ is equivalent to the 'local Mach number' and is given by $\hat{\mathbf{m}} = \hat{\mathbf{u}}/c$. This ensures the space marched solution is stable, but imposes a restriction that prevents any upstream influence affecting the current station.

Vigneron's approximation is restrictive in that it does not allow streamwise separation to be captured. Another method of dealing with $\frac{\partial p}{\partial x}$, which does not rely on the afore mentioned approximation, is to use multi-sweeping. Initially, a single sweep calculation is made over the flow domain, and then the program performs a "backward sweep", from the end of the domain to the beginning, using flow data that has been computed from the initial sweep. Successive forward and backward sweeps of the flow domain are made, until convergence is obtained on all stations. This solution method removes the need for suppressing the streamwise pressure gradient term, as upstream influences are fully taken into account. The multisweep function of the code greatly extends the capability of the code, since it allows the solver to deal with cases that involve streamwise flow separation, and detached shocks for supersonic flows over blunt bodies. Strictly speaking under these circumstances, the equations are actually known as the "Thin Layer Navier Stokes" equations, whereby all viscous derivatives in a direction parallel to body surfaces are neglected [6]. These mixed hyperbolic parabolic equations may be solved using time marching algorithms normally used to solve the compressible Navier Stokes equations, although they just as easily lend themselves to forward and backward space marching outlined above.

The above illustrates the key features of the code that need to be considered to incorporate a MHD solver into the program. IMPNS also includes a multitude of other convergence acceleration procedures, such as implicit techniques and multigrid algorithms. The current work will not take advantage of these functionalities, but the interested reader is referred to the IMPNS Theory and User Guides [91, 92].

CHAPTER 4

Review of Past Literature

4.1 Introduction

As its name suggests, magneto-hydrodynamics deals with the study of electrically conducting fluids, such as liquid metals or plasmas. Traditionally, the area has found applications in geophysical problems examining the influence of the Earth's magnetic field spanning several tens of thousands of kilometres from the surface of the planet, as well as in astrophysics. Almost all matter contained within the universe consists of some kind of plasma, whether it be the stars, nebulae, relativistic jets or the vast amount of interstellar and interplanetary medium consisting of hot plasma, and cosmic rays. Magnetohydrodynamics serves as useful tool in describing motion within this conducting medium. Within engineering too, magneto-hydrodynamics has found applications in the control of liquid metals, within plasma confinement in nuclear fusion reactors, and in propulsion device of sea travelling vehicles. This has the benefit that it does not make use of any moving parts, and has been demonstrated to work on Mitsubishi's Yamato 1, capable of reaching speeds up to 8 knots [72]. This section provides an outline as to research that has taken place in the areas spanning the topic of magneto-hydrodynamics .

This section provides an overview of the state of research to the present date, from the theoretical interest from after the second world war, through to the most recent advances in numerical computations, the applications proposed, as well as the experimental investigations so far. It will serve to illustrate some of the voids in the current knowledge of the area, wherein the current work will attempt to fill some of these holes.

4.2 Interest within Aerospace

Within the aerospace community, interest in magneto-hydrodynamics became apparent with the advent of hypersonic flight. In pursuit of the space race, it was clear that one of the key challenges posed was in the atmospheric reentry of space modules, and magneto-hydrodynamics had been proposed as a control mechanism, alongside other hypersonic technologies. Consequently, the concept of applying magnetic fields to ionised flows for aerodynamics problems can be traced back to the 1950's, where several authors investigated the theoretical implications of applying magnetic fields to flow problems.

Bush [22] demonstrated that for a hypersonic flow past a blunt body, in the presence of a magnetic field would reduce the surface pressure distribution on the body, and increase the shock stand-off distance. Lykoudis [93] was also able to demonstrate an increase in shock stand-off with a suitably orientated field, a useful consequence of which is that the skin friction coefficient and heat transfer coefficient to the body can be reduced.

Attention was not restricted to reentry blunt body like configurations. For example, Resler and Sears [131] examined the effects of applying a uniform field between two wall surfaces encompassing a two dimensional channel flow. They demonstrated that upon applying a field normal to the flow, the flow velocities were decelerated, with increasing field strength. In the same work, they showed that for a one-dimensional channel flow, a magnetic field could be applied to prevent choking. Rossow [136] examined the case of a two dimensional incompressible flow over a flat plate with a magnetic field, imposed normal to the flow. He demonstrated similar changes to the velocity profiles, as for the Resler and Sears channel flow problem, in that the profiles are pushed further back, the greater the field intensity. Furthermore, his work demonstrated that in the presence of a magnetic field , the heat transfer to the wall would decrease.

These results had important engineering consequences, in that they identified the use of magnetic fields as a potential flow control device. Indeed, in Lykoudis' article, the author identifies one application of magneto-hydrodynamics to be for objects travelling at hypersonic velocities, where the large amounts of kinetic energy are transformed into thermal energies.

After considerable theoretical progress into what initially seemed like a positive prospect for magneto-hydrodynamics , interest in its application to aerodynamics dwindled somewhat. The inability to generate strong enough magnetic fields, and the amount of energy that would have to be spent in generating magnetic fields strong enough to produce the desired effects on the flowfield, were some of the hindering factors.

4.3 TPS and Heat Transfer Mitigation

In examining the hypersonic flow environment, one of the key problems is with vehicle reentry. At speeds greater twenty times the speed of sound, reentry vehicles experience temperatures in excess of up to 10000 degrees Kelvin [7]. The inability to maintain control of vehicles in such conditions resulted in accidents such as Soyuz 1 in 1967, the sub-orbital flight of the X-15 in November 1967, and space shuttle Columbia in February 2003. The structural failure of Columbia was caused by damage to the thermal protection system (TPS), on the left wing. It's leading edge was in fact damaged by a piece of insulation foam breaking off from the external tank during take off. Upon reentry, failure

of the TPS ultimately lead to the shuttle disintegrating.

The above example is a pertinent one in the discussion of magneto-hydrodynamic flow control, as it provides an illuminating case as to how magnetic fields may be applied as a control mechanism. At the time of writing of the above works by Resler and Sears [131], Bush [22] and Lykoudis [93] practical limitations were in place over the strengths of the magnetic field achievable, and the amount of energy that could be spent in such a system. In the area of designing thermal protection systems for atmospheric reentry, advances in materials were proving to be more successful in heat transfer mitigation.

Modern day thermal protection systems (TPS) on a shuttle consists of several different materials at specific locations that are designed to provide resistance to differing heat loads. In the blunted nose and wing leading edges for example reinforced carbon-carbon is used to protect the body from temperatures exceeding 1500 Kelvin. This is also used in the nose cones for Intercontinental Ballistic Missiles. On other parts of the body, various types of surface insulation tiles line the surface of the body, again to tolerate different temperatures. Modern TPS systems have the advantage that they are lightweight and reusable, that have allowed shuttle programs to undertake several flights using the vehicle.

Nevertheless, the cost of lining reentry vehicles with TPS, and the lack of safeguards in place in case of failure, such as that witnessed during the last mission of Columbia in 2003, are obstacles that prevent the more widespread use of hypersonic flight as a commercial means of travel. Reinforced carbon-carbon tiles, for example, can exceed $2000 per panel [73], and considering the fact that an entire aircraft needs to covered with such panels, this pushes it well out of range of mass scale production for a potential commercial hypersonic vehicle. In view of this, there are still potential gains to be made in examining the viability of other thermal protection systems. In recent years, the concept of magneto-hydrodynamic flow control for such flows has begun to regain interest due to technological advances in various areas.

Electromagnets, for example are demonstrably advantageous over permanent magnets since they can generate a wide range of magnetic field strengths by controlling the amount of electrical current flowing through their wiring. In their simplest form they consist of a conducting wire wrapped into loops, but placing ferromagnetic materials within the core also magnify the field strength. The advancement of electromagnetism, has regenerated interest in the area, as it allows for greater field strengths to be created. In addition to this, flow ionisation techniques, such as glow discharge generation, radio frequency generation, and direct current discharge, has helped to widen the net of magneto-hydrodynamics to other classes of flows, that are not commonly associated with temperatures extreme enough to cause ionisation.

4.4 Experimental Investigations

A considerable number of studies have investigated the effects of introducing an ionised medium into the forebody region of hypersonic blunt body vehicles. Plasma is injected into the flow in the form of a counter-acting jet, from the body surface, upstream of the bow shock. Ganiev et al. [57] for example , were able to demonstrate favourable reductions in the drag coefficient over subsonic, transonic and supersonic Mach numbers. They found that the drag coefficient was also dependent on the temperature of the injected plasma. This intuitively makes sense, since a larger temperature results in a larger speed of sound, which is proportional to $\sqrt{T}$, and hence a smaller local Mach number. This means that a larger area must exist in front of the blunt body for flow to pass, and therefore a greater standoff distance for the bow shock, and also a reduction in drag coefficient. Bityurin et al. [16] also reported reductions in drag using upstream energy addition to the stagnation region of the flow, and Shang et al. [142] have demonstrated the effect both experimentally and computationally. Other flow control mechanisms also exist, as illustrated by Miles [106], who has focused on energy deposition using microwaves and electron beams.

Benefits in drag reduction of up to 60% have been reported by Ganiev et al, but this requires the generation of a uniform plasma in a controlled environment. In trying to address some of the issues such as maintaining a high enough temperature to prevent electrons and ions recombining, or in trying to deliver such a plasma into the flowfield, research has also gone into developing test facilities that are capable of maintaining and diagnosing the stability of plasmas. One such technique is based on emitting a radio frequency signal, which if sufficiently intense will cause air in the vicinity of an electrode to ionise [143]. Direct current discharge is also an attractive alternative, whereby a current is passed through a gas via a cathode and an electrode [137].

It has also been shown that forcing moments may be introduced to flow geometries using plasma deposition [82]. Depositing energy off the centre line in front of the vehicle is shown to generate a controlling steering moment. In the vicinity of the body, pressure waves due to energy addition interact with the body itself to divert it away from the deposition area. Further research into trying to control the region of plasma discharge are also in progress [105]. In examining off design conditions for a typical scramjet intake, Miles et al. [105] also present studies utilising magneto-hydrodynamic as a flow control device to control shock structure. The incident Mach number is locally reduced by introducing Joule heating, and by adding an opposing body force. These body forces have the addition benefit of acting as a medium for power extraction from the flow. Within the same study Miles et al present applications for plasmas and magneto-hydrodynamics in sonic boom

mitigation, as also investigated by Batdorf [12] and Crow and Bergmeier [37], and drag reduction techniques similar to plasma spike injection for blunt body flows.

4.5 Computational Methods for MHD

It is clear from the previous section that there are significant benefits to be gained over a wide number of applications from incorporating magneto-hydrodynamics into flow control mechanisms. Alongside the experimental endeavours to both understand the physics, and in identifying application areas, there has also been considerable efforts in the numerical computation of magneto-hydrodynamic flows.

The theoretical contributions of the authors in section [4.2] have been invaluable in addressing the significance of its effects on an ionised flowfield. However, the effects observed within their works, despite displaying correct behaviour, are reliant on several simplifications which may not be truly representative of behaviour in the physical world. It would be unwise to rely on a purely theoretical model to predict the effect of an imposed field on a complete system.

The problem lies in the fact that the results presented are limited by largely restrictive assumptions imposed to simplify the problems they have endeavoured to address. In Lykoudis' [93] article for example, in deriving an expression for the shock stand-off distance, he assumed the following;

- There exists a constant magnetic field, between the body and the shock.
- The electric field has no effect on the flow.
- Bow shock in front of the body is spherical or cylindrical.
- Electrical conductivity is a scalar constant.
- Flow is inviscid.

The second item in the above list may be justified with a reasonable degree of confidence, although it is strictly case dependent and relies on what the desired effects the researcher is hoping to achieve. Several computational studies make this assumption in that the contribution of the magnetic field to the Lorentz force is dominant over that of the electric field [71, 78]. In other works however, the electric field plays a crucial role in trying to accelerate the flow field through energy addition [121, 158]. The third point is restrictive in that it only permits the analysis of bodies that have a spherical front body region. This maybe the case for many hypersonic geometries, but does not allow a designer the option of considering radically different bodies.

The other assumptions made upon the physics of the flow need to be treated with caution. On the simplest level, by neglecting any viscous effects, any near wall behaviour is not accurately predicted. This has implications particularly for heat transfer, a crucial factor to consider when dealing with hypersonic vehicles.

A constant electrical conductivity and magnetic field is certainly a convenience, as it removes the requirement to compute these quantities, which are complex in themselves, often expressible as a tensor [59]. In a multispecies gas, it would require additional equations for its evolution due to the motion of electrons. Imposing the constant conductivity assumption would commonly reduce the accuracy of the model, as it does not allow the model to capture the physics of the real life system. The extent of ionisation, and consequently the conductivity of the fluid is largely a function of temperature. As the previous section outlined, at a certain temperature, N^2 begins to ionise, and then O^2 at higher temperatures. Indeed, as the ambient temperature rises, a larger proportion of these molecules lose their electrons, and consequently the conductivity is increased. It is known that the temperature between a bow shock, and a body is not constant, therefore a constant conductivity assumption is not reasonable. Furthermore, the effect of a magnetic field greatly depends on the conductivity of the flow, so misjudgements in predicting it may have unforeseen consequences.

The notion of a 'constant' magnetic field, may however be sensible in some situations. A magnetic field uniformly distributed in a particular direction would satisfy such an assumption, for example. This is clearly convenient as it removes the need for solving Maxwell's equations for the magnetic field . However care needs to be exercised, as the nature of the flow, its effects on the magnetic field , and the orientation of the field itself need to be determined apriori, before committing to such an assumption. For a general test case, this may not always be achievable, and furthermore, for an electrically conducting fluid in the presence of a field an induced magnetic field is generated due to the evolution of the flow, and the field will therefore not be constant.

Clearly, the hypotheses made in these works have to be relaxed if one is to make an attempt to model the physical system more accurately. One of the problems encountered in examining magneto-hydrodynamic flows is that it is a truly multidisciplinary topic [154]. For example, to be able to make use of applying a magnetic field to the flow, one needs to ensure a certain degree of ionisation. To examine this in turn requires an understanding of the thermodynamic phenomena entrenched within the flow. Equilibrium or non-equilibrium chemistry models may describe these, but also add to the complexity of the system. Furthermore, to determine the effects of an electromagnetic field, the constitutive properties of a plasma need to be understood, in addition to this. This might include the electron density distribution, the electrical conductivity, as well as its transport

properties.

4.6 Magneto Gasdynamic Models

4.6.1 Full Form

In order to obtain a quantitative understanding of the effects magnetic fields have on an ionised flowfield, it is necessary to prescribe an appropriate model to describe such phenomena. The objective here is to describe the magneto-hydrodynamic models to be subsequently used as part of the verification and validations processes.

The initial assumption to be made is that the medium to be analysed can be regarded as a continuum. The description contained herein therefore falls short of a microscopic gas dynamic approach, where Boltzmann's equation is combined with suitable electromagnetic terms. A consequence of the continuum assumption is that the Knudsen number, defined as $Kn = \lambda/L$, the ratio of λ, the mean free path, and L the characteristic length scale of the problem, is small, and that the fluid is dominated by collisions. Following this, the magneto-fluid dynamic model includes balance equations for mass, momentum and energy, akin to a normal fluid, as well as Maxwell's equations describing the evolution of the magnetic field.

In general for a magnetic field to have an influence on a fluid, it must be at least partially ionised. Typically, the main constituents of air, oxygen and nitrogen, disassociate from 2500K upwards, and will then ionise at temperatures in excess of 9000K. The degree of ionisation dictates the quantity of electrons present in the flow, and hence the conductivity of the fluid.

For a general gas mixture in chemical non-equilibrium, in the presence of a magnetic field, requires at the highest level, a solution to 10+n coupled partial differential equations, where n represents the total number of gas species to be modelled. This full system is presented here without proof, but the interested reader is referred to [41], [24] and [154] for their derivation.

$$\frac{\partial \rho_i}{\partial t} + \nabla \cdot (\rho_i \boldsymbol{u}) + \nabla \cdot \boldsymbol{J}_{m_i} = \omega_i \tag{4.6.1}$$

$$\frac{\partial \rho_c}{\partial t} + \nabla \cdot \boldsymbol{j} = 0 \tag{4.6.2}$$

$$\frac{\partial \rho}{\partial t} + \nabla \cdot (\rho \boldsymbol{u}) = 0 \tag{4.6.3}$$

$$\frac{\partial \rho \boldsymbol{u}}{\partial t} + \nabla \cdot (\rho \boldsymbol{u}\boldsymbol{u} + p\boldsymbol{I}) - \nabla \cdot \boldsymbol{\tau} = \rho_c \boldsymbol{E} + \boldsymbol{j} \times \boldsymbol{B} \tag{4.6.4}$$

$$\frac{\partial \rho e_t}{\partial t} + \nabla \cdot [(\rho e_t + p)\boldsymbol{u}] + \nabla \cdot (\boldsymbol{J}_U - \boldsymbol{\tau} \cdot \boldsymbol{u}) = \boldsymbol{j} \cdot \boldsymbol{E} \tag{4.6.5}$$

$$\nabla \times \boldsymbol{E} = -\frac{\partial \boldsymbol{B}}{\partial t} \tag{4.6.6}$$

$$\epsilon_0 c^2 \nabla \times \boldsymbol{B} = \boldsymbol{j} + \epsilon_0 \frac{\partial \boldsymbol{E}}{\partial t} \tag{4.6.7}$$

$$\nabla \cdot \boldsymbol{B} = 0 \tag{4.6.8}$$

The first equation represents the mass balance equation, for the convection (ρ_i**u**), diffusion ($\mathbf{J}_i$) and production (ω_i) of species i. ρ_c denotes the electric charge density, and the second equation is the mass balance equation for the quantity, where **j** represents the sum of the convection and conduction currents. Conservation of total mass is represented next, where $\rho = \sum \rho_i$, followed by the momentum and energy equations, then Faraday's induction law, and Ampere-Maxwell's law. The diffusive fluxes $\mathbf{J}_i$ and $\mathbf{J}_U$ depend on electromagnetic field, as well as on pressure and temperature gradients. For full details the reader is referred to [41]. The 10+n equations represent a large over head in terms of the computational requirement to solve such a system numerically, but the overwhelming difficulty lies in the disparate time scales of the fluid and electric field equations.

For example, Alfven waves associated with travelling oscillations in the plasma and the magnetic field, travel at the speed of light, where as acoustic waves associated with the flowfield travel at the speed of sound. Because of this, time accurate solutions are cumbersome to obtain, as extremely small time steps are needed to resolve the temporal variations of the magnetic field. Specialised methods such as that found in [43] are required to solve such systems that are numerically stiff.

In addition to the above, several sections of the full set of magneto-hydrodynamic equations do not lend themselves to a space marching solution algorithm, as it is not entirely obvious that second order derivatives appearing in this new model may be neglected in the streamwise direction. Fortunately, there are several approximations that can be made in dealing with magneto-hydrodynamic equations that allow the reduction of the system to a more manageable system of equations, which are easier to solve.

4.6.2 The Magneto Hydrodynamic Approximation

In view of the difficulties associated with solving the full magneto gas-dynamic equations, it is natural to expect that there would be several approximations to the system. The first such model is based on the assumption that the time scale for changes in the electromagnetic field is small compared to the characteristic time scale for changes in the flow field.

Omitting details, (refer to [146]) the relative magnitudes of terms appearing in the Ampere-Maxwell equation [4.6.7] are examined. The displacement current density $\epsilon_0 \partial E/\partial t$ and the displacement current $\rho_c v$ are considered negligibly small in comparison to the conduction current j. Furthermore $\rho_c E$ can be regarded as being small in relation to $j \times B$, in the momentum equations above, and hence neglected.

Following the above, it can be shown that the electric field E is no longer an independent variable, but a function of v and B. Furthermore, since the effects of non equilibrium thermodynamics are not considered in this work, restricting attention to a single gas also simplifies the system in that equation for the conservation of mass need only be solved for a single species.

With the above simplifications, the governing equations to be solved reduce to the following:

$$\frac{\partial \rho}{\partial t} + \nabla \cdot (\rho u) = 0 \tag{4.6.9}$$

$$\frac{\partial \rho u}{\partial t} + \nabla \cdot \left[\rho uu + \left(p + \epsilon_0 c^2 \frac{|B|^2}{2} \right) I - \epsilon_0 c^2 BB \right] = \nabla \cdot \tau \tag{4.6.10}$$

$$\frac{\partial B}{\partial t} + \nabla \cdot (uB - Bu) = \frac{\epsilon_0 c^2}{\lambda_e} \nabla^2 B \tag{4.6.11}$$

$$\begin{aligned} \frac{\partial \rho e_t}{\partial t} \quad + \quad & \nabla \cdot \left[\left(\rho e_t + p + \epsilon_0 c^2 \frac{|B|^2}{2} \right) u - \epsilon_0 c^2 B (v \cdot B) \right] \\ = \quad & \nabla \cdot (u \cdot \tau) + \nabla \cdot Q + \frac{\left(\epsilon_0 c^2 \right)^2}{\lambda_e} \left[(\nabla \times B)^2 + B \cdot \nabla^2 B \right] \end{aligned} \tag{4.6.12}$$

Clearly the above model is simpler compared to the full form model, as it more closely resembles the original Navier Stokes equations. The difference being the presence of coupling terms in the momentum and energy equations, and the introduction of an additional equation: the magnetic induction equation [4.6.11], which clearly takes into account the effects of flow changes to the magnetic field.

At this point it is instructive to introduce non-dimensional variables, where all variables appearing in the equations are normalised by some suitable choice of reference value, denoted by the subscript ∞. The following non-dimensionalisations are made;

$$\mathbf{u} = V_\infty \mathbf{u}^*, \quad \mathbf{B} = B_\infty \mathbf{B}^*, \quad \mathbf{x} = L\mathbf{x}^*, \quad t = Lt^*/V_\infty,$$
$$\rho = \rho^* \rho_\infty, \quad p = p^* \rho_\infty V_\infty^2, \quad e_t = e_t^* V_\infty, \quad \lambda = \lambda^* \lambda_\infty$$

Substituting the asterisk variables into the equations above (asterisks removed for sake of notation convenience), the following form is obtained:

$$\frac{\partial \rho}{\partial t} + \nabla \cdot (\rho u) = 0 \tag{4.6.13}$$

$$\frac{\partial \rho u}{\partial t} + \nabla \cdot \left[\rho uu + \left(p + S_m \frac{|B|^2}{2} \right) I - S_m BB \right] = \frac{1}{Re} \nabla \cdot \tau \tag{4.6.14}$$

$$\frac{\partial B}{\partial t} + \nabla \cdot (uB - Bu) = \frac{1}{Re_m} \nabla^2 B \tag{4.6.15}$$

$$\frac{\partial \rho e_t}{\partial t} + \nabla \cdot \left[\left(\rho e_t + p + S_m \frac{|B|^2}{2} \right) u - S_m B (v \cdot B) \right]$$
$$= \frac{1}{Re} (\nabla \cdot (u \cdot \tau) + \nabla \cdot Q) + \frac{1}{Re_m} \left[(\nabla \times B)^2 + B \cdot \nabla^2 B \right] \tag{4.6.16}$$

where Re is usual Reynolds number defined analogously for the Navier Stokes equations. Re_m is the magnetic Reynolds number defined as

$$Re_m = \frac{\lambda_\infty V_\infty L}{\epsilon_0 c^2} \tag{4.6.17}$$

and represents the "ease" with which the fluid flows through the magnetic field. It is a representation of the ratio between the convection and magnetic diffusion effects. The final parameter appearing in the model,

$$S_m = \frac{\epsilon_0 c^2 B_\infty^2}{\rho_\infty V_\infty^2} \tag{4.6.18}$$

is known as the magnetic force number, and is a measure of the ratio of the magnetic force to the inertia force of the fluid. Defining the Alfven velocity as $A = B_\infty \sqrt{\epsilon_0 c^2 / \rho_\infty}$, is it also possible to rewrite the magnetic force number as

$$S_m = \frac{A^2}{V_\infty^2} \tag{4.6.19}$$

The Alfven wave is associated with the speed of propagation of the magnetic field itself. This highlights the fact that where wave motion is important, the parameter is significant.

4.6.3 Further Approximations

Rewriting the model in terms of non dimensional parameters provides further insight into several more of the approximations that can be made to this model. This relies on investigating the limiting behaviour of non-dimensional parameters described above. This may be broken down into three separate cases.

- **1. Small Magnetic Force Number: $S_m << 1$**

  In this limit, any magnetic field terms appearing in the momentum and energy equations can be assumed to be negligible, resulting in the original Navier Stokes equations, and the induction equation for the magnetic field. This is in fact what would be expected as a small force number dictates that the field has very little effect on the flow, although the flow field may affect the evolution of the magnetic field significantly.

- **2. Large Magnetic Reynolds Number: $Re_m >> 1$**

  As Re_m becomes large, the effects of magnetic convection dominate over any diffusive behaviour, and as such any dissipative terms involving the field become negligible. Consequently the governing equations adopt the form;

$$\frac{\partial \rho}{\partial t} + \nabla \cdot (\rho u) = 0 \tag{4.6.20}$$

$$\frac{\partial \rho u}{\partial t} + \nabla \cdot \left[\rho uu + \left(p + S_m \frac{|B|^2}{2} \right) I - S_m BB \right] = \frac{1}{Re} \nabla \cdot \tau \tag{4.6.21}$$

$$\frac{\partial B}{\partial t} + \nabla \cdot (uB - Bu) = 0 \tag{4.6.22}$$

$$\begin{aligned} \frac{\partial \rho e_t}{\partial t} &+ \nabla \cdot \left[\left(\rho e_t + p + S_m \frac{|B|^2}{2} \right) u - S_m B (v \cdot B) \right] \\ &= \frac{1}{Re} (\nabla \cdot (u \cdot \tau) + \nabla \cdot Q) \end{aligned} \tag{4.6.23}$$

If one additionally makes the assumption that the flow is inviscid, ie we take the limit $Re \rightarrow \infty$ then any viscous terms appearing in the above may also be neglected.

This form is referred to as the "Ideal MHD equations", and is often cited in literature [65], [20].

- **3. Small Magnetic Reynolds Number: $Re_m << 1$**

  In the opposite limit, the effect of applying this assumption to the simplified form above is not immediately obvious. Instead, consider the governing equation for the magnetic field in Maxwell's equations

$$\nabla \times B = \frac{j}{\epsilon_0 c^2} \tag{4.6.24}$$

where the current is given by Ohm's Law

$$j = \lambda_e (E + u \times B) \tag{4.6.25}$$

In general, the magnetic field B can be recast as the sum of an applied component B_a , and an induced component b_i. Substituting this into (4.6.24) results in

$$\nabla \times b_i = \frac{j}{\epsilon_0 c^2} \tag{4.6.26}$$

which when re-written into non-dimensional form using $j = \lambda_\infty V_\infty B_\infty j^*$ gives

$$\frac{B_\infty}{L} \nabla \times b_i^* = j^* \frac{\lambda_\infty V_\infty B_\infty}{\epsilon_0 c^2} \tag{4.6.27}$$

equivalent to

$$\nabla \times b_i^* = j^* Re_m \tag{4.6.28}$$

In the limit $Re_m \rightarrow 0$, we see that the induced component of the field is negligibly small. Therefore the only component of the magnetic field we are left with is the applied component which remains fixed at all time.

It is this assumption we apply to the original full form model, which results in a simpler model. The original Navier Stokes equations are retained, plus source terms which take into account the effect of the Lorentz force, and the magnetic energy;

$$\frac{\partial \rho}{\partial t} + \nabla \cdot (\rho u) = 0 \tag{4.6.29}$$

$$\frac{\partial \rho u}{\partial t} + \nabla \cdot [\rho uu + pI] = \frac{1}{Re}\nabla \cdot \tau + S_m Re_m \mathbf{j} \times \mathbf{B} \qquad (4.6.30)$$

$$\begin{aligned} \frac{\partial \rho e_t}{\partial t} &+ \nabla \cdot [(\rho e_t + p)\, u] \\ &= \frac{1}{Re}(\nabla \cdot (u \cdot \tau) + \nabla \cdot Q) + S_m Re_m \mathbf{j} \cdot \mathbf{E} \end{aligned} \qquad (4.6.31)$$

Extending the above to the Parabolised Navier Stokes equations is relatively straight forward, as the only difference is the fact that streamwise viscous derivatives are neglected from the steady form the model. The source term remains unchanged.

The outline above has illustrated there are several models open to the user wishing to investigate the effects of applying a magnetic field to an ionised flow. For the purposes of the current study the choice of model was primarily dictated by the amount of computation time needed to obtain a typical calculation.

In view of this, the author chose not to implement the full form model, but rather the single gas model based on the magneto hydrodynamic assumption. With this form, the additional approximations made by taking limiting behaviour of the non-dimensional parameters, is easily taken into account by simply neglecting relevant terms in the computation. Separate to the above, due to its relative simplicity the low magnetic Reynolds number model was implemented in addition to this. Chapter [5] details the manner in which these models have been implemented into the IMPNS code, including the numerical subroutines used to calculate the additional terms, and the modified algorithms used.

Clearly a purely theoretical approach is limited in scope and applicability, and the experimental studies illustrating the potential of magneto-hydrodynamics is indeed promising. However, both these approaches lack the ability of being able to predict phenomena in the presence of plasmas and magnetic fields. In pursuit of this, considerable research has gone into developing a numerical framework that is capable of simulating such flow behaviour. Development has focused particularly on numerical schemes to solve the magneto-hydrodynamic equations, and in the simulation of these equations for various geometries of interest in hypersonic flows.

The ideal magneto-hydrodynamic equations can be deduced from the full system [4.6.1-4.6.7], with the additional assumptions that flow medium is assumed to be isotropic, the magnetic field induced by the motion of charged particles dominates the applied magnetic field, and viscosity and heat transfer are considered negligible. The resulting model is just the same as that of equations [4.6.9] through to [4.6.12] except all terms appearing on the right had side are considered negligible, and thus set to zero. An

alternative method of obtaining the "ideal" form, is to consider the limit of $Re \rightarrow \infty$ and $Re_m \rightarrow \infty$ .The eigenvalues of the resultant Jacobian matrix are given by

$$u - c_f, \quad u - c_a, \quad u - c_s, \quad u, \quad u + c_s, \quad u + c_a, \quad u + c_f \tag{4.6.32}$$

where

$$c_a = \frac{B_x}{\sqrt{\rho}} \tag{4.6.33}$$

$$c_f^2 = \frac{1}{2}\left[a^2 + \sqrt{a^4 - \frac{4\gamma p B_x^2}{\rho}}\right] \tag{4.6.34}$$

$$c_s^2 = \frac{1}{2}\left[a^2 - \sqrt{a^4 - \frac{4\gamma p B_x^2}{\rho}}\right] \tag{4.6.35}$$

are the Alfven waves, and the fast and slow characteristic speeds. In the above expressions,

$$a = \sqrt{\frac{\gamma p + |B|^2}{\rho}} \tag{4.6.36}$$

A close inspection of the eigenvalues of this system reveals that equations are not strictly hyperbolic, since there are certain cases where the eigenvalues are no longer distinct. In addition to this, the Jacobian itself is singular, presenting further numerical difficulty in obtaining numerical simulations. Nonetheless a considerable research effort has gone into trying to develop a characteristic based scheme that maintains the shock capturing capability of such approximate Riemann solvers.

Brio and Wu [20] linearise the magneto-hydrodynamic equations into Jacobian form, to construct a Roe matrix for the special case of $\gamma = 2$. For the general case of $\gamma \neq 2$ the Jacobian is instead constructed using an averaging procedure for the flow and magnetic field variables over the cell interface. In the same work, Brio and Wu also point to the fact that the magneto-hydrodynamic equations are non-convex. The characteristic fields are neither genuinely non-linear or linearly degenerate. A consequence of this is that it is possible to obtain compound wave structures, where shocks may be attached to rarefaction waves. As the y component of the magnetic field changes sign, the slow characteristic wave speed c_s (and fast, c_f) becomes smaller (greater) than the Alfven wave speed, c_a, a consequence of which is that the transverse component of the field goes through zero. This is a particularly important revelation in the study of numerical magneto-hydrodynamics routines, as it was able to provide insight into the complex

wave structures of the system.

Examining another approach for flux evaluation, Dai and Woodward have developed the piecewise parabolic method to treat multi dimensional magneto-hydrodynamic equations [39]. The equations in Lagrangian form are considered in their analysis, and the method is shown to be advantageous in the presence of strong shock waves, with little noise generation. In a separate work they also develop a simple approximate Riemann solver to be used in high order Godunov schemes, shown to be robust for shock tube examples involving multiple discontinuities [40].

Using a particle collision model, in the evaluation of the flux vector splitting, Xu proposes a kinetic flux splitting method for the governing equations [166]. A distribution function for the moving particles is considered on either side an interface, and macroscopic quantities on the left and right states across the interface may be inferred from this. These left and right states are subsequently used to construct $F^{+}_{i+1/2}$ and $F^{-}_{i+1/2}$, and summed to determine the total flux over the interface. A particle collision model is further introduced to overcome the problems of large numerical dissipation, which considers the equilibrium, averaged state of macroscopic variables at the interface itself. The model is claimed to require a third of the computational time of the above Riemann problem solvers, and avoids the numerical complications highlighted in the above studies relating to equation non-convexity and non strict hyperbolicity of the magneto-hydrodynamic equations.

D'Ambrosio and Pandolfi [42] also present a flux difference splitting upwind scheme based on an approximate Riemann solver, by extending the technique initially proposed by Osher and Solomon [116]. Admissible and inadmissible discontinuities are classified by investigating the time evolution of initial discontinuities of a shock tube problem numerically. Typically, inadmissible discontinuities tend to smear out the initial prescribed discontinuities, unlike those admissible ones that are preserved as the solution is marched in time.

One of the main restrictions for the above solution procedures is that for the one dimensional shock tube problem that is investigated, nothing is done to take into account the evolution of the x-component of the magnetic field. Rather, all the cases assume $B_x = constant$, which examining the equations does make sense, as in 1D, the equation forB_x is simply $\partial B_x/\partial t = 0$. Indeed, if one tries to construct a Jacobian by taking into account the variation of B_x, one quickly finds that the Jacobian is in fact singular.

Furthermore, the researchers also point to the fact that maintaining $\nabla \cdot \boldsymbol{B} = 0$ is an important requirement to ensure stability of the numerical schemes. A non zero divergence can be a symptom of the numerical error of the difference scheme. Ensuring this condition is satisfied is another area of investigation that has received considerable

attention.

The approximate Riemann solver developed by Powell et al [122] takes into account the eight wave structure of the governing equations. Given that the Jacobian matrix of the original seven-wave system is singular, an attempt is made to modify it such that in the eight wave system, the eigenvalues and eigenvectors for the original system remain unchanged, the eigenvalue corresponding to the eighth wave is u with its left and right eigenvalues non-singular, and that whenever B_x is constant, the eight wave problem reduces to the seven wave case. With these objectives in mind, the modified Jacobian can be shown to be a consequence of adding

$$-\begin{bmatrix} 0 \\ \boldsymbol{B} \\ \boldsymbol{u}\cdot\boldsymbol{B} \\ \boldsymbol{u} \end{bmatrix} \nabla.\boldsymbol{B} \tag{4.6.37}$$

to the right hand side of the governing equations. The eighth wave, the so called "magnetic flux wave" is the only wave that carries information regarding changes in the value of B_x, and affects only the equation for the x component of the magnetic field. Physically, this modification amounts to nothing more than adding a term equal to zero to the governing equations, since in reality $\nabla\cdot\boldsymbol{B} = 0$. In numerical computations however, it is the violation of this condition that is a common cause of numerical instability. The inclusion of the above source term actually convects errors in $\nabla\cdot\boldsymbol{B}$ out of the flow domain, and is therefore beneficial in maintaining stability during computations.

MacCormack [94] proposes to overcome the problem using a flux vector splitting approach, commonly associated with schemes such as Steger-Warming [153]. Since the governing equations for magneto-hydrodynamics are non-homogeneous, a straight forward splitting of the flux vector is not possible, and instead, the governing equations are solved in a non-conservative form. MacCormack overcomes this problem by introducing an additional equation representing a fixed constant, which restores homogeneity of the system of equations. Subsequent analysis reveals that the flux Jacobian is identical to the form proposed by Powell [123], which overcomes the problem of a singular Jacobian, and properly accounts for the evolution of B_x. The resultant Jacobian is split into left and right contributions similar to the method of Steger and Warming.

4.7 Numerical Investigations

In line with the theoretical and experimental treatises that have investigated the effects of magneto-hydrodynamics on blunt bodies, numerous attempts have been made to try and quantify the effects of applying magnetic fields to such problems, using a computational framework.

Dietiker and Hoffman for example, consider Mach 2.97 flow past an axisymmetric spherical body, in the presence of a magnetic field applied normally to the stagnation streamline [50]. The body force generated due to the presence of the field acts in the opposite direction to the advancing velocity field, and thus the shock stand off distance to the body increases. In simulating the case at several magnetic field intensities, the increasing shock stand off is in broad agreement with the theoretical results of Lykoudis [93], although there is some discrepancy, which can be attributed to the complexities in reproducing the assumptions made in the analytical solution. In arriving at his solution, Lykoudis makes the assumption that the field is constant between the shock and body surface, requiring an *a priori* determination of the bow shock location. Furthermore, in simulating the case using a simplified magneto-hydrodynamic model, due to the motion of the fluid, an induced field is generated thus violating the assumption.

Damevin et al. examine the flow properties of a Mach 10.6 flow past a 15 degree blunted cone, using different magnetic field configurations [45], [44]. An equilibrium gas model based on a curve fitting procedure is combined with a scalar model for the electrical conductivity as a function of flow temperature. The magnetic fields are assumed to be generated by magnets mounted on the body surface, and the effects of uniform, dipole and radial magnetic field distributions are investigated. The effects of magnetic field intensity are also investigated highlighting again the observation made by others that the standoff distance increases with increased field strength. However, for the radial field case, the effects are much less pronounced, as within the stagnation region, the orientation of the field lines is such that the Lorentz force does not act to oppose the flow. Rather, the main changes occur within the shoulder regions of the geometry. For a given field strength, the uniform field, with a y-component only is shown to have the biggest increase in shock stand off, which is expected given that the components of the generated Lorentz force act purely against the flow, in the stagnation region. More surprising is the fact the authors show that for this configuration, a secondary expansion wave may be generated, resulting in a reduction in the pressure coefficient on the stagnation streamline. In contrast, the dipole field does exhibit an increase in standoff, and a decrease in the pressure coefficient, although the effects are not as pronounced as the uniform case.

Further comparison is made to the theoretical models of Bush [22] by Poggie and

Gaitonde [120]. For an axisymmetric flow past a spherical body at Mach 5, a dipole is located at the centre of the body radius, with varying strengths. The increase in shock standoff to body radius ratio is in qualitative agreement with the trends predicted by Bush, although once again there is discrepancy due to the inherent assumptions in the theoretical model. The most notable assumption in Bush's work is that a constant density hypothesis is made, which tends to under predict the distance between the body and the shock. The heat transfer coefficient on the stagnation point is also shown to decrease with field strength, placing emphasis on the potential merits of magneto-hydrodynamics as a control device in reentry aerodynamics, as was initially proposed.

The results for the blunt body case are consistent with those obtained by MacCormack [95], Augustinus et al. [10], Deb and Agarwal [46], Kahn et al [81] and several other groups. Most have examined the problem using the simplified magneto-hydrodynamic model, but there have also been investigations that make use of the low magnetic Reynolds number formulation [120?]. Both models predict an increase in the shock standoff distance and a deceleration of the flow in the stagnation region.

Another application area that has received attention by the magneto-hydrodynamic research community, is in the area of viscous drag reduction. The main studies to date in this area have involved the application of magnetic fields to laminar and turbulent flat plate boundary layers. As outlined earlier, Rossow [136] argued that in the presence of a field acting normal to a uniform a flow, the flow would become decelerated thereby reducing skin friction and heat transfer.

Using a low magnetic Reynolds number formulation, Dietiker and Hoffmann were able to confirm this numerically [49]. A series of tests for a Mach 2 supersonic flow past a flat plate were conducted, in the presence of a uniform field acting normal to the plate only. Their results indicated that as the magnetic force number was increased, flow throughout the domain was decelerated, and beyond a critical value, separation would occur. Similar behaviour was also observed for the case of a turbulent boundary layer, flow decelerating, but separation occurring at a larger value of magnetic force number. The effects were similar regardless of the turbulence model used. Furthermore, their work illustrated the fact that the skin friction coefficient would decrease, over the whole length of the plate, with increasing field strength, thereby reducing the drag coefficient. In a similar work, Kato et al [77] demonstrated good agreement with these computations of Dietiker and Hoffmann [49], using a Parabolised Navier Stokes solver.

Using direct numerical simulation (DNS), Cheng et al. have investigated the effects on the stability of a boundary layer, in applying a magneto-hydrodynamic effects [25]. The gas is assumed to have a constant electrical conductivity, with magnetic dipoles

placed underneath the flat plate. Numerical investigations examining the effects of different strengths and orientations of two dipoles are considered, particularly on the second-mode instability waves. The authors confirm the results shown by Dietiker and Hoffman [49] and Kato et al [77], that a sufficiently strong field will tend to cause separation. However, using a low magnetic Reynolds number model, they illustrate that magnetic fields can serve to stabilise the modes, and thus inhibit transition to turbulence, in regions where the boundary layer profile is substantially modified. In a separate work investigating the effects of magnetic fields on turbulent boundary layers, Dietiker and Hoffmann show that turbulent flows may become relaminarised [48]. Skin friction profiles for turbulent calculations in the presence of a uniform field orientated at 45 degrees to the plate show that for sufficiently strong fields, a laminar profile is approached. The effects were seen to be more prominent for cases where the field was perpendicular to the incident flow direction.

Magneto-hydrodynamics has also been considered in modifying shock structures, the main application area for which is in controlling shock impingement locations for hypersonic inlets, operating at off design conditions. The main advantages of using magneto-hydrodynamic as control device, rather than purely mechanical and electrical devices is the response time for the control device to have effect. Typically, control mechanisms for mechanical devices may have actuation times on the order of tenths, or at best, hundredths of a second, which are inadequate for hypersonic applications. In contrast, the response times for electro-magnetic flow control mechanisms are on the order of tens to hundreds of nanoseconds [83]. Therefore the timescales to achieve active control are on the same order as the timescales for modifications to the local flowfield. Additionally, using magneto-hydrodynamic as a flow control mechanism has the additional advantage that modifications can be made to flows at comparatively larger distances from the energy source.

Harada et al [65] have examined a supersonic flowfield through a compression-expansion channel. In the presence of a magnetic field, the authors show that the shock angles are modified in the presence of a field, resulting in changes in the shock impingement and reflection locations. Although the case examined is through a channel, it is precisely this idea that is the basis of magneto-hydrodynamic flow control on scramjet intakes, as it illustrates the consequential variations in shock angle.

The scramjet intake has received considerable considerable theoretical investigation [99],[98],[141],[117],[84]. The studies have stressed the importance of shock boundary layer interaction at the ramp junctions on inlet performance, the ramp structure prior to the inlet, field orientation and the effects of energy addition through Joule heating on the flow structure. In a computational study, Schneider and Kuranov investigated magneto-hydrodynamic interaction on a two dimensional scamjet intake, with two ramp angles of

6.5 degrees and 8.5 degrees respectively [145]. A low magnetic Reynolds number formulation is used, with the magnetic field simulating an electromagnetic coil within the body. A beam of electrons are introduced into the flow, in a direction opposite to the main flow direction, so that the ionised region of the flow can be arbitrarily modified. Within the low magnetic Reynolds number model, the degree of ionisation and its conductivity is calculated using approximating functions. Two different types of current distributions, giving rise to different magnetic field densities are investigated, and demonstrate that the magnetic field generated from a circular current provides greater increment of air capture in the hypersonic inlet. Furthermore, the field generated from two currents acting in opposite directions is observed to be more effective in improving air capture ratios.

In other areas, Poggie and Updike et al. have investigated the use of magneto-hydrodynamics in controlling boundary layer shock wave interactions along a compression ramp [119], [158]. For sufficiently high compression angles, in the corner region, the flow is seen to locally separate. For control instruments such as flaps, separation causes the flap to become ineffective. To overcome this, the authors propose using magneto-hydrodynamics and heating to accelerate the flow in the corner region to accelerate the flow, thus expanding the effective region of operability of the flap. Corke et al examine a similar idea, using plasma actuators to enhance lift and control separation over transonic aerofoils, by maintaining a favourable pressure gradient over the upper surface [32].

4.8 Conclusions

This section has provided an illustration as to the current state of research within magneto-hydrodynamics . It has shown that considerable investigations have gone into trying to resolve the difficulties in finding numerical solutions of the ideal MHD equations, using flux difference splitting and flux vector splitting techniques to approximate fluxes, and through the addition of extra terms into the model that represent the physical requirement that the field is non-divergent. In trying to gain better understanding into the underlying physics of ionised flowfields in the presence of electromagnetic fields, experimental work has been carried out. The potential benefits highlighted by these studies in reducing drag coefficients, and the ability to control shock structures in hypersonic inlets, and blunt body configurations is certainly promising, whilst computational results into other applications are diverse, suggesting a lot may be gained by incorporating magneto-hydrodynamics into broader engineering applications.

There are however several issues that ought to be addressed before such incorporation may take place. As performing experimental work as a design tool is considerably expensive, designers often use computational tools instead. With magneto-hydrodynamics ,

this is certainly possible, as illustrated by the numerous numerical simulations that have been performed to date, but it seems validation of these results to experimental data is lacking. Certainly there are cases where comparison of predicted and experimental data have been made, but these are but a handful. There therefore exists an uncertainty as to what the potential errors may be in using numerical results, and consequently, more stringent verification and validation procedures are required.

Additionally, although several studies have been performed to examine the effects of ionisation degree, and magnetic field properties such as strength and orientation, thorough optimisation studies have not at present been performed. Indeed Knight [83] points to this fact in a recent review article discussing the applications of magneto-hydrodynamics. This is crucial in exploring the design options, if magneto-hydrodynamics is to be used as a more practical flow control mechanism.

CHAPTER 5

Implementation of MHD Model

The following section outlines the governing equations to be solved as a result of incorporating the simplified magneto-hydrodynamic model into the Parabolized Navier Stokes equations. Naturally, the addition of extra terms into the governing equations necessitates an assessment as to the impact they may pose on the original form of the model. The numerical routines based on Tannehill et al's implementation [77] was used, since they have implemented the model into their own parabolised Navier Stokes solver. A description of the solution procedure, and the algorithms used to obtain numerical solutions to them are also described here.

5.1 SMHD Model

As explained in section [4.6.2] the magneto fluid dynamic equations may be simplified by using the magneto-hydrodynamic assumption, resulting in a reduced system. In the present thesis, attention is restricted to the case of a single gas. Furthermore, viscous derivatives in the streamwise direction are neglected in the momentum and energy equations, a common feature of the PNS model. The continuity equation remains unchanged, and the full system of equations, in non-dimensional form is given by;

$$\frac{\partial \rho}{\partial t} + \nabla \cdot (\rho \boldsymbol{u}) = 0 \tag{5.1.1}$$

$$\frac{\partial \rho \boldsymbol{u}}{\partial t} + \nabla \cdot \left[\rho \boldsymbol{u}\boldsymbol{u} + \left(p + \frac{S_\infty |\boldsymbol{B}|^2}{2} \right) \boldsymbol{I} - S_\infty \boldsymbol{B}\boldsymbol{B} \right] = \frac{1}{Re} \nabla \cdot \tau \tag{5.1.2}$$

$$\frac{\partial \boldsymbol{B}}{\partial t} + \nabla \cdot [\boldsymbol{u}\boldsymbol{B} - \boldsymbol{B}\boldsymbol{u}] = \frac{1}{Re_m} \nabla^2 \boldsymbol{B} \tag{5.1.3}$$

$$\frac{\partial \rho e_t}{\partial t} + \nabla \cdot \left[\left(\rho e_t + p + \frac{S_\infty |\boldsymbol{B}|^2}{2} \right) \boldsymbol{u} - S_\infty \boldsymbol{B} (\boldsymbol{v} \cdot \boldsymbol{B}) \right] = \frac{1}{Re} (\nabla \cdot (\boldsymbol{u} \cdot \tau) + \nabla \cdot Q) \tag{5.1.4}$$

In the above equations, $|B|^2 = B_x^2 + B_y^2 + B_z^2$ denotes the magnitude of the magnetic field. As will be described in more detail subsequently, the main solution algorithm proceeds by solving the magnetic field equations [5.1.3] and the remaining flowfield equations [5.1.1,5.1.2,5.1.4] in a decoupled manner. First the solution procedure to update the magnetic field terms is described.

5.2 Magnetic Induction Equation

Expanded out in full, the convective terms of the magnetic induction equations yields the following;

$$\frac{\partial}{\partial t}\begin{bmatrix} B_x \\ B_y \\ B_z \end{bmatrix} + \frac{\partial}{\partial x}\begin{bmatrix} 0 \\ uB_y - vB_x \\ uB_z - wB_x \end{bmatrix} + \frac{\partial}{\partial y}\begin{bmatrix} vB_x - uBy \\ 0 \\ vB_z - wBy \end{bmatrix} + \frac{\partial}{\partial z}\begin{bmatrix} wB_x - uB_z \\ wB_y - vB_z \\ 0 \end{bmatrix} = \text{Viscous Terms} \tag{5.2.1}$$

The above form highlights the singular Jacobian matrix of the governing equations, as described in [4.5]. The fact that the respective x,y,z components of their own derivatives is zero is the cause of the problem. Eigenvalue analysis of the entire system shows that in the x direction for example, the eigenvalue associated with the B_x equation is zero. To overcome the issue an extra term is added to the governing equations, as described in numerous works [122, 48, 77]. With regard to the induction equations specifically, the terms added can be expressed as;

$$\begin{aligned}
\begin{bmatrix} u \\ v \\ w \end{bmatrix}\nabla.B &= \begin{bmatrix} u \\ v \\ w \end{bmatrix}\left(\frac{\partial B_x}{\partial x} + \frac{\partial B_y}{\partial y} + \frac{\partial B_z}{\partial z}\right) \\
&= \begin{bmatrix} \frac{\partial uB_x}{\partial x} + \frac{\partial uB_y}{\partial y} + \frac{\partial uB_z}{\partial z} \\ \frac{\partial vB_x}{\partial x} + \frac{\partial vB_y}{\partial y} + \frac{\partial vB_z}{\partial z} \\ \frac{\partial wB_x}{\partial x} + \frac{\partial wB_y}{\partial y} + \frac{\partial wB_z}{\partial z} \end{bmatrix} - \begin{bmatrix} B_x\frac{\partial u}{\partial x} + B_y\frac{\partial u}{\partial y} + B_z\frac{\partial u}{\partial z} \\ B_x\frac{\partial v}{\partial x} + B_y\frac{\partial v}{\partial y} + B_z\frac{\partial v}{\partial z} \\ B_x\frac{\partial w}{\partial x} + B_y\frac{\partial w}{\partial y} + B_z\frac{\partial w}{\partial z} \end{bmatrix} \\
&= \nabla.\left[B\begin{bmatrix} u \\ v \\ w \end{bmatrix}\right] - B.\nabla\begin{bmatrix} u \\ v \\ w \end{bmatrix}
\end{aligned} \tag{5.2.2}$$

which when added to [5.2.1] gives an induction equation of the form;

$$\frac{\partial}{\partial t}\begin{bmatrix} B_x \\ B_y \\ B_z \end{bmatrix} + \frac{\partial}{\partial x}\begin{bmatrix} uB_x \\ uB_y \\ uB_z \end{bmatrix} + \frac{\partial}{\partial y}\begin{bmatrix} vB_x \\ vB_y \\ vB_z \end{bmatrix} + \frac{\partial}{\partial z}\begin{bmatrix} wB_x \\ wB_y \\ wB_z \end{bmatrix} - \boldsymbol{B}\cdot\nabla\begin{bmatrix} u \\ v \\ w \end{bmatrix} = \text{Viscous Terms} \quad (5.2.3)$$

The inclusion of this term resolves the issue of degeneracy, albeit at the expense of including another non-conservative term. Physically, the addition of a term proportional to $\nabla \cdot \mathbf{B}$ does not present anything new into the governing equations, since Gauss' law for magnetism dictates that $\nabla \cdot \mathbf{B} = 0$. Therefore if this condition satisfied by the field initially, will be true at all time. Numerically however, there are circumstances where this condition is violated, thus necessitating its inclusion here, as a correction mechanism.

The implemented model therefore seeks to solve the above form, along with the modified PNS equations with the magnetic field terms and contributions from this source term added. As with other numerical schemes designed to solve equations using a finite volume formulation, the equation [5.2.3] can be cast as;

$$\frac{\partial B}{\partial t} + R(B, u) = 0 \quad (5.2.4)$$

where R is a function of B and u, taking into account the contributions of the inviscid and viscous fluxes and source terms. An explicit iterative scheme of the form

$$B^{n+1} = B^n - \Delta t R(B^n) \quad (5.2.5)$$

is used to update the field variables. It remains to demonstrate how the various contributions to R are made before each update of the magnetic field variables.

- **1. Convective Part**

  Approximations to the convective fluxes appearing in the induction equations may be determined by considering systems of hyperbolic conservation laws. Consider the simple one dimensional system;

$$\frac{\partial}{\partial t}\begin{bmatrix} B_x \\ B_y \\ B_z \end{bmatrix} + \frac{\partial}{\partial x}\begin{bmatrix} uB_x \\ uB_y \\ uB_z \end{bmatrix} = 0 \quad (5.2.6)$$

This is analogous to a system of hyperbolic conservation laws

$$\frac{\partial Q}{\partial t} + \frac{\partial F}{\partial x} = 0 \quad (5.2.7)$$

to which we can apply a generalised procedure to find an approximation for F. The flux Jacobian, defined as $A = \partial F/\partial Q$ for the current system in 1-D is given by

$$A = \begin{bmatrix} u & 0 & 0 \\ 0 & u & 0 \\ 0 & 0 & u \end{bmatrix} \tag{5.2.8}$$

which clearly has three identical eigenvalues of $\lambda = u$. The corresponding eigenvectors for which are

$$k = \begin{pmatrix} 1 \\ 0 \\ 0 \end{pmatrix}, \begin{pmatrix} 0 \\ 1 \\ 0 \end{pmatrix} and \begin{pmatrix} 0 \\ 0 \\ 1 \end{pmatrix} \tag{5.2.9}$$

Given these eigenvalues and eigenvectors, it is clear that the field is linearly degenerate, since

$$\nabla \cdot \lambda k = 0, \forall B \in \Re^3 \tag{5.2.10}$$

Note that in the equation above, $\nabla \equiv \left(\partial/\partial B_x, \partial/\partial B_y, \partial/\partial B_z\right)^T$. For such a case, the flux reduces to a simple form, as outlined in Toro [156] as;

$$F(U)_{i+1/2} = \begin{cases} F(U_0) & \text{if } u_0 \geq 0\,,\, u_1 \geq 0 \\ F(U_1) & \text{if } u_0 < 0\,,\, u_1 < 0 \\ F(U_0) + F(U_1) & \text{if } u_0 > 0\,,\, u_1 < 0 \\ 0 & \text{otherwise} \end{cases} \tag{5.2.11}$$

where U_0 denotes the conserved variables to the left of the flux interface, and U_1 are variables to the right of the interface. Exactly the same technique is applied to the flux terms in the $\partial/\partial y$, and $\partial/\partial z$ directions, thus accounting for all contributions to R from the convective terms.

- **2. Dissipative Part**

  Calculation for the dissipative flux over an interface is calculated based upon a staggered cell, whose volume spans two adjacent cells with its centre located at the centre of their interface, as shown in figure [4]. Consider the dissipative contribution to the right hand side, for the B_x equation. Written explicitly, this is given by $\nabla \cdot \nabla B_x$. To calculate this quantity, consider an auxiliary cell volume V' as illustrated. For an arbitrary volume, we know from Gauss that;

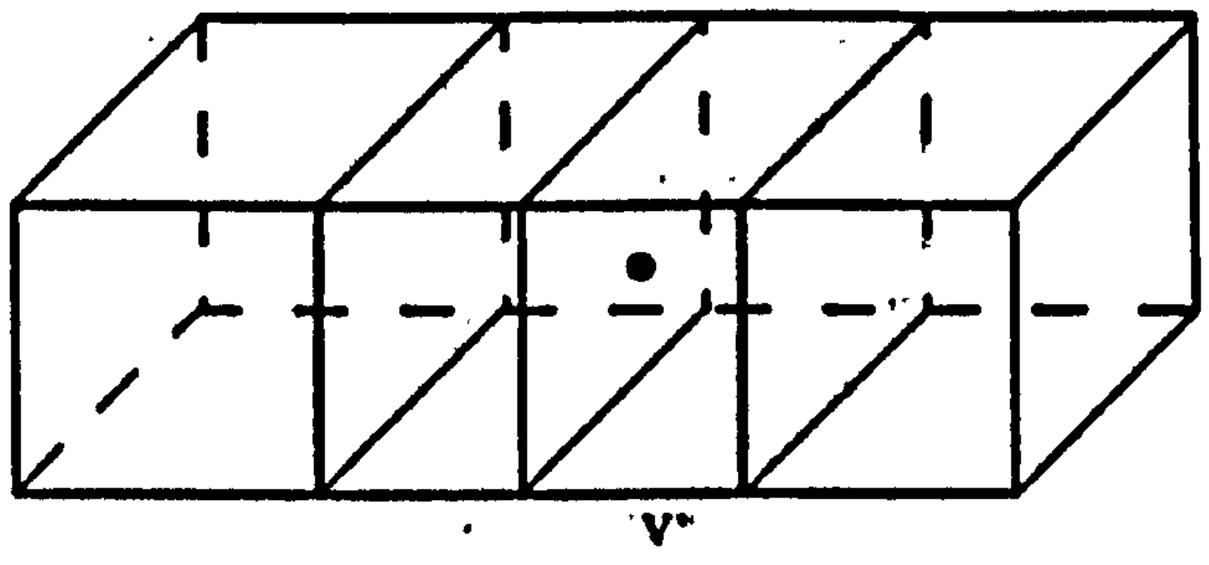

Figure 4: Staggered Cell V', spanning two cells

$$\int_{\delta V'} \nabla \cdot \nabla B_x dV' = \oint_{\delta S'} \nabla B_x . n dS' \tag{5.2.12}$$

As the primary interest is in the cell average value of the integrand appearing within the left hand side of the above, the following approximation can be assumed;

$$\int_{\delta V'} \nabla \cdot \nabla B_x dV' = \delta V' \left[\nabla \cdot \nabla B_x\right]_{AVE} \tag{5.2.13}$$

The quantity on the left hand side of equation (5.2.12) is determined by performing a summation over all interfaces for the given cell volume V'.

$$\oint_{\delta S} \nabla B_x \cdot n dS = \sum_{i=1}^{6} \nabla B_x \cdot n_i \tag{5.2.14}$$

from which it is inferred that

$$\frac{1}{\delta V'} \sum_{i=1}^{6} \nabla B_x \cdot n_i = \left[\nabla \cdot \nabla B_x\right]_{AVE} \tag{5.2.15}$$

The quantity on the left hand side of the above is evaluated by first determining the value of B_x on each interface of the auxiliary cell. This is done by taking an average of the surrounding cell centre values, and can be explained further with the aid of figure [5].

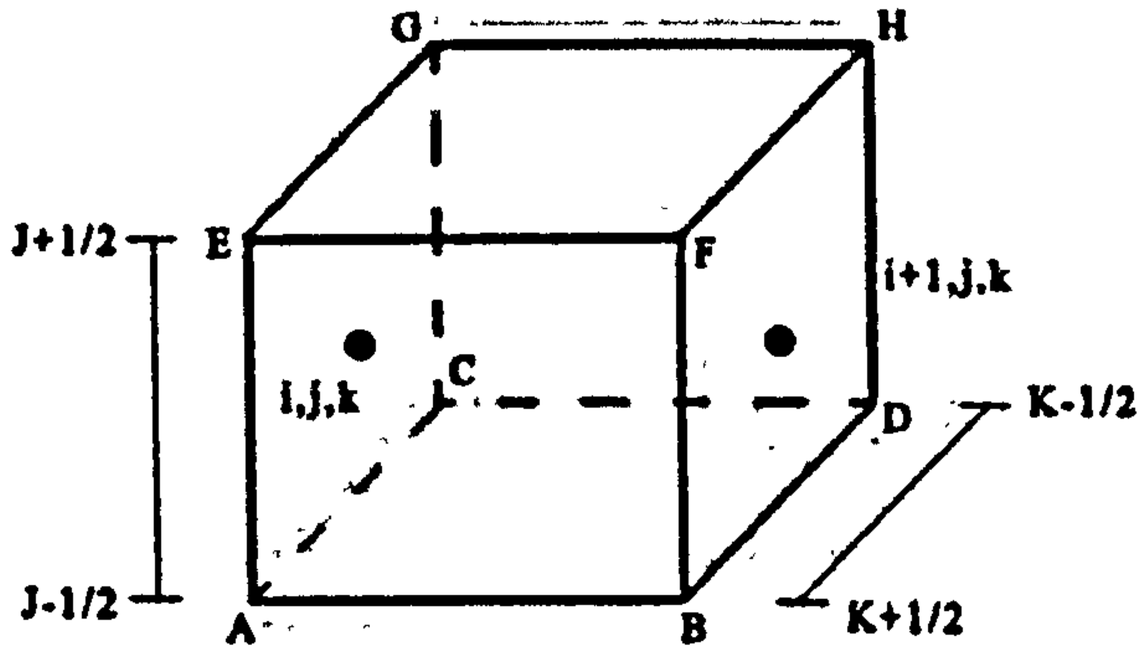

Figure 5: Cell V', used to calculate viscous flux

Expressed in full, the above summation, using the notation provided in figure [5] (and neglecting "x" suffix here for convenience in notation) may be written as;

$$\begin{aligned}\sum\cdots &= \frac{1}{\delta V}[B_{i+1,j,k}\mathbf{S}_{BDFH} + B_{i,j,k}\mathbf{S}_{ACEG} \\ &+ B_{i+1/2,j+1/2,k}\mathbf{S}_{EFGH} + B_{i+1/2,j-1/2,k}\mathbf{S}_{ABCD} \\ &+ B_{i+1/2,j,k+1/2}\mathbf{S}_{ABEF} + B_{i+1/2,j,k-1/2}\mathbf{S}_{CDGH}] \qquad (5.2.16)\end{aligned}$$

where $B_{i+1/2,j\pm1/2,k} = \frac{1}{4}\left[B_{i,j,k} + B_{i,j\pm1,k} + B_{i+1,j,k} + B_{i+1,j\pm1,k}\right]$, and $B_{i+1/2,j,k\pm1/2} = \frac{1}{4}\left[B_{i,j,k} + B_{i,j,k\pm1} + B_{i+1,j,k} + B_{i+1,j,k\pm1}\right]$. The surface area vectors on the auxiliary cell are computed by taking an average of the neighbouring surface area vectors of the original grid, and is described by the following;

$$\begin{aligned}\mathbf{S}_{BDFH} &= \frac{1}{2}\left[\mathbf{S}_{\xi_{i+1,j,k}} + \mathbf{S}_{\xi_{i,j,k}}\right] \\ \mathbf{S}_{ACEG} &= \frac{1}{2}\left[\mathbf{S}_{\xi_{i,j,k}} + \mathbf{S}_{\xi_{i-1,j,k}}\right] \\ \mathbf{S}_{EFGH} &= \frac{1}{2}\left[\mathbf{S}_{\eta_{i+1,j,k}} + \mathbf{S}_{\eta_{i,j,k}}\right] \\ \mathbf{S}_{ABCD} &= \frac{1}{2}\left[\mathbf{S}_{\eta_{i,j-1,k}} + \mathbf{S}_{\eta_{i+1,j-1,k}}\right] \qquad (5.2.17)\end{aligned}$$

$$\begin{aligned}\mathbf{S}_{ABEF} &= \frac{1}{2}\left[\mathbf{S}_{\zeta_{i+1,j,k}} + \mathbf{S}_{\zeta_{i,j,k}}\right] \\ \mathbf{S}_{CDGH} &= \frac{1}{2}\left[\mathbf{S}_{\zeta_{i,j,k-1}} + \mathbf{S}_{\zeta_{i+1,j,k-1}}\right] \qquad (5.2.18)\end{aligned}$$

The summation in equation [5.2.15] is thus computed in the above manner, and incorporated into the right hand side vector R.

- **3. Non-Conservative Source Term**

It remains to determine how to calculate $-B \cdot \nabla u$. It is worth noting here that the "∇" here is a *Grad* operator acting on each component of u, for each of the magnetic field equations. Thus restricting attention to the B_x equation once again, we find that the contribution is given by;

$$-\left(B_x \frac{\partial u}{\partial x} + B_y \frac{\partial u}{\partial y} + B_z \frac{\partial u}{\partial z}\right) \tag{5.2.19}$$

Here we require a modified form of Gauss' divergence theorem. If for a general vector, $F = c\alpha(x,y,z)$, where c is a constant vector, then the divergence theorem reduces to

$$\int_{\delta V} \nabla \cdot F dV = c \oint_{\delta S} \alpha dS \tag{5.2.20}$$

Using the fact that $\nabla \cdot Bu = B \cdot \nabla u + u \nabla \cdot B$, and noting the second term is identically equal to zero, we obtain

$$\int_{\delta V} B \cdot \nabla u dV = \int_{\delta V} \nabla \cdot Bu dV \tag{5.2.21}$$

Note that in the above expression, we assume that B is constant. This is a reasonable assumption to make, since the domain is being discretised into finite volumes, over which we assume that flow and magnetic field variables are fixed. In a similar fashion to the evaluation of the dissipative terms, we approximate the right hand side of this as the average value over the cell volume, multiplied by the cell volume, and use Gauss once again;

$$\delta V [\nabla \cdot Bu]_{AVE} = \sum_{i=1}^{6} Bu \cdot n_i \tag{5.2.22}$$

where the summation takes place over all cell faces of a volume. The additions to the B_y, B_z equations are entirely analogous, the only difference being the u velocity being replaced by v and w respectively.

Having determined all components of R, B is updated using the explicit procedure described above. Once the magnetic variables are updated, a similar task takes place in updating the flow variables. Once again contributions to R, this time for the PNS equations

are calculated, and flow variables updated. The following section discusses the additional terms that need to be included into the $\boldsymbol{R}$ vector as a consequence of adding the magnetic field model.

5.3 Additional PNS Terms

Several methods have been assessed in the incorporation of the magnetic field terms into the PNS model. Here the methods used to calculate the contributions from these extra terms is outlined. Broadly speaking the extra terms may be grouped into those terms arising due to the magneto-hydrodynamic model, and those due to the addition of Powell's source term. Although the method used to evaluate these terms is similar to that used to find the dissipative and non-conservative terms in the induction equations, a brief overview is provided herein.

- **Field Contribution from MHD model**

  From equation [5.1.2] the contribution to the u-momentum equation arising from the introduction of the magnetic field is given by $\nabla.\boldsymbol{A}_u$, where;

$$\boldsymbol{A}_u = \begin{bmatrix} (-B_x^2 + B_y^2 + B_z^2)/2 \\ -B_x B_y \\ -B_x B_z \end{bmatrix} \tag{5.3.1}$$

  Once again, in analogy with the evaluation of dissipative and viscous terms in the induction equation, this is rewritten in finite volume form as;

$$\int_{\delta V} \nabla.\boldsymbol{A}_u dV = \delta V \left[\nabla.\boldsymbol{A}_u\right]_{AVE} \tag{5.3.2}$$

  taking the cell centre value to be the average value over the cell volume, and recast using divergence theorem to obtain the same result, requiring the vector quantities at the cell interfaces, taking their product with their respective unit normals, and then making a summation over all faces. For the v and w momentum equations, the same technique is applied to the vectors;

$$A_v = \begin{bmatrix} -B_y B_x \\ (B_x^2 - B_y^2 + B_z^2)/2 \\ -B_y B_z \end{bmatrix}$$
$$A_w = \begin{bmatrix} -B_z B_x \\ -B_z B_y \\ (B_x^2 + B_y^2 - B_z^2)/2 \end{bmatrix} \quad (5.3.3)$$

and for the energy equation;

$$A_E = \begin{bmatrix} u|B|^2/2 - B_x(u \cdot B) \\ v|B|^2/2 - B_y(u \cdot B) \\ w|B|^2/2 - B_z(u \cdot B) \end{bmatrix} \quad (5.3.4)$$

The above vectors are substituted into equation [5.3.2] and evaluated using the same procedure used for the dissipative terms in the induction equation. It is also worth noting that the evaluation of the source terms appearing in the low magnetic Reynolds number model are also computed in the same fashion.

- **Contribution from Powell's source**

Powell's source term introduces $B\nabla \cdot B$ into the momentum equations, and $(u \cdot B)\nabla \cdot B$ into the energy equation. Expressing the above source term concisely as $H\nabla \cdot B$,where $H = (0, B, u \cdot B)^T$, we derive a finite volume approximation using the following;

$$\int_{\delta V} H\nabla \cdot B dV = H_{AVE} \int_{\delta V} \nabla \cdot B dV = \frac{H_{AVE}}{\delta V} \sum_{i=1}^{6} B_i \cdot n_i \quad (5.3.5)$$

where the cell centre values are taken to be the average over the cell volume, and the divergence theorem used to determine contributions from each face.

5.4 Solution Algorithm

With the techniques used to update the magnetic field variables, and methods used to determine the contributions from the additional terms appearing in the momentum and energy equations, it remains to explain the procedure used to tie these components together into a unified solution algorithm. Initially, on the first forward sweep, the Parabolised Navier Stokes equations in the absence of any magnetic field effect are computed, for all streamwise stations. This allows the solution to achieve a reasonable estimate of the

flow prior to introducing magnetic effects. On the first back sweep, and on all subsequent sweeps, the modified parabolized Navier Stokes model taking into account of B is solved, and the magnetic induction equation is solved in the manner described in the previous section.

For each streamwise station, the flow variables in the modified PNS equations are updated using the methods above to calculate the right hand side vector. Next the update occurs for the B in the induction equations, keeping all flow variables fixed during the update. For each station, the procedure repeats itself until the convergence level is attained for the flow variables, and the algorithm proceeds onto the next or previous streamwise station, depending on the marching direction. The sweeping procedure is repeated until no further iterations need to be performed on the flow variables, for all stations within the domain.

CHAPTER 6

Verification of the Low Re_m Model

This section presents two cases to validate the implementation of the low magnetic Reynolds number model . As explained in section [4.6.3], the advantage of the low magnetic Reynolds number model over the simplified model is that the magnetic induction need not be solved for the field. Analytical solutions exist for the model, such as a simple Hartman flow which models flow through a channel in the presence of a uniform field, or the Rayleigh problem, where an initially stationary plate moves with a given velocity. In view of the fact that the base model for the IMPNS code, that is the parabolised Navier Stokes equations seeks solutions to steady, predominantly supersonic problems, such analytic test cases are intractable.

As for comparing flow solutions to experimental data, there exist many cases that have assessed the potentials of MHD in hypersonic aerodynamic applications, as outlined in section [4.4], but often involved artificial ionisation procedures or seeding of ionised particles into the flow domain, which the current model does not permit.

In view of these restrictions, the model has been validated against several numerical computations of other research groups that have also looked into magneto-hydrodynamic flow control using the low magnetic Reynolds number model. Two such cases are presented here, which capture the fundamental effects of applying a specified magnetic field to flow problems encountered in hypersonic aerodynamics.

6.1 Uniform Field applied to a Flat Plate

Prior to the resurgence of interest in magneto-hydrodynamics as a flow control mechanism by the aerospace community, a large part of the research examining the effects of turbulent flows with MHD had been investigated with astrophysical applications, or with liquid metals. Theoretical treatises by Lykoudis [93] and other works [131, 136] point to conclusion that the introduction of magnetic fields tend to inhibit turbulence. Indeed Narasimha [112] suggests that a process of relaminarisation is a feature of turbulence with MHD effects.

Turbulence can be attributed to be the primary cause of flow characteristics such as heat transfer and drag, quantities that are of particular interest in examining flows past hypersonic vehicles. Therefore the current case is pertinent and justified not only as a

means of validating the model, but also to understand whether the model captures the physical characteristics of the interaction of magnetohydrodynamics and turbulence.

Numerical investigations into the effects of applying a field normal to laminar and turbulent flows past a flat plate have been investigated by Dietiker and Hoffmann. [49], and also by Kato et al. [78]. Their results are in excellent agreement with each other, and comparisons to both sets of data is made here. A supersonic flow past a flat plate of length $L = 0.08m$ is considered under the following flow conditions;

$$\begin{aligned} M_\infty &= 2.0 \\ p_\infty &= 1atm \\ T_\infty &= 300K \\ Re_\infty &= 3.75 \times 10^6 \\ \sigma_\infty &= 800mho/m \\ Re_m &= 0.058 \end{aligned}$$

Both groups present results to the flow problem outlined above. Note that the value of the magnetic Reynolds number is sufficiently less than unity, indicating that the choice of model is suitable for the case in question. A uniform flow is applied normal to the flow direction, ie $B_x = 0$, and B_y is non zero. The normal component, B_y is varied from $0.0T$ to $1.2T$, and is manifested in the governing equations by choosing appropriate values for S_∞, the magnetic force number;

$$S_\infty = \frac{\epsilon c^2 B_y^2}{\rho u_\infty^2} \tag{6.1.1}$$

A grid consisting of 150 points in the streamwise direction and 200 points normal to the wall, employing clustering near the wall surface such that the height of the cell is $10^{-6}m$ above the wall. A single sweep algorithm is used intially with the flux-conservative Vigneron's approximation for subsonic portions of the boundary layer [91]. A second order upwind discretisation is used to evaluate the streamwise flux, and for the crossflow flux the flux difference splitting scheme of Osher and Solomon [116] is used. MUSCL interpolation [160] of primitive variables is employed in calculating the crossflow fluxes to increase spatial resolution to second order. The solution is space marched explicitly, using a CFL number of 0.75.

Figures [6] illustrate the results of iterative and grid convergence studies. The velocity profiles in the absence of the magnetic field show that a convergence criteria for the residuals of 10^{-6} and a grid consisting of 150×200 points, are sufficient to ensure that the

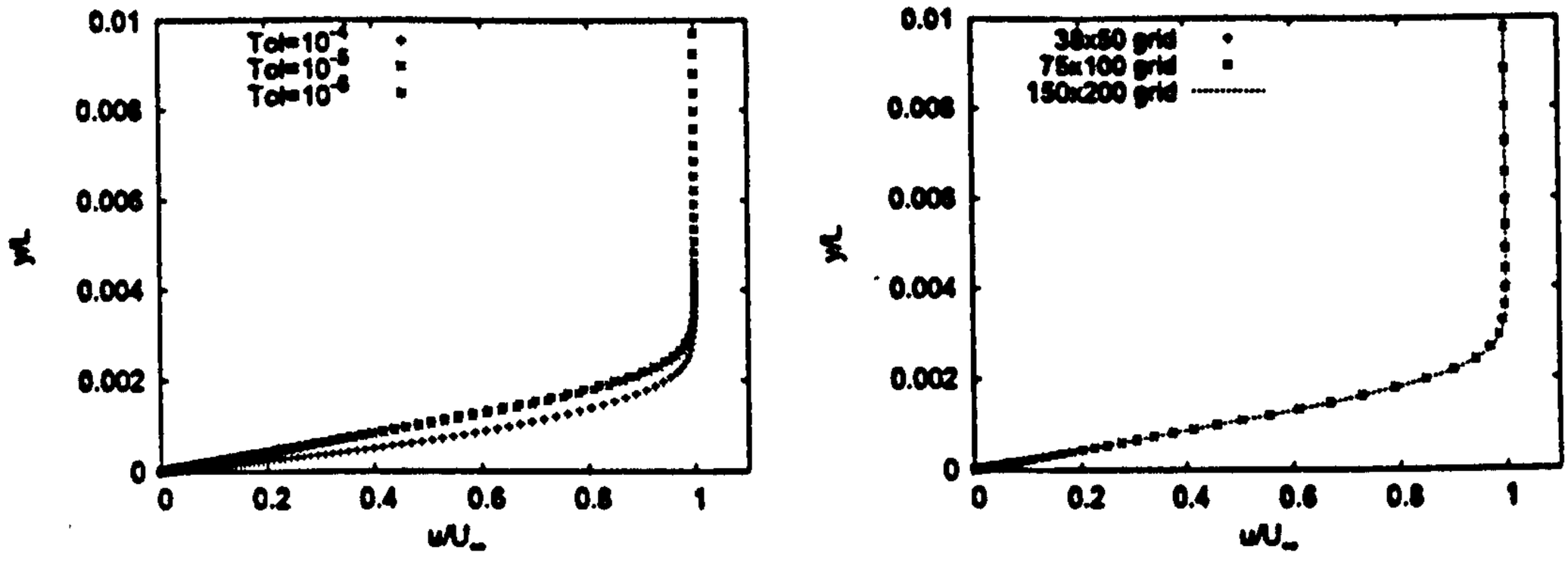

Figure 6: Iterative (left) and Grid Convergence (right) of U velocity Profile

output solution is within the asymptotic range of convergence. A similar examination of the velocity profiles in the presence of the field, for a given value for the magnetic force number has been made. This is to check if the presence of the field was having any unforeseen effects on convergence. The plots show that the solution is asymptotically converged for the same grid and residual tolerances, thus a meaningful comparison of the effects of applying a field can be obtained by using the same grid and convergence tolerance for all strengths of S_∞.

6.1.1 Laminar Flow

Initially, laminar velocity profiles under the influence of several field strengths were investigated, as a check to ensure that the Lorentz force generated from a magnetic field normal to an ionised flow acts in the opposite direction to the flow direction. Initially, a single sweep calculation was made, the results of which are plotted in figure [7].
The effect of the field decelerating the flow is clearly illustrated, and the modified PNS equations demonstrate good agreement with the results of Dietiker and Hoffman, particularly outside the boundary layer. Within the boundary layer, and for the case where streamwise separation occurs ($S_\infty = 1.840$), the agreement deteriorates somewhat.

In single sweep mode, a portion of the pressure gradient in suppressed by the IMPNS code to ensure the equations remain hyperbolic in the subsonic part of the boundary layer. Therefore since portions relating to upstream influence of the $\frac{\partial p}{\partial x}$ term are neglected, agreement within the boundary layer is affected. Furthermore, no upstream influence is taken into account in this mode, and therefore, the solver is incapable of detecting separation. However, for the separated case, the model is still capable of predicting the velocity profile outside the boundary layer, as the good agreement with the results of Dietiker and Hoffman indicate.

To overcome this, the same calculations were also preformed using the multisweep

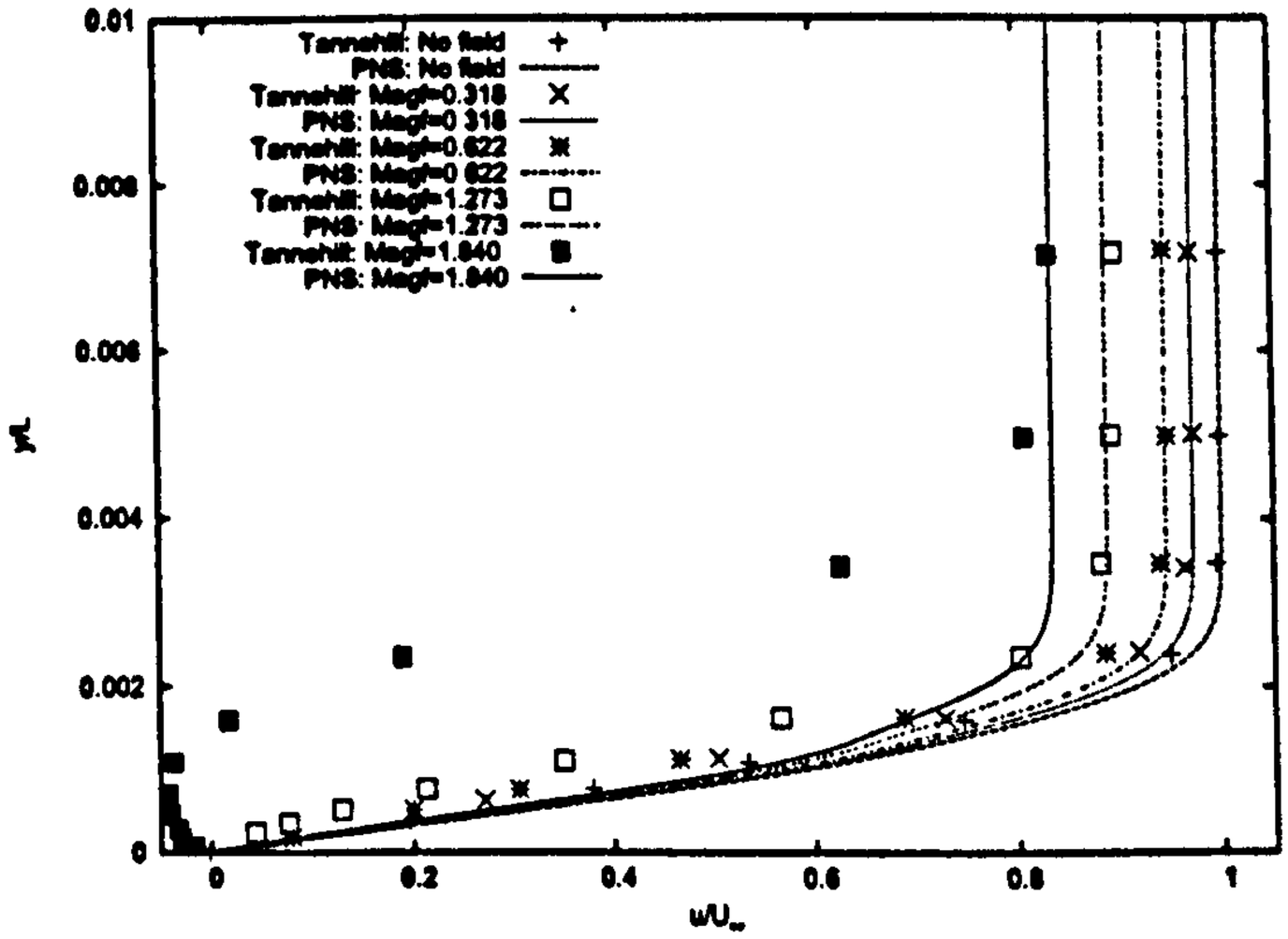

Figure 7: Laminar velocity profiles, single sweep

algorithm. Within the IMPNS solver, three initialisation coarse sweeps are performed, the upstream boundary condition is assumed to be freestream, and the downstream boundary condition is extrapolated from the interior on each sweep. Fig [8] shows the improvement in the agreement with [49] due to the additional computational effort. Agreement in the boundary layer is visibly better than using single sweep alone, and the PNS solutions do also predict separation for the largest value of S_∞ considered. For this case however, there is over prediction of the reverse flow velocities in the boundary layer.

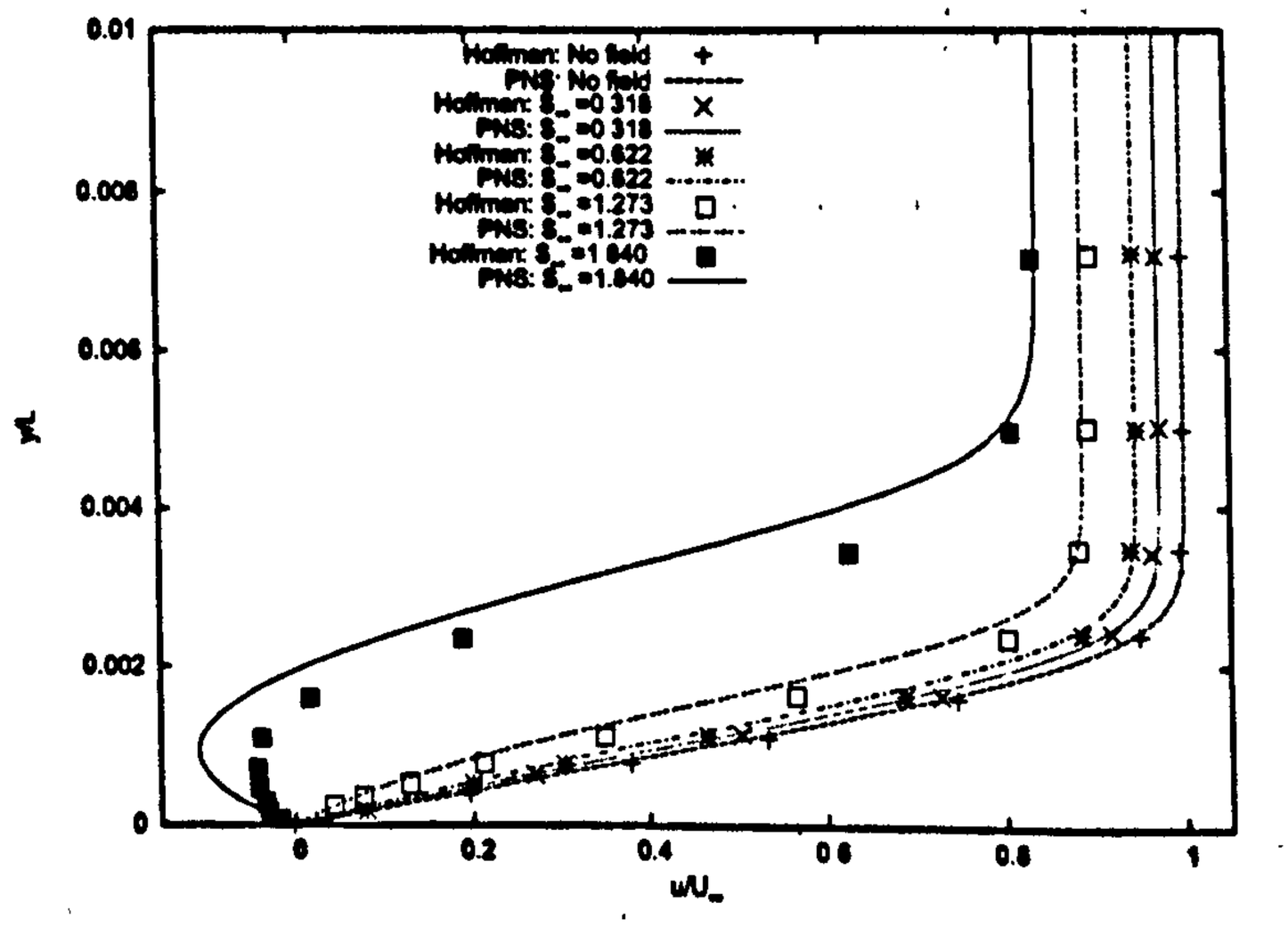

Figure 8: Laminar velocity profiles, multi sweep

This can be attributed to the fact that the model is incapable of dealing with large streamwise separated regions that do not reattach. The case in question does not reattach before the outflow boundary. The i=imax boundary is set on the assumption of a supersonic outflow boundary, therefore the boundary conditions are ill posed for the separated case, and is a probable cause for the observed discrepancy.

When multisweeping is used as the solution algorithm, no approximation is made with regard to the streamwise pressure gradient term, and in actual fact, the equations being solved are the "Thin Layer Navier Stokes " equations. A direct comparison of the no field calculations using single sweep and multisweep technique, demonstrates the marked improvement in agreement that is the consequence of allowing the code to take into account any upstream influence. As these are calculations made in the absence of the field, one can infer that the difference observed is indeed an outcome of the algorithm used, and not the presence of the low magnetic Reynolds number model. Therefore, for the case involving magnetic fields of various strengths, the better agreement is due to utilising multi-sweeping. The agreement outside the boundary layer remains unchanged, as here no approximation is made on the streamwise pressure gradient.

For the separated case, as the algorithm takes into account upstream influence, the revised algorithm also predicts separation, although agreement in the boundary layer is poor. This is the result of not being able to prescribe a suitable boundary condition ahead of the last station in the streamwise direction. The boundary here is either extrapolated from the interior, or assumed to be a supersonic outflow, both of which are inappropriate as the flow is travelling into the domain in the boundary layer. With no knowledge as to what ought to be prescribed here, agreement is most likely to be compromised as a result.

6.1.2 Turbulent Flow

Under the same conditions outlined above, the effects of a uniform field applied to a turbulent flow were also considered. The effects of turbulence were simulated using the Spallart-Allmaras model for the turbulent viscosity, with transition taking place at station $i = 75$, halfway along the length of the plate. The velocity profiles illustrated in [9] show steeper gradients in the streamwise velocity profile, a typical feature of turbulent flows, given that there is typically more kinetic energy in the near wall region compared to laminar boundary layers.

The results highlight the fact that the effect of the field is the same as that of the laminar profile. The field acts to decelerate the incident flow, abd separation takes place at a higher magnetic force number, due to the turbulent nature. Unlike the laminar case, the flow does not separate for the $S_\infty = 1.840$ case, or for magnetic interaction parameters

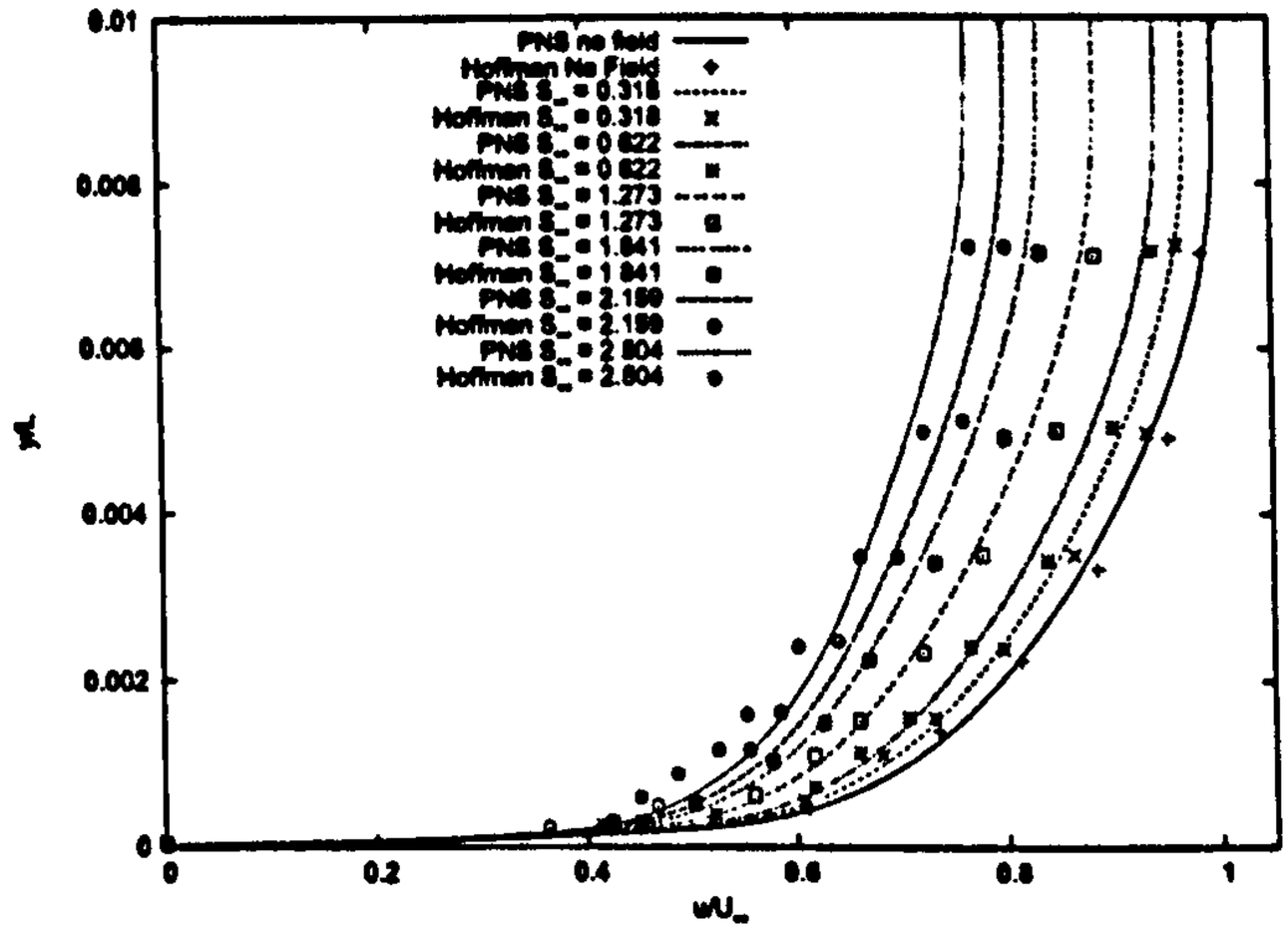

Figure 9: Turbulent velocity profiles

greater than this, owing to the greater kinetic energy in the boundary layer.

The deceleration of the flow has consequences on the drag experienced by the plate. This can be shown by considering the variation of the skin friction coefficient along the flat plate, as in figure [10]. As the magnetic field strength is increased the skin friction profiles shift downward, resulting in decreased drag over the length of the entire plate, as shown. Comparisons of the skin friction profiles in the turbulent region show some discrepancy to the computed data, but this it is important to note that in Hoffman and Kato et al's work, the Baldwin-Lomax algebraic turbulence model has been utilised.

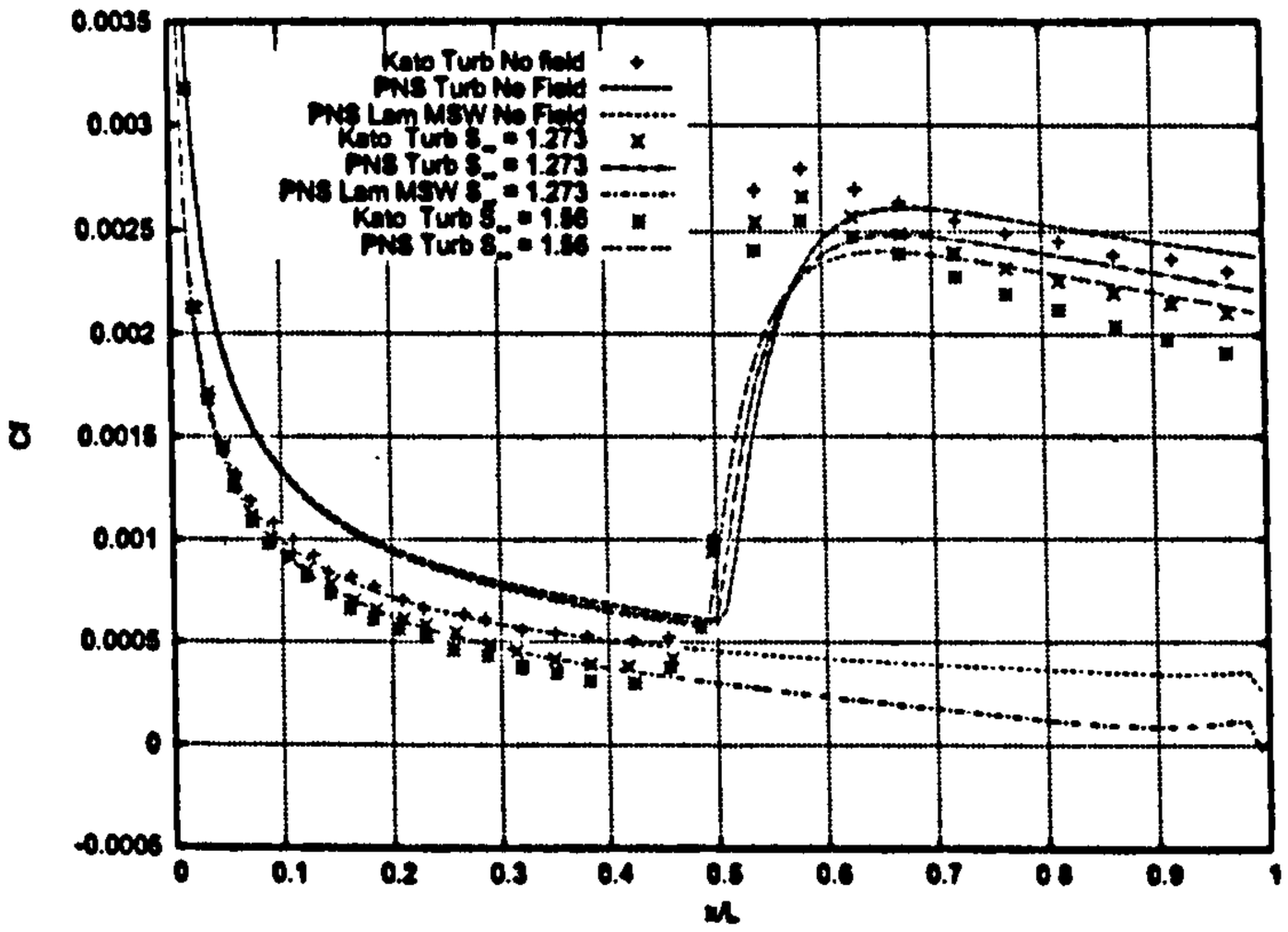

Figure 10: Effect on Skin Friction Coefficient

Despite being able to predict the underlying trend caused by applying a magnetic

field agreement in the near wall region could be better. Figure [9] shows that the discrepancy between PNS results and that of Hoffman et al get worse as the near wall region of the boundary layer is approached. For example, for the case where the magnetic interaction parameter is equal to 2.504, at $y/L = 0.0006$, there is a difference in streamwise velocity of approximately 9%.

Discrepancy is also seen in figure [10] for the PNS cases labelled "turb". As an illustrative example, consider the case where no magnetic field is applied, ahead of the turbulence transition point, at $x/L = 0.35$. The turbulent PNS calculation predicts a skin friction coefficient of 7.308×10^{-4}, and Kato and Tannehill's results return a value of 5.3×10^{-4}. This gives a discrepancy of approximately 40%, and is visibly clear in figure [10]. However, if a laminar calculation, that allows for multi-sweeping, is employed, then the PNS code predicts a value of 5.373×10^{-4}, an error of about 1.5%.

Given that the the above cases considered did not include the use of a magnetic field, there remains the possibility that the difference between the turbulent PNS results and those found in the literature may be the cause of different turbulence models being used. This cannot be ruled out entirely, but there is a strong evidence to suggest that it is the use of multi-sweeping that is an over-riding factor in determining the extent of agreement.

Beyond the transition point, the source of error is twofold: that due to multi-sweeping and that due to difference in turbulence model. As is the case for the laminar region, the differences in skin friction coefficient magnitude may be attributable to the lack of multi-sweeping. Figure [10] also shows that the peak skin friction coefficient values occur further downstream for the turbulent PNS calculations compared to Kato and Tannehill. Such an issue is more likely to be an issue related to the choice of turbulence model. Unfortunately, the PNS code does not allow for a turbulent calculation to be made when multi-sweeping is employed, and so such a test is left as future work. As far as the low magnetic Reynolds number model validation is concerned, discrepancies can be attributed to other factors, but the model shows agreement for both laminar and turbulent calculations.

6.2 Blunt Body Calculation

The second validation test case was that of a hypersonic flow past a blunted cone, corresponding to that found in Khan et al. [81] and MacCormack [96]. A set of two dimensional axisymmetric calculations are performed to investigate the effects of applying a field, on shock stand-off distance. The computational grid is shown in figure [11].
The flow is assumed to be inviscid and the conditions are specified by the following;

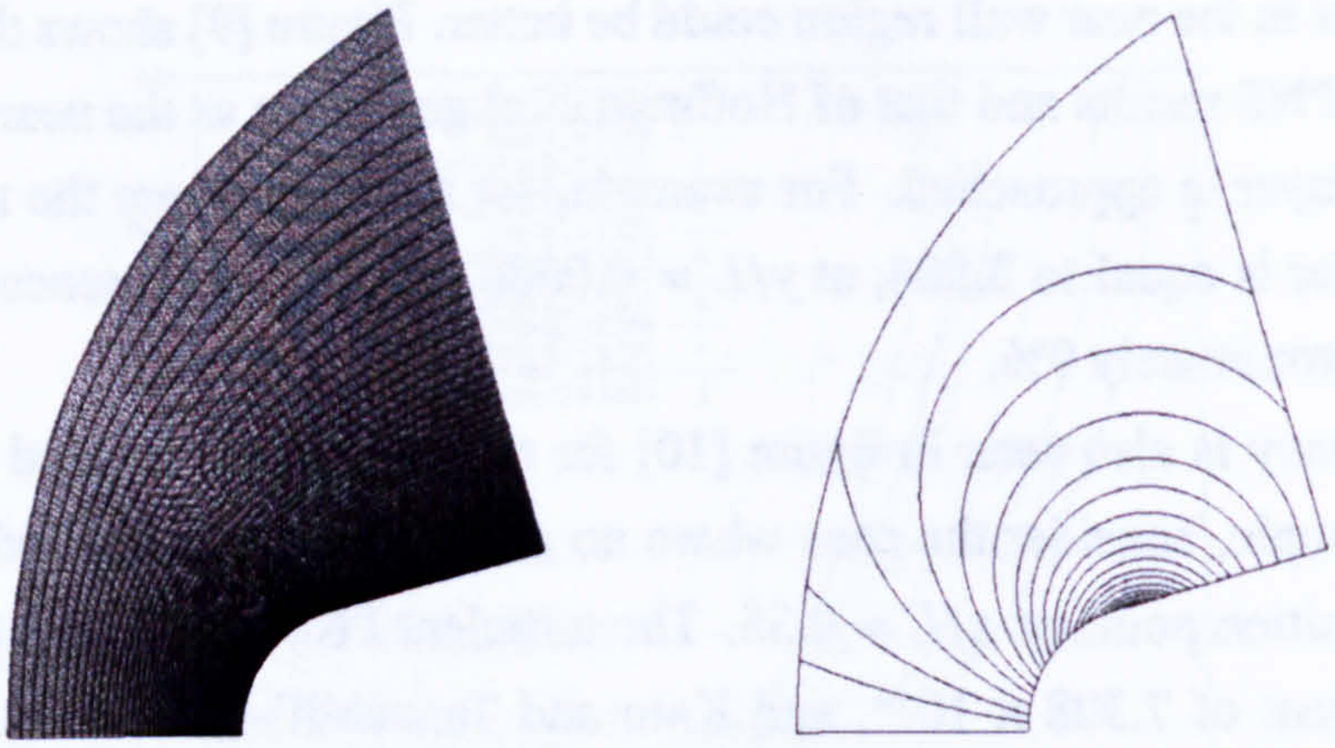

Figure 11: 2D Axisymmetric Blunt Body Grid, and Magnetic Field Lines

$$M_\infty = 15.0 \tag{6.2.1}$$

$$p_\infty = 36.6Pa \tag{6.2.2}$$

$$T_\infty = 294K \tag{6.2.3}$$

The applied magnetic field being given as a dipole of variable strength, the field lines for which are illustrated in figure [11]. The blunted portion of the body is a circular section, and dipole core is placed at its centre. On the body surface, a zero slip condition for the velocity field is imposed, the pressure gradient normal to the wall is zero, and the wall is also assumed to be adiabatic. The multi-sweep algorithm is employed throughout the domain using three initialising coarse sweeps, with a singular line boundary condition on the upstream boundary, and an extrapolated boundary on the downstream boundary. The Steger and Warming [153] flux vector splitting scheme is used in both streamwise and crossflow directions. Flow variables are updated explicitly, using a CFL number of 0.5.

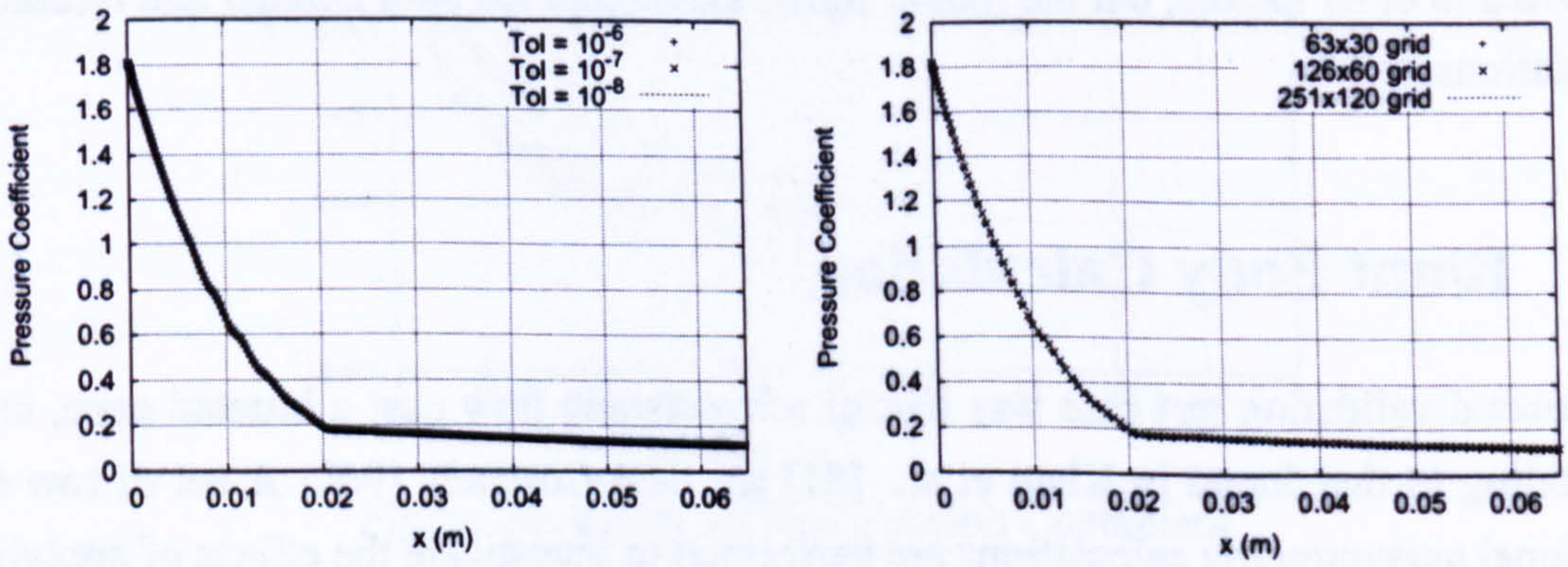

Figure 12: Iterative (left) and Grid Convergence (right) of Pressure Coefficient Distribution

Akin to the flat plate boundary layer, an iterative and grid convergence examination was initially undertaken. Figure [12] shows the pressure coefficient distributions along the surface of the body, for several residual tolerance values. The pressure coefficient is shown to be within the asymptotic range of convergence for the residual tolerance of 10^{-6}, with little change being seen in its profile for smaller tolerances. For the three iterative convergence levels investigated, the shock standoff distance along the stagnation line is also identical, and therefore an iterative tolerance of 10^{-6} for the main calculation is justified. The figure also shows that there is little difference in the pressure coefficient distribution for the three grids investigated.

Grid	Standoff / body diameter
63×30	0.635210
126×60	0.631244
251×120	0.633228

Table 1: Shock Stand-off Distances on Grid Levels

Table [6.2] shows the shock stand-off distances for three different grid levels. As the figures suggest, the quantity is a lot more sensitive to grid spacing than the pressure coefficient distribution. There is a 0.3% difference between the results for the 126×60 and 251×120 grid cases, which is small enough to ensure 251×120 is a sufficiently fine grid.

As discussed in chapter [4.1], there has been a substantial amount of interest in the effect of applying magnetic fields to blunt geometries. As Anderson explains [7], spherically blunted geometries such as the one investigated here arise as a consequence of the requirement to withstand heat conduction to the body surface for hypersonic flows. Conic sections result in shock attachment on the leading edge, a consequence of which is that there is a greater degree of heat transfered to the body. At such high Mach numbers, the use of suitable geometries alone, cannot guarantee the structural integrity of the body, hence the adoption of various thermal protection systems. The ability of magnetohydrodynamics is also attractive in this regard, since given a magnetic field that is orientated in such a fashion, it is possible to decelerate the incident flow if it is sufficiently ionised. In the present case, a dipole field is applied to a Mach 15 flow, and investigations into the effect of changing the field strength is made by varying the magnetic interaction parameter;

$$Q = \frac{\lambda B_0^2 L}{\rho_\infty U_\infty} \tag{6.2.4}$$

which upon close inspection can be shown to be the product of the magnetic force number S_∞ and magnetic Reynolds number Re_m. The force number premultiplies the source term

contributions appearing in the momentum and energy equations [4.6.30 & 4.6.31], thus controlling the magnitude of the magnetic field effect.

Three separate cases are considered, corresponding to field strengths of $B_0 = 0$, 2 and 8 Tesla, corresponding to a value of $Q = 0$, 6, and 96 respectively. The shock standoff distance has been calculated by determining the location of the sonic line ($M = 1$) contour from the body surface, along the stagnation streamline, results of which are shown in figure [13].

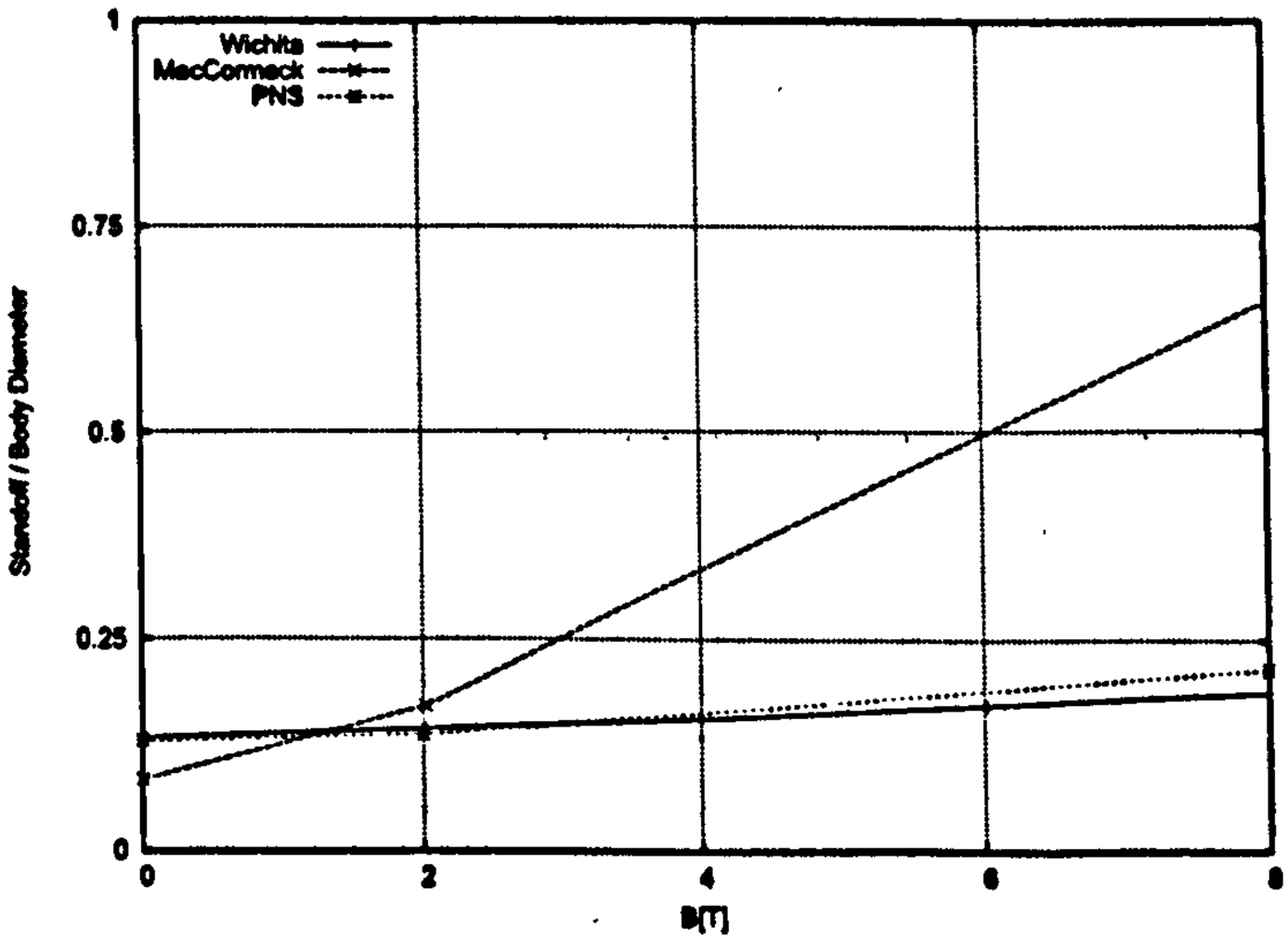

Figure 13: Shock standoff Distance as a function of Q_∞

The shock standoff normalised by body diameter is plotted against the magnetic field strength. For the case of no magnetic field, the PNS solution shows good agreement to that of the Wichita group [81] and the analytical solution [36]. As the field strength is increased, so too does the shock standoff distance. For larger values of B_0, there is some discrepancy to Wichita results, possibly due to the method in which shock standoff has been calculated, although the underlying trend of increased standoff is evident. Conversely, agreement to MacCormack's data is poor, although there remains some doubt as to the grid convergence of MacCormack's results, as in that work, a grid consisting of 52x52 points has been used, compared to the 251x130 points used in the current study.

Despite the fact that a field has been applied, figure [13] seems to suggest that the gains in terms of the change in shock stand-off distance seem some what negligible. This can be explained by examination of the Lorentz force field in the body vicinity, as a result of adding the field. The current is given by the equation,

$$\mathbf{J} = \mathbf{E} + \mathbf{v} \times \mathbf{B} \tag{6.2.5}$$

As no electric field is applied, the current acting is perpendicular to the incident flow and the magnetic field lines. The resulting body force acting on the fluid is perpendicular to the current vector, and the magnetic field lines. Combining the magnetic field lines and the flow vector yield a body force, known as the Lorentz force, and given by $\mathbf{L} = \mathbf{J} \times \mathbf{B}$. For the flat plate boundary layer, it is clear that this body force acts to oppose the incident flow, since the flow vector, and the magnetic field lines are perpendicular to each other. For the blunt body, the field is generated with a dipole, a consequence of which is that the field lines and flow vectors are not necessarily perpendicular everywhere.

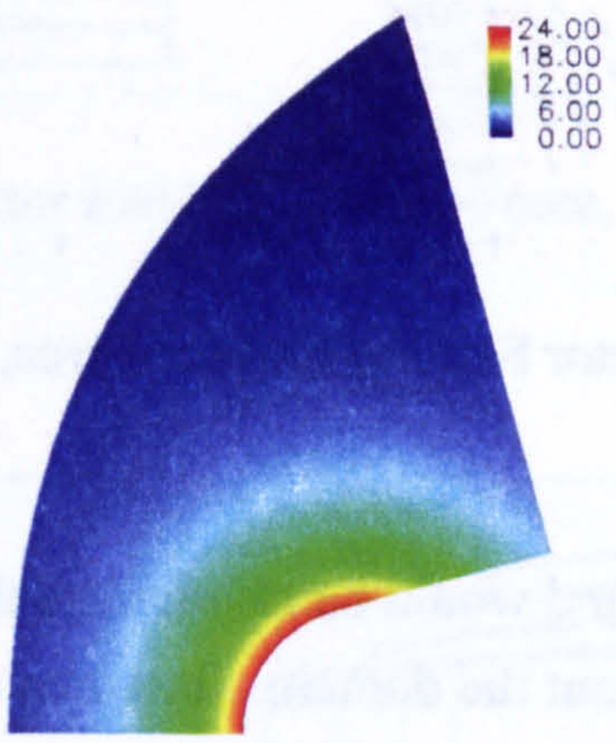

Figure 14: Magnitude of Magnetic Field, in Tesla

The manner in which the flow can be seen to decelerate the flow may be observed by considering the magnitude of the magnetic field about the body, as shown in figure [14].

One will notice that the magnitude of this force is greatest near the shoulder region of the body. This observation can be explained by considering the functional form of a dipole field. First, since the magnetic field scales with $1/R^{3/2}$, where R is the distance from the dipole, one can infer that the magnitude of the field is greater nearer to the body. Thus it is to be expected that the magnetic field has greater influence nearer the body. However, the magnitude of the magnetic field alone does not account for how it influences the flow field.

Close inspection of the local Lorentz force vectors accounts for how the field influences the flow, and is shown in figure [15].

The vector field illustrates the direction in which the magnetic field acts to try and redirect the flow. The figure indicates that the Lorentz force acts in the opposite direction to the incident flow around the shoulder region of the body, thereby decelerating it. However, as one traverses across the body, towards the stagnation line, the Lorentz force is directed perpendicularly downward to the flow field, which is ineffective in decelerating

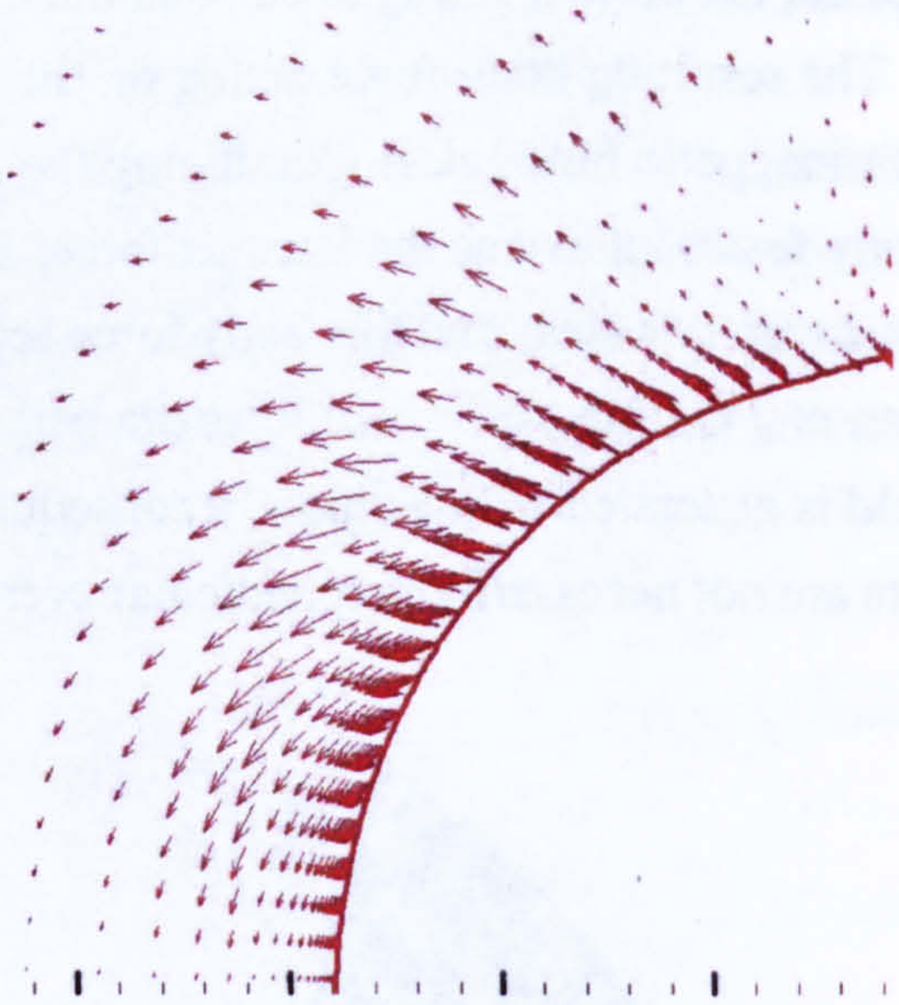

Figure 15: Vector Field of Lorentz Force, Dipole Field

the flow. A more effective method would be to orientate the field such that it acts in the the positive y-direction throughout the domain. Based on observations discussed for the flat plate boundary layer case, this would mean that the resultant body force is acting in the direction opposing the flow velocity, even along the stagnation region. For the dipole field this behaviour only occurs in a small vicinity as indicated, on the shoulder region of the body, and not over the entire domain as for the flat plate case. The deceleration, and consequently the increase in shock stand-off distance, is not as pronounced as one might expect. The flat plate boundary layer investigations illustrated that a field orientated perpendicularly to the wall was effective in decelerating the flow to the extent of separation.

Evidence to suggest this phenomena can be explained in figure [16], which shows the Lorentz force vector field, for the case where a uniform magnetic field is applied. Clearly the force acts to oppose the oncoming flow field over a larger region around the body, in contrast to the dipole case. Consequently, it is to be expected that the increase in shock stand-off distance will be greater with this type of magnetic field orientation. This is demonstrated further by applying a uniform magnetic field, to the same flow conditions above. Figure [17] shows the density variations along the stagnation line;

The magnetic interaction parameter is increased from 0 corresponding to the no magnetic field case up to $Q_\infty = 6$, which is the case for $B_0 = 2T$. As the field strength is increased, the graph indicates that the discontinuity in the density profile moves further away from the body surface, indicating an increase in shock stand-off. The jump in density over the shock also decreases, indicating that the shock is progressively weaker with increasing

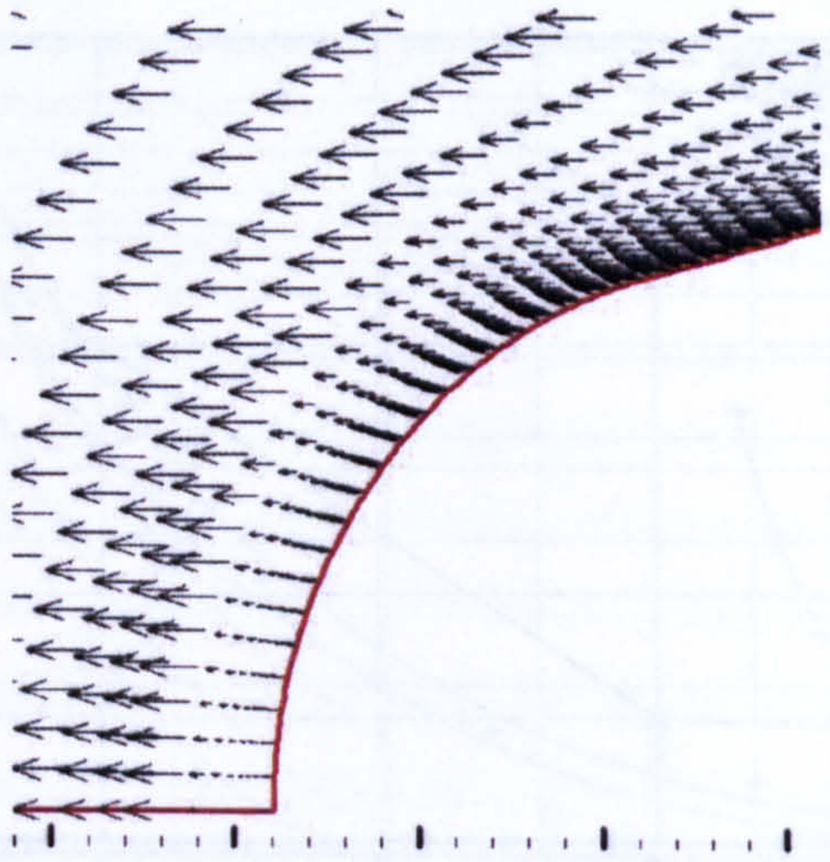

Figure 16: Vector Field of Lorentz Force, Uniform Field

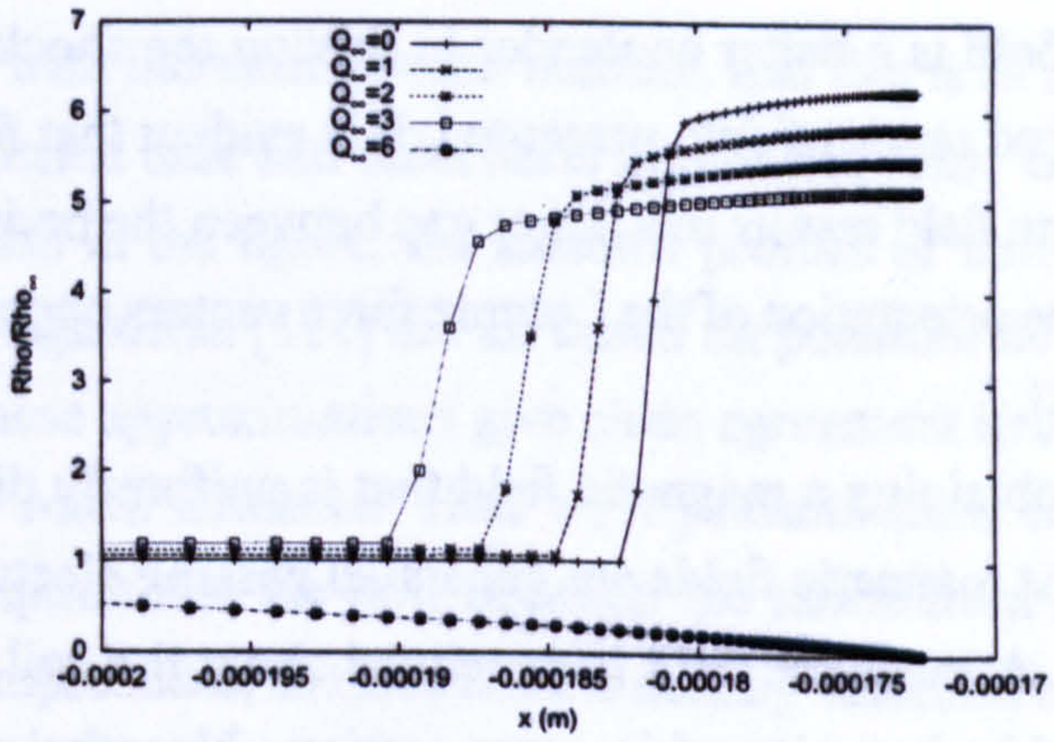

Figure 17: Density Profiles along Stagnation Line

Q_∞. The density profile for $Q_\infty = 6$ appears inconsistent with the rest of the observed trend. This is because in this instance, the field is strong enough to push the detached shock out of the flow domain, thus any behaviour cannot be accurately captured. Hence the odd behaviour in this case. It therefore makes sense not to consider the output for cases where $Q_\infty \geq 6$.

The improved performance in shock stand-off distance is shown in figure [18], showing a direct comparison of the two field orientations, for the trend in shock stand off distance ratios against magnetic field strength, in Tesla. The dipole field case corresponds to the same parabolized Navier Stokes data presented in figure [13]. For the uniform field case, the shock stand off ratios for fields greater than 2 Tesla are not shown, for the reasons indicated above. Nevertheless, the figure confirms the fact that a uniformly

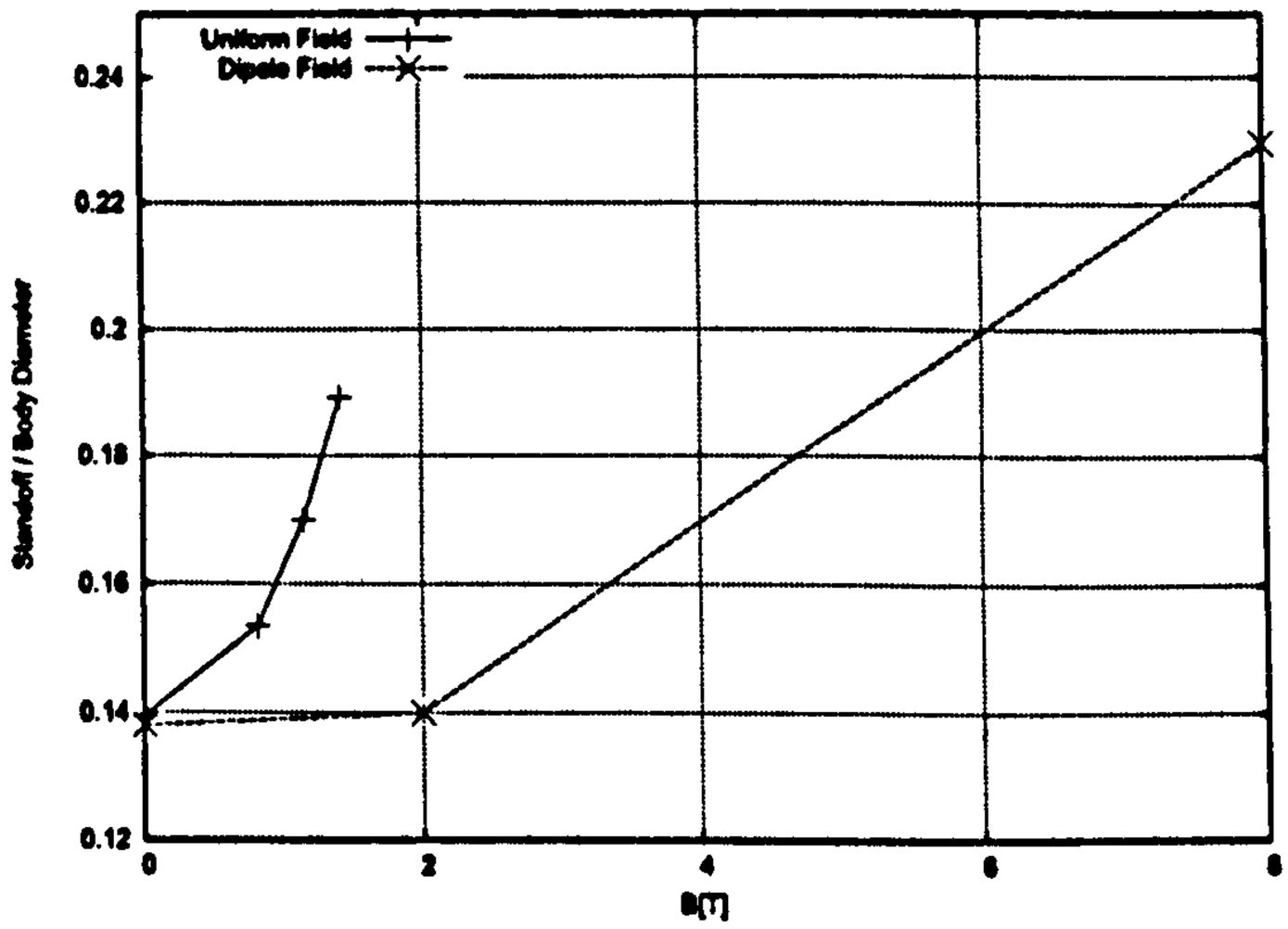

Figure 18: Shock Stand-off, Uniform and Dipole Fields

distributed magnetic field is a better contender in driving the shock front away from the body, as over the limited range of data presented, it is evident that for the same magnetic field strength, a uniform field results in a larger gap between the body and the shock front. This is explained by the orientation of the Lorentz force vectors opposing the fluid motion, as shown in figure [16].

Unfortunately, obtaining a magnetic field that is uniformly distributed in reality is a non trivial task. Most magnetic fields are generated passing electrical currents through conducting materials. A magnetic field is generated about the coil, which more closely resembles a dipole field when viewed in cross section. Nonetheless, the low magnetic Reynolds number model accurately predicts the effect of such a uniform flow field, and serves to illustrate the type of field orientation one desires, given a particular design objective, such as widening the shock stand off distance.

A reassuring and important point to note in figure [13] is the very good agreement in the baseline, no magnetic field case, of the shock standoff distance to the analytic solution found within Cox and Crabtree [36]. As further validation of the parabolized Navier Stokes solver, additional computations have been performed for the shock front location are computed, using Mach number as an independent variable. Since the iterative and grid refinement studies have already been performed, the same conditions have been used to simulate standoff distances. The effects on the standoff to body diameter ratio, as a function of freestream Mach number are illustrated in figure [19].

The figure contrasts the several analytic solutions and experimental observations [130] against data obtained using the PNS model. PNS calculations have been made using Mach numbers of 1.25, 2.0, 5.0 and 10. The simulations illustrate the asymptotically decreasing

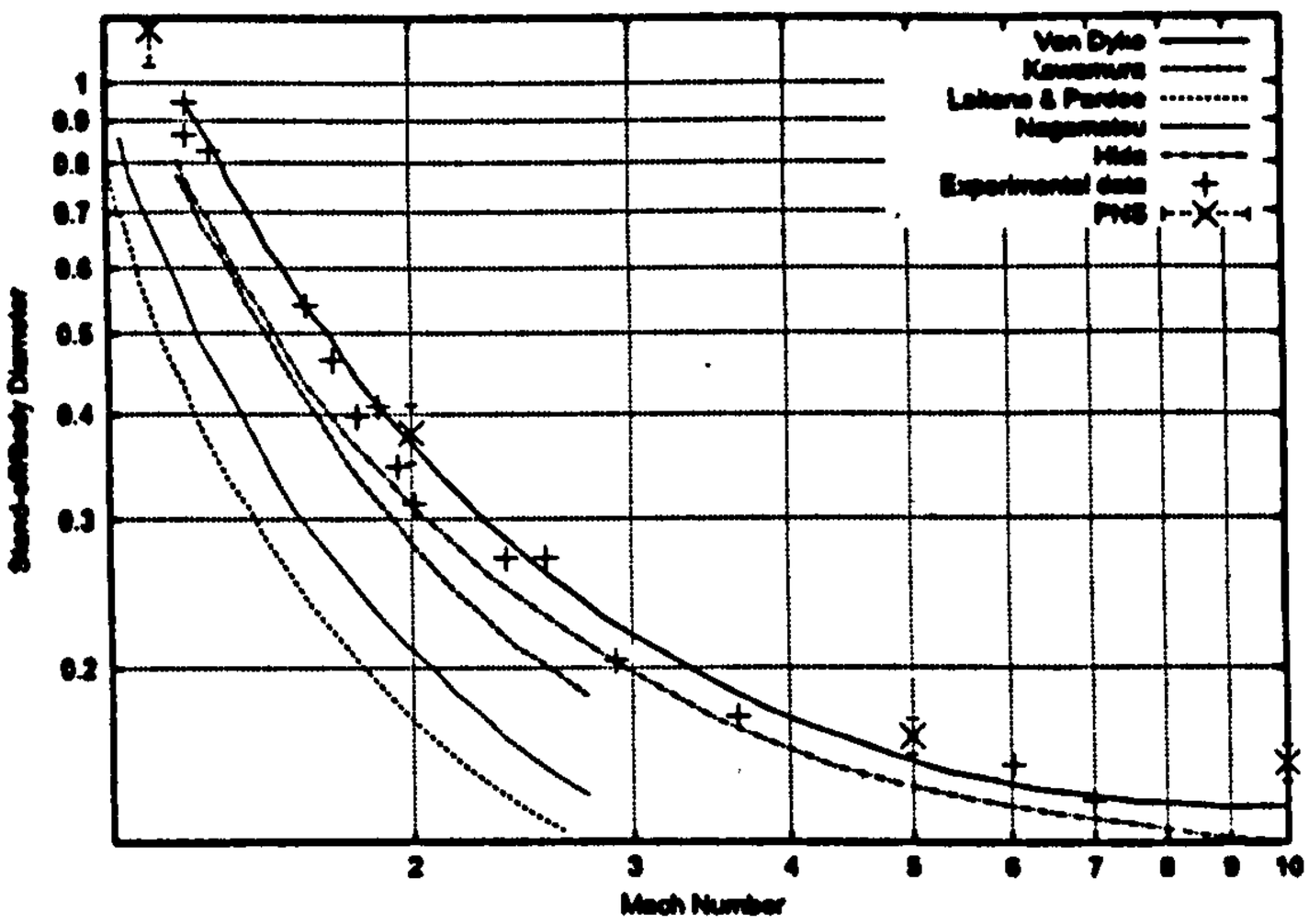

Figure 19: Shock standoff Distance as a function of M_∞

nature of the standoff with increasing Mach number, and this is in qualitative agreement with both the experimental data and theoretical approximations. Of the numerical simulation results presented in the figure, the standoff profiles of Laitone and Pardee [85], Kawamura [79] and Nagamatsu [111] are all based on potential flow approximations. It is clear that none of these approximations give close agreement to the experimental data, particularly for larger Mach numbers. Hida's [70] results show improvement, and are based upon the assumption that the flow between the shock front and the body surface can be treated as incompressible, as there is little density variation in the region.

Despite the apparently good agreement to the stand-off results in figure [13] at lower mach numbers, the above figure highlights that there is in fact a certain degree of discrepancy with the theory proposed by the works listed in some of the diagrams. In contrast to the available experimental data, Van Dyke's numerical solution seems to offer the best agreement [159]. Van Dyke makes use of an inverse method, whereby the shock is initially assumed to have a shape of a conic section, which is a reasonable hypothesis as most hypersonic geometries have spherical or elliptical noses. The Euler equations are rewritten to yield two partial differential equations, for the density and stream function, and are solved for by marching from the shock to the body. The figure shows Van Dyke's results to have remarkable agreement for the spherical body geometry, but Cox and Crabtree [36] point out that the methods chief weakness is in its inability to reproduce distinguishable shock profiles for bodies that are radically different. The PNS solutions over predict the stand off distances, and this over prediction is seen to increase with increasing Mach number. One possible explanation for this lies in the models examined. Van Dykes' simulations make use of a spherical geometry, whereas the model considered

here is a blunted cone, albeit with a spherical nose. The shock front location is not only a function of the incident Mach number, but is also dependent on the sonic line, beyond which the flow is supersonic again. The location of the sonic line is highly dependent on the geometry, and may therefore account for the observed discrepancy.

As the below discussion shows, some of the discrepancy seen can be explained due to the grid employed in the calculation. The beginning of this section shows that iterative convergence is achieved using a convergence tolerance of 10^{-7}, and grid convergence is sufficient using 251x120 grid points.

Turning attention to the shock stand-off distance however, figure [19] shows that there is a degree of discrepancy between the PNS results, and the experimental observations depicted therein. Given this, it is instructive to shed light on the error one might expect from the PNS solutions, as a result of using any particular grid.

In the previous figure, shock stand-off distances are computed by finding the cell at which there is an increase in the pressure coefficient or density profile, or an decrease in the velocity profile, along the stagnation line. In practise, one would observe an almost discontinous jump in these quantities, but there is some "smearing" over several cells. The issue then arises as to which position to take the stand-off measurement from, that is the point at which pressure starts to increase (front of the bow shock), or becomes constant (rear of bow shock). For the present case the author took measurements from the rear of the bow shock.

As the flow domain is discretised into a finite number of cells, all standoff measurements refer to the centre of any given cell. In practise however, any given observation may lie anywhere within the cell, and is therefore subject an error. The error can be alleviated to some extent by adding more points, but regardless of this number all measurements will be subject to an error, as all shock stand-off measurements are taken at discretely positioned cell centres. Therefore it makes more sense to examine the errors for the PNS result instead of further discretizing the flow domain.

If an observation is made at distance x away from the body, the error bounds on this value is therefore $[x - h, x + h]$, where h is the grid spacing for within which the observation x is made. As we know how h varies with distance away from the body surface, it is therefore possible find the error bounds on PNS calculations observed in figure [19].

For each of the three grids used in the convergence study, the following table shows the grid spacing in non-dimensionalised units at the beginning and end of the edge used as the stagnation line. Here, subscript "beg" refers to the furthest most grid spacing, next to the inflow boundary, and "end" refers to the spacing next to the stagnation point on the body surface.

Grid	δs_{beg}	δs_{end}
126x60	$1.0x10^{-5}$	$5.904x10^{-3}$
251x120	$1.0x10^{-5}$	$2.6931x10^{-3}$
501x240	$1.0x10^{-5}$	$1.1801x10^{-3}$

Table 2: Grid properties

The grid spacings are given in the form of a geometric progression, $a, ar, ar^2, \ldots$ for a starting value of a and a common ratio r. For the grids used in the current study, we know that

$$ar^n = \delta s_{end} \tag{6.2.6}$$

where a is equal to the grid spacing at the end of the stagnation line, and n is the number of grid points in the cross flow direction. From this it is possible to deduce that the common ratio r is given by

$$r = \sqrt[n]{\frac{\delta s_{beg}}{\delta s_{end}}} \tag{6.2.7}$$

Therefore, using the formula above, and given that for the three cases presented n = 60,120,and 240 we find that;

Grid	r
126x60	0.899021
251x120	0.954438
501x240	0.978590

Table 3: Grid Common Ratio Values

The above figure compares the shock stand off distance against numerical and experimental results. To determine the error bounds for the PNS calculations one must determine the grid spacing within which the observation is made. As shock stand off distance is measured from the the stagnation point, one must find the index first index i_x for which

$$\sum_{i=i_{end}}^{i_x} ar^i > d \tag{6.2.8}$$

where d is the PNS observation. From this we can conclude that cell $i_x - 1$ is where the observation is made, and that the spacing h needed to compute the error bounds is given by ar^{i_x}.

The error bounds on each of the PNS observations are superimposed onto the grid-centered results in figure [19]. PNS results generally tend to over-estimate the shock standoff distance. For the Mach 2 calculation, there is a considerable difference between the experimental result, although without any accuracy bounds on the experimental data, it is hard to make a quantitative judgement as to what the discrepany may be. At Mach numbers of 5 and 10, the error bounds are naturally smaller given the closer grid lines are present as the body surface is approached. If numerical bounds are considered, then the former case, shows improved agreement with Van Dyke, although for the latter this ceases to hold true. Without experimental data for the higher Mach number cases, it is difficult to assess true accuracy of the PNS simulation, as comparison to other numerical simulations is insufficient. Therefore for larger Mach number simulations (greater than 5) that require capture of shock standoff distances, caution must be interpreting the results.

6.3 Conclusions

In this section the low magnetic Reynolds number model has been validated against computational investigations of several groups. The cases identified are fundamental to ensuring that the model behaves in a manner that is consistent with theoretical results. As the literature review chapter outlined for example, it is known that a uniform field applied to a flat plate boundary acts to decelerate the flow. This was observed for both laminar and turbulent cases, although a certain degree of of disagreement with the other numerical results were observed.

Within the boundary layer for example, the single sweep case highlighted poor agreement owing to the fact that elliptic influence of the streamwise pressure gradient had been neglected. In contrast, use of multisweeping substantially improved agreement. The benefits of using this algorithm in predicting separation are evident for the case where the field was strong enough to induce this behaviour, although the extent of agreement was hindered due to inappropriate boundary conditions. Hence it is reasonable to assume that multisweeping is required, when using the model for cases where streamwise separation or near wall behaviour is important. Thus said, for cases where such factors are not an issue, the low magnetic Reynolds number model provides good agreement with other computation results, as the agreement outside of the boundary layer region illustrates, for the single sweep case.

Heat transfer mitigation on blunt bodies are also a pertinent area in hypersonic aerodynamics and have received widespread interest from magneto-hydrodynamic research groups, and as such a spherically blunted geometry in the presence of a dipole magnetic

field was also investigated. Shock standoff data as a function of magnetic interaction parameter highlighted agreement with the results of Kahn et al [81]. As an additional test on the predictive capability of the IMPNS code, more computations of blunt body shock standoff distances were carried out, in the absence of a magnetic field, to compare to analytical and experimental results. Independently of the low magnetic Reynolds number model, simulations of the axisymmetric blunt body at several Mach numbers illustrate that the asymptotic decrease in shock stand off with increasing Mach number. The predicted distances were in good agreement with the theoretical results of Van Dyke, and with several experimental predictions.

On applying the magnetic dipole field to the configuration, parabolized Navier Stokes results exhibited the same trend in increased shock stand off distance, though the change seemed to be relatively small. This could be explained by examination of the Lorentz force generated from the dipole source, as it indicated that the force vector in the vicinity of the stagnation region were actually acting perpendicularly to the flow direction, and not against it. A uniformly distributed field was shown to reproduce a Lorentz force that acted in the opposite direction to the flow. These effects were confirmed with further numerical simulations of the body under a uniform field, which highlighted the effectiveness of such an orientation over the dipole. Additional simulations examining the behaviour of shock stand off distance on free stream Mach number, in the absence of a magnetic field , were made, and showed good agreement with experimental data and Van Dyke's numerical simulations.

CHAPTER 7

Verification of Simplified MHD Flow Solver

7.1 Introduction

This section outlines some of the commonly used verification and validation procedures within computational fluid dynamics , and particular attention is paid to the verification of the numerical implementation of the simplified magneto-hydrodynamic model outlined in section [4.6.2]. The procedure asserts confidence in the implementation of the model, and therefore serves as an important tool in ensuring its reliability.

In developing an MHD solver to be incorporated into the PNS equations, one of the key problems is in trying to analyse the errors generated by the flow solver. Indeed, as the advances in computer speed and parallel architectures have allowed CFD practitioners to use more and more complex models, engineers must be provided with confidence in the simulated results as a representation of reality. The AIAA for example have introduced a set of guidelines aiming to standardise the methods by which CFD simulations are scrutinised [35]. With any form of code development, ensuring that the program executes its intended task efficiently, robustly, and most importantly, correctly, are of tantamount importance. Identifying the sources of errors are commonly performed through two procedures, namely validation and verification. In a broader context, these two terms are often used interchangeably, but to CFD practitioners, they are quite distinct.

Validation attempts to provide answers to the query as to whether the model being utilised are correct for the problem at hand, and questions whether reality is represented by the model. For example, an inviscid Euler code, no matter how well implemented, would not be capable of predicting boundary layer profiles over a laminar flat plate at moderate Reynolds numbers, nor would the boundary layer equations be suitable for trying to predict the strong interaction region between the mean flow and the near wall region, at the leading edge of a plate in the hypersonic flow regime. Verification on the other hand addresses the issue as to whether the chosen equations are being solved correctly. It is a mechanism that allows the developer to critically assess if the model implementation accurately represents the description of the governing equations. A broad but succinct explanation is provided by Roache; "verification deals with the mathematics and validation deals with the physics" [132].

In trying to obtain models that accurately represent observed experimental or "real

life" behaviour, validation is commonly performed by comparison of computationally predicted results to experimental data, or high quality numerical data, such as DNS solutions to the corresponding problem. Comparing model results to analytical solutions such as Blasius' solution for a laminar flow past a flat plate, are common verification techniques, as analytical solutions can often be shown to be derivable from the model in question, and thus serve as a means of checking whether implementations are correct. With CFD codes in particular, in addition to identify coding errors, it is also necessary to check for iterative convergence, and in the limit of an infinitely fine grid, that the solution is asymptotically convergent. These issues are commonly solution dependent, and hence it is therefore necessary to perform grid and iterative convergence investigations on a problem by problem basis.

7.2 Compression Expansion Corner

In order to critically assess the implementation of the simplified magneto-hydrodynamic model, a test case must be identified to make meaningful comparisons to the analysis code. As section [7.3] explains, there remain problems in making comparisons to experimental and analytical solutions, in the realm of magneto-hydrodynamics , due to the complexity in reproducing experimental operating conditions for the former, and because restrictions on the existing IMPNS solver, for the latter. Thus, a numerical solution to the governing equations was sought and the case identified is that of Harada et al [65], whose work consists of the numerical simulation of a compression-expansion corner, under the influence of a magnetic field.

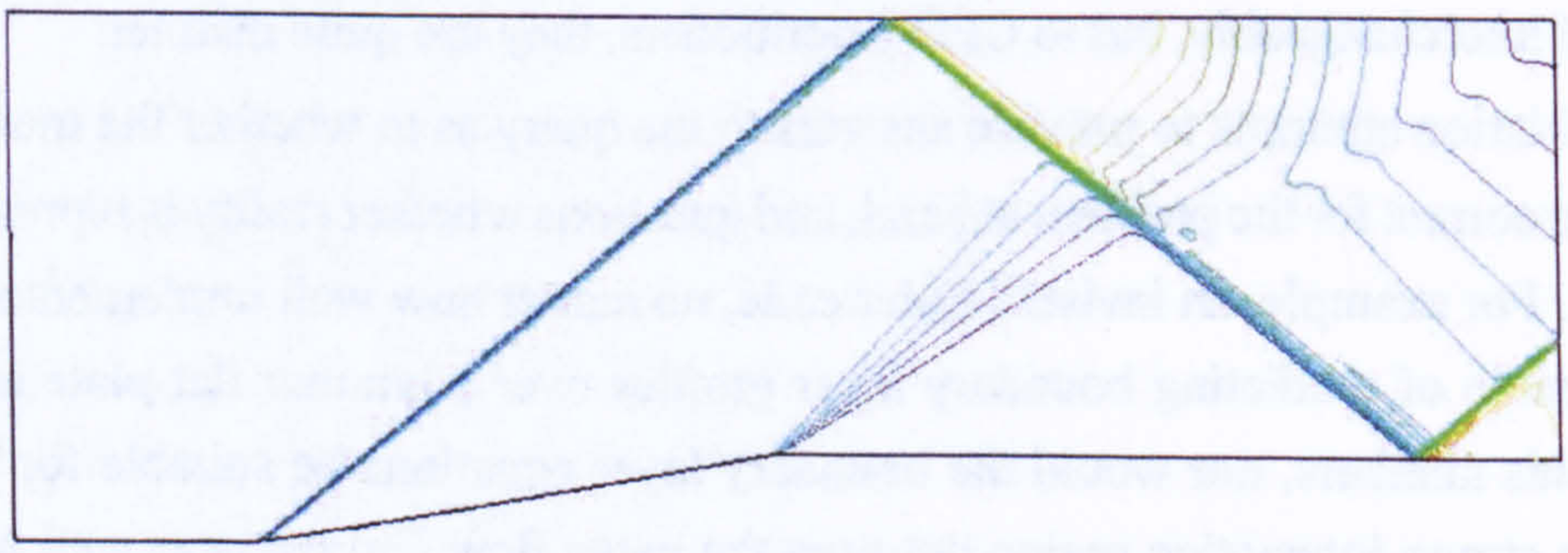

Figure 20: Shock and expansion waves through compression-expansion channel

The flow is assumed to be inviscid, with a free stream pressure of $100KPa$, and an operating temperature of $300K$. Flow is assumed to enter the channel at a Mach number of 2, and the influence of several field orientations has been investigated. The walls on the upper and lower surfaces are assumed to be adiabatic. A multi-sweep algorithm has been used, with Steger and Warming [153] flux vector splitting for the streamwise and

crossflow flux evaluation. Three initialisation sweeps on a coarse grid is performed. To calculate fluxes on the cell interfaces, flow variables are interpolated to enhance spatial resolution using the MUSCL [160] scheme. The upstream boundary condition is assumed to take freestream conditions, and on downstream boundary, the solution is extrapolated from the interior. Both the flow variables and magnetic field variables are updated explicitly using a CFL number of 0.5. The two dimensional geometry with the shock and expansion wave structures is shown in figure [20].

As an initial baseline case, the parabolized Navier Stokes result was computed and compared to Harada et al, for the situation of no magnetic field applied. The grid and iteratively converged results are compared to their results in figures [21(a)] to [21(d)]. Pressure profiles with respect to streamwise location, at various j-stations show good agreement in terms of the values through the shock.

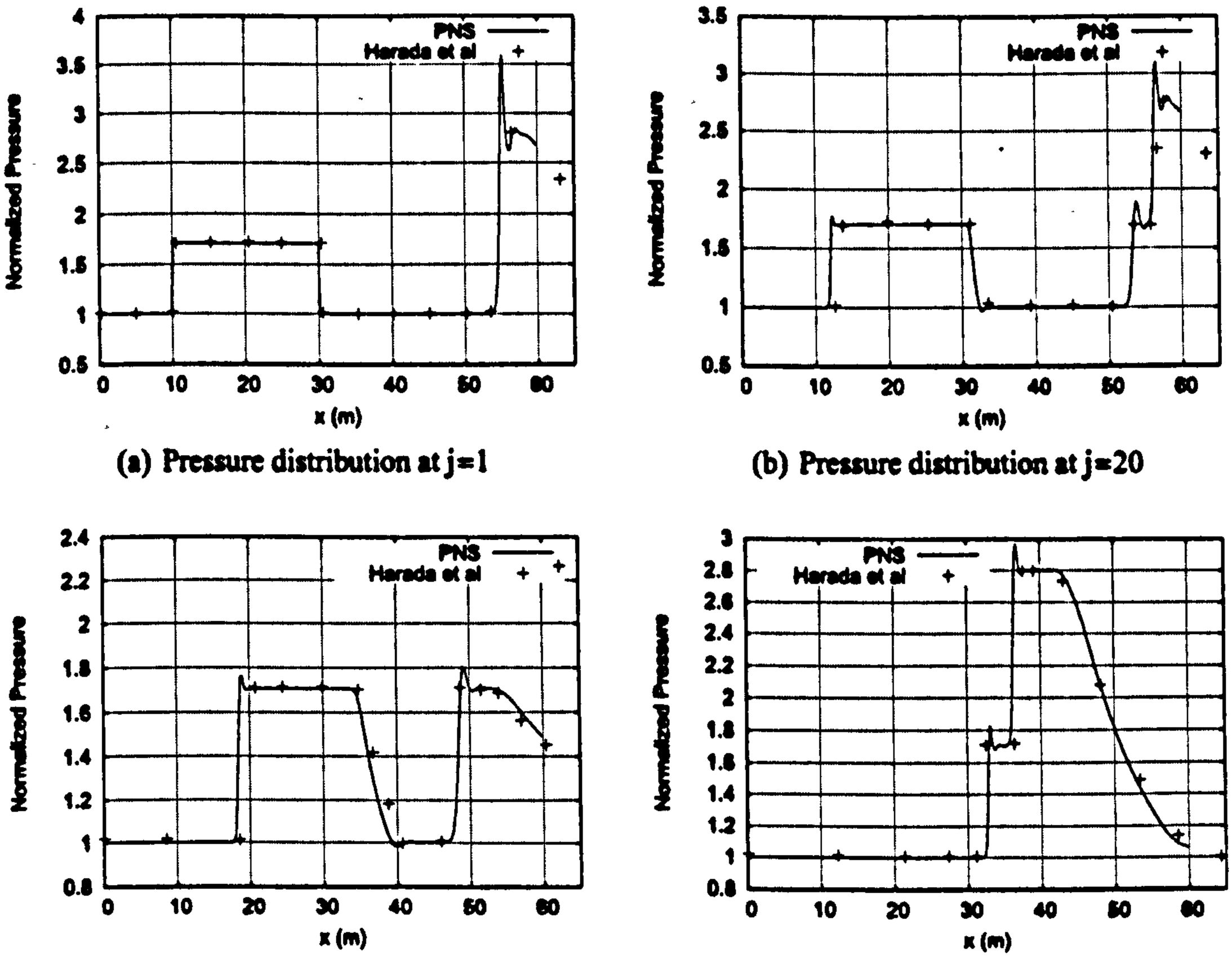

(a) Pressure distribution at j=1

(b) Pressure distribution at j=20

(c) Pressure distribution at j=50

(d) Pressure distribution at j=110

Figure 21: Normalised pressure distributions, no magnetic field

Despite the correct predictions in values after the shock, behind the expansion, and after the reflected shock, there are oscillatory regions at the points of discontinuity, for all j-stations. As the parabolized Navier Stokes solutions are both grid and iteratively

converged, additional grid refinement does not alleviate this behaviour however, nor too does running additional iterations, suggesting that unphysical behaviour in the main flow solver. The flux evaluation scheme used is that of Steger and Warming [153], which has been shown to produce more numerical dissipation in comparison to Osher [116]. Nevertheless, the converged solutions exhibit an element of inaccuracy at shock and expansion interfaces.

To account for the presence of a magnetic field, non-dimentionalised values of $B_x = 1.0$, and $B_y = 2.0$ were applied at the upstream inlet of the domain, and as an initial condition for field values within the domain. The magnetic force number is $S_\infty = 0.01786$, and no value is imposed for the magnetic Reynolds number, since the calculation does not assume any dissipation for both the fluid and for the magnetic field. On the channel surfaces, a zero normal boundary condition is imposed, such that $\frac{\partial \mathbf{B}}{\partial n} = 0$, for all magnetic field components. The governing equations that are solved for the test case are therefore in fact the ideal magneto-hydrodynamic equations, which neglect any second order derivatives in all components of the governing equations.

In the presence of the magnetic field however, the modified code fails to converge to a stable solution. After the initial pass using only the parabolized Navier Stokes equations, the solver proceeds to march by iterating over both the magnetic variables, and the flow variables. On the third forward sweep, the solution results in negative pressures, causing the solution to stop. The pressure profiles prior to the calculation terminating are illustrated in figures [22] through to [25]. Note that as the analysis code terminates prior to completing a forward sweep, the pressure profiles are only included up to $x = 55.0$.

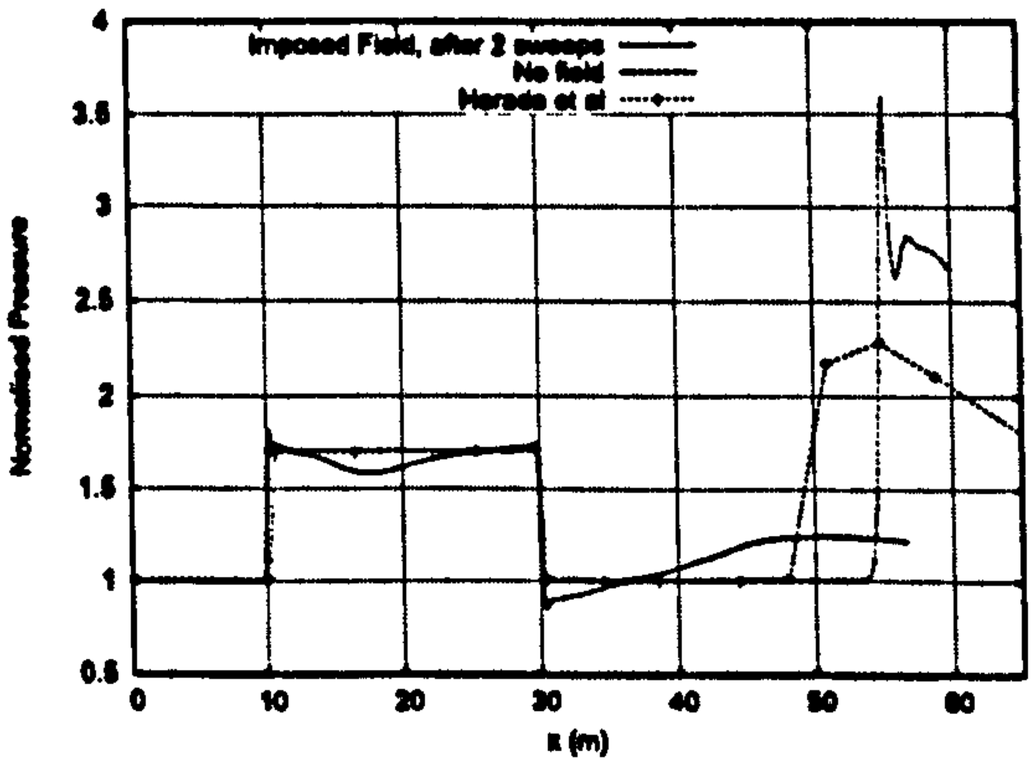

Figure 22: Field Imposed After 2 Sweeps, Pressure Distribution at j=1

Although the solution is not fully converged, it is worth pointing out some of the characteristics of the above profiles. For stations $j = 1$ and $j = 20$, the model is able to predict the location, and the extent of the discontinuity in normalised pressure with reasonable accuracy compared to the results of Harada et al. However, their post shock values suggest that pressure is constant between the shock and expansion, a feature that is clearly

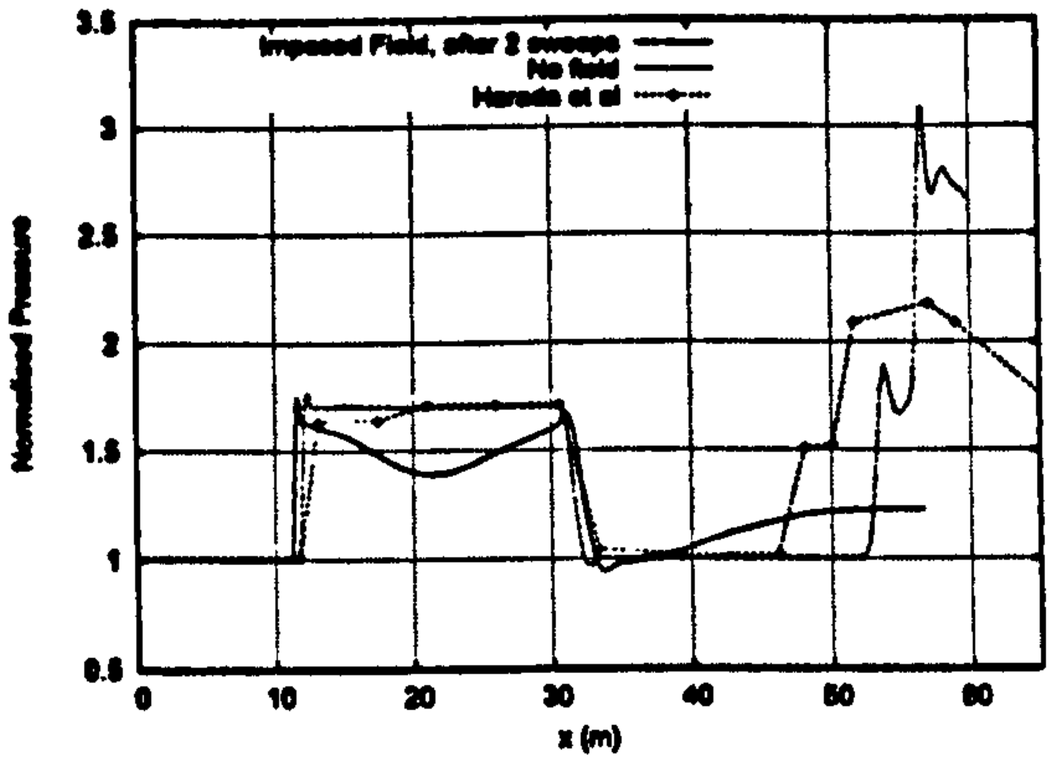

Figure 23: Field Imposed After 2 Sweeps, Pressure Distribution at j=20

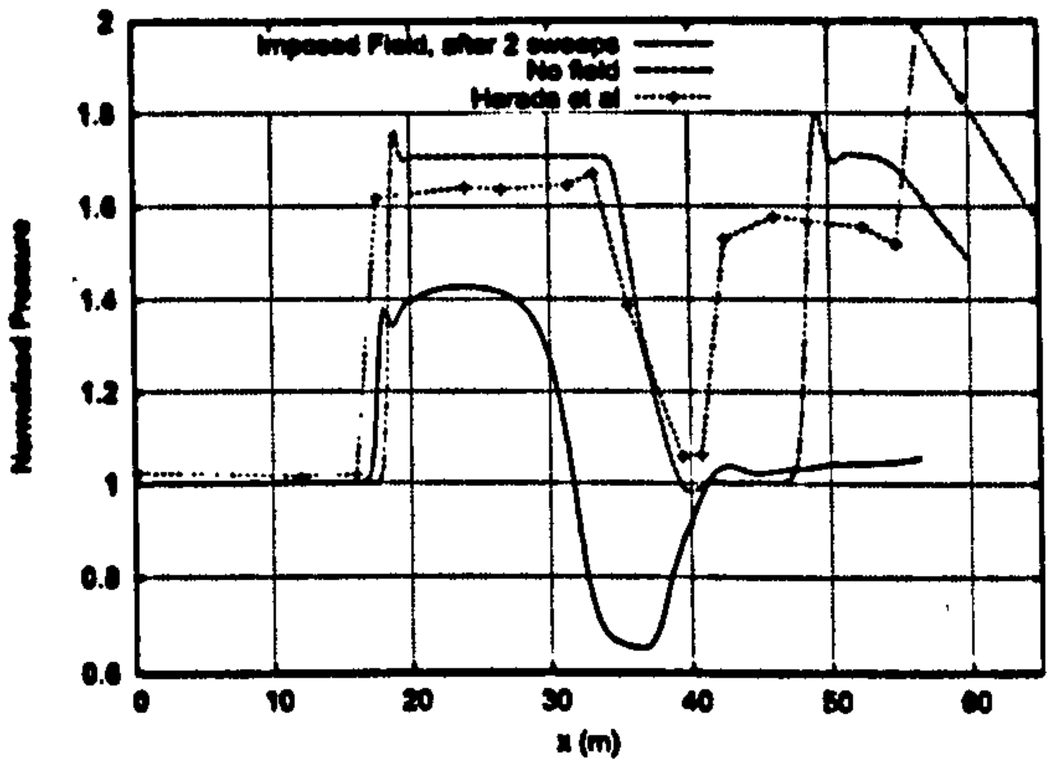

Figure 24: Field Imposed After 2 Sweeps, Pressure Distribution at j=50

absent in the PNS results. In the post shock region, one would expect a constant velocity distribution, which, based on the form of the induction equation would suggest that in the absence of any gradients, the field too should be constant. If the field is constant, then there should be no contribution to total energy in the equation [5.1.4], as here too, field variables only appear within gradients. Further downstream, the PNS results show greater discrepancy to Harada et al, which suggests another increase in pressure behind the reflected shock. Without the required increases in pressure in this region, subsequent updates in pressure are consequently more likely to result in negative values, causing termination. This is illustrated further in profiles at $j = 50$ and $j = 110$, where the discrepancy is considerably greater. For $j = 50$, the initial shock-front is placed reasonably accurately, but the post shock pressure value, the point at which it decreases over the expansion, and further downstream show considerable difference. At $j = 110$ the agreement is worsened as shock front location is not captured either. With the predicted pressure values considerably less than that predicted by Harada et al's results, it seems to be the likely cause for subsequent negativity.

To clarify unusual behaviour due to the presence of the additional terms in the parabolized Navier Stokes equations, a secondary test imposing a constant magnetic field

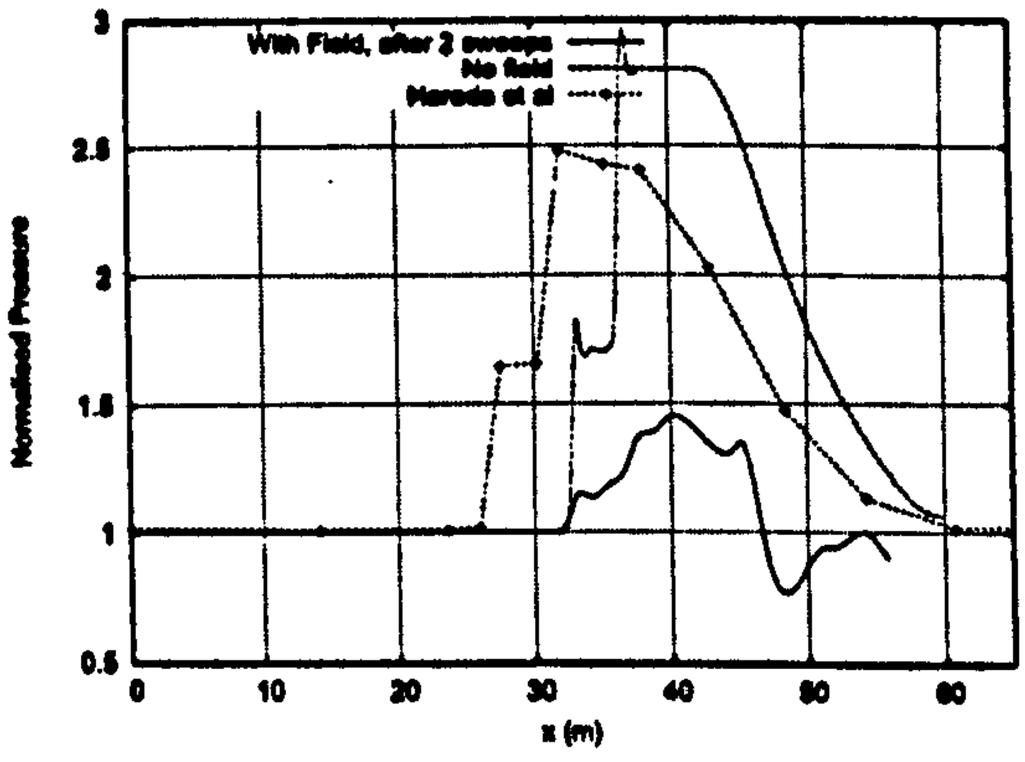

Figure 25: Field Imposed After 2 Sweeps, Pressure Distribution at j=110

is investigated. The analysis code is run with the magnetic field conditions outlined above, although update of the magnetic field variables occurs during the flow solution. The plots within figure [26] show that the normalised pressure profiles under these circumstances are in fact identical to the case of no magnetic field being applied.

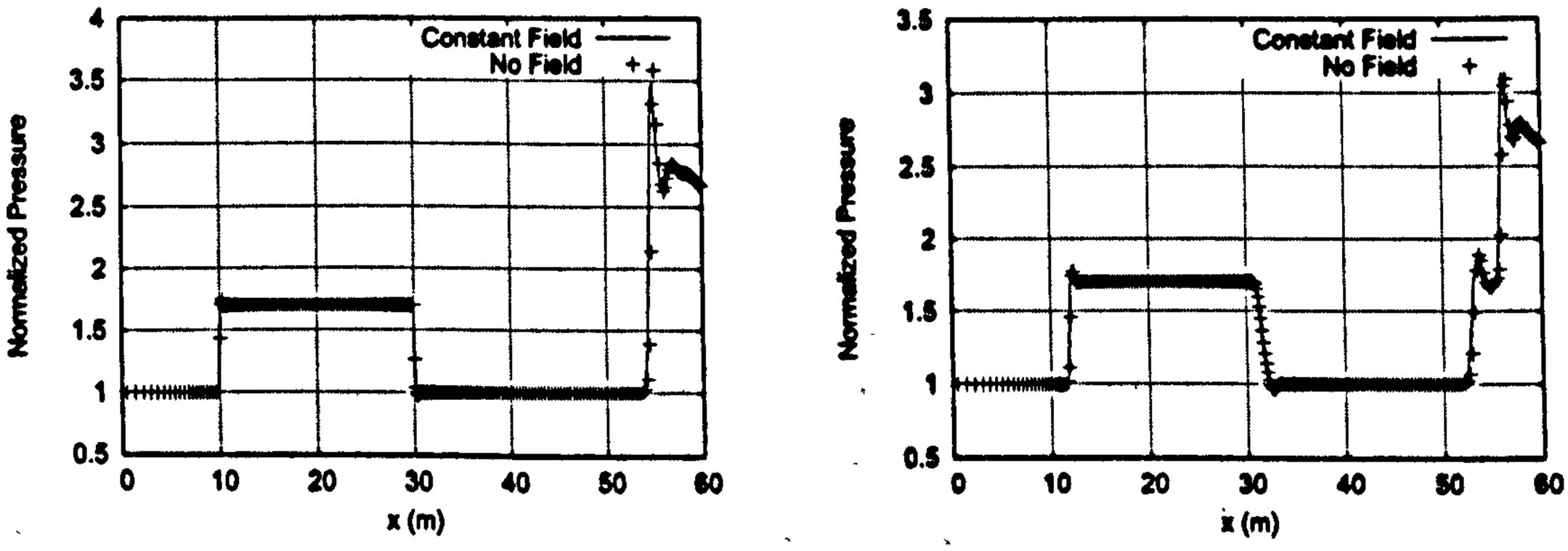

Figure 26: Constant Field Pressure Distributions, j=1 and j=20

To understand why there is no alteration to the original solution of the governing equations, in the presence of a constant magnetic field, examine equation [4.6.21]. One is drawn to the fact that all magnetic field terms in the governing equations appear in the form of convective derivatives. The extra terms are therefore of the form $\nabla \cdot |B^2|$ or $\nabla \cdot BB$, which are identically equal to zero for the present situation, since the field is fixed to be constant everywhere. The analysis code therefore handles the case in a manner that is to be expected.

Turning attention to the magnetic induction equations instead, a similar test may be applied to equation [5.2.3]. On the initial downstream sweep, only the variables in the original PNS equations are solved. For all subsequent sweeps in both directions, flow field variables are kept constant so as to retain their initial forward sweep values, and therefore no update takes place. Only the magnetic field variables are updated. The flow variables

return a solution that is identical to the no-field calculation, as expected, and although magnetic field profiles converge to a solution (figures [27(a)] and [27(b)]), whether or not the solution is actually correct cannot be quantified.

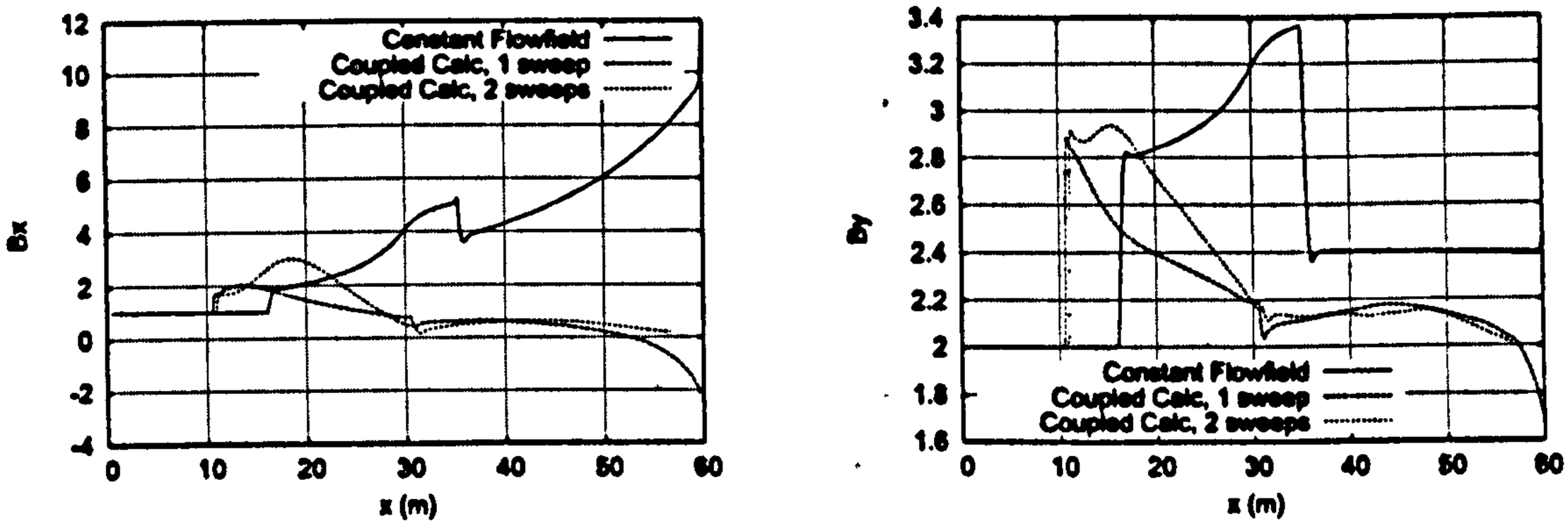

Figure 27: Constant Flow, B_x and B_y Distributions, along j=1

In the work of Harada et al, the authors do not present any data for the magnetic field profiles, as such no inference could be made as to the accuracy of any of the magnetic field profiles. For the fixed flow field calculation, the figures illustrate an increase in the magnetic field values at about $x = 16.0$, and a subsequent decrease at approximately $x = 35.0$. This can be explained by the fact that there is a shock, and subsequently an expansion over the flow domain, although the discontinuity, and the subsequent increases and reductions in B_x and B_y seem to be "offset", compared to the beginning and end of the compression ramp in the geometry. Indeed, for the no magnetic field calculations, which are in good agreement to Harada et al's results, the increase and decrease in normalised pressure occur at $x = 10.0$ and $x = 30.0$ respectively, as figures [21(a)] to [21(d)] show. Indeed, for the calculation in which the magnetic field and flow variables are updated simultaneously, despite the lack of convergence, after the first and second sweeps on the variables, the profiles for B_x and B_y suggest that the discontinuity does in fact occur at the leading and trailing edges of the compression corner, thus coinciding with the form of the geometry.

From examination of this data alone, it is not clear whether or not the observed offset is due to the fact that a slightly modified algorithm is being used here, since no flow variables are updated to take into account changes in the field, or whether there is something wrong in the manner in which the induction equation is solved. To assess whether or not the induction equation is being solved in a consistent manner, it is therefore necessary to seek an alternative method that will resolve the issue. To isolate any potential problems associated with the simulation of the modified parabolized Navier Stokes equations, from the magnetic induction equations, it is necessary to choose a method that can be applied to the equation for the evolution of the magnetic field alone.

7.3 Problems with MHD Equations

As the introductory section outlining physical characteristics of hypersonic flows reiterated, there are quite a few mechanisms at work in regimes where magneto-hydrodynamic effects may become influential over the flow region. Disassociation, recombination and radiation to name but a few of the chemical processes. Unfortunately, this in turn also imposes additional modelling requirements on the implementation thus adding to the computational cost. In view of the computational overheads, the current work focuses on the simplified MHD model, consequences of which are the difficulties faced in validating and verifying computational fluid dynamics results for magneto-hydrodynamic problems. The complexity lies in not being able to reproduce experimental conditions numerically.

For example, in many experimental cases that assess the effects of applying a magnetic field to an ionised flow, a plasma is artificially introduced into the flow and allowed to flow downstream through the field. Isolating portions of the flow to be ionised in such a manner is not a straight forward task in the context of partial differential equations. Furthermore, several experimental cases [144] involve chemical reactions, which require the use of additional modelling, such as non equilibrium chemistry models. Implementation of such models adds to the computational time, and is beyond the scope of the current thesis. These examples thus serve to illustrate the difficulties in validating the magnetic field models to experimental data. Examination of the magneto-hydrodynamic effects in isolation, is not entirely feasible when making comparisons to experiments.

In addition to experimental results, there are several analytic solutions available, to simplified problems such as the MHD Rayleigh problem. A magnetic field is applied normally to a doubly infinite flat plate, which is assumed to move impulsively with a given velocity in the streamwise direction at time $t = 0$. Another configuration capable of receiving an analytic treatment in magneto-hydrodynamic channel flow, coined "Hartmann flow" whereby a field is applied normal to a flow bounded by walls. Couette flow is yet another channel type problem, except that one of the walls are assumed to move with a specified velocity at time $t = 0$. Under all of the above circumstances the MHD equations reduce to a simple form, as detailed in the text by Sutton and Sherman [154], the solution for which determines the motions of the induced flow and magnetic field at a later point in time.

As the solutions to these problems are known and can be represented in closed form, many of the recent numerical implementations of the simplified magneto hydrodynamic equations have been verified against these [50, 56, 97]. However, in the context of the current implementation, they are not viable methods with which a meaningful assessment of code verification can be applied, as they are all subsonic, time dependent

problems, two important conditions that violate the underlying assumptions that govern the PNS equations.

In light of the above issues, relating to the inability to compare to both experimental data and analytical solutions, and given that the comparison of the compression-expansion corner numerical solution to Harada et al's simulations yielded inconclusive results regarding the accuracy of the implementation, it is clear that an alternative form of verification is required to test the model. Fortunately another method exists that guarantees credibility of the implementation. The method chosen and described in the following section is that of the method of manufactured solutions.

7.4 Method of Manufactured Solutions

For numerical routines designed to solve differential equations, the method of manufactured solutions presents a simple yet effective method of verifying that the solver does indeed find the solution to the equations it addresses. Using the method of manufactured solutions for the purposes of grid convergence and code verification was initially proposed by Roache and Steinberg to solve elliptic partial differential equations [133]. Nelson and Roy for example make good use of the technique in assessing the observed order of convergence for the Wind CFD code, examining in detail the effectiveness of some of the options available in the program [114]. Using the method they were able to identify problems with the viscous scheme, as well as issues with the outflow boundary conditions for subsonic cases.

Instead of trying to find an exact solution to the system of partial differential equations, the idea is to manufacture a user defined solution, and a corresponding new system of equations, slightly modified from the original, which is satisfied by the defined solution. One need not be concerned so much with the physical realities of the proposed solution, as the procedures primary aim is to verify that the computer code solves the governing equations it represents. Consequently, it is useful in identifying coding errors, and provides an independent method of verifying numerical subroutines, without using external sources of data as a means of comparison. This provides additional comfort as no reliance is made on the accuracy of data used in assessing reliability. The following section is a description as to how to implement the procedure.

Initially, a continuum solution is chosen for the variables that are to be solved for in the original system. Although physical characteristics do not matter in the context of the procedure, it is worth bearing in mind that many CFD solvers are designed to throw exceptions in the event of unphysical behaviour such as negative pressures or densities, and therefore a certain degree of caution is required. With the manufactured solution defined,

the modified governing equations are obtained by substituting the solution into the original equations, and expanding over the derivatives, products and summations appearing in the system.

The result is an analytic source term, which is subsequently input into the code implementation in closed form. Roy [138] argues that this is one of the main disadvantages of the method of manufactured solutions, in that the procedure is code intrusive, in contrast to some of the other widely used verification methods, such as comparison to analytic solutions, and grid refinement. Nevertheless it is a more robust method for assessing the accuracy of the code itself. With the above in place, the next step is to solve the modified equations on several grids of differing density, and evaluate the observed order of accuracy as the grids are refined. The observed order is compared to the formal order of accuracy to assess if it matches.

The choice of manufactured solution should allow the code to achieve a degree of accuracy, even on a relatively coarse grid, and as such, smoothly varying functions, whose derivatives are also smooth and well defined, such as trigonometric or polynomial forms are recommended. Furthermore, in some circumstances it is possible for good accuracy in one variable to mask potential errors in another variable, depending on the relative magnitudes of the terms, and therefore the manufactured solutions should impose the additional constraint that the variables represented are of the same magnitude. Roy [138] points out that it is necessary that none of the derivatives vanish, but this is not entirely the case. Recall that the method aims to investigate code implementation. The power of the method lies in the fact that the solution is entirely arbitrary, and can therefore be manufactured to exercise whichever terms we desire. This flexibility means that potential errors can be identified on a term by term basis.

For example, suppose we wish to seek code verification for a general Navier Stokes solver. Suppose further that we wish to assess whether the inviscid terms are accurately resolved, and specifically portions of the code aimed at computing the flux contributions in the y and z directions, but *not* the x direction. Under such circumstances a wise choice for the manufactured solution would be a function dependent on y and z only (and possibly time, depending on whether the code was steady or unsteady), with the additional constraint that the second order derivatives of the function identically vanished. The analytic source term representing this solution will take this form into account, in that it too will not possess any contributions in x, nor any portions due to second order derivatives. Assuming all things are working with the code, the simulated solution will converge towards the analytic form, as the grid is refined. More importantly, had the numerical solution not converged to the manufactured solution, we can say with confidence that there are errors in the calculation of the y and z convection terms. This type of knowledge

is extremely beneficial for the purposes of code debugging, increasingly so as systems of equations become more complex, and is a good illustration of the contribution the method has to offer.

7.5 MHD Verification

The method of manufactured solutions may be applied to any form of governing equation, but for the present instance, the magnetic induction equations from the simplified magneto-hydrodynamic model are examined. The governing equations to be solved maybe are expressed as;

$$\frac{\partial B}{\partial t} + \nabla \cdot F + S_{MHD} = 0 \tag{7.5.1}$$

where $B = \left(B_x, B_y, B_z\right)$, and F and S_{MHD} are the respective flux and source terms appearing in the rest of the magnetic conduction equations, as delineated in section [4.6.2], both of which are functions of the magnetic field B, and the velocity vector u.

Having chosen the form of the governing equations to be solved numerically, a manufactured solution is chosen. This is typically a closed form analytic expression, to which we apply the governing equations to obtain an analytic expression for a source term. Thus, we choose;

$$B = B_{MS} \tag{7.5.2}$$

where B_{MS} is the solution expression chosen and expressed in more detail later in this section. This is substituted into equation (7.5.1), to yield;

$$\frac{\partial B_{MS}}{\partial t} + \nabla \cdot F(B_{MS}) + S_{MHD}(B_{MS}) = S_{MS} \tag{7.5.3}$$

In the above equation, S_{MS} is the source term corresponding to the manufactured solution, and is obtained by simply analytically evaluating the derivatives appearing in the left hand side of the equation. Symbolic manipulation software such as MuPad, or Mathematica are recommended for this, to ensure the resultant form is correct. This term is added to the original governing equation (7.5.1), which results in;

$$\frac{\partial B}{\partial t} + \nabla \cdot F + S_{MHD} = S_{MS} \tag{7.5.4}$$

In the context of solving this new partial differential equation numerically, the new term S_{MS} presents no difficulty, as it is evaluated in a manner similar to that of the source term appearing in the low magnetic Reynolds number model. For any given cell volume, S_{MS}

is calculated as a function of its location x, to which the cell volume is multiplied.

Having added the source term to the governing equations, the equations are solved for numerically using the same routines outlined in section [5.1]. Grouping all terms except that involving the time derivative into R, the equation to be solved is therefore;

$$\frac{\partial B}{\partial t} = R \tag{7.5.5}$$

which for a steady solution is achieved when $R = 0$. Clearly for the modified equation this is obtained as $B \rightarrow B_{MS}$. This demonstrates the effectiveness of the method of manufactured solutions, as B_{MS} is known in advance. The remainder of this section presents a series of tests performed upon the simplified MHD model implementation.

7.5.1 Test 1: MMS as a Corrective Tool

As the introductory section of this chapter explained, the method of manufactured solutions is a powerful method for easily identifying coding errors. Although the method is code intrusive, the additional portions of code that are easily identifiable and separable from the main subroutines. Throughout the development process of the magneto-hydrodynamic model, the technique proved to be useful in this manner, as the following example demonstrates.

Unknown to the author, during the implementation of the magneto-hydrodynamic model, there remained an error in the evaluation of the source term $\mathbf{B} \cdot \nabla \mathbf{u}$, and in the portion of code dealing with the imposition of boundary conditions in the cross flow direction, for the magnetic field variables. As with most implementation faults, it is not immediately obvious where the error is to be found. Fortunately, the method of manufactured solutions provides a systematic procedure to break the analysis code down into simpler components. To investigate the accuracy of the implementation, initially the following functions for the x an y components of the magnetic field were chosen;

$$B_x = 5.0 sin\left(\pi(1.5x + 1.0)\right) - 4.0 cos\left(\frac{3\pi}{4} y\right) \tag{7.5.6}$$

$$B_y = -5.0 cos\left(\pi\left(\frac{x}{2} + 1.5\right)\right) + 6.0 sin\left(\pi(1.25y + 1.0)\right) \tag{7.5.7}$$

The functions were chosen such that their variation over the skewed quadrilateral domain was smooth. A plot of the manufactured solution for the B_x component of the field is illustrated in diagram [28]. The domain was chosen to take this form to ensure that cell interfaces were not simply lines of constant x and y, thus allowing the MMS procedure to check if the normal components of fluxes across a general interface were being evaluated

correctly.

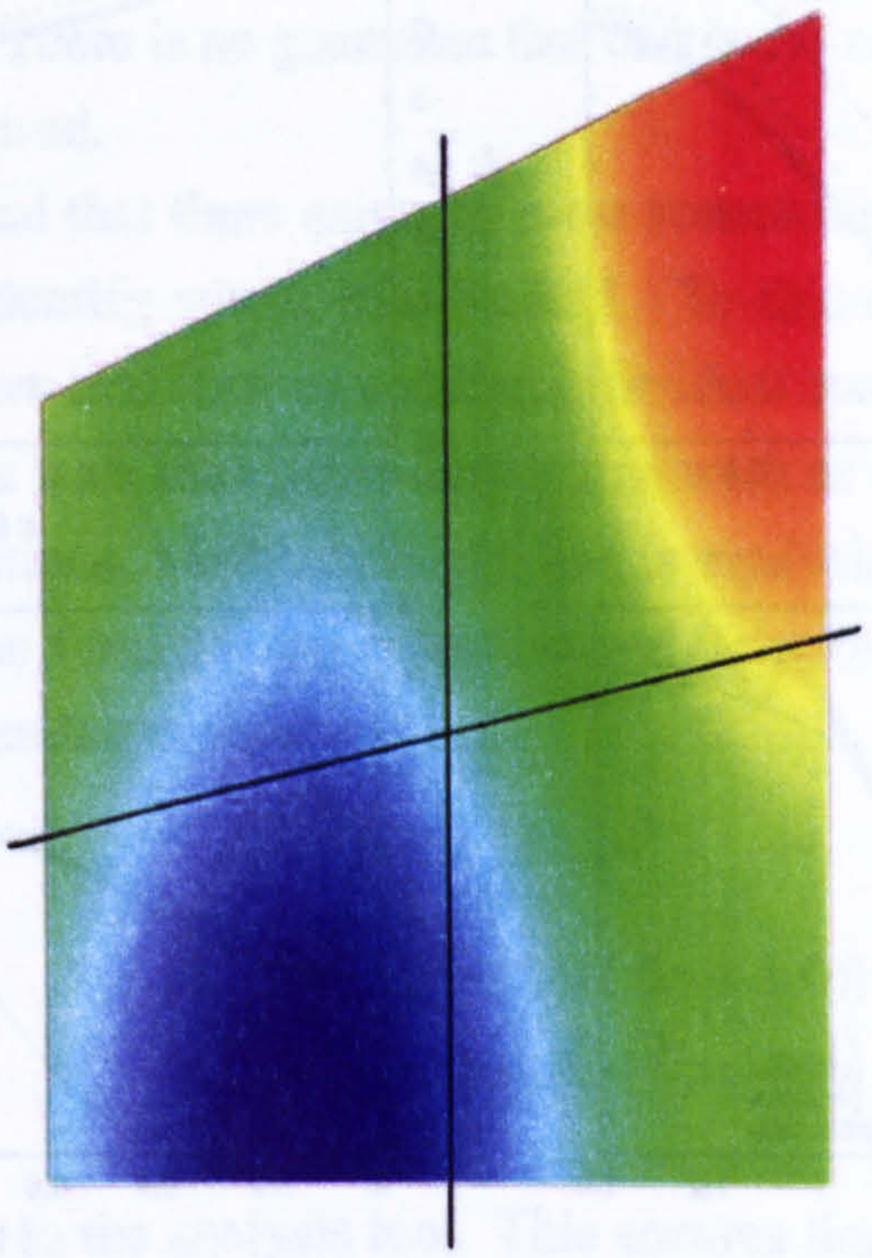

Figure 28: Manufactured Solution for B_x: Test 1

It is important to note that the magnetic induction equations also include contributions from the velocity field. These primitive variables, alongside density and pressure, are updated separately in the mean flow equations. MMS in this instance is being used to assess the validity of the magnetic field induction equation implementation, and not the PNS equations, and so rather than choosing **u** to take an analytic expression, they were chosen to be constants, $u_0 = 0.948$ and $v_0 = 0.174$, corresponding to non-dimensional values for the case where the flow is at an incidence of 10°.

Equations [7.5.6] and [7.5.7] are substituted into the induction equations, with terms updated analytically to yield a manufactured source term. The sources terms are simply stated here, without a lengthy derivation;

$$\begin{aligned} S_{B_x} &= 11.25\pi^2 sin\left(\pi\left(1.5x + 1.0\right)\right) - 2.25\pi^2 cos\left(\frac{3\pi}{4}y\right) \\ &+ 7.5\pi u_0 cos\left(\pi\left(1.5x + 1.0\right)\right) - 3.0\pi v_0 sin\left(\frac{3\pi}{4}y\right) \end{aligned} \tag{7.5.8}$$

$$\begin{aligned} S_{B_y} &= 9.375\pi^2 sin\left(\pi\left(1.25y + 1.0\right)\right) - 1.25\pi^2 cos\left(\frac{x}{2} + 1.5\right) \\ &+ 7.5\pi v_0 cos\left(\pi\left(1.25y + 1.0\right)\right) + 2.5\pi u_0 sin\left(\frac{x}{2} + 1.5\right) \end{aligned} \tag{7.5.9}$$

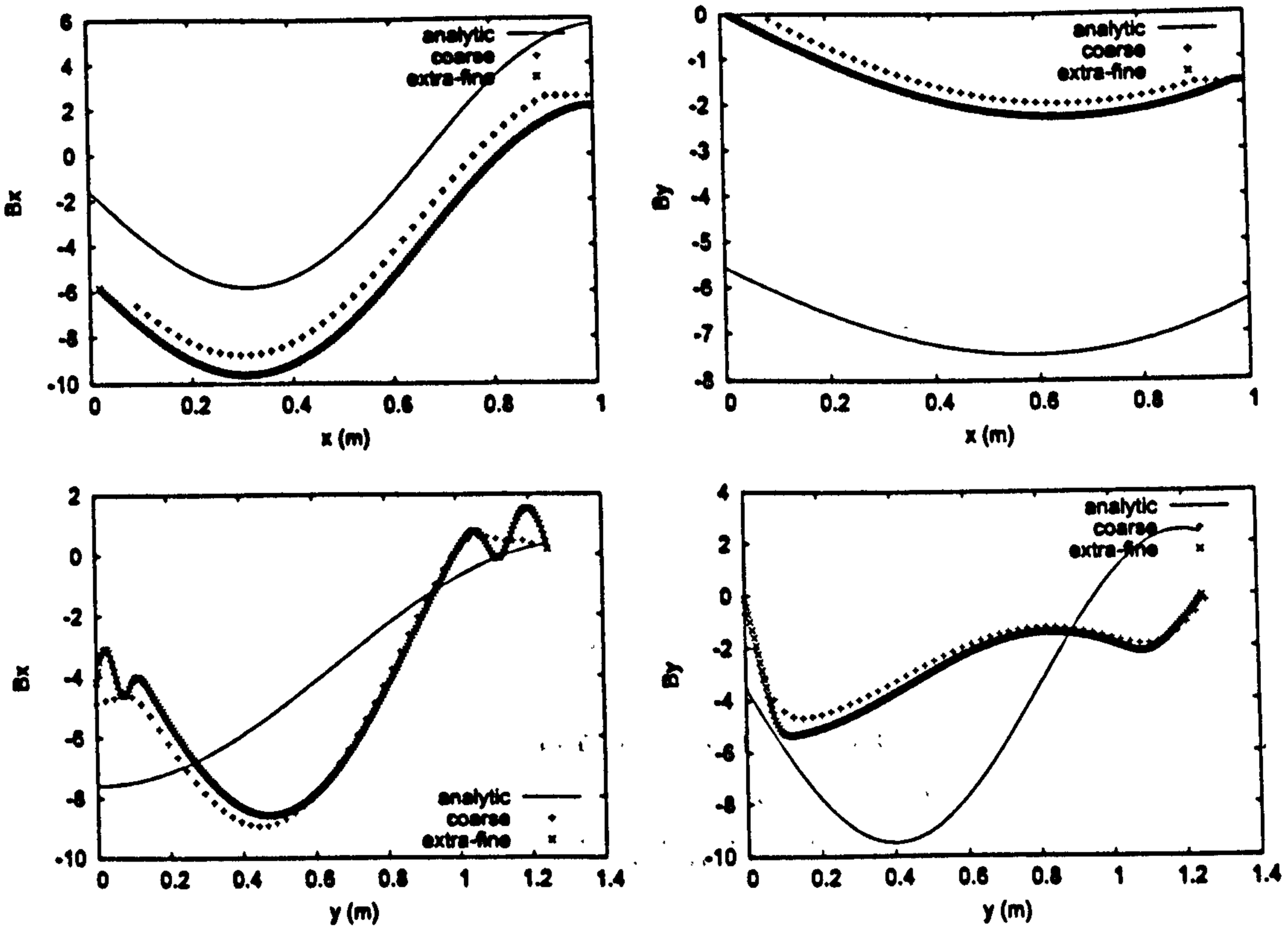

Figure 29: B_x,B_y Profiles for Multiple Grid Levels, in x and y

and are subsequently added to the right hand side of the corresponding governing equations. The resulting equations are solved on multiple grid levels, consisting of 50x50, 100x100 and 150x150 grid points. On the boundaries of the domain, the velocity components are prescribed their constant values u_0 and v_0. The boundary values for the magnetic field are calculated by determining the x and y locations for a particular point on the boundary, and the expressions for the manufactured solutions, equations [7.5.6] and [7.5.7] are used to determine B_x and B_y respectively.

The solid lines in the figures [29] represent the analytic solutions given by equations [7.5.6] and [7.5.7]. The parabolized Navier Stokes solutions are illustrated for two grid levels, the coarse (50x50) and fine (150x150) levels. The solutions are iteratively converged, as solutions were simulated for several multi sweep iterations until no difference could be observed in output.

Despite these precautions the plots in figure [29] are clearly in disagreement to the known solution. The cross flow variations (with respect to j-station) for both components of the magnetic field are particularly erroneous, and are unable to capture the underlying trend of the analytic solutions. In contrast, the B_x,B_y variations in i, despite their disagreement, do nevertheless indicate that the predicted solutions exhibit the visible trend. This

would seem to suggest that the field variables are offset by some constant "shift" parameter, indicating perhaps that with regard to the streamwise variation, the implementation is reasonably correct. There is no guarantee that this is the case at this point however, and caution must be exercised.

Having identified that there exists an error somewhere in the implementation, the task is therefore to identify where it is located. To this end a natural approach is to break the problem down into tests on smaller, individual components. One approach is to simplify the equations such that either only streamwise or cross flow derivatives appear in the governing equations. Mathematically, this is equivalent to imposing the condition $\mathbf{B} = \mathbf{B}(x)$. The same form for the manufactured solution was chosen, except for the removal of any y-dependence, thus;

$$B_x = 5.0sin(\pi(1.5x + 1.0)) \quad (7.5.10)$$

$$B_y = -5.0cos\left(\pi\left(\frac{x}{2} + 1.5\right)\right) \quad (7.5.11)$$

No changes are made to the analysis tool. This ensures that the test is now to determine y-component derivatives correctly predict that the magnetic field variables are constant with respect to y. The predicted solutions, are presented in figure [30].

The analytic solution indicates that the magnetic field variables should be constant with respect to y, but nevertheless there is still erroneous behaviour present, as shown. The streamwise variations again differ, but once again, there is an evident shift parameter present. The disagreement however, provides further insight as to what may be causing error. Comparing the figures in [30] and [29] directly, it seems as though very little, if no improvement has been made in the magnetic field variable profiles in y. Yet the manufactured solution has now been chosen such that there can be no contribution from the y-derivative components whatsoever, given its construction. Therefore the only contributions to the right hand side vector, in equation [5.2.3] are the streamwise contributions to the convective and viscous fluxes, and the modified source term.

Strictly speaking, there should be no contribution to the right hand side vector from the source term, as it involves derivatives in velocities u and v. In the present case, u and v are fixed to constant values throughout the domain, thus any derivatives must equal zero. There is a certain degree of confidence for the variations in x, and as such, the next simplification that can be made is to neglect the call the source term $\mathbf{B} \cdot \nabla \mathbf{u}$. The magnetic field is still assumed to be a function of x only, and thus [7.5.10] and [7.5.11] are used as manufactured solutions once again. The predicted solutions are illustrated in figure [31].

The figures show a marked improvement in agreement to the analytic expressions, which can be seen to get better upon grid refinement. The magnetic field variable trend

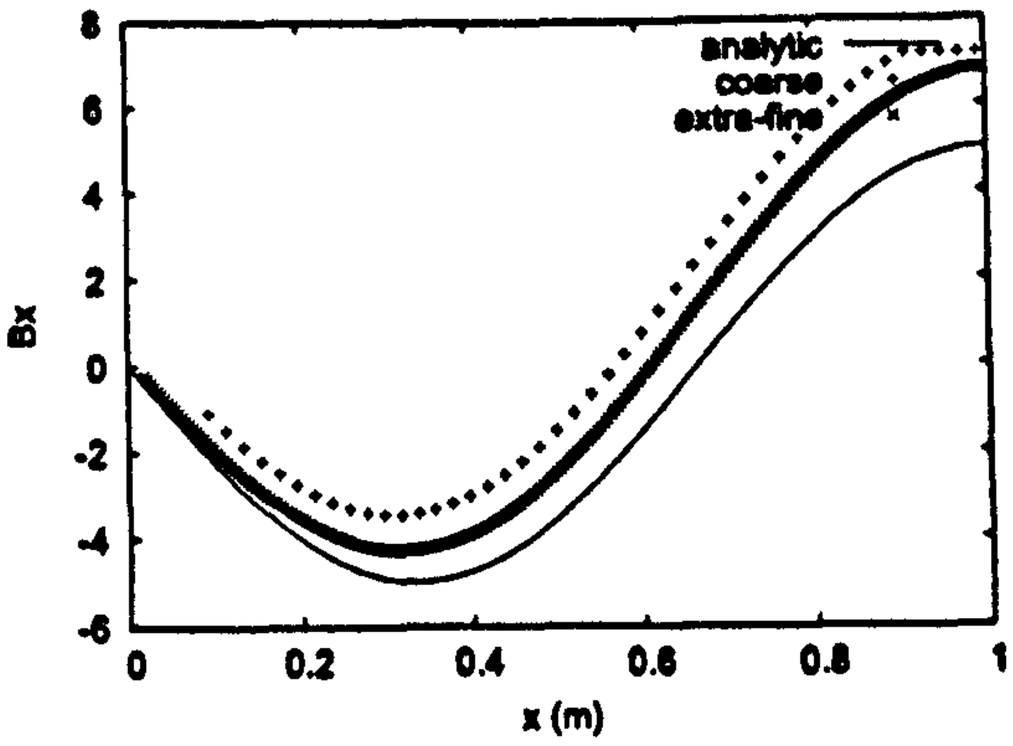

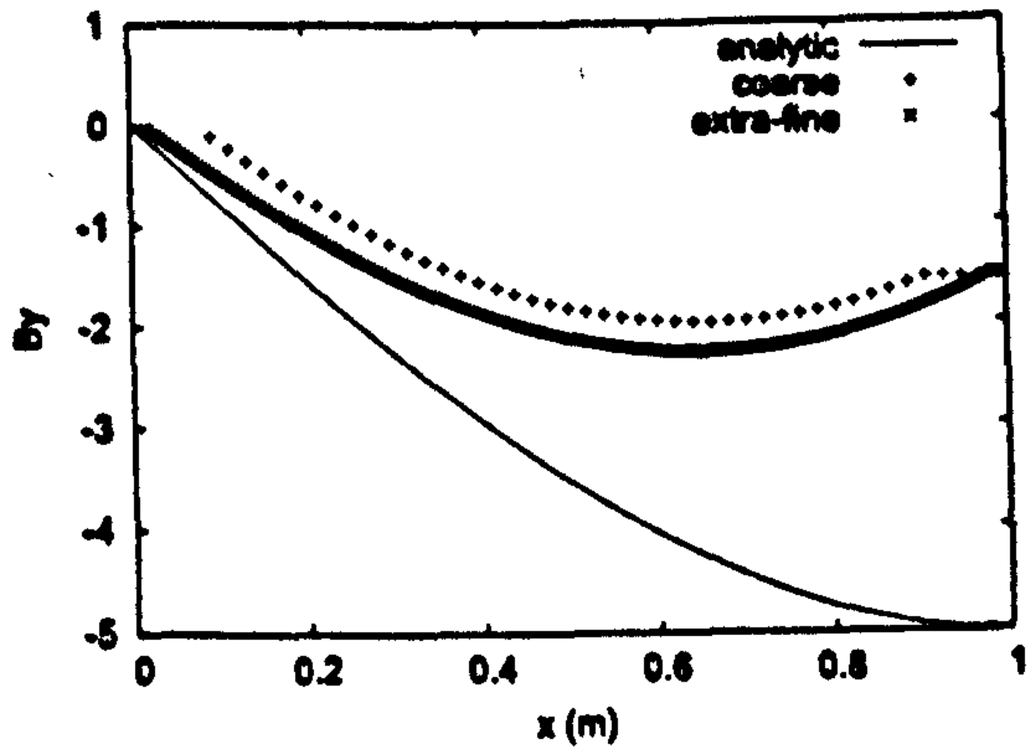

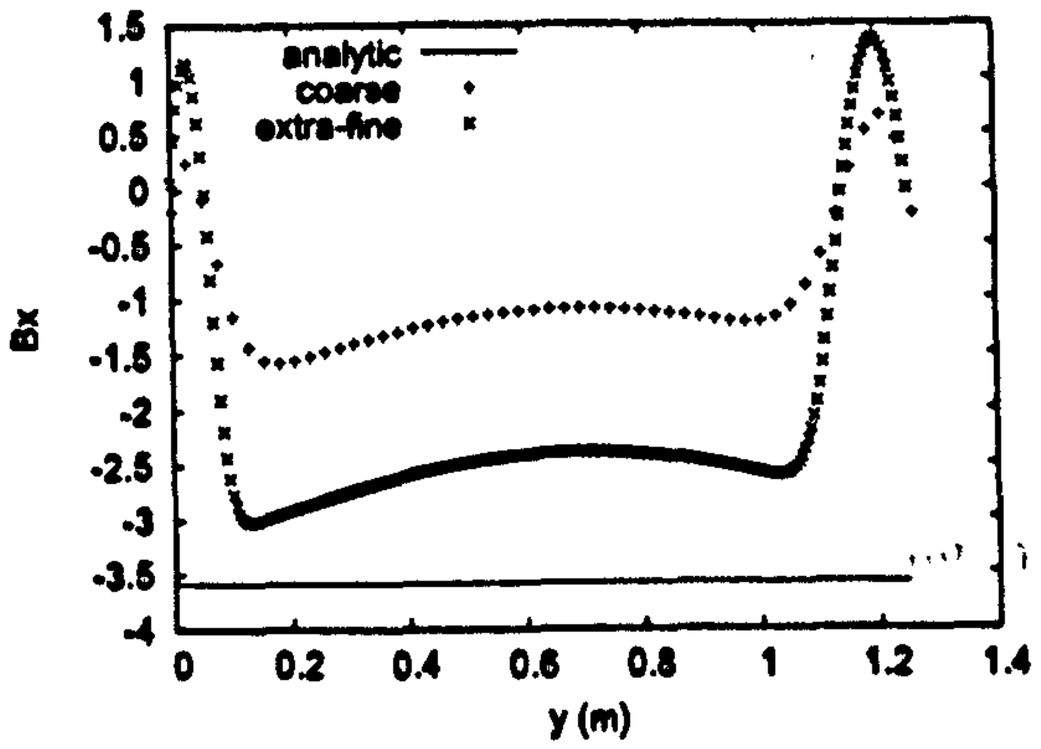

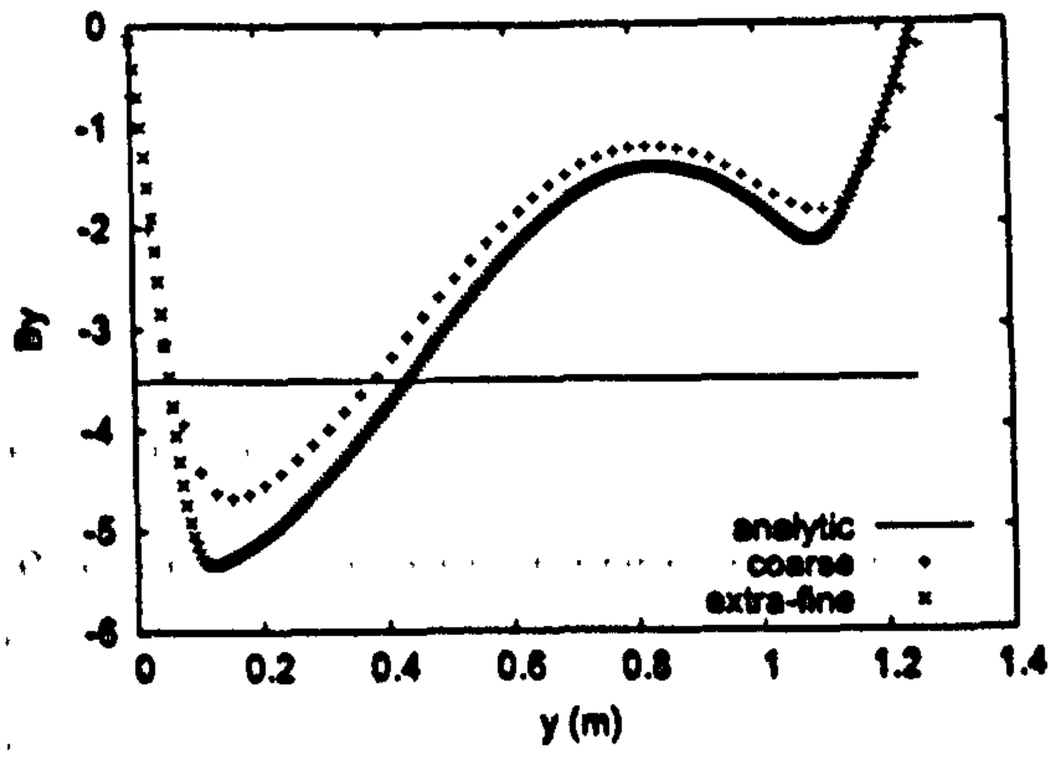

Figure 30: B_x,B_y Profiles in x and y, Solution a function of x only

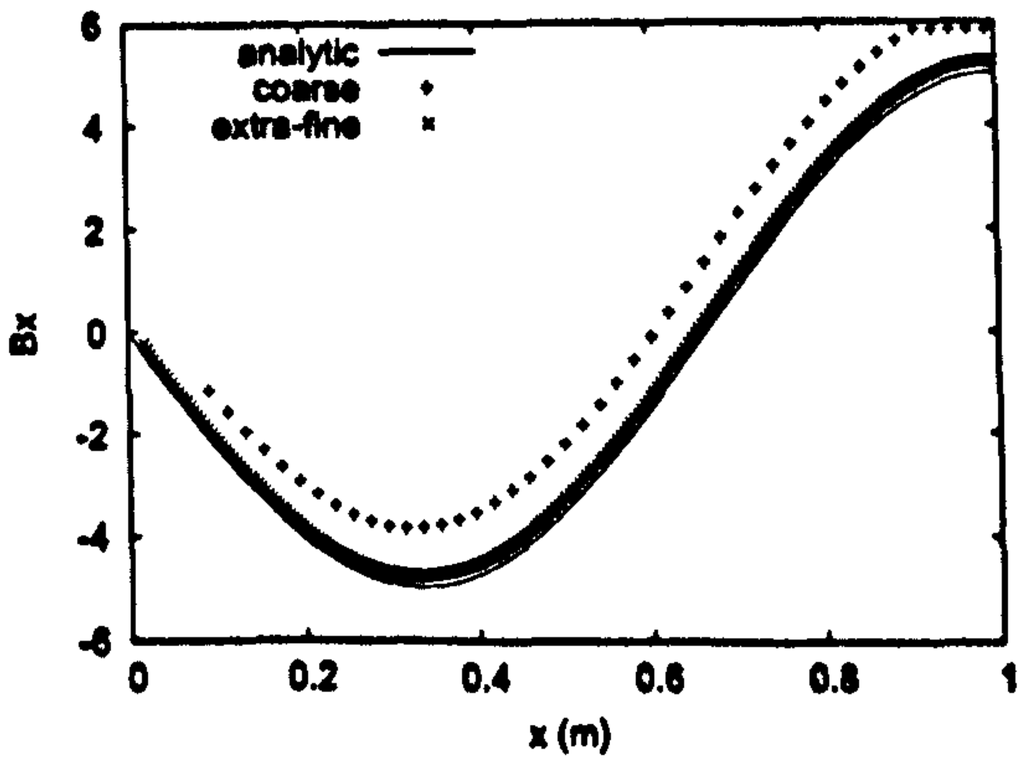

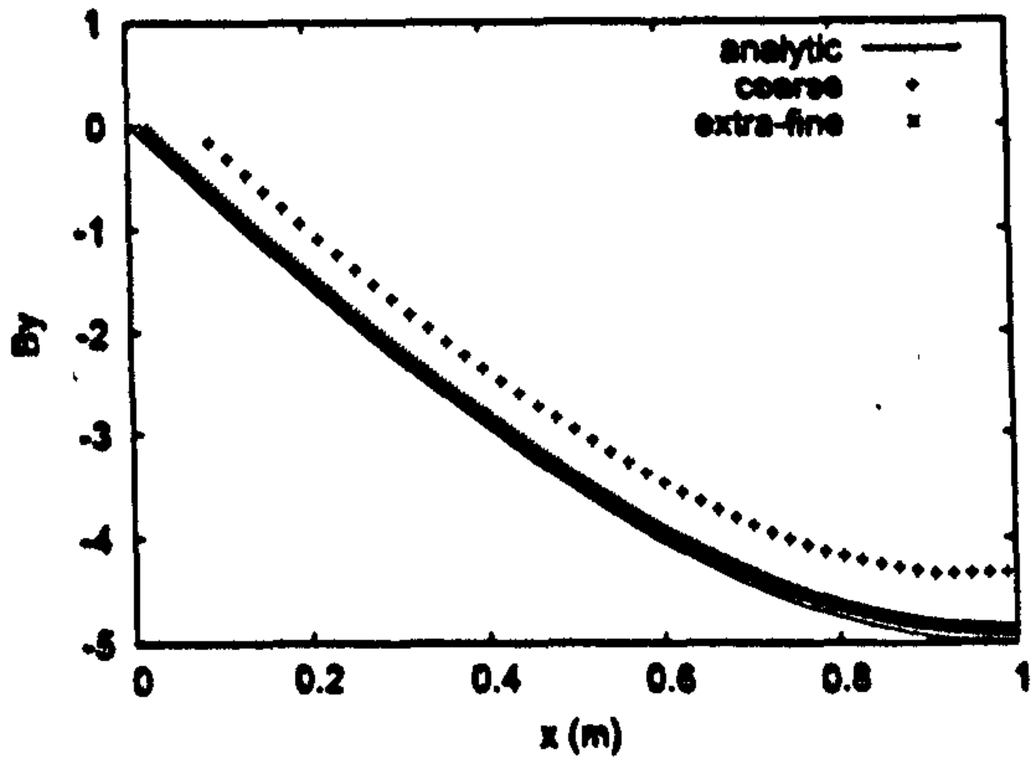

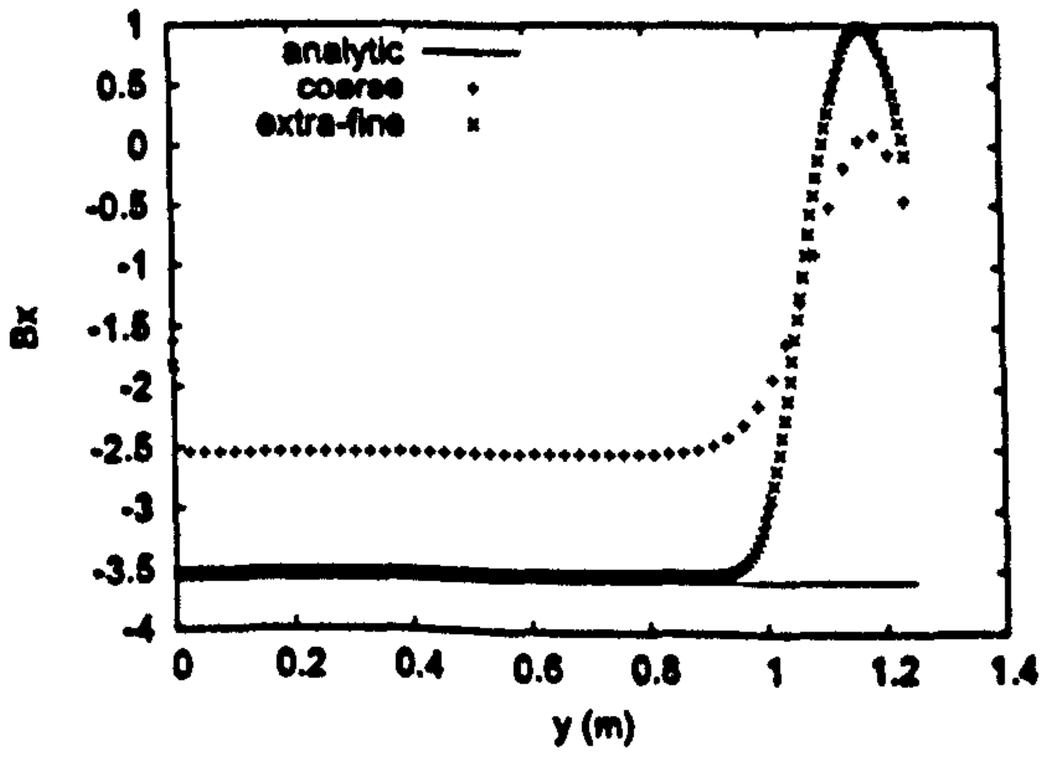

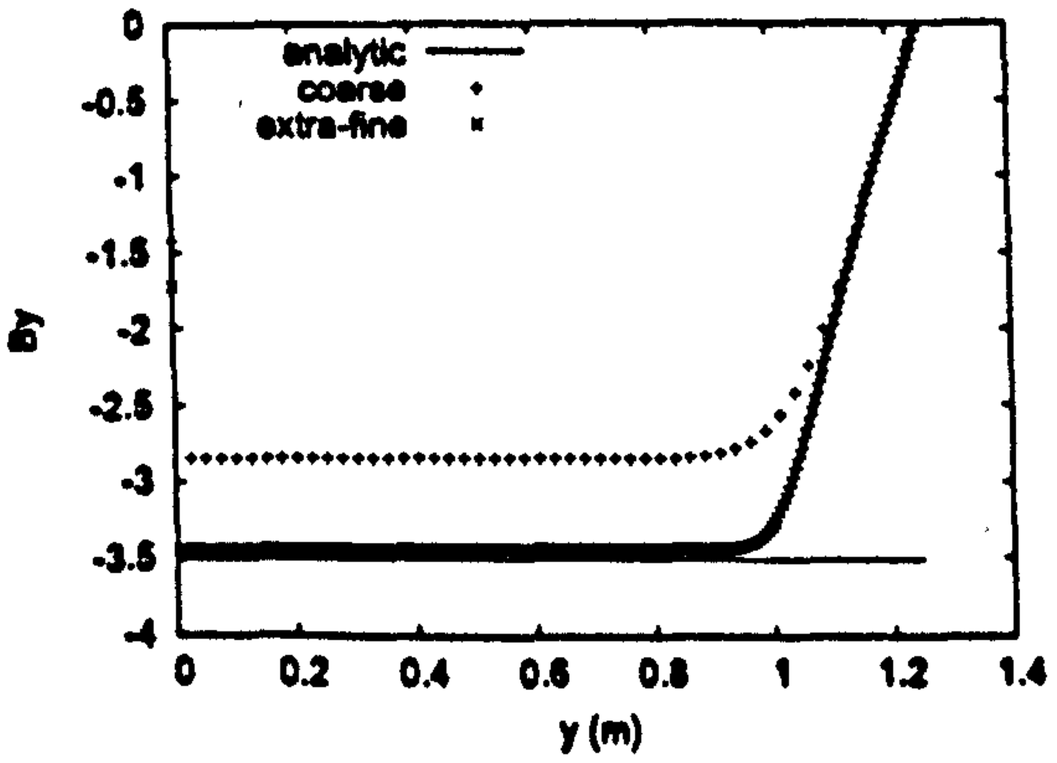

Figure 31: B_x,B_y Profiles in x and y, Source term removed

in the streamwise coordinate closely matches the analytic expression for all stations. The cross flow predictions have also improved, in that the analysis code predicts a constant field value, although there still remains a problem on the upper j boundary. Despite there still being an issue, the improvement in prediction has been facilitated by the removal of the source term evaluation. Therefore there must be an unintended contribution to the residual vector from this term. Close evaluation of the portion of code revealed in fact a confusion in variables, that was resulting in the calculation of $\mathbf{u} \cdot \nabla \mathbf{B}$ rather than $\mathbf{B} \cdot \nabla \mathbf{u}$, a clear error.

The graphs in figure [31] show improvement, although on the upper j boundary there remains some discrepancy. The initial test involved examination of the implementation of the streamwise derivatives, by making the manufactured solution a function of x only. The above test confirms that the evaluation of the streamwise derivatives is indeed correct, as the only terms being exercised are the streamwise convective and dissipative terms in the induction equation. Having also identified an error in the source term evaluation, there nevertheless remains some discrepancy in solution in the figures above for y-variation, and as such an additional test is to check the evaluation of the cross flow derivatives. In analogy to the x-derivative case, the manufactured solutions for the magnetic field are altered to be a function of y only, and hence;

$$B_x = -4.0 cos\left(\frac{3\pi}{4} y\right) \tag{7.5.12}$$

$$B_y = 6.0 sin\left(\pi (1.25y + 1.0)\right) \tag{7.5.13}$$

In addition to the above modification, the amended source term is reintroduced, as a further test of correctness. The manufactured source terms are re-evaluated to reflect their modification. Figure [32] shows the predicted profiles in the absence of any streamwise variation of the field;

The prediction in the cross flow variation is visibly improved compared to the original test, suggesting that the evaluation of the corresponding terms are in fact correct. However there is still an error on the upper boundary for both B_x and B_y, in a similar region as the previous test. Although the magnetic field is now a function of x only, the graphs above show some streamwise variation, even for the analytic solutions. It is worth noting here that the x-variation is in fact showing a variation of the magnetic field with respect to the i station. On the computational domain, the lines of constant i are not actually horizontal, but is given by the black slightly inclined line in figure [28], and thus the plots actually show a variation in variables. Despite this, the numerical results are in agreement to the analytic solution.

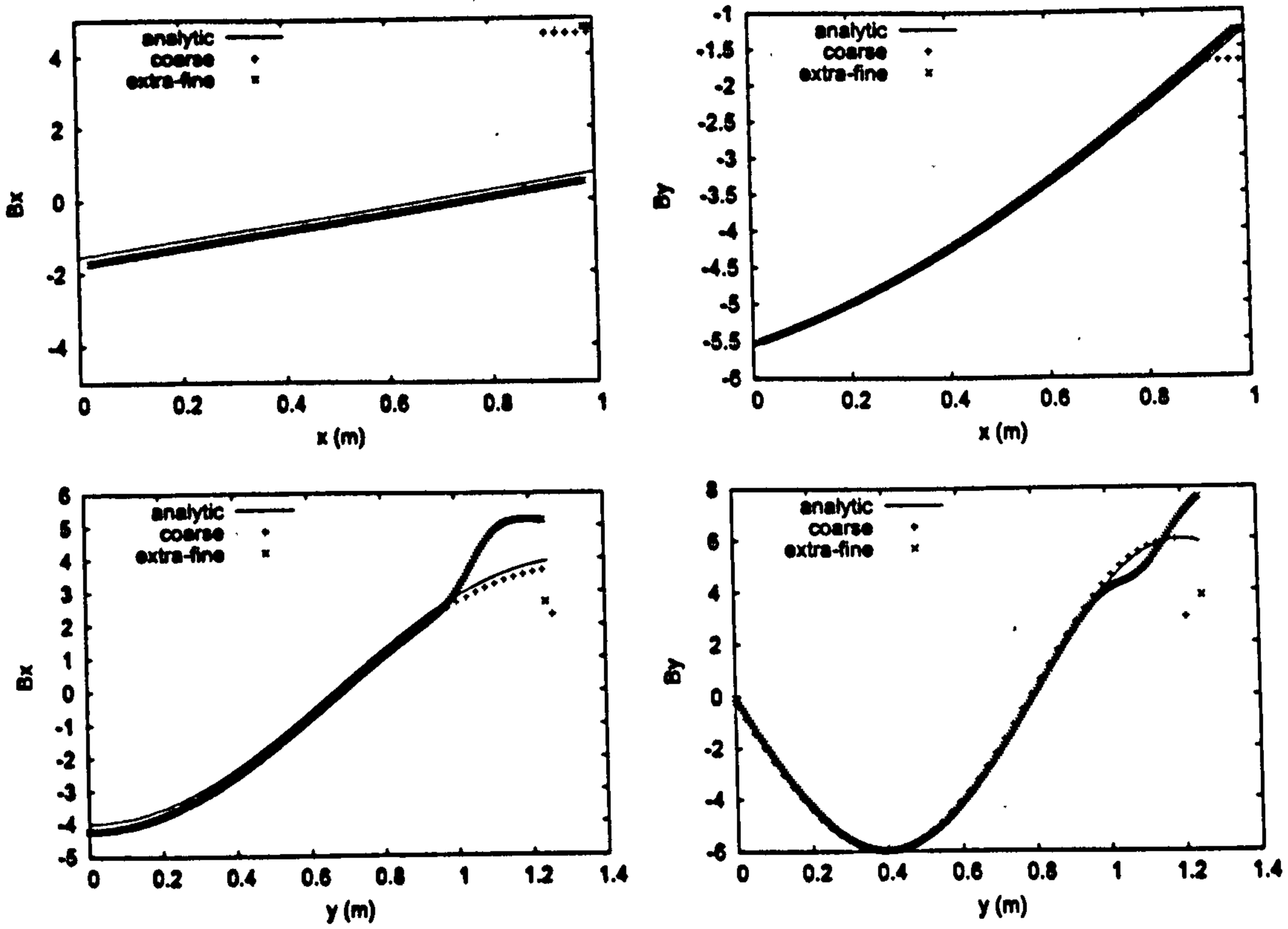

Figure 32: B_x,B_y Profiles in x and y, Solution a function of y only

At this point, the calculation of the x-derivatives has been shown to be correct, and the necessary corrections to the source term has been made, to provide further improvements in prediction. The cross flow variations in figure [32] show agreement throughout the domain, except for the upper boundary. The fact that there is agreement would suggest that the evaluation of the y-derivatives are also correct, but since the disagreement is located at the top of the domain, and that all terms have now been investigated, the discrepancy may be due to an factor external to the actual governing equations. The proximity of the errors to the upper boundary provide further indication of this, suggesting perhaps that it is a consequence improper boundary condition specification.

Indeed, the original code imposed a zero normal gradient boundary condition on the upper boundary, given by $\partial \mathbf{B}/\partial n = 0$. This condition maybe required in a physical calculation, but in the current theoretical exercise, the analytic solution must be specified on the boundaries. In other words, B_x and B_y are determined by the form of the analytic solution chosen, at these points. In the framework of the method of manufactured solutions , it is in fact possible to test whether the boundary condition implementation for such a condition as $\partial \mathbf{B}/\partial n = 0$ is in fact correct, although this necessitates an additional condition on the manufactured solution, that it too satisfies the condition for vanishing normal derivatives on the boundary.

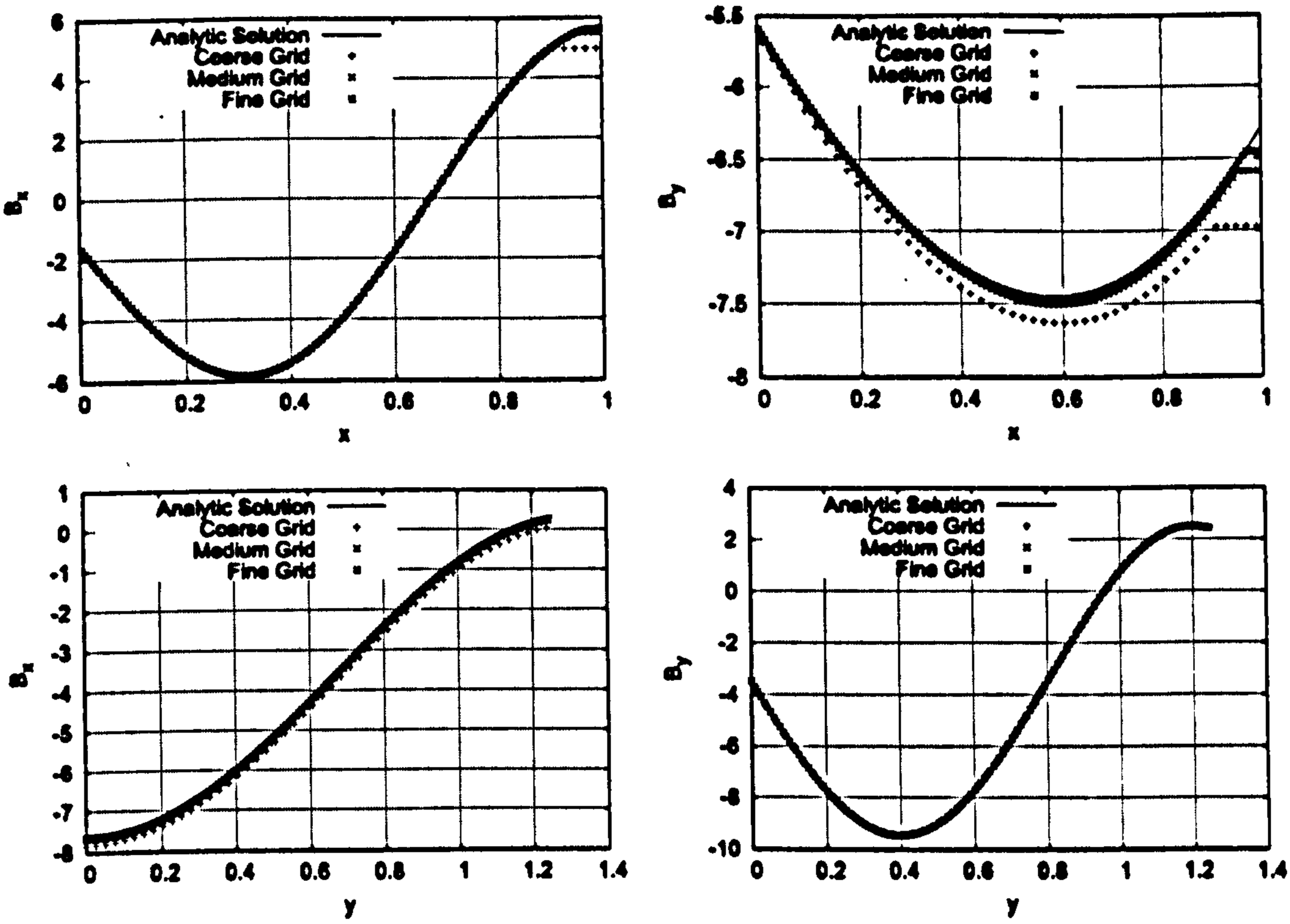

Figure 33: B_x,B_y Profiles for Multiple Grid Levels, in x and y

Having imposed the boundary condition $\mathbf{B} = \mathbf{B}_{MMS}$ instead of the zero normal gradient condition on the upper boundary, and reintroduced all terms in the governing equations, a further calculation for $\mathbf{B} = \mathbf{B}(x,y)$ is presented in figure [33]. The predicted profiles for the magnetic field components are illustrated for the three grids, coarse, medium and fine corresponding to the 50x50, 100x100 and 150x150 grids respectively. Profiles are taken from lines of constant x and y, along the midsection of the flow domain. This ensures that the profiles are well developed, and are in the regions furthest away from any influence of the boundary conditions. In stark contrast to the initial predictions in figure [29], both the B_x and B_y profiles show good agreement with the manufactured analytic solution, in both directions, even on the coarsest mesh. The B_x profile on the coarsest grid shows some discrepancy, although on subsequent finer grids, the agreement is visibly better.

In the streamwise direction, the coarse grid highlights some discrepancy to the analytic profile for B_y, although once again, grid refinement ensures better agreement. Note that for both x-variation profiles, there exists a region of constant B_x and B_y values at the edge of the domain, prior to $x = 1$. This behaviour is not part of the solution, but a consequence of the restrictions in having to terminate the multisweep region before

the last station in the flow region. Here too, the region of constant magnetic field values diminishes as the grid is refined, providing assurance that the induction equations are converging towards the manufactured solutions. The use of method of manufactured solutions clearly identifies the errors existing in the original source code, and ensures a systematic framework that can be applied to identify coding error.

7.5.2 Test 2: Oscillatory Manufactured Solution

The first test proposed a relatively simple function in that variations over the domain were smooth. The trigonometric functions were linear in space, thereby assuring that even on the coarsest of grids, a reasonably good prediction could be made by the solver. In order to reliably assess whether the solver was indeed grid convergent, and that the behaviour above was not the consequence of some other undetermined factor, another test was implemented, purposefully designed to break down for meshes involving fewer grid points.

The second manufactured solution chosen is another function involving trigonometric functions, which is continuous, and has continuous second order partial derivatives;

$$B_x = xsin(\pi(50.0x + 1.0)) + cos\left(\pi\left(20.0y^2 + 1.0\right)\right) \quad (7.5.14)$$

$$B_y = xsin(\pi(15.0x + 1.0)) + ycos(\pi(50.0y + 1.0)) \quad (7.5.15)$$

Clearly both functions are well defined and have continuous derivatives, although the fundamental difference between this and the first case is that the frequency of oscillation in the solution, as a result of the nonlinearity within the arguments of the trig functions. This frequency can be illustrated graphically, as shown in figure [34]. The figure shows the fact that the B_x profile oscillates more rapidly in increasing x and y.

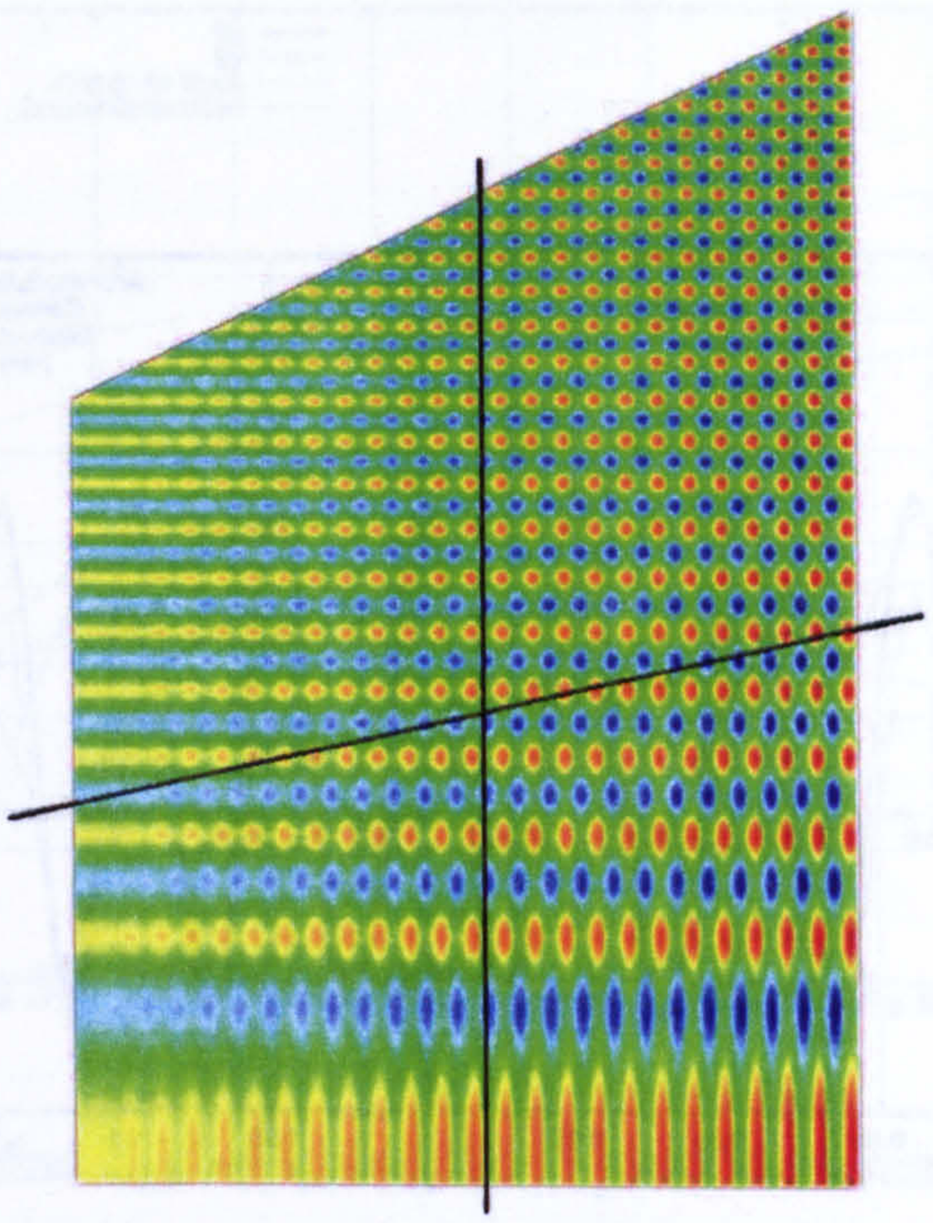

Figure 34: Manufactured Solution for B_x: Test 2

As in the first case, components of the velocity field were held to be the same constants u_0 and v_0, and boundary conditions were chosen so that field components take on their values dictated by the manufactured solution. The field components, plotted along the mid sections of the domain, with respect to x and y are shown in figures [35] and [36].

The profiles illustrate the effectiveness of the test, as the field profiles in both directions show poor agreement for the 50x50 grid test case. Furthermore, better agreement for the 100x100 and 150x150 cases is clearly evident, thus providing more confirmation that the solver satisfies the condition that $\mathbf{B} \rightarrow \mathbf{B}_{MS}$ as the grid spacing $h \rightarrow 0$. This is further confirmed in figure [37], where the L2 norm as function of grid spacing is illustrated.

The L2 norm is calculated by summing the squares of the discrepancy between the predicted solution, either in B_x or B_y, and the exact solution, over all grid locations within the domain. It is concisely expressed as

$$L_{2,B} = \sqrt{\frac{\sum_{i=1}^{N} (B_{PNS,i} - B_{MMS,i})^2}{N}} \tag{7.5.16}$$

where N refers to the total number of points sample, which is typically grid dependent, and B here denotes the idea that the norm may be calculated for either component of the magnetic field. Figure [37] verifies that the current implementation of the simplified magneto-hydrodynamic model, does provide a solution to the governing equations [4.6.9].

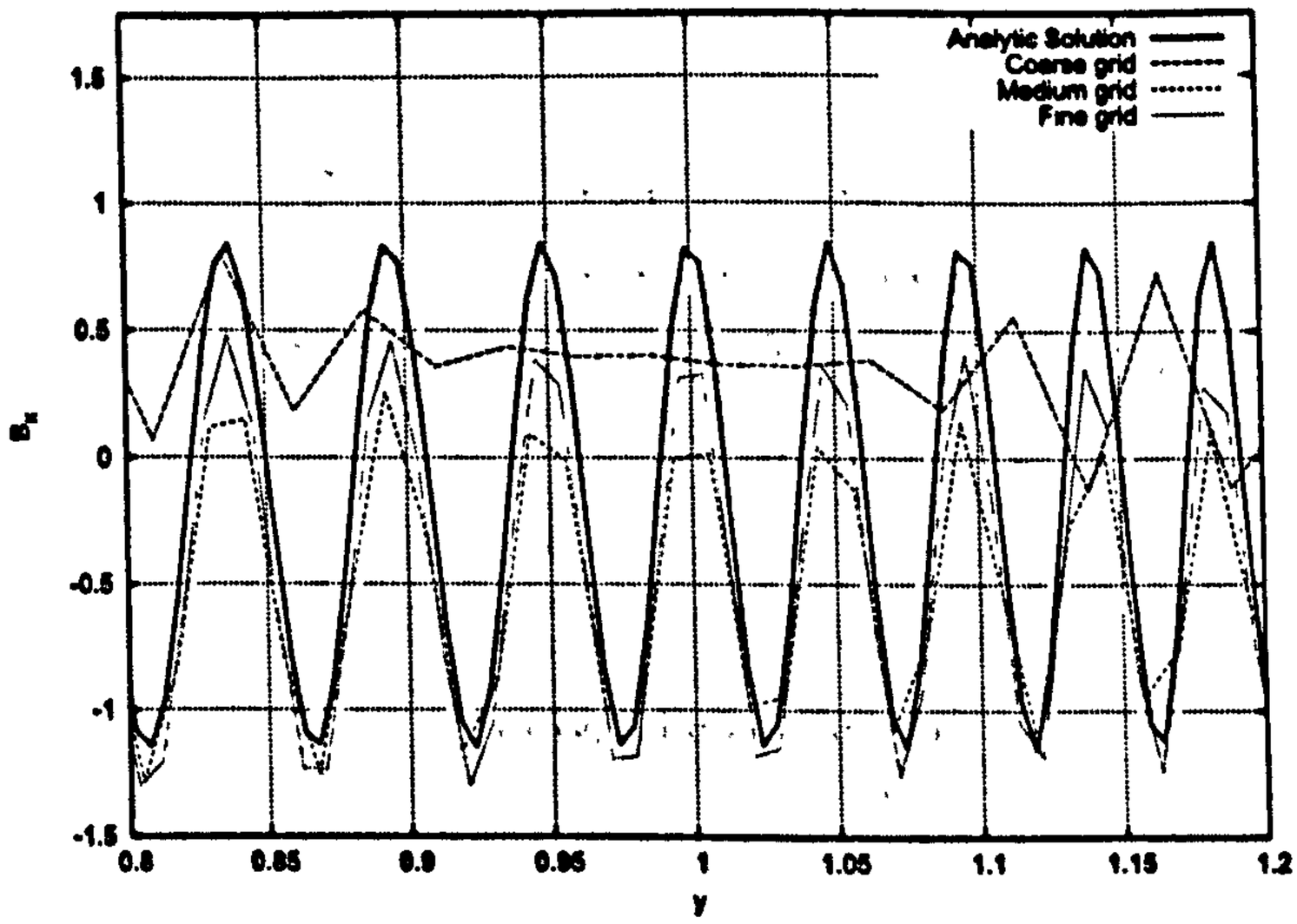

Figure 35: B_x, Profile for Multiple Grid Levels, in y

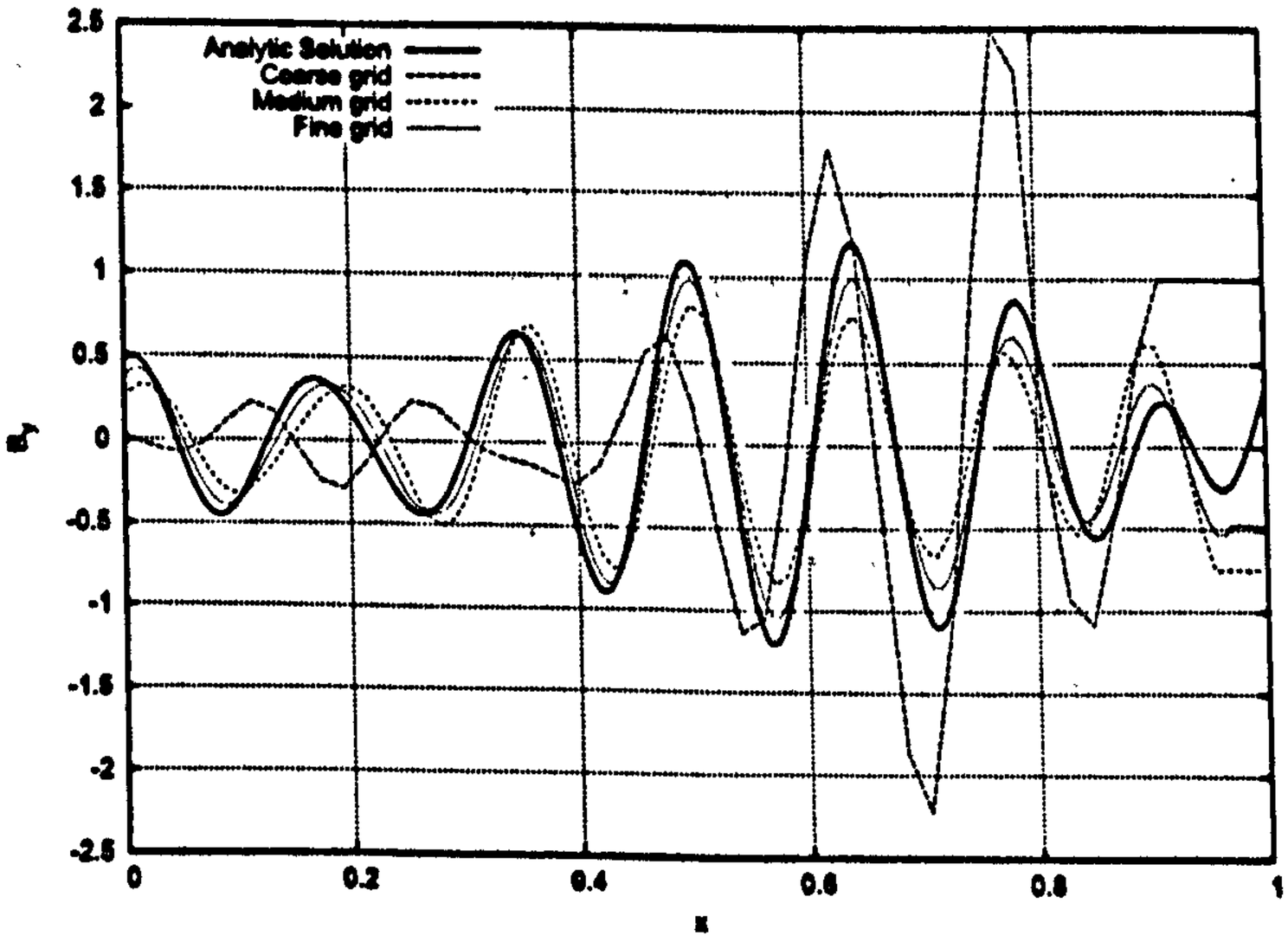

Figure 36: B_y Profiles for Multiple Grid Levels, in x

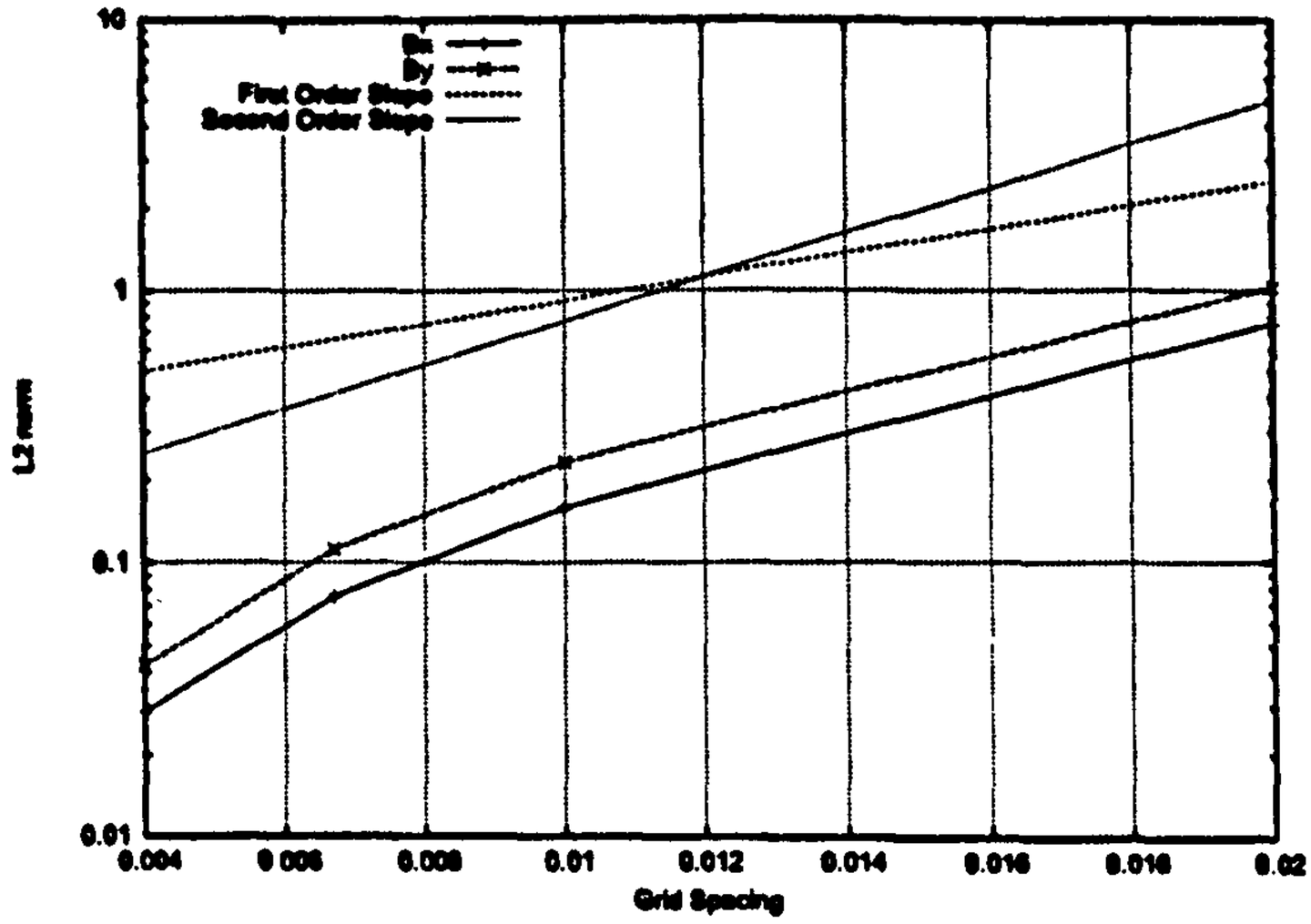

Figure 37: L2 Norms of Solution Error, in B_x and B_y

In the limit $h \rightarrow 0$, we find $L_{2,B} \rightarrow 0$, and the original numerical solution converges towards the manufactured solution, even for this highly oscillatory test case. By examining the gradients of the B_x and B_y lines above, one can obtain an understanding of the order of the induction equation solver. Over the grid spacing range of [0.01,0.02] one can see that if the if the grid spacing is doubled, then the L2 norm also doubles, for both variables, indicating first order convergence, over the coarser grid resolutions. Over the finer grids however, the error measurement decreases at a faster rate with decreasing grid resolution, indicating that second order can be achieved with a fine enough grid resolution.

7.6 Consequences of MMS

As section [7.5.1] showed, the original implementation of the magneto-hydrodynamic induction equation concealed several errors, including the method in which the non-conservative source term was being calculated. The method of manufactured solutions has been able to identify the error, and with the correction subsequently implemented, it therefore makes sense to revisit the initial compression- expansion corner calculation outlined in [7.2]. To visualise the improvement in the induction equation performance, the same test is performed for the magneto-hydrodynamic model. An initial sweep for the parabolized Navier Stokes equations is run with no magnetic field applied, and for each subsequent sweep, only the magnetic induction equations are solved for, with the flow variables held constant.

Figures [38(a)] and [38(b)] show the x components of the magnetic field variable, along the surface j=1, before and after the correction to the source term, as a result of the method of manufactured solutions procedure. Both diagrams illustrate the effect of

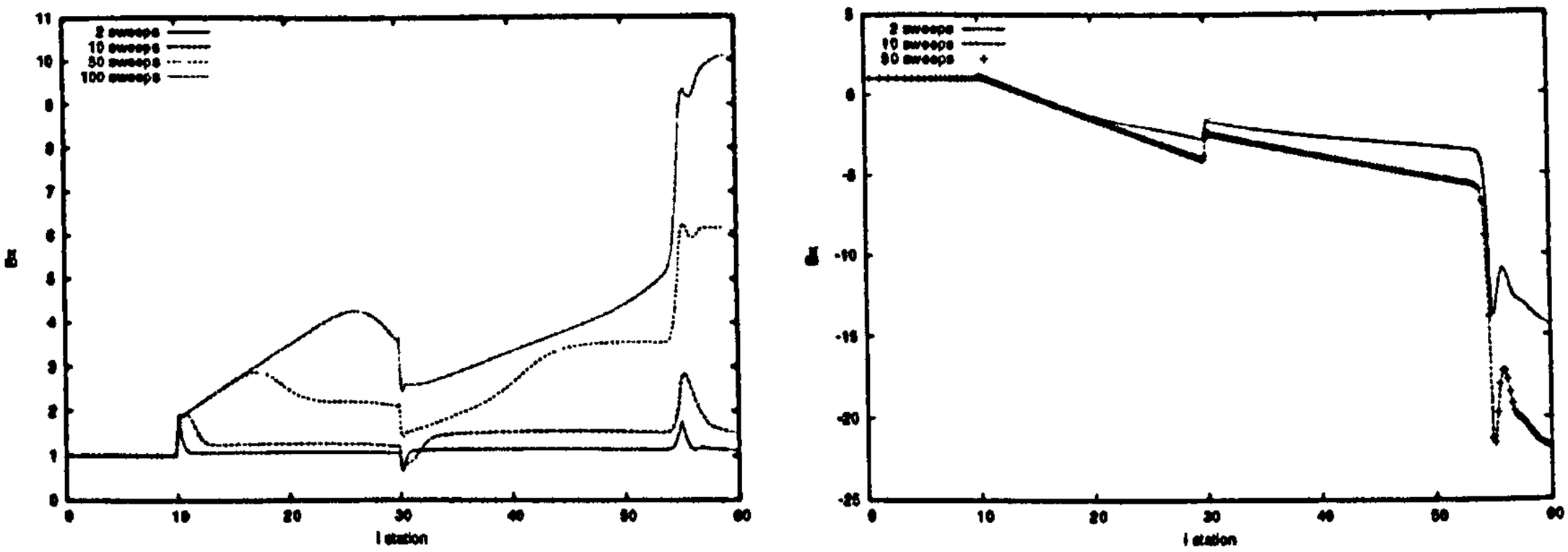

(a) Before MMS correction (b) After MMS correction

Figure 38: B_x distributions, along j=1

iterating over the magnetic induction equations over a different number of of multi-sweep iterations. In the limit of a large number of multi-sweeps, one would expect the magnetic field profiles to converge to a unique profile asymptotically, as this indicates iterative convergence in the magnetic field . The B_x profiles before the correction highlight that the solution is not converging iteratively, as the number of sweeps is increased. Instead, the post-shock values for B_x continues to increase over a larger region, as the number of sweeps is increased. Figure [38(a)] shows no indication of the profile converging iteratively. In contrast, the magnetic field distribution with the correction applied demonstrates iterative convergence, as there is no difference in solution for the 10 and 50 multi-sweep profiles.

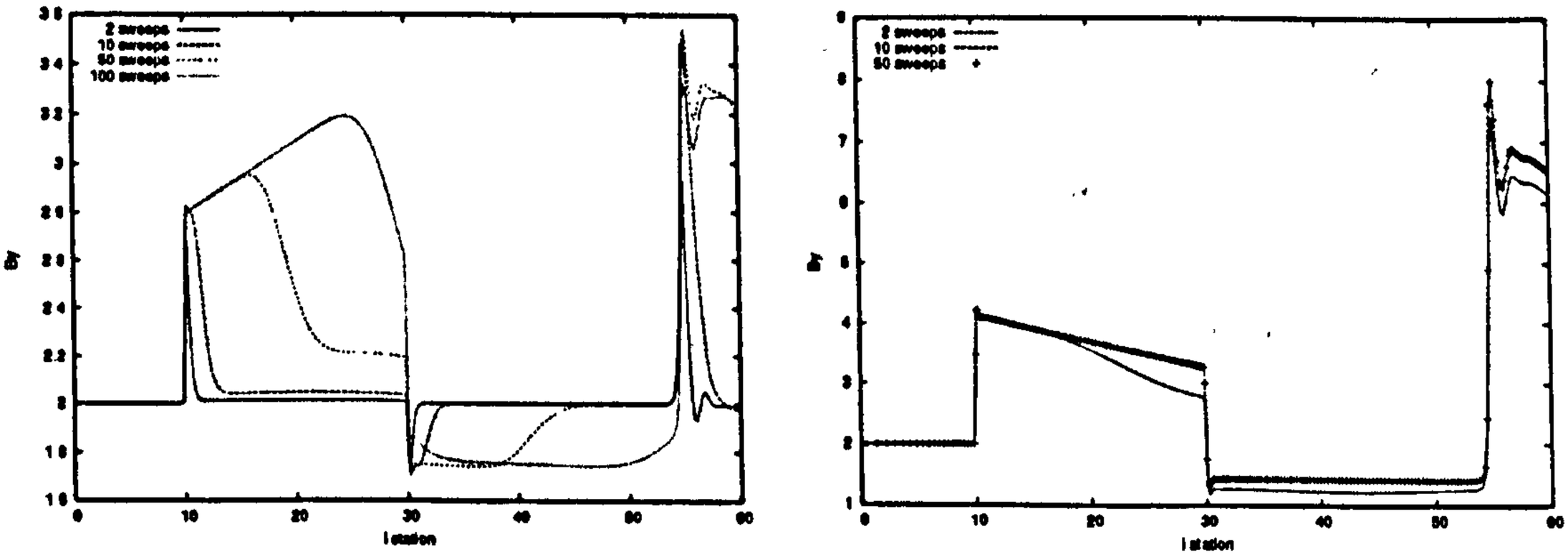

(a) Before MMS correction (b) After MMS correction

Figure 39: B_y distributions, along j=1

The profiles in [39(a)] and [39(b)] also illustrate a similar behaviour. Without

the required correction, the B_y value increases over a wider range, with increasing multi sweep number, but is iteratively converged after 10 sweeps, once the corrections are applied. The above figures are therefore a clear indication of the benefits brought about by the identification of the source term error using the method of manufactured solutions procedure. Tests in sections [7.5.1] and [7.5.2], have been able to ensure the program solve the intended governing equation, and the above profiles ensure that the induction equations are iteratively convergent.

However, despite the above improvements in induction equation, when the two sets of equations are coupled together and updated in tandem, the code still fails to converge. As with the original simulation in section [7.2], the solver returns negative pressures on the third forward sweep, with the same pressure distributions as in figures [22 to 25]. Since the magneto-hydrodynamic induction equations have been shown to be solved for in a correct manner, using the method of manufactured solutions , this therefore suggests there may remain errors in the modifications to the parabolized Navier Stokes equations. Component tests on the contributions to the right hand side vectors from the extra magnetic field terms also illustrate that they perform as expected. The results for this are included in the Appendix A.

The component tests for the extra terms in the momentum and energy equations indicate that the method in which they are implemented are correct. Thus all components, in the momentum, energy and magnetic induction equations are implemented correctly. Investigating them collectively however via running the present numerical test case results in non-convergence. The solution algorithm employed, the method used to enforce the zero divergence condition on the magnetic field, or the non-convective nature of the extra terms in the parabolized equations may be causes for the observed behaviour, but due to lack of time, not all avenues could be pursued. Subsequent investigations into the causes of non-convergence are therefore left as future work.

7.7 Conclusions

Verification and validation of computational fluid dynamics codes are of paramount importance in trying to assure the credibility of solutions for novel problems. Traditional methods for verifying the magneto-hydrodynamic equations include comparison to experimental data, whose operating conditions are difficult to mimic, due to the requirement for additional modelling in the form of non-equilibrium chemistry models which capture the process of disassociation and ionisation. This imposes an additional cost on the computational overhead, and is not within the scope of the current work. Comparison to

analytic, simplified solutions are possible alternative, but are due to the restrictions imposed by the assumptions inherent in the base PNS code. Instead the numerical results of Harada et al [65] for a compression expansion corner simulation have been compared to. For the baseline case, in the absence of a magnetic field, good agreement is achieved, although there is a degree of overshoot at the beginning of the shock front, and through the expansion, which is accounted for by the order of the streamwise discretisation.

With the magnetic field applied, the solver was not able to return a converged solution, although the pressure profiles after two sweeps suggest that the locations and the extent of the discontinuities through the shock and expansion wave agree with Harada near the lower surface. Further away, the agreement deteriorates. As an assessment of the accuracy of the induction equation, the case was also run by fixing the flow solution, although the shock and expansion locations seemed to be inconsistent to the coupled calculation. In view of the ambiguity in solution for the induction equations, the objective of obtaining confidence in the implementation of the simplified magneto-hydrodynamic equations, was addressed using the method of manufactured solutions.

It has been known that the method of manufactured solutions is a robust procedure for code verification. A common problem in the area of computational fluid dynamics, or indeed in most areas requiring numerical solution to systems of partial differential equations, is whether the set of equations are truely represented by the simulation code. Assessment of whether the implementation reflects the mathematics must be determined before any inference can be made about the model's predictive accuracy in representing the of real world.

Used in a systematic manner, as shown in the current chapter has therefore demonstrated the flexibility of the technique, as opposed to its widely held perception as simply being a verification tool. Prior literature, such as in works by Nelson and Roy [114, 138], have emphasized use of the technique as a means of understanding the order of numerical schemes used within a CFD code, but has not paid attention to its use as a diagnostic procedure. The chapter has therefore filled this void by focussing on the way in which the method of manufactured solutions may be used to resolve inexplicable behaviour of a numerical scheme used to solve the simplified magneto hydrodynamic equations. The form of the manufactured solution can be chosen judiciously such that only those parts of the system of equations that wish to be investigated, can be tested.

To this end, the first test, which examined the code's behaviour for a relatively simple smooth function, highlighted several errors in the analysis code, to do with the source term evaluation, and the calculation of boundary conditions. The second test on a non-linear oscillatory function, whose frequency of oscillation was smaller than the grid spacing for the coarse grid, illustrated that such a function could not be accurately using

the coarsest grid. However, in the limit of grid spacing approaching zero, the L2 norm of the error between the predicted and actual solutions tended to zero, further confirming the fact that the implementation obtains numerical solutions to the equations, in the limit of small grid spacing.

With this novel application of the method of manufactured solutions verification procedure to the magneto-hydrodynamic equations, it is therefore safe to assume that the magnetic field solver provides an accurate numerical solution to the simplified magneto-hydrodynamic model, and it can be stated with confidence that coding errors preventing the correct operation of the solver have been identified during the development process. Indeed, the identification of the error in the source term evaluation, manifested itself in the compression expansion corner calculation, by ensuring that the induction equation was iteratively convergent. Prior to the modification, iterative convergence had not been achieved in the induction equation.

Correctness of solution for the induction equation, and additional component tests on the magnetic field terms in the parabolized Navier Stokes equations, were not able to resolve the issues of non-convergence in the fully coupled flow solver however. The solution algorithm itself, the manner in which the extra terms are evaluated, and the enforcement of the $\nabla \cdot \mathbf{B} = 0$ condition, are some of the areas that ought to be addressed as part of future work.

CHAPTER 8

Numerical Optimisation

In performing optimisation various factors need to be considered in order that the limits and scope of the study may be fully comprehended. Issues such as sampling procedures, algorithm choice as to how to best optimise quantities of interest, issues of accuracy and trade offs between several quantities of engineering interest must all be taken into consideration. In the past gradient based techniques have been utilised considerably, based on direct use of an analysis tool. An analysis tool here refers to any tool (whether it be computational fluid dynamics simulations, or empirical models) used to obtain a value for an optimisation variable, given a set of inputs. With the increase in computational power and resources, both academics and engineers within industry have continued to use more complex numerical routines as analysis tools, which despite advances in hardware continue to take considerable time to obtain solutions. Gradient based techniques and genetic algorithms that rely on the direct use of high fidelity routines, can often prove to be unfeasible due to the longer computational durations needed for the analysis tool. An alternative method is to use substitute models for the analysis tool, one that substantially reduces the overheads in computing time.

This section illustrates the alternative models available in the search procedure of an optimum. A wider description of the sampling procedures and optimisation techniques is provided, and representative applications making use of the techniques are also discussed.

8.1 Sampling Procedures

Sampling procedures for exploring the design space are often described by design of experiments theory, within which procedures and tools are discussed. Analysis of the design of experiments is based on the analysis of variance, where the variability of observations is split into components, arising from variability of the different factors, in this case design the variables that are to be tested.

Many optimisation studies involve trying to understand the effects of two or more factors. Full factorial designs are efficient procedures for such studies as they involve a complete replication of all possible combinations of the levels of each factor being investigated. For example, if there are n design variables, with l levels, then a full factorial design would constitute taking observations (or objective function evaluations) from l^n samples.

This technique is clearly more efficient than simply taking observations by varying one factor at a time, and is advantageous when dealing with instances where there may be unforeseen interactions between input variables. Clearly this is due to the property of full factorial designs that given a fixed number of levels for each design variables, each and every combination is investigated. Despite this thorough approach, the main disadvantage of the full factorial approach is that the number of samples increases exponentially in the number of design variables. A study consisting of 7 design variables, each with 4 levels would require taking sample data from $4^7 = 16384$ individual cases, for example. Thus realistically, full factorial designs are only affordable if the analysis tool used to obtain the observation is relatively computationally inexpensive. For high fidelity CFD calculations, this may not always be the case, therefore alternative sampling procedures are necessary, that do not require a vast number of simulations.

One alternative, designed to broaden the design space, is the central composite design [52],[18]. In the presence of a uniformly distributed error better approximations can be made by taking samples on the boundaries of the design space. A central composite design consists of taking a 2 level factorial design, with 2^n samples, and then adding to this $2n$ axial samples at a distance α away from the faces of the space, and n_c central points. Examples of this with $n = 3$ is illustrated in figure [40].

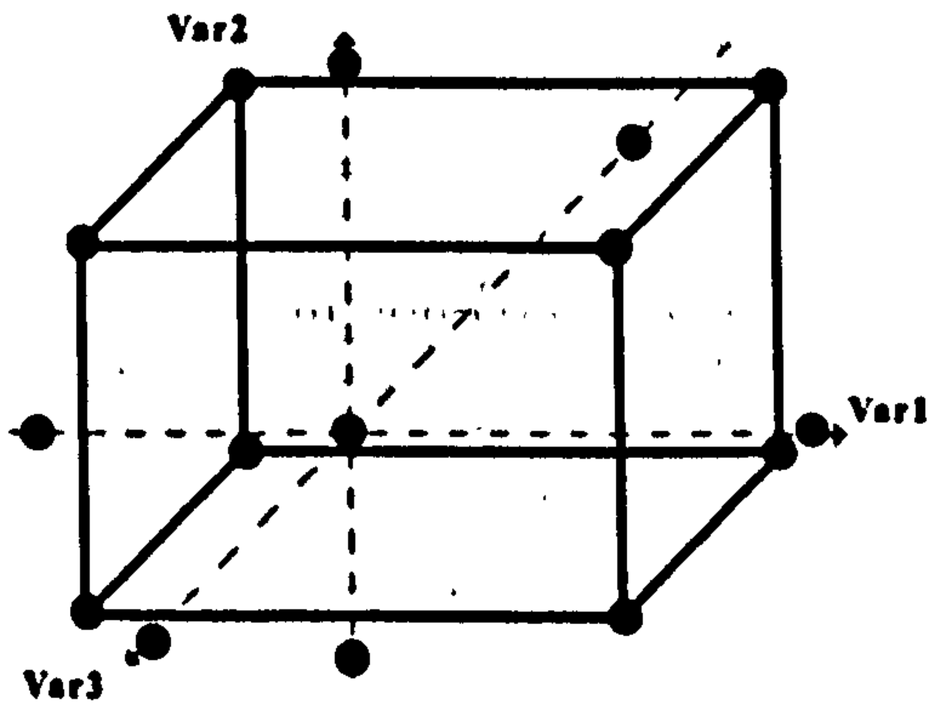

Figure 40: Central Composite Design with $n = 3$ variables

The 2^n factorial design points are located over the vertices's of the design space, the axial points on the intermediate axes of the space. The effectiveness of the sampling procedure is dictated by choices for α and n_c. α is chosen to be equal to $\sqrt{n}$, the design variables are scaled such that they lie in the range [-1,1], containing between 3 and 5 central points. This ensures the variance of the entire sample has a uniform distribution, and that the prediction quality is approximately the same over the design space. In instances where the bounds on the design variables are strictly specified, axial points may be placed on the faces of the design space without any substantial change in the uniformity of the variance distribution.

Another method aimed at providing a uniform sampling distribution is the D-Optimal design, as found in [110]. The main idea of the method is to maximise the determinant of the matrix $X^T X$, for a given regression model. This ensures the variance of the regression coefficients is minimised. The method has been used to generate quadratic response surfaces in several aerodynamic optimisation studies [157], [4], [113] , but has been shown not to be robust in cases where there has been model specification, commonly caused by there being too few "centre" runs in the design. This leaves regions in the design space where there may be large values for the variance, which is clearly undesirable.

Both central composite designs and D-optimal designs are based on the assumption that the designer/experimentalist has some insight into the underlying trends of the function to be approximated. In other words a model must be supplied for the design before samples can be generated. They are both advantageous over full factorial designs as a judicious choice can be made as to which samples to actually investigate, and D-optimal designs have the added benefit of being able to deal with restrictions on combinations of factors that may be unfeasible or impossible to run.

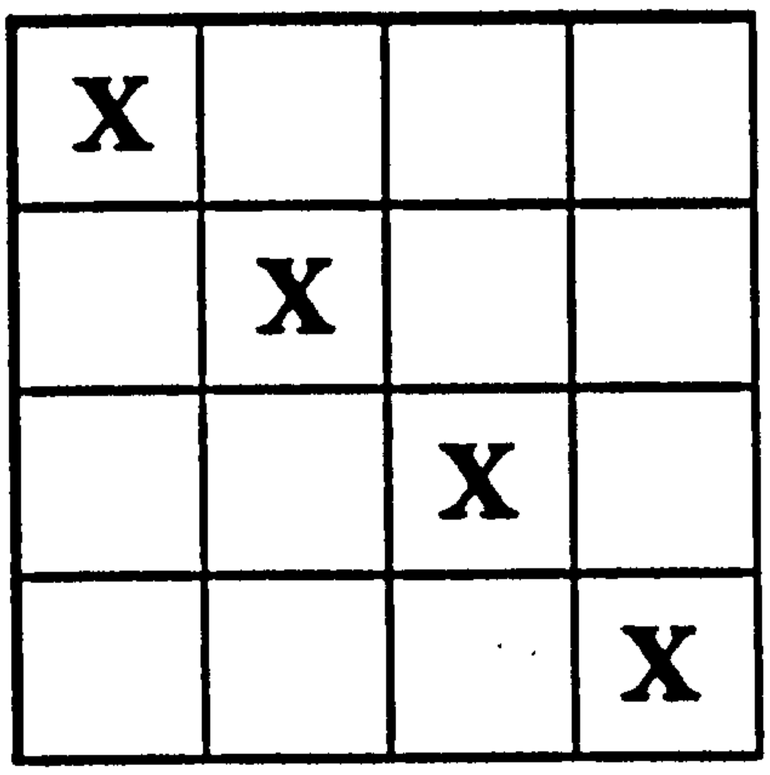

(a) Simple Latin-square Distribution

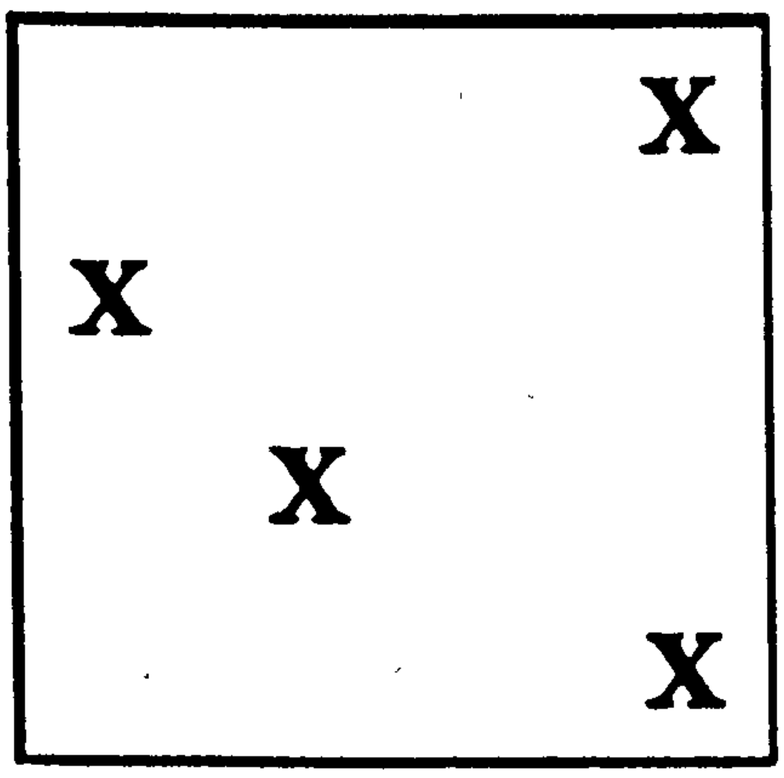

(b) No consideration for previous points

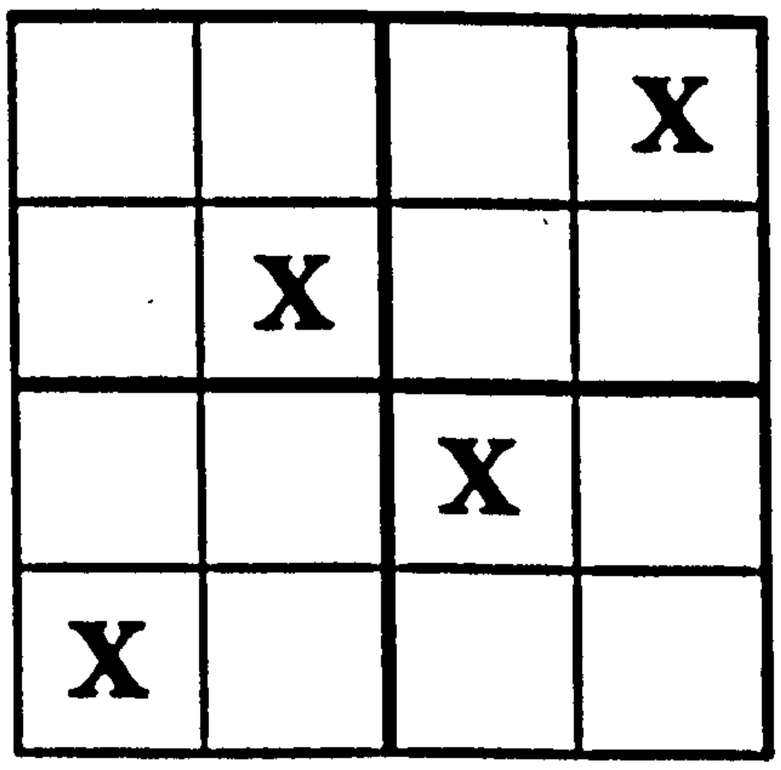

(c) Probable sub-space Latin-square Distribution

Figure 41: Orthogonal Sampling Procedures

However, within the context of magneto-hydrodynamic optimisation, in general, no knowledge may be assumed over the underlying model, making these techniques inappropriate.

An alternative, specifically tailored for computational investigations is that of the latin hypercube. The original idea proposed by Mckay et al [103], aimed at generating a sample data-set that would minimise the variance caused by circumstances associated with input variable uncertainty, as is the case with computational experiments. Each design variable has bounds place on their respective values, and these intervals are divided into an equal number of sub-intervals. A random point is chosen within these sub-intervals, and continues to do so until every interval for each variable has been explored. For example, consider a two-dimensional case with two parameters consisting of four intervals, as shown in figure [41 (a)] The grid is said to be a Latin square, if and only if there is one sample in each column and row.

Random sampling methods have also been proposed as space filling designs. Samples are obtained by selecting points at random within the variable intervals [60]. Points are taken without taking into account previously selected points, as in figure [41 (b)] . In contrast to other methods, due to this stochastic nature of the sampling technique, there may well be regions unexplored by the selection procedure. To overcome this, stratified or orthogonal sampling adds the requirement that the points are sampled evenly [157]. Illustrated by figure [41 (c)] above, the sample space is divided into four equally probable sub-spaces. All sample points are then chosen equally such that each sub-space is explored with the same number of samples, and that the resulting design satisfies the Latin square criterion. A Latin hypercube is an analogy of this extended for cases involving three or more parameters. The orthogonal sampling method is more efficient compared to simply applying the requirement for a latin hypercube, although in practise it is more difficult to implement.

The hypercube method is capable of ensuring variation of each design variable over several intervals, since there is flexibility in the number of samples. This property has been taken advantage of in several studies, such as in [148]. Note that the number of samples generated from the design procedure is independent of the number of dimensions/variables. Rather, it is equal to the number of intervals used to split each of the intervals. Hence, it is ideal for studies involving a large number of parameters compared to full factorial design which is exponential in the number of design variables.

One other method to obtain a uniform sample of experiments is that of Audze and Englais [9]. The technique is model independent, and is based on the Latin hypercube, in that only one sample is taken from each interval, although the authors had the insight of attempting to minimise the Euclidean distance between the sample points. The idea is similar to minimising the potential energy of repulsive forces, given a set of point charges

distributed in space.

8.2 Optimisation Procedures

Once a dataset, provided using one of the numerous procedures outlined above, has been determined, the numerical or experimental investigator must identify a suitable optimisation procedure. The current section serves as an illustration of the various techniques that have been developed over the past couple of decades, and have been successfully applied to aerospace optimisation problems. Numerical optimisation commonly refers to the design process of trying to minimise or maximise an objective function, with the use of mathematical models to simulate and predict characteristics of a particular design. Such procedures have become increasingly common in engineering due to relatively cheaper costs of running numerical simulations as opposed to developing experimental procedures or prototypes at the outset.

If x is a vector of possible design variables, with $f(x)$ the objective function to be optimised and $g(x)$ the vector of constraint functions, the optimisation problem is formed as follows;
minimise/maximise

$$f(x) \tag{8.2.1}$$

such that the non-equality constraints;

$$g_j(x) \leq 0 \tag{8.2.2}$$

are satisfied for $j = 1, \cdots, n_{con}$ and with the additional constraints on the design variables;

$$x_i^L \leq x_i \leq x_i^U \tag{8.2.3}$$

for $i = 1, \cdots, n_{var}$. In the above condition x_i^L and x_i^U represent the lower and upper bounds on the i-th design variable respectively.

In general, there will be several local minima/maxima for any given optimisation problem, and as such, the solution to most optimisation problems may not have a unique solution. From a designers perspective the ultimate goal is to determine the global minimum/maximum of the objective function, but no techniques investigated to date can guarantee that this will be achieved.

Many of the algorithms investigated to date are based upon calculation of sensitivity derivatives of the objective function, to changes in the design space. Gradients of $f(x)$, with respect to x are used to determine paths of steepest descent/ascent, in the search

for minima/maxima. The technique is highly dependent on the initial sample point, as is illustrated in the following simple one variable case;

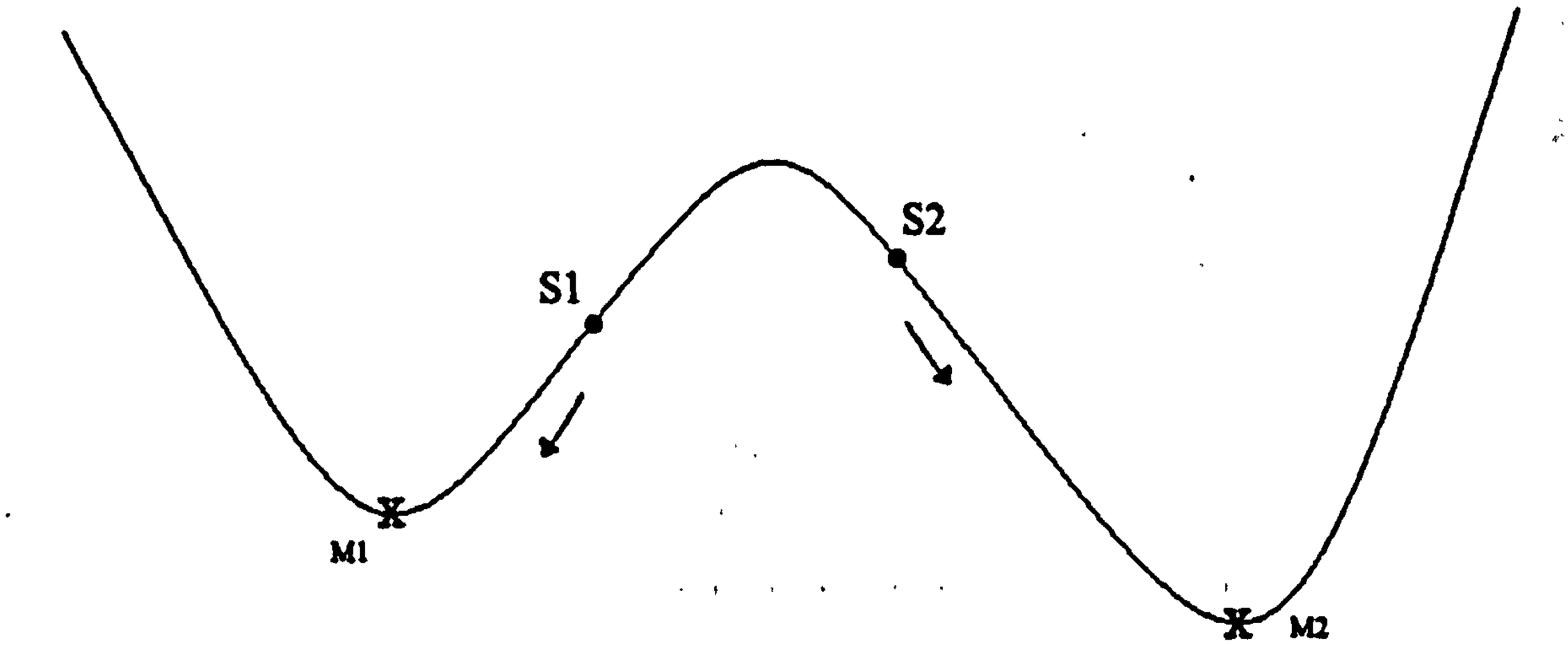

Figure 42: Optimal solution dependency on initial point

Suppose we wish to minimise f, given by the above curve. Clearly local minima exist, denoted by points m_1 and m_2 with the latter being the global minimum. From the above, if the designer were to choose s_1 as the initial sample point, the method would tend to approach m_1. Given that there is a local maxima to the right of this point, there is no way one could obtain the global minimum m_2. This is not the case had s_2 been chosen, and serves to highlight the fact that initial sample points strongly govern the potential optimum solution.

The most current method in gradient based search procedures is that of sequential quadratic programming based on the works of Biggs [13], Han [64] and Powell [124]. The idea is based on the criterion known as the Kuhn-Tucker conditions that must be satisfied to ensure optimality for solutions to constrained optimisation problems. It states that for a given objective function f and constraints g_j, as described by equations [8.2.1] and [8.2.2], and the point $\mathbf{x}^*$ in the design space is an optimum solution to the problem, then there exists constants $\lambda_j \geq 0$, $j = n_{eq} + 1, \cdots, n_{con}$ such that;

$$\nabla f|_{\mathbf{x}=\mathbf{x}^*} + \sum_{j=1}^{n_{con}} \lambda_j \nabla g_j|_{\mathbf{x}=\mathbf{x}^*} = 0 \qquad (8.2.4)$$

$$\nabla g_j|_{\mathbf{x}=\mathbf{x}^*} = 0 \qquad (8.2.5)$$

for $j = 1, \cdots, n_{eq}$ in the last equation above, where n_{eq} is the number of equality constraints. Note that ∇ is the gradient operator with respect to the n_{var} design variables $\mathbf{x}$. The first equation in the above criterion is analogous to saying that the Lagrangian;

$$L(\mathbf{x}, \lambda_1, \lambda_2, \cdots, \lambda_{n_{con}}) = f(\mathbf{x}) + \sum_{j=1}^{n_{con}} \lambda_j g_j(\mathbf{x}) \tag{8.2.6}$$

vanishes at the optimum points. In gradient based optimisation, the SQP process makes an approximation of the Hessian of the above function, building a quadratic representation, which is subsequently used to determine a search direction for a gradient search. The process is iterated until an acceptable minimum is obtained, which is verified by computing objective function values in the vicinity of the proposed point.

Genetic Algorithms have also enjoyed interest as optimisation procedures. The main advantage of which lies in its ability to examine the objective function from a multitude of design points [62], and not just that in the vicinity of the current point, as is the case with SQP. This therefore allows a wider exploration of the design space. Additionally there is no need to compute derivative information, since the technique is based on encoding the parameter set, rather than on the design parameters themselves.

As an initial step, the design space is encoded so that it can be represented as a chromosome. Each variable is converted into a binary string of 1's and zeroes. Then an evolutionary process is applied to an arbitrarily chosen initial sample "population", which consists of three parts; selection, mutation and crossover. Selection is based on choosing the designs that are fittest, ie provide the best optimal function value, to ensure these chromosomes remain within the design space. After this selection, a new generation of samples are created by allowing members of the survived samples to exchange design characteristics. This is done by simply swapping individual components of the strings from 1's to 0's and vice versa, with the swapping location chosen randomly. After the above, an arbitrary number of chromosome sites are allowed to undergo mutation, again randomly. This is a crucial step in the evolutionary process, as it allows designs to go out of the box, and protects against any samples not being investigated by the consideration of selection and crossover alone. The evolution of successive generations comes to a stop once a solution is found to satisfy the minimum/maximum criteria, a fixed number of generations has been obtained, or once a particular fitness level for a given function has been obtained, which cannot be exceeded by additional generations.

In light of the above, optimisation based on genetic algorithms are advantageous as the mutation portion of the evolutionary process enables the exploration of designs that may initially be outside of the scope of the study. Thus said, there are disadvantages with the method, most notably, the method in which constraints given by $g(x) \leq 0$ are handled. For samples not satisfying the respective constraints, the objective function is modified to incorporate a penalty function, which may be unphysical and unrepresentative of the design space. Because of this, genetic algorithms are best suited to problems involving a

limited number of constraints. Additionally, there are issues as to the importance of mutation and crossover in the evolutionary process, and opinion is divided over which should be the dominant process. Also, applying the procedure to adaptive, dynamic sample sets is some what more difficult, as chromosomes tend to converge to a particular point in the sample space early in the iterative process, which may be void as additional sample data becomes available.

Thus said evolutionary algorithms have enjoyed success in numerous aerospace related applications. Several studies have focused on wing design problems, with the aid of a CFD tool. Jones et al, for example consider an aerodynamic and acoustic optimisation problem, aiming to minimise both drag and noise for a given aerofoil [76]. The genetic algorithm was based on twenty design variables representing the aerofoil surface. Liu considers several different types of GA procedures to general aircraft optimisation, proposing a modified "intelligent Genetic Algorithm", involving a crossover operator that can take into account of factorial design of experiments for each new generation [90]. The main disadvantage of such approaches however, is that they rely on using the analysis tool itself, which may, as is the case in the present thesis, be prohibitively expensive when one considers the number of objective function evaluations that need to be made throughout the search process.

8.3 Surrogate Models

Use of either of the two procedures with the analysis tool used directly as the means of evaluating the cost function can be impractical if tool is time consuming or expensive to determine. This is commonly the case with three dimensional computational fluid dynamics solutions. Despite the increase in computing resources over the past couple of years, such as greater processor speed, this rise has been accompanied by a more common use of higher fidelity models that involve a higher degree of complexity, by computational fluid dynamics practitioners.

An alternative is to replace the expensive numerical models with cheaper alternative models that are capable of providing the underlying trend in the objective function. The most widely used technique for this is through the use of Response Surfaces, which serve as an approximation to the objective function evaluated through the use of an analysis tool. The surface is generated from analytic evaluations of the objective function, over a given set of initial design points. The Design of Experiments methodology, described in section [8.1] provides guidance on choosing this set of initial design points. Naturally, the number, distribution and locations of these points are critical to the accuracy of the surface.

The additional problem arises as to how to find the most suitable functional form for the response surface, which must be accurate enough to mimic the trends in the objective and constraint functions. However, once this approximation is obtained, any one of the gradient based optimisation procedures may be used to perform an optimisation study, as successive objective function evaluations are now replaced by inputting design variables and calling the surrogate model. This section outlines the methods available for the construction of approximating functions, and their uses to date in aerospace optimisation problems.

Response surfaces are beneficial in that one can build successively response surfaces over small portions of the design space, and thereby build a wider design region. The principle advantage of this is that the process is more likely to return the global optimum, as several starting points can be investigated over a wider ranging design space. This ideal is further compounded by the fact that after each iteration of the optimisation procedure, successive approximations can be made around the last optimum to create further sub-domains, thus "homing in" closer on the optimum. This feature has been exploited by Rodriguez et al. [134], who examined the construction of sequential response surfaces for solving multi-disciplinary optimisation issues.

The process is also ideal in that the approximating functions for response surfaces are likely to smoothen high frequency noise within the objective function, and that numerous objectives and constraints may be imposed without over-burdening the procedure. The model construction is done outside of the main analysis code, so code modifications to the tool need not be necessary.

8.4 Response Surface Representation

To take advantage of the benefits of surrogate models, one must obtain a test function that yields a relationship between the independent sample variables, and the dependent objective function. Using the notation used in section [8.2], the form of this function can generally be expressed as

$$y = f(x) + \epsilon \tag{8.4.1}$$

where f is the unknown function to be optimised, and ϵ is an error term arising from factors not considered in the determination of f at sample points x_i. Estimation of this error depends on the method employed to obtain evaluations of f; for computational experiments, for example, this error may arise due to incomplete grid or iterative convergence, or discretisation errors [140], whereas for experimental work, measurement errors are frequently occurring [110]. Several methods have been proposed to approximate the real

objective function $f(x)$, which are outlined and discussed in the present section.

Polynomial regression is one such common technique for developing an empirical model. Usually, a low order polynomial is used in a specified region of the independent variables is used. For example, if a linear response is deemed suitable, then a possible approximation function may look something like;

$$y = \beta_0 + \beta_1 x_1 + \beta_2 x_2 + \cdots + \beta_k x_k + \epsilon \tag{8.4.2}$$

where k is the number of independent variables, x_i for $i = 1, \cdots, k$ are the independent variables, and β_i are coefficients to be approximated. In situations where there may be curvature present in the objective function, a linear model may become unsuitable, and a natural choice would be to use a quadratic approximation of the form;

$$y = \beta_0 + \Sigma_{i=1}^{k} \beta_{ii} x_i + \sum_{i=1}^{k} \sum_{j<i} \beta_{ij} x_i x_j + \epsilon \tag{8.4.3}$$

or in a more convenient matrix notation;

$$y = x^T B x + \beta^T x + \beta_0 + \epsilon \tag{8.4.4}$$

requiring the determination of additional regression coefficients. In the most general of circumstances it is unlikely that a polynomial regression would be a suitable approximation over the entire design space, but in a small localised regions they usually perform better. To complete the model description, the regression coefficient given by the β's must be determined.

A common method to estimate these parameters is to use a least squares fit. The designer will normally have a set of observations of the objective function given a set of sample points. If the residuals are defined to be the difference between the observed values and the predicted values from the surrogate model, the coefficients are determined such that the sum of the squares of the residuals in minimised.

Consider a set of n experiments generated from a set of sample points x_n, and observations y_n. Using a quadratic polynomial model, if x_{ij} denotes the value of the j-th independent variable on the i-th run, then the data may be tabulated into the following form.

In this form, the residual is simply the difference between the observed value and the predicted value on the i-th experiment and is expressed by;

$$e_i = y_i - \left(x_i^T B x_i + \beta^T x_i + \beta_0 \right) \tag{8.4.5}$$

Introducing some additional notation, let

y	x_1	x_2	$\cdots$	x_k
y_1	$x_{1,1}$	$x_{1,2}$	$\cdots$	$x_{1,k}$
y_2	$x_{2,1}$	$x_{2,2}$	$\cdots$	$x_{2,k}$
$\vdots$	$\vdots$	$\vdots$	$\vdots$	$\vdots$
y_{nrun}	$x_{nrun,1}$	$x_{nrun,2}$	$\cdots$	$x_{nrun,k}$

Table 4: Table of sample data for regression coefficients

$$y = \begin{pmatrix} y_1 \\ y_2 \\ \vdots \\ y_n \end{pmatrix} \quad e = \begin{pmatrix} e_1 \\ e_2 \\ \vdots \\ e_n \end{pmatrix} \tag{8.4.6}$$

$$\beta^T = [\beta_0, \beta_{1,1}, \beta_{2,2}, \cdots, \beta_{kk}, \beta_{1,2}, \beta_{1,3}, \cdots, \beta_{1,k}, \cdots, \beta_{k,k}, \beta_1, \beta_2, \cdots, \beta_k] \tag{8.4.7}$$

$$X = \begin{bmatrix} 1 & x_{11}^2 & \cdots & x_{1k}^2 & x_{11}x_{12} & \cdots & x_{11}x_{1k} & \cdots & x_{1,k-1}x_{1,k} & x_{11} & \cdots & x_{1k} \\ 1 & x_{21}^2 & \cdots & x_{2k}^2 & x_{21}x_{22} & \cdots & x_{21}x_{2k} & \cdots & x_{2,k-1}x_{2,k} & x_{21} & \cdots & x_{2k} \\ \vdots & \vdots & \vdots & \vdots & \vdots & \vdots & \vdots & \vdots & \vdots & \vdots & \vdots & \vdots \\ 1 & x_{n1}^2 & \cdots & x_{nk}^2 & x_{n1}x_{n2} & \cdots & x_{n1}x_{nk} & \cdots & x_{n,k-1}x_{n,k} & x_{n1} & \cdots & x_{nk} \end{bmatrix} \tag{8.4.8}$$

Given these expressions, one can rewrite equation [8.4.5] using the vector of observed variables y and regression coefficients β as;

$$e = y - X\beta \tag{8.4.9}$$

To find the least squares fit response surface, the following function must be minimised for an suitable choice for β;

$$L(\beta) = \Sigma_{i=1}^{n} e_i^2 = (y - X\beta)^T (y - X\beta) \tag{8.4.10}$$

which when expanded is;

$$L(\beta) = y^T y - 2\beta^T X^T y + \beta^T X^T X\beta \tag{8.4.11}$$

Optimality is imposed on the above expression by ensuring the first derivative with respect to the regression coefficients vanishes;

$$\frac{\partial L}{\partial \beta} = -2X^T y + 2X^T X\beta = 0 \tag{8.4.12}$$

To solve for the coefficients, multiply both sides of the above equation by the inverse of matrix $X^T X$. The least squares estimator of β is then given as;

$$\beta_{lsq} = \left(X^T X\right)^{-1} X^T y \tag{8.4.13}$$

Using these coefficients, the response surface approximation fitting the observed objective function is given by

$$y = \beta_{lsq} x \tag{8.4.14}$$

It is important to note that as the surrogate model generated approximates the data in a least squares sense, it may not necessarily reproduce the objective function values from the originally available sample data points. Due to the uncertain nature of the observations, there will inevitably be uncertainty associated with the regression coefficients. Analysis of variance (ANOVA) tests may be used to determine which terms within the regression model are poor estimates. Because of the nature of the approximation, such estimates can affect the accuracy of the model [110]. Therefore coefficient quality needs to be considered when dealing with cases where several differing objective function values are witnessed for the same sample data, such as is the case for experimental studies. With the case of quadratic response surfaces, Keane and Nair [80] point out that if over a small enough region all continuous surfaces may be approximated adequately using a quadratic representation as in equation [8.4.14]. Thus the form above is useful when considering an objective function variation over a limited space, for example.

To take this into account, often a modelling error representing departure from the true solution is added to [8.4.3], which is dependent on the sample location [140]. In the realm of numerical experiments, modelling error is often included in the measurement error term ϵ, and is therefore treated as random white noise. This assumption is questionable when dealing with numerical experiments where solutions are deterministic. The errors are not random, but are generated by not considering higher order terms that are not considered in the regression model.

The Kriging methodology provides a procedure to try and model this type of bias error, by assuming a model to take the form of

$$y(\mathbf{x}) = p(\mathbf{x}) + Z(\mathbf{x}) \tag{8.4.15}$$

where y is the function to be modelled, p the known polynomial function of $\mathbf{x}$ used to approximate the data, and $Z(\mathbf{x})$ is the deviation from the polynomial, a normally distributed random process with zero mean, and a variance of σ^2.

Since p is a global representation of the objective function, Z focuses on the potential local deviations from the polynomial model. These deviations are based on the assumption that the departures from the regression model at points $\mathbf{x}_i$ and $\mathbf{x}_j$ will, in general, be correlated, the extent of which is dependent on the the distance between the pair of points. Mathematically, this would be equivalent to saying that the covariance matrix of Z is given by;

$$Cov\left[Z(\mathbf{x}_i), Z(\mathbf{x}_j)\right] = \sigma^2 \mathbf{R}\left(R(\mathbf{x}_i, \mathbf{x}_j)\right) \tag{8.4.16}$$

where the correlation matrix $\mathbf{R}$, is a function of the correlation function R. This function is user-defined, but as the covariances are expected to depend on inter-point distances, a common form is given by

$$R(\mathbf{x}_i, \mathbf{x}_j) = exp\left[\sum_{h=1}^{N} \theta_h \left\| x_h^i - x_h^j \right\|^{\alpha_h}\right] \tag{8.4.17}$$

In the above expression, the correlation function is similar to a Euclidean norm, with θ_h and α_h being unknown correlation parameters used to fit the data. $\mathbf{x}_h^i$ is the h-th component of sample point $\mathbf{x}^i$. This representation is able to account for different degrees of non-linearity and smoothness through the parameters. Larger values for θ_h mean that correlations to the point $\mathbf{x}_h$ are larger, and thus function variations in the vicinity of $\mathbf{x}_h$ will also have steeper gradients. Function smoothness is controlled by the exponent with $\alpha_h = 2$, a for smooth variations, which then diminishes with decreasing α.

In the Kriging framework, it is actually common place to remove the regression model entirely, and to replace it with a simple sample average of the stochastic process, μ. The response of the system is then $y = \mu + Z(\mathbf{x})$. Once a number of observations have been made, parameters μ, σ,θ_h and α_h are estimated by maximising the likelihood of the observed sample [162]. Once specified, the predicted function is given by;

$$y(\mathbf{x}) = \mu_0 + \mathbf{r}^T \mathbf{R}_0^{-1} (\mathbf{y} - \mu_0) \tag{8.4.18}$$

where μ_0, $\mathbf{R}_0$ are determined by the maximum likelihood estimate, $\mathbf{y}$ is the vector of observed objective function values, and

$$\mathbf{r}(\mathbf{x})^T = \left[R(\mathbf{x}, \mathbf{x}^1), R(\mathbf{x}, \mathbf{x}^2), \cdots R(\mathbf{x}, \mathbf{x}^N)\right] \tag{8.4.19}$$

Equation [8.4.18] maximises the likelihood that the prediction made at a given point and

the observation made at the sample points were obtained by the same model. It can therefore be demonstrated that the approximation interpolates through the sample observations. Specific details relating to the manner in which the parameters are determined can be found within [162].

There have been several studies investigating the capability of Kriging models. Chung and Alonso conducted a project regarding aerodynamic optimisation of a supersonic business jet at cruise condition [30]. The study consisted of tests involving 7 and 14 design variables, and were able to conclude that the performance of Kriging models is strongly influenced by the location and number of sample points. There was a small difference in model accuracy compared to linear regression models, but Kriging models were also found to be more expensive due to the time required to perform the extra step of determining the parameters. Simpson et al also draw attention to the complexity involved in obtaining the parameters [147],[149]. Here Simpson performed a multi-disciplinary optimisation study on an spike nozzle, using both computational fluid dynamics and finite element methods for the structure. He illustrated little difference in model accuracy in comparison to a low order polynomial regression model.

An alternative approach for developing an analytic expression for the objective function is to make use of radial basis functions . These are multi-dimensional interpolating functions, which, unlike linear regression models, do not assume any particular form. The idea was originally proposed in a work by Hardy [66], used to approximate geographical surfaces. Subsequently, they have been used to represent surface data, and have also found applications in the solutions to partial differential equations. In the context of multi-disciplinary optimisation, they have relatively recently gained attention for the development of surrogate meta models. Hussain et al [74] made direct comparisons of radial basis functions to polynomial regression models and were able to illustrate their predictive advantages in reproducing several analytical test functions. Simpson et al also review some of the meta modelling procedures available, alongside a survey of some of the experimental design methodologies [149]. There are typically two forms, normalised and unnormalised, which can be expressed as the superposition of linear models. The unnormalised radial basis function is given by;

$$\hat{\mathbf{y}}(x) = \sum_{i=1}^{N} a_i \rho(\|\mathbf{x} - \mathbf{c}_i\|) \tag{8.4.20}$$

Normalised radial basis functions are similar to this form, but are given by;

$$\hat{\mathbf{y}}(x) = \sum_{i=1}^{N} a_i \phi(\|\mathbf{x} - \mathbf{c}_i\|) \tag{8.4.21}$$

where

$$\phi(\|\mathbf{x}-\mathbf{c}_i\|)=\frac{\rho(\|\mathbf{x}-\mathbf{c}_i\|)}{\sum_{i=1}^{N}\rho(\|\mathbf{x}-\mathbf{c}_i\|)} \tag{8.4.22}$$

which are designed to non-dimensionalise the domains so that each design variable onto shares the same scale.

Here, $\hat{y}$ is the surrogate form for the true response. In the above expression, N is assumed to be the number of pieces of sample data, with $\rho(\cdot)$, a radial basis function defined for each sample point. The function is dependent on the distance between a sample point input vector $\mathbf{x}$ and a basis function centre $\mathbf{c}_i$, $i = 1, \cdots, N$, and a_i are weights to be determined by the data. The radial basis functions can take various forms, and is user dependent, commonly reflecting the nature of the underlying data distribution. Some of the commonly used forms include the Gaussian distribution;

$$\rho(\|\mathbf{x}-\mathbf{c}_i\|)=e^{-\beta\|\mathbf{x}-\mathbf{c}_i\|^2} \tag{8.4.23}$$

which have the property that data in the vicinity of $\mathbf{c}_i$ have influence on the function over a particular region. Cubic splines take the form;

$$\rho(\|\mathbf{x}-\mathbf{c}_i\|)=\|\mathbf{x}-\mathbf{c}_i\|^3 \tag{8.4.24}$$

the two dimensional analogy of cubic splines known as thin plate splines;

$$\rho(\|\mathbf{x}-\mathbf{c}_i\|)=\|\mathbf{x}-\mathbf{c}_i\|^2\, log(\|\mathbf{x}-\mathbf{c}_i\|) \tag{8.4.25}$$

and multiquadratics are given by;

$$\rho(\|\mathbf{x}-\mathbf{c}_i\|)=\left(\|\mathbf{x}-\mathbf{c}_i\|^2+h\right)^{\xi} \tag{8.4.26}$$

In contrast to Gaussian radial basis functions, these multiquadratics have the property that all data points have influence on the form of the function at all other locations. In particular, they have been used to construct multivariate response surfaces for several multidisciplinary optimisation problems [75],[102].In the above expressions $\mathbf{c}_i$, a_i, β and h are chosen to optimise the agreement between $\hat{y}$ and the sample data. Optimisation being usually performed over some function of the error between the sample objective function value, and that predicted by the meta model.

Given a set of data points $(\mathbf{x}_i, y_i)$, the coefficients a_i are determined through the solution of a system of linear equations.

$$\mathbf{M}\cdot\mathbf{a}=\mathbf{b} \tag{8.4.27}$$

where $\mathbf{M}_{i,j} = \rho_j(\mathbf{x}_i)$, and $\mathbf{b}_i = \mathbf{y}_i$, the vector of observed objective functions.

The remaining parameters such as β and h in the Gaussian and multiquadratic radial basis functions , are determined by optimising a suitable objective function, commonly a least squares function of the difference between the observed and predicted objective functions.

$$K(\mathbf{w}) = \sum_{t=1}^{\infty} [y(t) - \hat{y}(\mathbf{x}(t), \mathbf{w})]^2 \tag{8.4.28}$$

In this expression w denotes the set of parameters or 'weights' over which optimisation is performed. and the index denoted by t is an index spanning over the observed data sets. Note that optimisation of the above is explicitly dependent on the vector of weights. Finding the optimal choice of parameters is an area that has acquired considerable interest, and remains one of the main challenges posed in trying to obtain better representations of sample data [163],[109]

Function smoothness may also be introduced into the above as another optimisation function. The weights that optimise the objective function are determined through a learning procedure. There are several procedures available in finding these weights, one common approach being based on gradient descent. For every iterative time step, the weights are adjusted in a direction opposite to the gradient of the objective function. For the unnormalised case, the weight learning algorithm is given by;

$$a_i(t+1) = a_i(t) + \nu [y(t) - \hat{y}(\mathbf{x}(t), \mathbf{w})] \rho(\|\mathbf{x}(t) - \mathbf{c}_i\|) \tag{8.4.29}$$

and for the normalised radial basis function ;

$$a_i(t+1) = a_i(t) + \nu [y(t) - \hat{y}(\mathbf{x}(t), \mathbf{w})] \phi(\|\mathbf{x}(t) - \mathbf{c}_i\|) \tag{8.4.30}$$

In the above expressions ν is a 'learning rate' parameter, which serves to control the influence of previous data points to new data points added to the data set. The basis function centres $\mathbf{c}_i$ are chosen to be the sample data points used to generate the observed objective function evaluations.

The key feature of radial basis functions is that the function generated actually interpolates through all observed function points, unlike the linear regression model, which can be beneficial when dealing with cases where one can determine for certain that the observations are indeed the true response. This property can be advantageous for computational tests involving deterministic results, but in circumstances where this is not the case, caution needs to be exercised as an inaccurate point may easily give rise to a function that mispredicts the real underlying trend of the physical variable. In contrast, as linear regression attempts to provide a 'best fit' curve through the sample points, this problem

is not as evident within the generation of the response surface, but there is more emphasis on identifying suitable sample point data to explore the design space sufficiently. Additionally, one of the main disadvantages of of radial basis functions is that the designer has little control over the final form of the surrogate model. Even after parameter optimisation, the function may can present spurious local maxima and minima that do not represent the true variation [109]. This point is of crucial importance when applying gradient based optimisation techniques, as the resultant optimum may be a function of the surrogate model, rather than being representative of the true point.

8.5 Response Surface Validation

In order to assess the capability of the sampling, least squares fitting, and optimization procedures outlined in the previous sections, a series of tests are presented in this section highlighting the effectiveness of the methods proposed. The section therefore provides the confidence in the routines that will be relied upon in subsequent sections of the thesis.

8.5.1 Polynomial Surface

Given that the response surface model to be used in representing an objective function is a second order polynomial with respect to the sample variables, it is reasonable to assume that the model is capable of predicting exactly the minima of functions that are multi-dimensional second order polynomials.

Although the test is basic in the sense that one may obtain the optimum of a multi-dimensional polynomial through analytical, closed form methods, it is for this reason a good test, not only of the response surface generation procedure, but also of the sampling procedure. The test described herein therefore also assesses whether the sample distribution is adequate in representing the polynomial surface.

The second order polynomial to be investigated is given by the following function;

$$f(x,y) = x^2 + 9y^2 + 3xy - 2x - 15y + 7.25 \tag{8.5.1}$$

For any function $f(x,y)$, its optimal point can be shown to satisfy;

$$\begin{aligned} \frac{\partial f}{\partial x}_{(x_0,y_0)} &= 0 \\ \frac{\partial f}{\partial y}_{(x_0,y_0)} &= 0 \end{aligned} \tag{8.5.2}$$

where (x_0, y_0) is the optimal point. For the function [8.5.1], it is easily shown that;

$$\begin{aligned} \frac{\partial f}{\partial x} &= 2x + 3y - 2 \\ \frac{\partial f}{\partial y} &= 18y + 3x - 15 \end{aligned} \tag{8.5.3}$$

and equating these to zero under the condition above gives two simultaneous equations in two unknowns, easily solved to give an optimum of $(x_0, y_0) = (-1/3, 8/9)$, which is easily checked that the condition on the second order discriminant, $f_{xx}f_{yy} - f_{xy} > 0$ at this point and that $f_{xx}(x_0, y_0) > 0$, are satisfied, and therefore the point is a minimum. As a check of the optimization procedures, the following test was performed. A domain encompassing this minimum was chosen, over which a set of sample points were generated using the latin hypercube technique. For each sample point the objective function was computed using the above polynomial form, and using this data set, the response surface was created. The surrogate model created is a response surface with the following expression;

$$\begin{aligned} f_{RS}(x,y) &= 1.000000000011561x^2 + 8.999999999117479y^2 \\ &+ 3.000000000022974xy - 2.000000000012497x \\ &- 14.999999999859561y + 7.249999999436562 \end{aligned} \tag{8.5.4}$$

which is similar to the analytic function [8.5.1]. The coefficients are identical to the original analytic function up to an accuracy of 10^{-8}, which is to be expected as all numerical computations have finite precision. Passing this function into the sequential quadratic programming routine returns a minimum at $(x, y) = (-0.333333, 0.888889)$, which is the same as that predicted by the analytical method described above. Thus the sampling procedure, the surrogate model generation function based on least squares regression, and the sequential quadratic programming routines all collectively ensure that they are able to return the analytic optimal value to within machine precision, for a function that should be reproduced exactly by the response surface. For more complicated functions not exhibiting behaviour that is exactly quadratic one would expect a certain degree of deviation of the response surface model from the true objective function, but as the objective function here is a second order polynomial, one would expect the approximation provided by the surface to be an exact one, which it is.

8.5.2 Power Law Body

The initial test provided a means of validating the optimization procedures on a purely mathematical basis, as it did not require the use of an analysis tool. The following section is a more practical study, in that it involves use of the IMPNS code. The geometries to be examined are a series of bodies of revolution, termed "power law bodies" so called due to the manner in which they are generated. The objective is to determine the body of revolution that minimises the drag coefficient.

There has been a considerable amount of interest in minimum drag geometries, spurred on primarily due to their applications in the design of high speed missiles. Adams for example was able to generate three different families of geometries, which minimised wave drag under three different sets of restrictions [2]. He generated bodies of revolution minimising wave drag, given (I) fixed length, base area and contour passing through a fixed point between nose and tail, (II) fixed length, base area and maximum area, and (III) fixed length, base area and body volume. Harris and Landrum experimentally investigate drag coefficient values for a series of low drag bodies of revolution, for Mach numbers in the range [0.6, 4.0] [67]. They consider Haack-Adams bodies, which are optimal configurations based on wave drag minimisation for bodies of fixed length, volume and base area, and compare drag coefficient values to their theoretical predictions. They conclude that the theoretical wave drag values are overestimated as the Mach number is increased, despite the good agreement near $M_\infty = 1.0$. This observation is explained by the fact that the theoretical minimum is obtained using slender body theory which requires a large body fineness ratio $r = \textit{length/diameter}$, compared to $\sqrt{M_\infty^2 - 1}$. For larger Mach numbers, r needs to be a lot larger for the condition to be satisfied, thus accounting for the discrepancy between theory and experimental data.

Prior to the widespread use of computational fluid mechanics, such theoretical axisymmetric bodies were generated based on such assumptions of slender body theory, linearised theory, Newtonian theory, Newtonian-Busemann and hypersonic small disturbance theory. A common technique was to employ calculus of variations that would generate optimum body profiles. A concise treatise on the subject is provided in the collection of works by Miele [104].

The simplifying assumptions used to determine such minimum drag axisymmetric bodies may render them out of date given that there are more advanced computational techniques available that area able to find optimal bodies that are also able to take into account more complex geometries. Nevertheless, because of the fact that their respective optimal configurations may be determined analytically, they remain a particularly valuable tool in validating both analysis tools, and the optimisation procedures used for wider design studies. Cheung et al [28] for example verify their parabolized Navier Stokes

solver and gradient based optimisation procedure, by trying to find the optimal Sears-Haack geometry. The sample variables are chosen to be design parameters that govern the shape of the body of revolution, and optimization is performed using the PNS solvers' prediction for the drag coefficient as the objective function. Mason and Lee make use of the power law body to validate their own code [100], and for the examination of their inverse design methodology, whereby pressure distributions are specified, for which a geometry satisfying the distribution is obtained [87].

In analogy to the verification procedures used in some of the above studies, this section makes use of the known optimal geometry to validate the analysis tool, the PNS code, and the response surface optimization routines. The body of revolution under investigation is chosen to be the power law body, owing to its relatively simple procedure in obtaining grids. As its name suggests, the power law body is generated by assuming that the radius of the body is proportional to the axial station value, raised to some power n. That is

$$r \propto x^n \tag{8.5.5}$$

where r is the body radius, x the streamwise location and n the power. The power law body is determined by some optimal value for n, such that the axisymmetric body of revolution generated by the above relationship has a minimal wave drag compared to all other possible values for n. The effect on the body profile for several values of n is shown in figure [43].

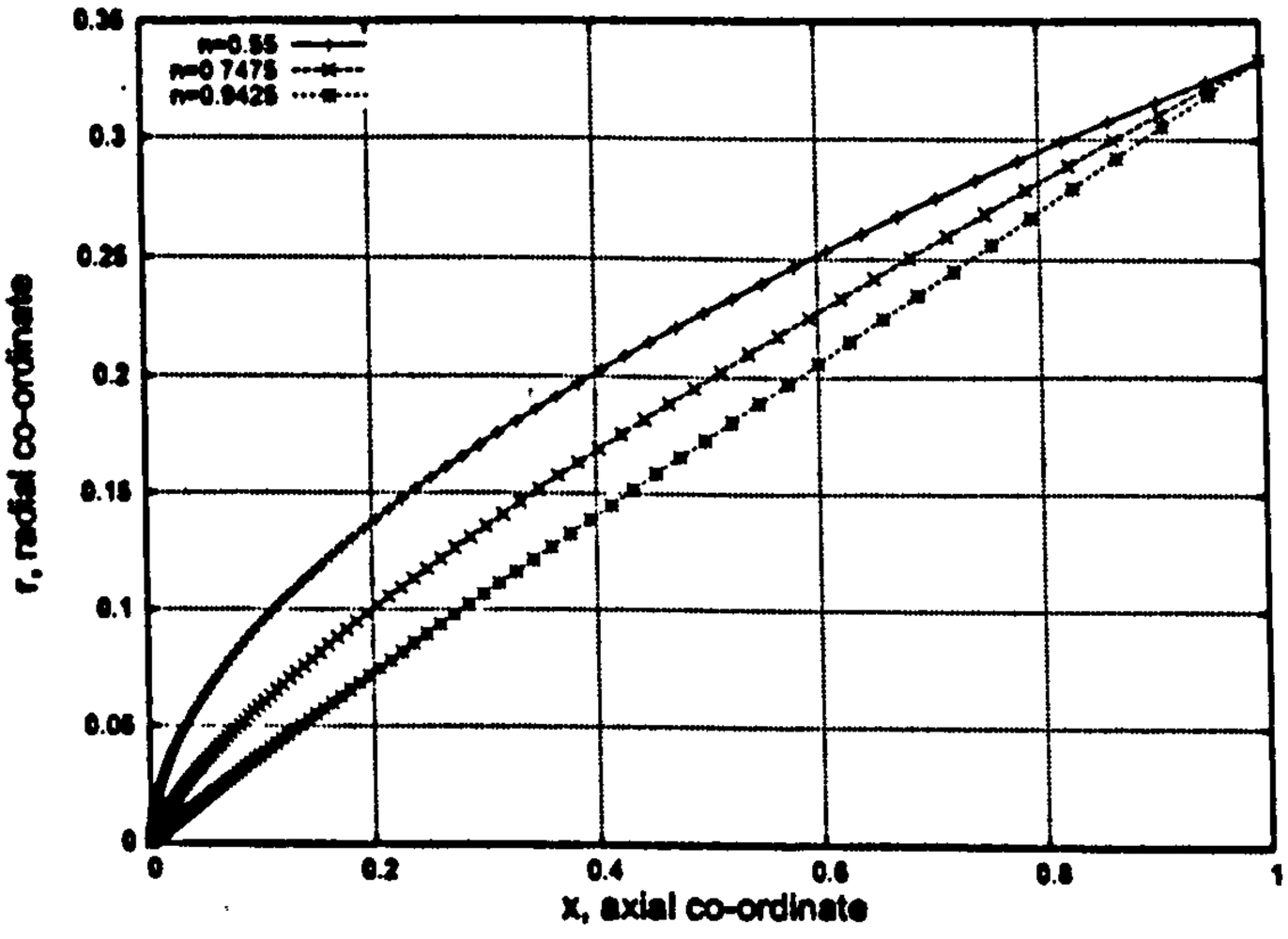

Figure 43: Power Law Body profiles

It is evident that for values of n that are close to unity, the cross-sectional profile

of the body resembles a cone-like geometry, whilst as the value of n is reduced, the body becomes more blunted at the leading edge. Thus for sufficiently small values of n, we expect eventually that the conical shock will be detached from the nose of the body.

The results of Eggers et al indicate that under a Newtonian assumption, equivalent to taking the incident Mach number to infinity, the optimal value for n is 0.75 [51]. Under a Newtonian-Busemann slender body assumption however, which also takes into account that the conical shock may be detached off the nose of the geometry, Cole was able to show that the optimum actually occurs for $n = 0.66$ [31].

A typical power law geometry grid used for the study is illustrated in figure [44]. For convenience the streamwise station is varied from $x = 0$ at the nose, to $x = 1$ at its base. As explained above, the radius is given by the above rule, for some chosen value for n. This exponent is taken to lie in the range [0.6,1.0], where the case $r = 1.0$ corresponds to a cone body. For values of n less than the above, the tip of the body becomes more blunted, which subsequently yields higher drag values, as the subsequent results will show.

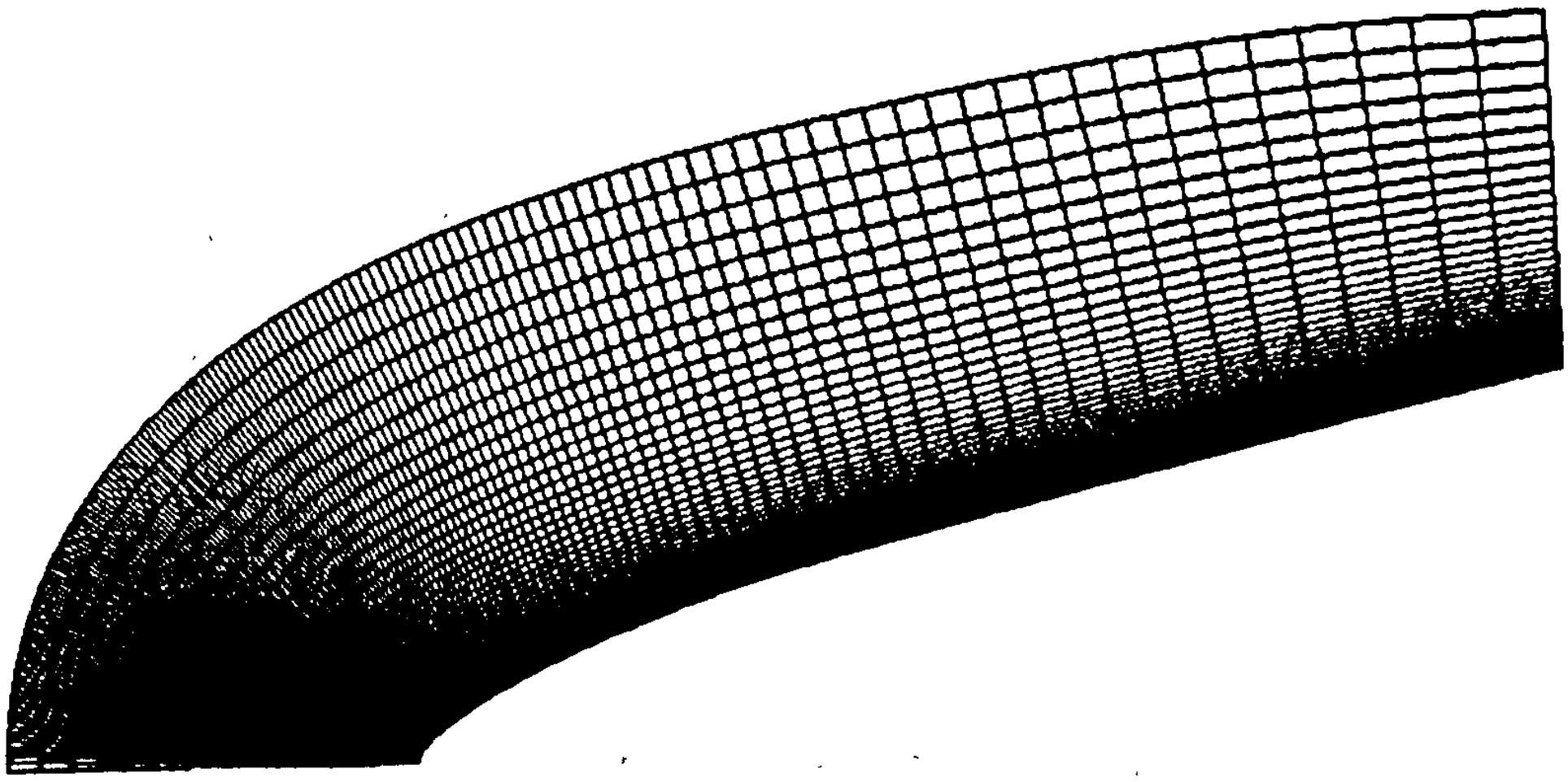

Figure 44: Power Law Grid, for n=0.6575

In order to assume grid independence of the predicted drag coefficient, the solution for three different grids were computed for the value of $n = 0.65$. Strictly speaking, it is necessary to perform the same analysis on all grids, but due to time constraints, only the geometry with a blunted profile was chosen for this. The table of drag coefficients shown in [8.5.2] indicate that a grid of 150×150 grid points is sufficiently fine, as the difference in objective function values between the this and the finest grid is on the order of 10^{-4}%. On this grid therefore, an iterative examination determined that a convergence criterion of 10^{-6} is sufficiently small enough to show that the objective function is iteratively

converged.

Con. Tolerance	Cd	Grid Level	Cd
10^{-6}	0.0760373	100×100	0.0756160
10^{-7}	0.0760364	150×150	0.0760373
10^{-8}	0.0760364	200×200	0.0760372

Table 5: Iterative and Grid Convergence for Power Law Body, n=0.65

In this investigation, the only design variable is the exponent n, and as such it does not make sense to generate a hypercube for the sampling procedure. Instead, twenty equally spaced design points have been chosen over the interval [0.6,1.0], their grids generated using an automatic scripting routine, and run using the IMPNS code as the analysis tool, under inviscid conditions at Mach numbers of 3.0,4.0 and 5.0.

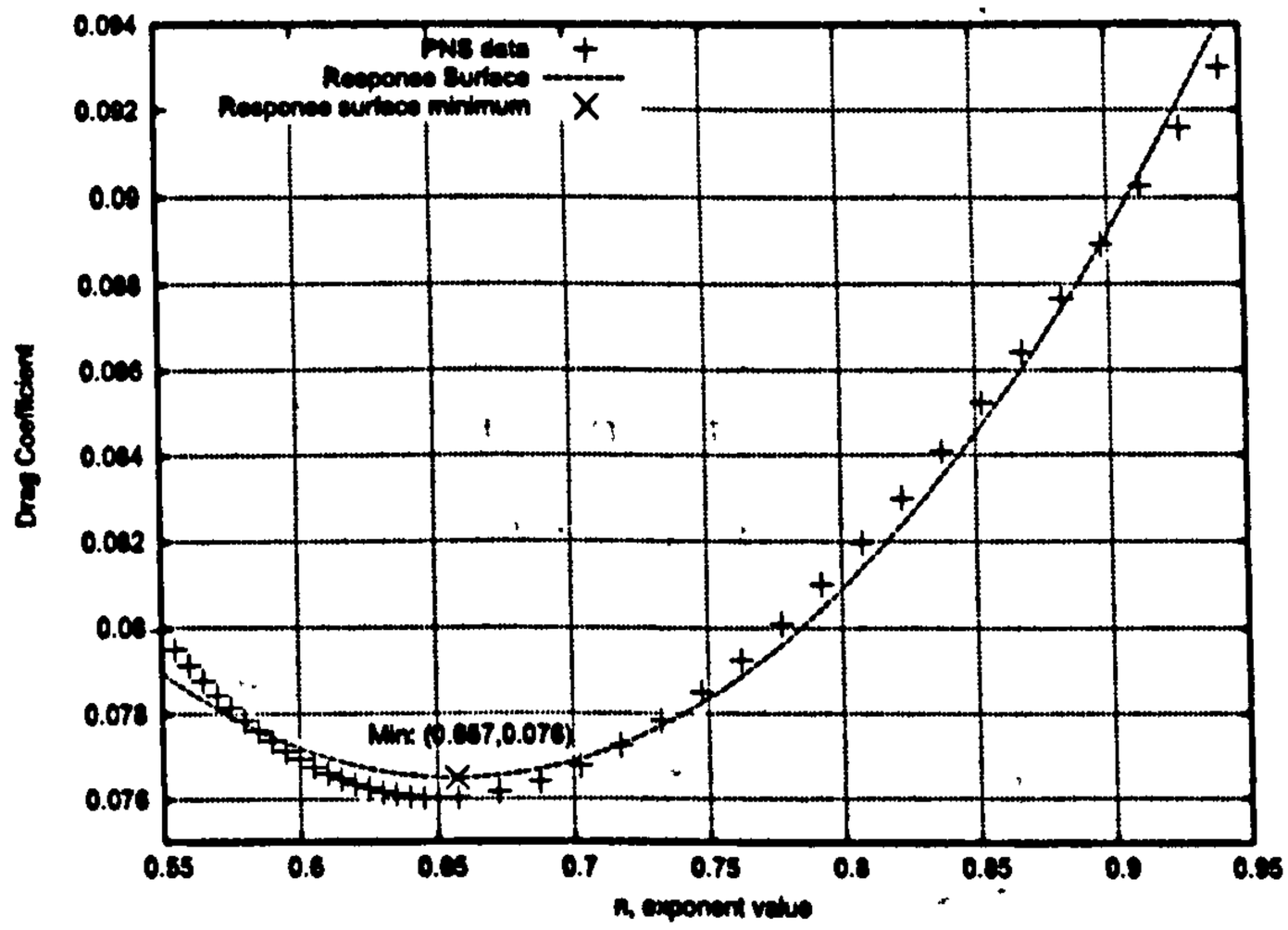

Figure 45: PNS and Response Surface predictions of Drag Coefficient, $M_\infty = 5.0$

Figure [45] shows the objective function values for the Mach 5.0 simulations, for each sample point, suggesting a minimum close to that predicted by Cole [31] . Superimposed onto this graph however is the least squares fit, response surface representation of the data, given by the polynomial;

$$C_D \approx 0.21519n^2 - 0.28281n + 0.16942 \qquad (8.5.6)$$

Sequential quadratic programming on this surrogate model predicts a minimum drag value of $C_D = 0.0764988$, obtained for a value of $n = 0.657101$, which is in good agreement with the result obtained by Newtonian-Busemann slender body theory. Given

that this theory predicts $n = 0.66$ [100], this is a discrepancy of approximately 0.44%. However, the discrepancy is greater when compared to the pure Newtonian theory of Eggers et al [51]. This is because the IMPNS calculations take into account that for the smaller values of n, the shock may become detached. Multisweep is employed in the fore-body region for all calculations in the event of such detachment, but the work of Eggers et al does not take into account such a possibility. Cole's work however acknowledges this as a possibility, and thus the better agreement.

M_∞	Optimum n	$C_D(l/d)^2$
3.0	0.632469	0.388281
4.0	0.650329	0.361318
5.0	0.657101	0.344245

Table 6: Effect of Mach number on Optimum Parameter

For the $M_\infty = 3.0$ and 4.0 calculations, similar response surfaces to figure [45] are also obtained, but with different values for the optimum parameter n, and drag coefficient values. This data is tabulated in [6], and illustrates the effect of increasing Mach number. One will notice in figure [45] that the parabolized Navier Stokes solution seems to under predict the drag coefficient value, compared to the analytical result, and that the response surface approximation seems better. Recall the comment earlier from Keane and Nair [80] indicating that better data representation can be achieved if one takes a smaller domain of interest. As subsequent studies will demonstrate, this is indeed the case, and one can infer that if a smaller region encompassing the observed minimum is used as a sample domain, the data will closely model the parabolized Navier Stokes form. The Newtonian-Busemann slender body theory used by Cole to arrive at his value of $n = 0.66$ as the optimum parameter value, is also based on the assumption that the Mach number is large. The table above shows that as the Mach number is increased, the shape parameter does indeed approach Cole's optimum value, consistent with the assumption employed. Cole predicts $C_D(l/d)^2 = 0.334$, and the values above also approach this value with increasing Mach number, although the relative error is some what greater. For the $M_\infty = 5.0$ case for example, this gives an error of approximately 3.1%.

This discrepancy in the value $C_D(l/d)^2$ computed from the parabolized Navier Stokes simulations may be attributed to the fact that the current case requires two types of grids. The problem with this body is that two different grid topologies need to be used, depending on whether the shock is attached or detached. Theory dictates that for values of n less than the optimum, the shock will become detached as the body becomes more blunt, and attached for values of n larger than the optimum. In the present case however,

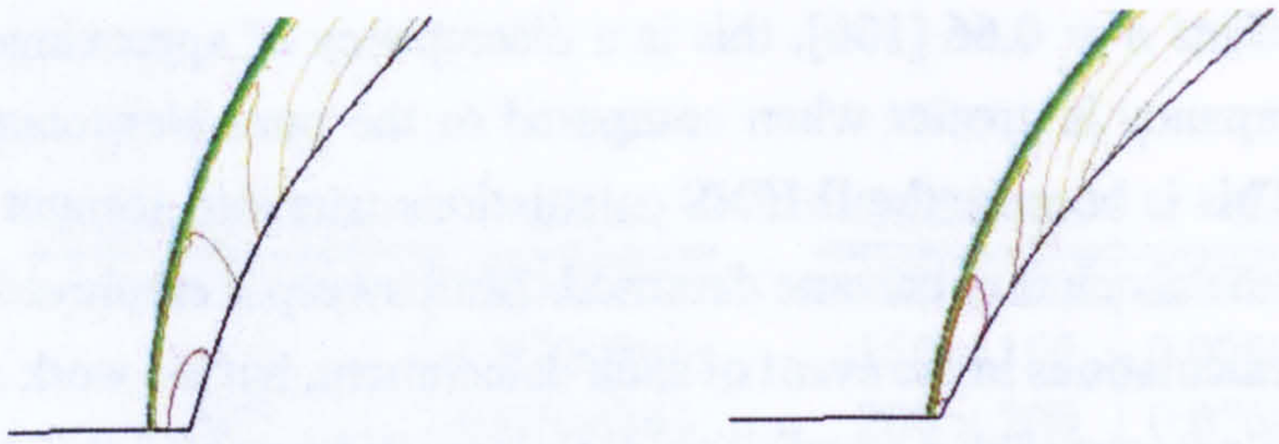

Figure 46: Shock Standoff for n=0.625, and n=0.7025

a grid allowing for a detached shock was generated for all n, as it was not possible to adapt the topology accordingly, within the confines of the automatic scripting procedures. Indeed in reality one would need to know whether the shock is attached or detached at the grid generation stage, which is not possible for the general case where the optimum would be unknown. Because of this, for attached calculations, the conical shock generated is not aligned with the cells normal the body, and as such a certain degree of accuracy may be lost. In fact, as the figures in [46] show, the shock is markedly detached for $n = 0.625$, a value for the exponent less than the optimal predicted. For $n = 0.7025$ however, which would correspond to an attached situation, one would expect a conical shock to emanate from the nose, but due to the topology there still remains a detached region, albeit small. Since two possible topologies are needed, automating the grid generation procedure to accommodate both types is difficult, as before the calculation is made, there is no information to indicate detachment or otherwise. Because of this inaccuracy, the predicted drag coefficient values for calculations that should involve attached shocks may be inaccurate. A remedy might be to rerun these calculations on a more suitable topology, one where there is no region upstream of the nose of the body. Nevertheless both the IMPNS code, and the surrogate model predict an optimum that is in good agreement with Cole's analytical result, that places confidence both in the analysis tool, and in the procedures used to generate and predict optimal values.

CHAPTER 9

SHyFE Optimisation Study

The following section investigates the potential for using magneto-hydrodynamics as a flow control mechanism for a supersonic ramjet intake. A test case having practical interest has been identified, and numerically investigated using the IMPNS code to determine the main governing characteristics of the intake, along with the design operating conditions. An optimization study making use of the low magnetic Reynolds number model validated in section [6], and the numerical optimization framework built in section [8] provide the backbone of the study, having initially determined the fundamental factors governing this engineering problem.

9.1 Introduction

The Sustained Hypersonic Flight Experiment (SHyFE) is a programme funded by the UK Ministry of Defence, aimed at developing the engineering tools for designing and building a hypersonic cruise vehicle. The objective of the study is to flight demonstrate a low cost ramjet powered vehicle, operating at Mach 6. After release from a rocket booster, the SHyFE vehicle will accelerate to Mach 6, at which point it will cruise for distances of approximately 200km. The targets of the programme were aimed at providing a significant technical challenge, including low cost, restrictions on vehicle size, avoidance of variable geometry methodologies, and low operating Reynolds numbers.

Due to the integrated nature of hypersonic vehicles as a whole, independent component development was unlikely to generate a viable vehicle. Thus, a collaborative study involving Qinetiq, Oxford University, Cranfield University, Imperial College, CGC Technology, MT Aerospace and TNO Defence has been undertaken over the past couple of years, investigating pertinent factors governing the design of a hypersonic cruise vehicle, such as intake aerodynamics and combustion mechanisms within the vehicle. Boon and Hillier [17] have examined inviscid and viscous interactions of the ramjet intake, by examining the flow characteristics in the presence and absence of the cowl. By running the calculations at an incidence angle of 5°, they are also able to show that viscous interactions are one of the main causes of inlet unstart. Goodman and Ireland make use of a set of thermal models to assess the surface temperatures and heat transfer within the combustion chamber internally, within the Mach 4-6 range [61]. Attention is also paid to

making use of thermal models in the design of experimental cooling mechanisms. The current status of the project, along with an overview of the milestones to date is presented in a paper by Dadd et al [38].

9.2 Intake Aerodynamics

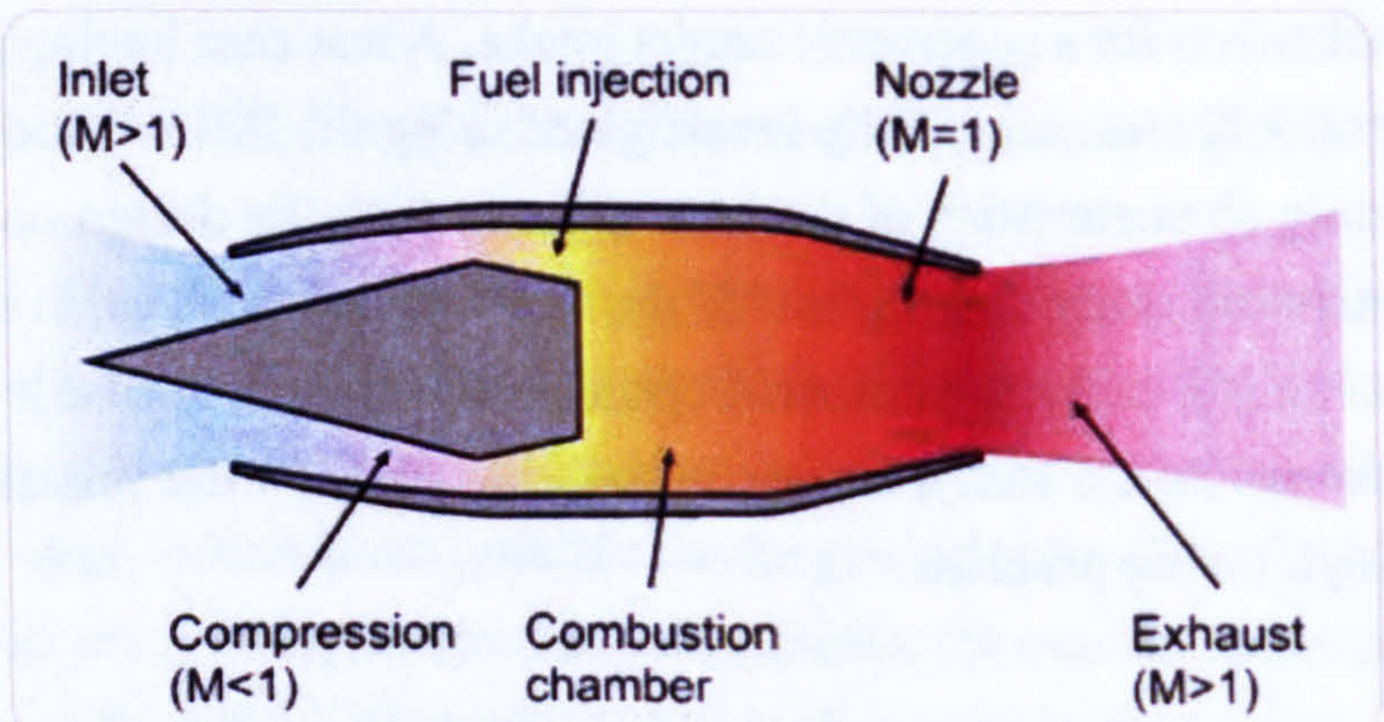

Figure 47: Ramjet Schematic

A simple schematic for a ramjet propelled system is shown in figure [47], which in its simplest form consists of an inlet, a fuel injector, combustion chamber and nozzle. The unit is designed to be operable at supersonic flows, and this alleviates the requirement for a unit responsible for compression, or a turbine. The propulsive efficiency of a ramjet engine is heavily dependent on the flow "quality" into the engine intake, and has thus the design of the intake has received considerable interest.

Figure [48] illustrates one such axisymmetric SHyFE inlet. A series of intakes have been manufactured for testing, including making use of boundary layer trips to improve the low Reynolds number performance [23]. However, in the presence of trips, the boundary layer was still shown to separate, and thus alternative designs have been considered. The main physical features of the intake are also displayed in figure [48].

The blunted conical nose section at the front of the body gives rise to a detached conical shock. Behind this, the intake ramp is designed such that the flow compresses isentropically, focusing downstream to form a triple point. At the junction with the cowl, an oblique shock emanates from the leading edge of the cowl lip, impinging onto the centre body, aft of the shoulder. The shoulder is designed in such a way that the produced expansion wave stabilises the interactions between the internal boundary layer, and the cowl shock. It is also designed with the step like profile to ensure boundary layer separation does not propagate forward into the isentropic compression region, as this is a major cause for intake unstart.

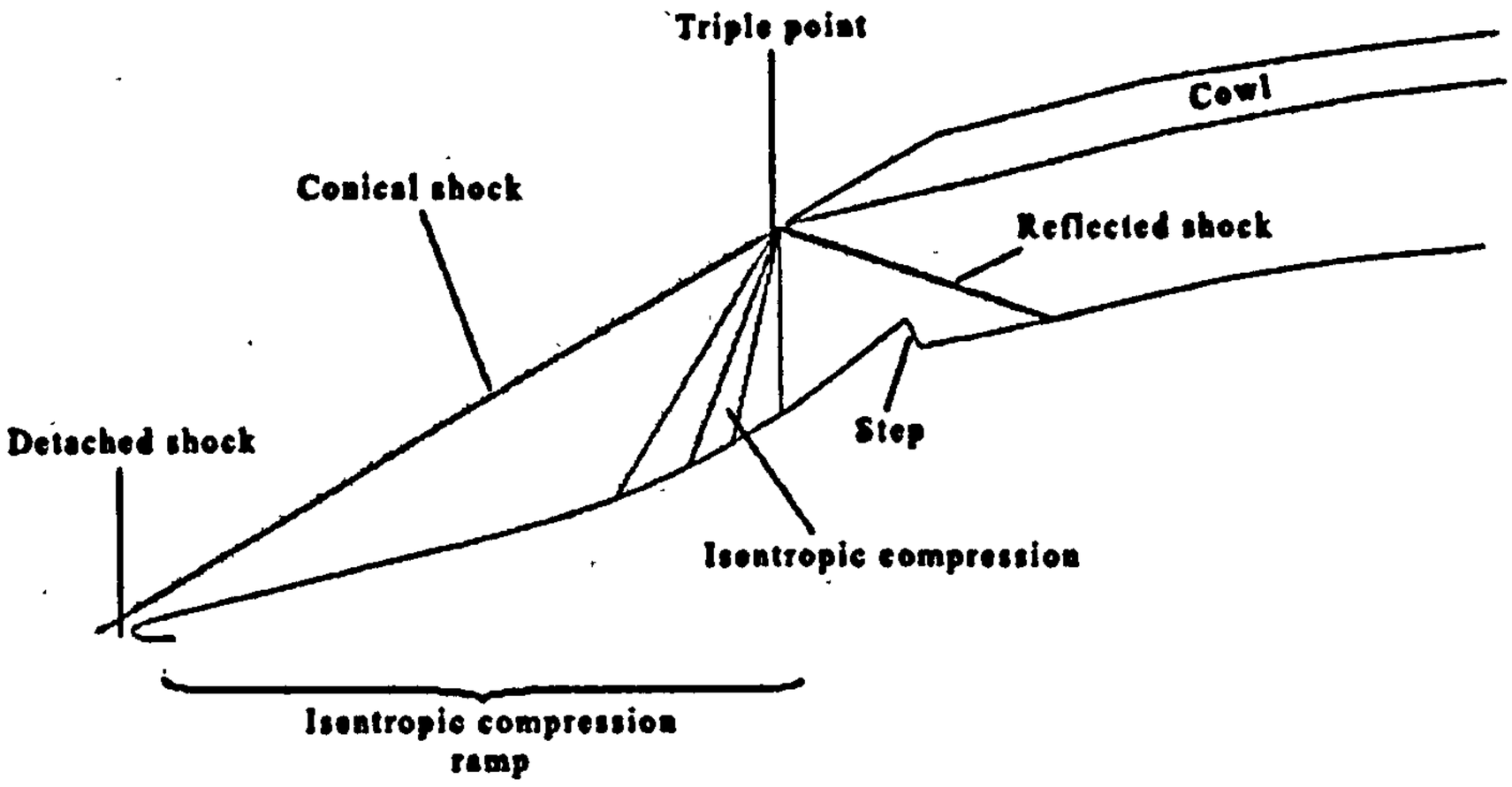

Figure 48: Physical features of the SHyFE intake flowfield

The intake configuration achieved thus far, has been designed to operate at a specific Mach number. The cowl position, and the isentropic compression ramp profile are designed to ensure that the triple point, where conical shock and compression waves meet, coincides at the lip of the cowl. This ensures maximum mass flow capture is achieved with spillage kept to a minimum. This is coined the "shock on lip" condition, and is associated with a design Mach number, M_{∞_d}, which for the current case is 6.

As the geometry is fixed, the conical shock and the compression waves will change position for $M_\infty \neq M_{\infty_d}$. A similar situation may occur when the flow into the intake is not axisymmetric, for example when the body is operating at incidence. When the operating Mach number is less than the design value, the triple point will move upstream, and cease to interact with the cowl lip. The result is a decrease in the propulsive efficiency of the intake, as a proportion of the compressed mass from behind the conical shock is allowed to flow over the cowl and not through the intake. Alternatively, if the converse is true, that is, the operating Mach number exceeds the design Mach number, then the triple point occurs closer to the compression surface, and the focused shock front, which would otherwise reflect from the cowl lip at design conditions, is directed towards the underside of the cowl surface, by the expansion wave generated by the cowl lip. This type of interaction can lead to a Mach reflection, which may propagate upstream to form a detached shock in front of the cowl, and lead to unstart, where flow within the inlet actually reverses direction out of the intake area.

Clearly these off design conditions pose significant challenges to the vehicle designers, as it imposes bounds on the operating regions of the body. The vehicle has in fact been designed to start at an operating Mach number of 4, and has shown to produce

thrust at such conditions, albeit less than that for M_{∞_d}. Calculations from Imperial College estimate 73.6% mass capture at Mach 4. Intake unstart at Mach numbers larger than the design M_{∞_d}, or when the body is operating at incidence is still a cause for concern that needs to be addressed. Within scramjet intake design, due to the fixed geometry considerations, the application of magneto-hydrodynamics has gained attractiveness [83], due to the high actuation speeds compared to mechanical devices. A similar idea can be applied in these circumstances.

For an over-sped inlet operating at $M_\infty > M_{\infty_d}$, one proposed method is to generate a Lorentz force acting in opposition to the oncoming flow direction, thereby decelerating the flow to achieve shock on lip. A suitably orientated magnetic field would enable higher mass flow rates through the intake, thereby improving engine performance. The potential of this technique applied to fixed geometry hypersonic inlets is a subject that has been investigated numerically by several groups [83], for specific operating conditions. As an extension of this work, the remainder of this section seeks to identify the optimum configurations necessary for a magnetic field, given a set of flow conditions. The ultimate aim of the flow control device is to ensure the vehicle is operating back at design conditions, thus improving engine performance.

9.3 Preliminary Study & Geometry Simplification

The geometry of interest is a two dimensional axi-symmetric configuration of the SHyFE ramjet intake, provided by Qinetiq. A sample illustration of the geometry, and the resultant grid, is shown in figure [49], with particular attention drawn to vicinity of the cowl lip and intake geometry. The grid employs clustering on all boundaries, and particularly in the region of the cowl. In the left diagram, every third grid line has been removed for clarity. The grid is required to be fine in this region as it is rich in complex features such as detached shocks, and recirculation regions.

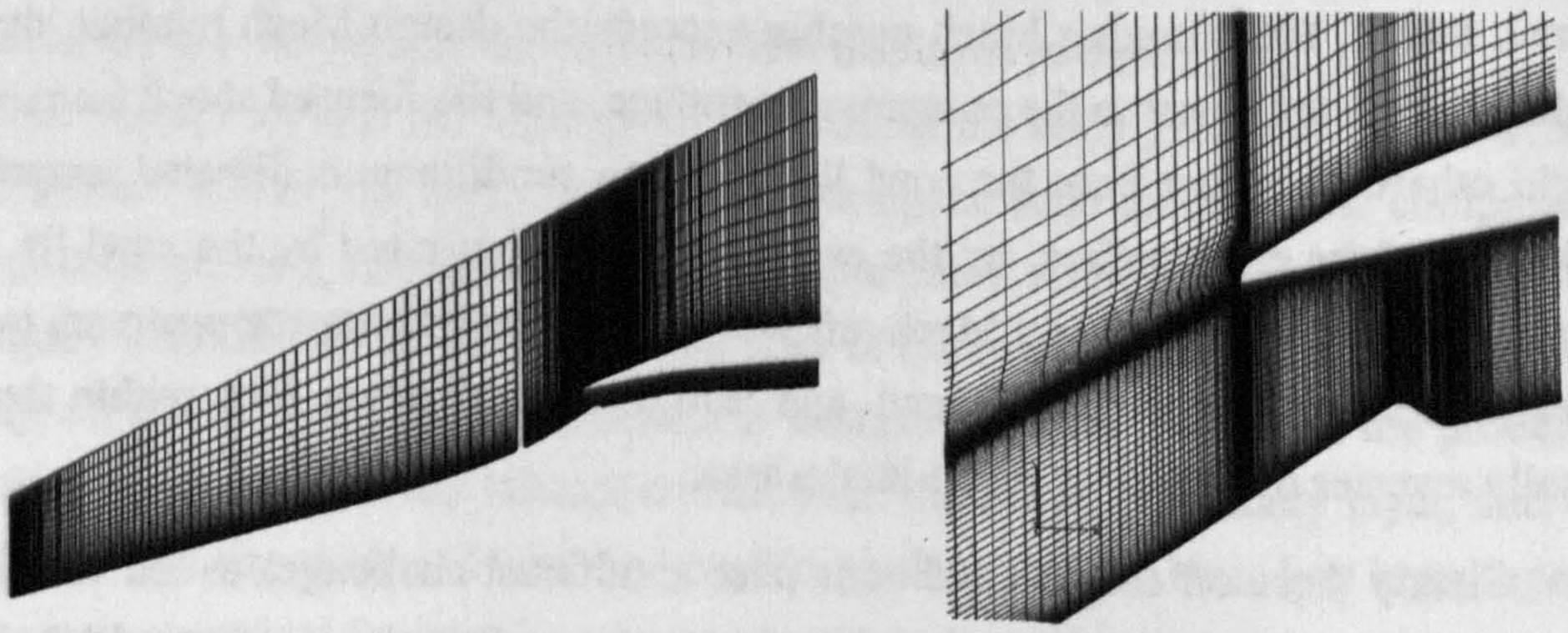

Figure 49: SHyFE grid, and vicinity of the cowl

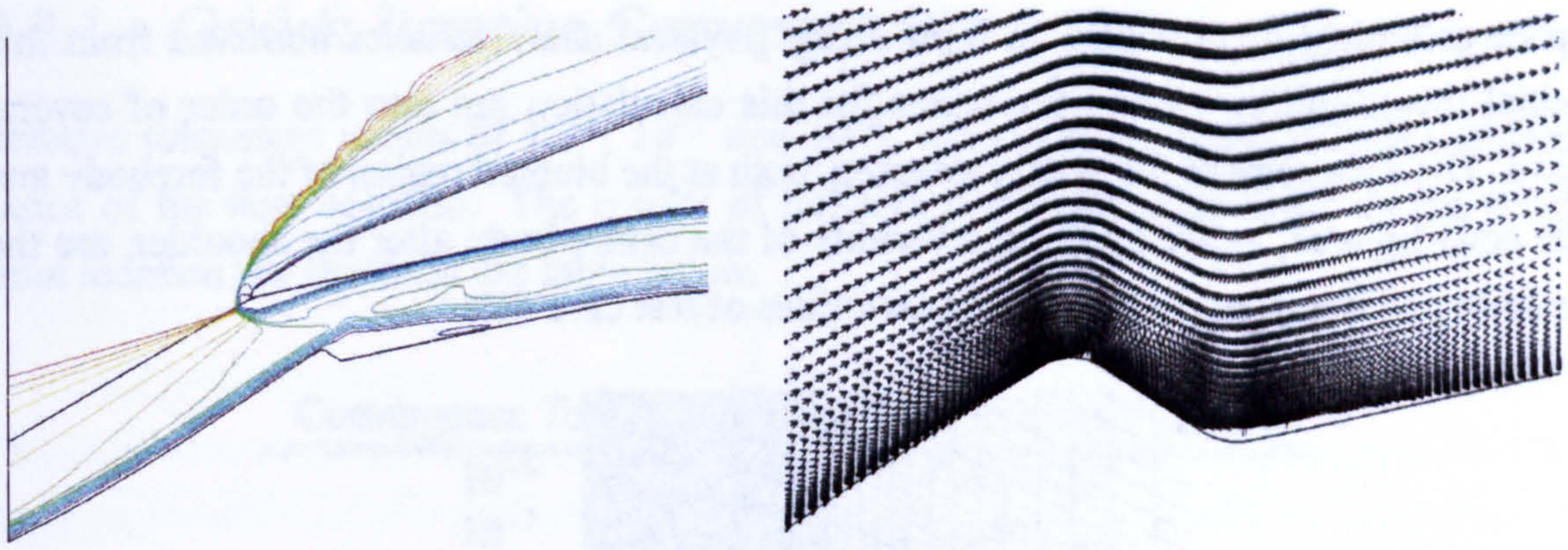

Figure 50: Mach number contours ahead of cowl, velocity vectors over the step

The flow domain consists of a multi-block grid, comprised of three parts, one ahead of the cowl, and regions spanning the flow domain above and below the intake. The sizes of which of these regions are 101x45, 45x241 and 101x341 respectively. As the close up of the cowl illustrates, this ensures that a suitable resolution of the cowl region is obtained. For the subsequent grid convergence study, the domain sizes are 52x23, 23x121 and 52x171 for the medium grid, and 26x12 12x61 and 26x85 for the coarse grid.

The flow conditions corresponding to the design operating conditions at an altitude of 32km are given by;

$$M_\infty = 6.0, \quad Re_\infty = 3372.73, \quad T_\infty = 51.85K \tag{9.3.1}$$

The flow is assumed laminar, with an adiabatic condition imposed along wall boundaries. Due to the nature of the flow multi-sweeping has been employed in the vicinity of the cowl lip, as well as in the blunted nose region of the fore-body. Since both the grid and operating conditions were provided by Qinetiq, an initial investigation into the prominent flow characteristics was performed. As no experimental data has been provided, a necessary step is to determine the extent to which optimality has been obtained, given the flow conditions provided.

As the Mach number contours in figure [50] illustrates, ahead of the cowl, a detached shock is witnessed. On first inspection, this seems as though it is a non optimal condition, however the velocity vector field on the right illustrates that the separated region behind the step has not extended upstream into the isentropic compression area. This indicates that the flow has not separated sufficiently to cause unstart.

Given that the objective of the current section is to identify an optimal magnetic field configuration based on the sampling and optimisation methodologies discussed in chapter [8], it is clear that a large sample data set must be obtained to explore the design

space as widely as possible. In light of the physical characteristics observed from this initial investigation, typical run times for this calculation ran into the order of several days. The requirement for multi sweeping, both at the blunted region of the forebody and the cowl lip area, as well as in the vicinity of the centre body after the shoulder, are the main impediments to obtaining vast quantities of test case data.

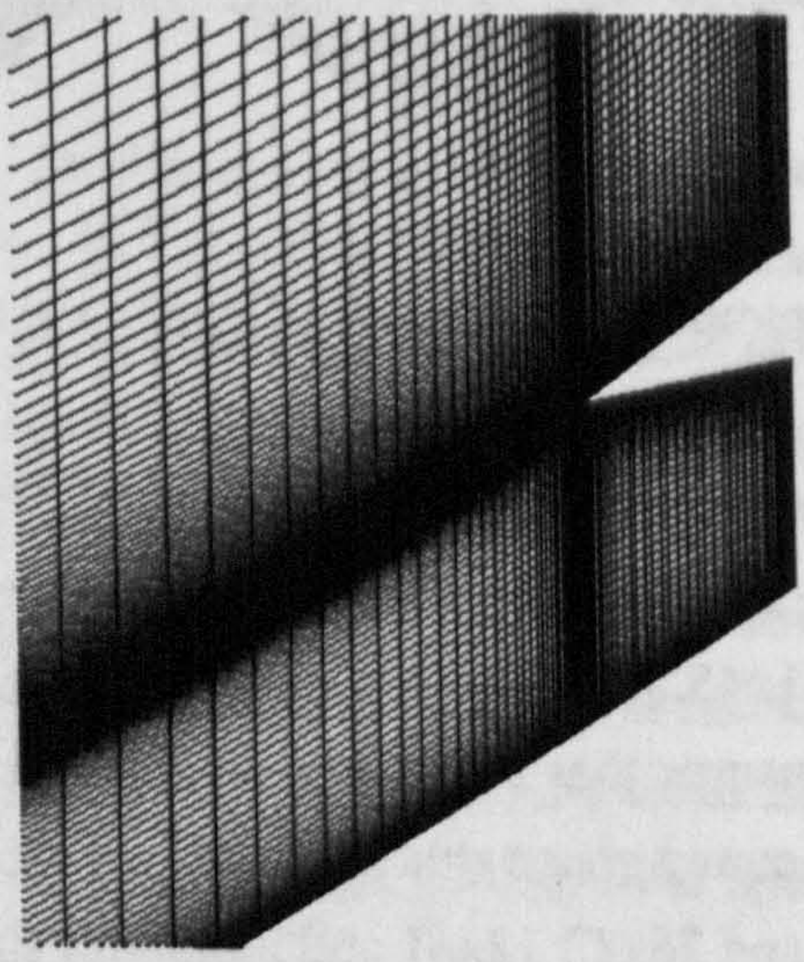

Figure 51: Geometry after Modifications

In view of the above, it was deemed necessary to make slight modifications to the flow geometry to ensure the necessary quantity of solutions could be sought. As the prominent obstructions to this end are regions requiring the use of the multi-sweep, these regions were of keen interest. Figure [51] is an illustration of the geometry in the vicinity of the cowl, once changes have been made. The key alterations include a sharpening of the compression ramp nose which is outside the figure, although the removal of bluntness at the cowl lip and simplifying the shoulder step area, behind which a separation region was forming, is clearly evident. The shoulder region is not included in the geometry, as the focus of the investigation is on the shock impingement location on the cowl, as opposed to flow physics within the cowl itself, and so it therefore makes sense to impose such a simplification.

To ensure the optimality condition of this new geometry had not been compromised by the simplification process, it is necessary to perform a series of tests to confirm that the operating conditions that provide shock-on-lip have not been changed. To quantify the extent to which shock-on-lip had been achieved for a given run, the following criteria had been identified. The y-location of the shock lip is situated 0.0275m above the centre line of the centre body. At the initial streamwise station where the cowl is situated, the y-position of the shock front was located by determining the point at which the density values are within a few percentage values of the freestream value.

9.3.1 Grid & Iterative Convergence

Iterative tolerances values of 10^{-6}, 10^{-7} and 10^{-8}, were used to assess iterative convergence of the flow solution. The results of iterative convergence analysis on the shock front location are shown in the table below.

Convergence Tolerance	*y*-position of shock front (m)
10^{-6}	0.0275226
10^{-7}	0.0275226
10^{-8}	0.0275226

Table 7: Shock stand-off positions at different convergence tolerances

The results indicate that there is no change in the shock impingement location, despite running for more iterations, justifying that an iterative tolerance of 10^{-6} is sufficiently small for convergence. Surface pressure coefficient distributions along the body surface, at these tolerances also show little variation between one another, serving as another justification for using, the above value as a convergence criterion.

To maintain confidence in so far as the solution is sufficiently grid converged, solutions obtained on three grids, consisting of 101×45, 52×23, 26×12 grid points in x any y respectively, have been examined.

Grid Dimensions	*y*-position of shock front (m)
101×45	0.0275226
52×23	0.0277223
26×12	0.0361004

Table 8: Shock stand-off positions for grid levels

As for grid convergence study, shock impingement locations in table [9.3.1], and pressure coefficient distributions in figure [52] illustrate limited variation between that obtained on the 101×45 and 52×23 grids, suggesting that the finest grid solution is well within the asymptotic limit for convergence.

9.3.2 Optimality Condition

Having established confidence in the solution in terms of numerical convergence, tests are carried out to confirm the shock on lip condition is identical to the unmodified grid geometry. They key issue is to determine the operating Mach number that would ensure

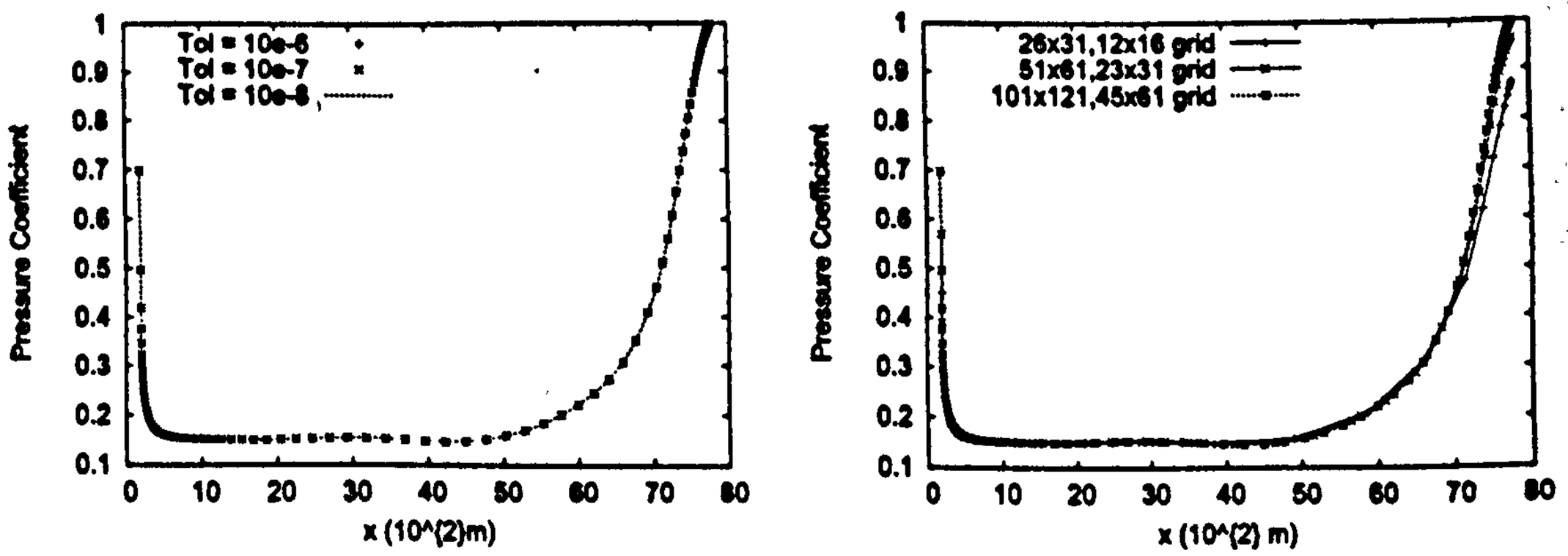

Figure 52: Pressure coefficient profiles for iterative and grid convergence

that the shock would impinge on the cowl lip. This is in effect an optimisation study in itself, and thus use could be made of the optimisation algorithms verified in section [8.2].

To confirm the design Mach number, a series of tests were performed for different values of freestream Mach number. To quantify shock on lip, as discussed earlier, a measure of the y location of the point at which density is within several percent of the free stream value is calculated. Given that the position of the cowl is given by $y_{cowl} = 0.0275m$, it makes sense to quantify the deviation of the point at which the density contour passes, from the cowl location. The requirement is that the shock front be as close as possible to the cowl, thus the quantity for which the minimum is sought is the difference between y_{cowl}. However, given that the shock location may lie above or below the cowl position, to turn the optimisation quantity into a variable that has an identifiable minimum, the absolute value of the difference is used.

In the attempt to find the design Mach number M_{∞_d}, for the modified geometry, the optimisation problem may be posed as follows;

$$\textit{Minimise} \quad |y_{cowl} - y_{\rho_\infty}| \tag{9.3.2}$$

subject to

$$M_{\infty_{min}} \leq M_\infty \leq M_{\infty_{max}} \tag{9.3.3}$$

for various values of M_∞. In the above expression, y_{ρ_∞} is defined as the y-value, taken normal to the incident flow direction, at which $\rho = \rho_\infty$. This is in fact an idealised definition, as in practise there is a certain degree of shock smearing, even in the presence of a discontinuity, and therefore the locations at which density was between 1 and 5 percent of the freestream value, was investigated. Given this problem formulation, the

optimal sample point will coincide with the design Mach number, as it will provide the value closest to ensuring that the shock front will impinge on the lip of the cowl.

As the sample space is one dimensional, there was no need to generate a latin hypercube data set at which to make functional evaluations using IMPNS. Rather, a uniform distribution of points over a range of Mach numbers was utilised. This range was chosen to ensure that the original design Mach number of 6 was contained within the sample. Consequently, in equation [9.3.3], $M_{\infty_{min}}$ was chosen to equal 4, the lower bound on the operating condition for the SHyFE intake, and $M_{\infty_{max}} = 9$, which although significantly larger than the initial design condition, was identified as appropriate to ensure severe off design conditions could be easily highlighted.

Figure [53] illustrates the variation of the objective function with respect to incident Mach number. The locations of the density values, within 2, 3 and 5% of the freestream value are compared to assess the qualities of using such a condition to judge optimality.

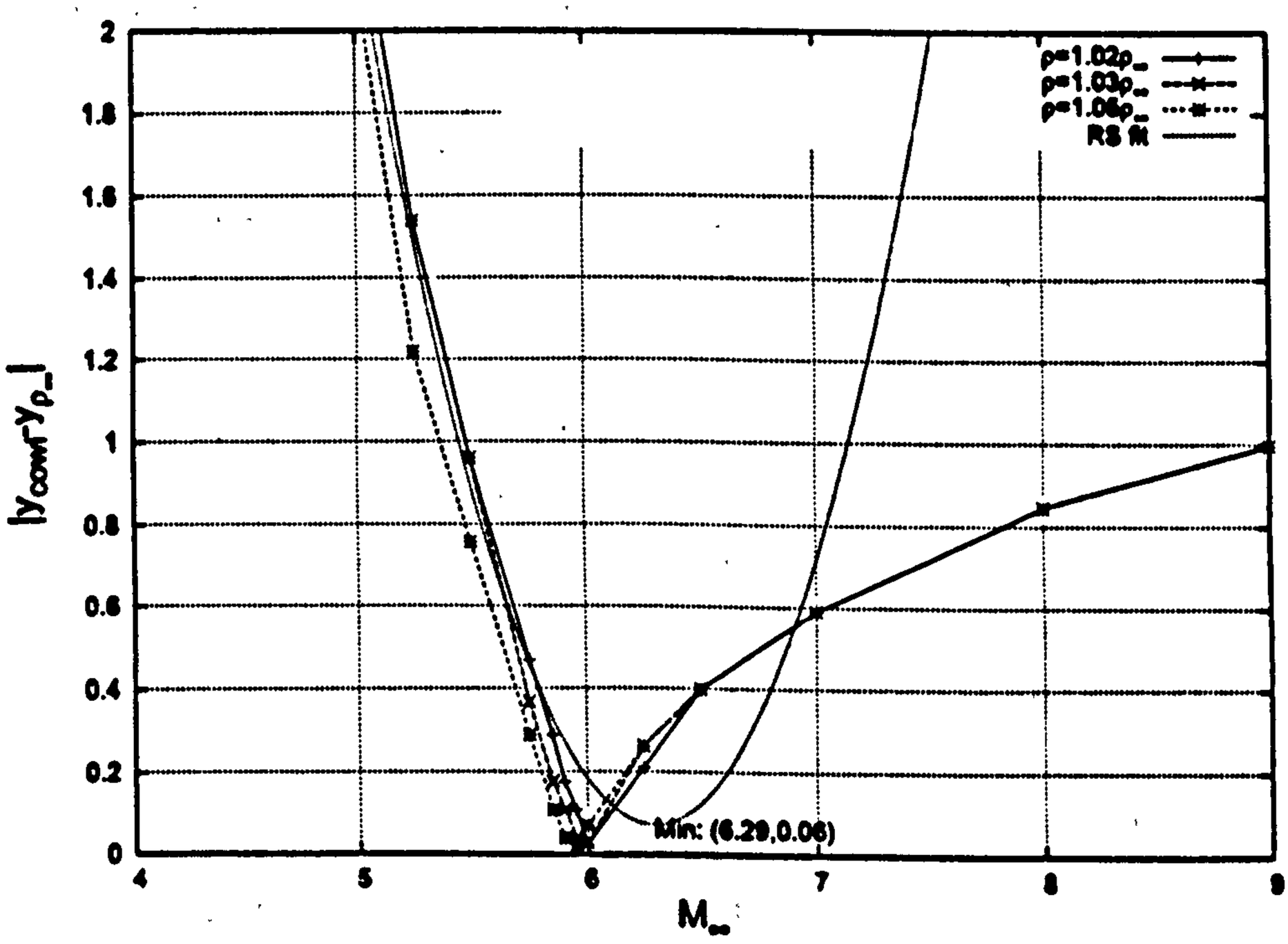

Figure 53: Shock front location as a function of Mach number

The graph illustrates little discrepancy between the condition chosen for the freestream density choice, although clearly a smaller deviation from ρ_∞ would be ideal. Graphically, numerical simulations for the $\rho = 1.02\rho_\infty$ case identify the optimal point to be $M_\infty \approx 6$, which is closely in line with that of M_{∞_d} for the unmodified SHyFE geometry, indicating that the changes made to the intake geometry have not imposed significant changes to the optimal operating conditions for the intake.

The optimum value for the modified geometry for this investigation is easily identifiable given the relatively simplistic graphical representation of function trends with respect to Mach number. Nevertheless, it is instructive to make an assessment as to how the optimisation routines perform given the current problem. The least squares polynomial regression model, denoted by the line "RS fit" is included in the graph above to represent this. The approximation is progressively worse for larger Mach numbers larger than 7, but as discussed in section [8.4], this is due to the fact that the model is non interpolant, instead minimising the least squared error between the sample data and the function. The optimum predicted by the function is at $M_\infty = 6.29$ with the objective function value of 0.06, which compared to the PNS value of 0.25, is in error by more than 100%.

Improvements in the prediction of the minimum can be obtained by making additional samples in the region of interest. It is clear from the graph above that the minimum predicted by the response surface is offset from the sample minimum. Clearly the optimum is the region of most interest, and as such, it is desirable to make a better representation of the objective function in this region. Therefore, more sample points were added within an interval encompassing the minimum.

The results in figure [54] show the effects of sampling additional points, with the new quadratic regression model superimposed. The revised minimum is found to occur at $M_\infty = 6.11$, representing an improvement to the initial estimate, compared to the minimum from the sample data.

Furthermore, in addition to improvements to the sample minimum, the percentage error of the sample data point also improves. For the revised response surface model, the absolute distance function at the prescribed minimum is 0.062, an error of 36% compared to the numerical data, but nevertheless a substantial improvement. Iterating this process, of adding data points in the vicinity of the predicted minimum and computing a new optimum from an newly generated response surface, therefore ensures that a better approximation of the true optimum is obtained.

Figure [54] illustrates a worsening approximation of the observed objective function over the Mach numbers for which $M_\infty > M_{\infty_d}$, but this is compensated by the fact that the response surface provides a better representation where there are more sample points, ie; in the vicinity of the minimum. This identifies one of the disadvantages in using the current linear regression method. The quadratic model is a good representation over a limited sample range, in the vicinity of the minimum in this case. However, extra caution needs to be exercised when trying to use the curve as a surrogate model for data points further away from this region. This can be attributed to the differences in the functional forms of the regression model to the sample data. It is analogous to trying to make a quadratic representation of a function $y = |x|$. Depending on the domain of interest,

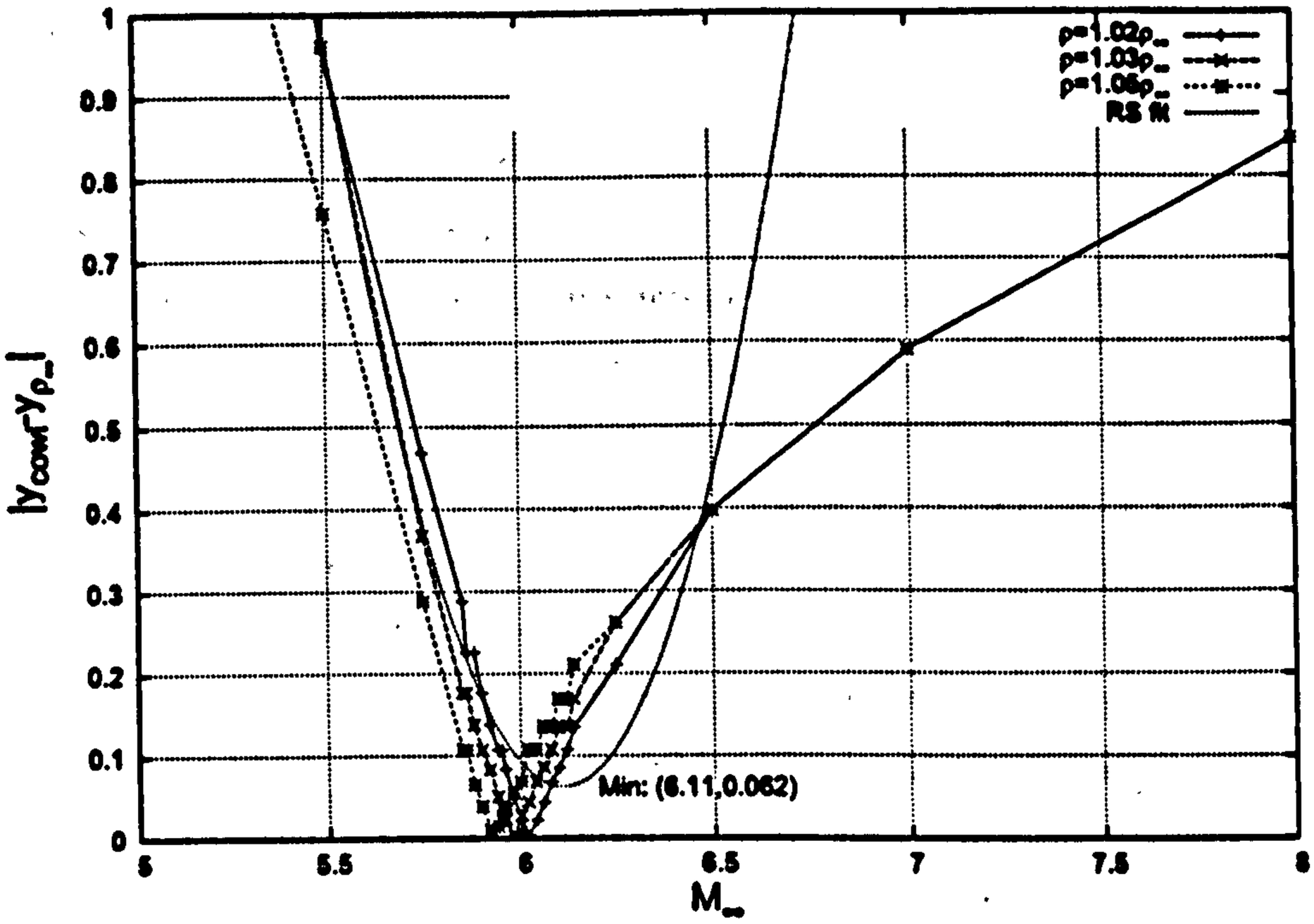

Figure 54: Shock Front locations, having added sample data in vicinity of original minimum

there will be regions where the quadratic will differ vastly from the absolute value. In the same way, objective function values will differ considerably. Nevertheless the quadratic representation is advantageous as it is able to identify the optimum sample point, as the current case is a good illustration of this.

9.4 Magnetic Field Effects

Having identified the optimal operating Mach number for the new geometry to be the same as that specified by the literature, a study into the feasibility of applying a magnetic field was undertaken. As described in chapter [4] the potential of using magnetic fields has been investigated by several groups in hypersonic flow regime applications. The current section aims to investigate another application area, that of hypersonic intake aerodynamics, and provides an initial extension of the work to date by seeking to find optimal magnetic field conditions for a given flow problem.

Section [9.2] gave an overview of the main obstacles that impede ramjet performance when flow conditions are suboptimal, whether it be due to the flow structure being non-axi symmetric due to incidence, or because parameters are such that shock on lip is not achieved. Whatever the causes, the effects are commonly detrimental, worst case

resulting in intake unstart, that is, mass flows in a reverse direction out from the ramjet intake into the external regions, which if sufficient enough, will cause the engine to cease running.

Under such operating conditions where the cost of intake failure has severe implications, the ability to achieve flow control for conditions outside the ideal operational envelope has considerable benefits. Conventional flow control measures may include flaps, vortex generators or other mechanical devices. However, for the present configuration, the use of such variable geometry instruments falls outside of the design remit.

Due to this design constraint, the application of a magnetic field is proposed to ensure design conditions may be achieved. The current section attempts to identify the optimal operating conditions for a given field, so that even at off design conditions the conical shock generated from the compression ramp impinges on the cowl lip.

As a hypothetical test case, the flow Mach number is taken to be greater than M_{∞_d}, corresponding to the case where the conical shock angle is smaller than for the design case, thus impinging on the underside of the cowl. A similar situation would be encountered on the windward side of the body running at incidence. Such a configuration would require a full three dimensional calculation, but given that a large number of calculations are necessary, a two dimensional axisymmetric flow with $M_\infty = 6.5$ has been chosen to represent the problem instead. For this case, in the absence of a field, PNS calculations revealed that $|y_{cowl} - y_{\rho_\infty}| = 0.398$. All other flow parameters are chosen to be identical to that of the preliminary study.

To isolate the effects of the strength of the field, independently of other factors, at first a dipole was placed ahead of the mid section at $x = 0.0175m$ on the isentropic compression, beneath its surface. The dipole was chosen to have a fixed location, with an arbitrary field strength. The magnetic field lines for a two dimensional dipole with centre $\mathbf{r}_0$ is given by;

$$\mathbf{B} = B_0 \frac{3\mathbf{r}_0(\mathbf{r}_0 \cdot \mathbf{x}) - R^2\mathbf{x}}{R^{\frac{5}{2}}} \tag{9.4.1}$$

where $\mathbf{B}$ is the magnetic flux density, $\mathbf{x}$ is a general point in space, R is the distance between any point $\mathbf{x}$ and the dipole origin, and B_0 is a measure of the strength of the magnetic field. Ahead of the leading edge of the geometry, the flow is assumed to be ionised, a requirement for the magnetic field to have influence on the flow. In practise, this may be achieved using one of the techniques discussed in the review article by Shang [144], such as radio frequency ionisation. A graphical representation of this magnetic field for the geometry is shown in figure [55].

As the main concern is the effect of magnetic field strength, the design variable identified was B_0, the field strength. The objective therefore was to find the optimal

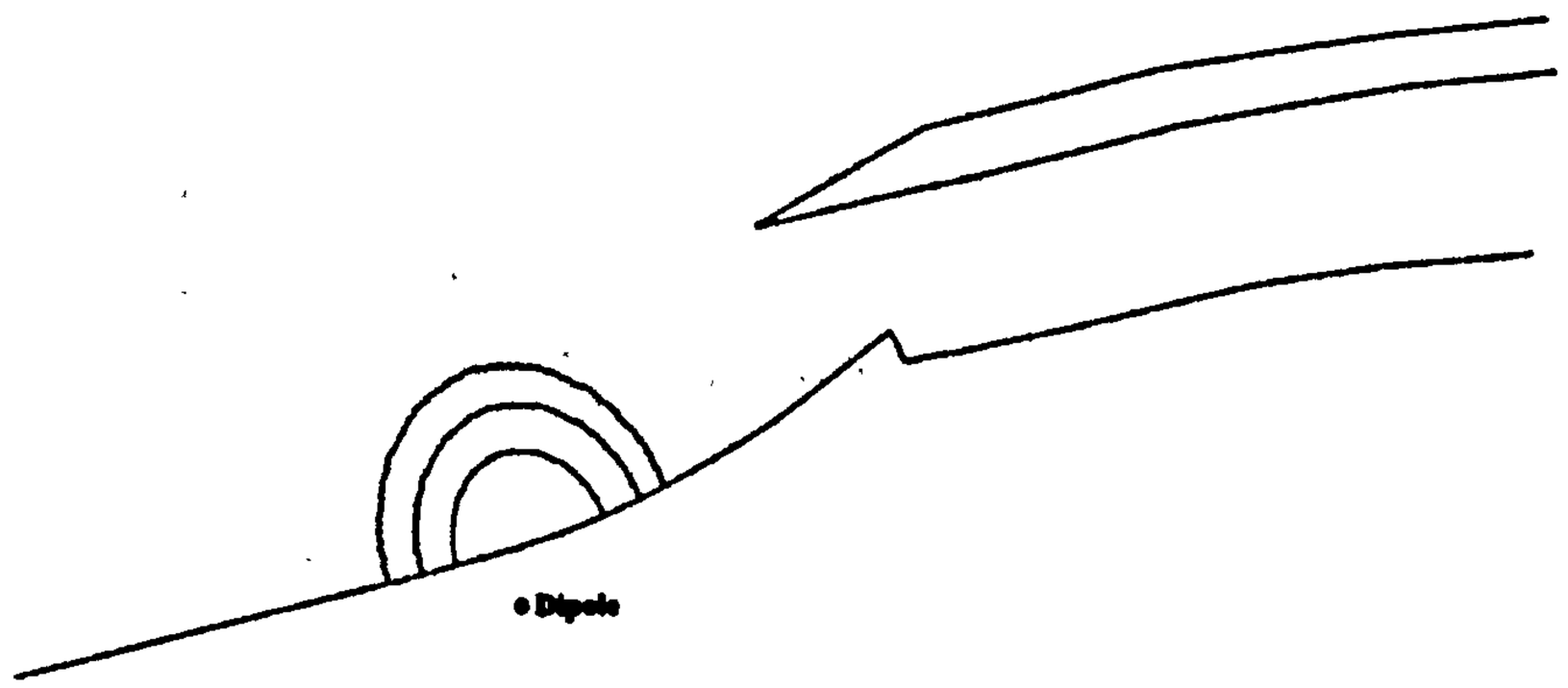

Figure 55: Magnetic Field Line Schematic for SHyFE Geometry

value that would minimise the objective function [9.3.2]. The reader will recall from section [4.6.2] the two non-dimensional parameters appearing in the low magnetic Reynolds number model;

$$S_\infty = \frac{\varepsilon_0 c^2 B_0^2}{\rho_\infty u_\infty^2} \tag{9.4.2}$$

$$Re_M = \frac{\sigma_0 u_\infty L}{\varepsilon_0 c^2} \tag{9.4.3}$$

The magnetic field strength is therefore taken into account in the magnetic force number S_∞, and an appropriate range for this variable must be identified over which the field could be seen to have influence over the flow. In the above expressions,ε_0 and c^2 are the permittivity of free space, and the speed of light in a vacuum, and are both known constants ($\varepsilon_0 \approx 8.854 \times 10^{-12} Farads/m$ and $c \approx 2.998 \times 10^8 m/s$). At the given operating altitude of 32km, we know that the freestream density is approximately $0.013 kg/m^3$, and the ambient speed of sound $308.45 m/s$. From the given information, and given the fact that the freestream Mach number is now 6.5, we may deduce that

$$S_\infty = 15.23 B_0 \tag{9.4.4}$$

$$Re_M = 1.96 \times 10^{-3} \sigma_0 \tag{9.4.5}$$

To obtain reasonable estimates for B_0 and σ_0 above previous works dealing with hypersonic scramjet intakes in the presence of magnetic fields has been used as a guideline. Macharet et al argue that for a hypersonic vehicle employing appropriate electron seeding, the fluid conductivity would be on the order of a couple of hundred *mho/m* [98], and

as such a conservative value of $100mho/m$ has been chosen, representing a lower bound the conductivity of the fluid for which magnetic fields have an effect on the flow. In trying to revert the off design flow conditions, magnetic flux densities are on the order of $1T$. It is important to note that this choice of electrical conductivity returns $Re_M = 0.196$, which is consistent with the inherent assumptions of the low magnetic Reynolds number model that $Re_M < 1$. Use of the low magnetic Reynolds number model is therefore justified with the flow conditions specified.

At this point it is more convenient to introduce another variable, the magnetic interaction parameter, defined by;

$$Q_\infty = S_\infty Re_M \tag{9.4.6}$$

which under the flow conditions illustrated above suggest that Q_∞ is of $O(1)$ to influence the flow. Changing the magnetic flux density/strength B_0 is equivalent to modifying values of Q_∞, and therefore there is no difference in using this as the design variable with which to conduct the optimization study.

Like the preliminary investigation, initially Q_∞ is the only design variable, which on the basis is of being unit order, was chosen to span the interval [0,3]. A uniformly distributed set of thirty points for values of Q was chosen, and the objective function computed. The resultant 2^{nd} order polynomial regression model was given by

$$|y_{cowl} - y_{\rho_\infty}| = 0.146317 \times Q_\infty^2 - 0.490203 \times Q_\infty + 0.48871 \tag{9.4.7}$$

which the sequential quadratic programming routine predicted to have a minimum at $Q_\infty = 1.68$ with an objective function value of 0.078. The results are illustrated graphically in figure [56] below;

Graphically, the minimum predicted by the meta model is in agreement with the computed data, but as with the preliminary study, the predicted value for the objective function has a discrepancy. Compared to the PNS computation of $|y_{cowl} - y_{\rho_\infty}| = 3.3 \times 10^{-3}m$ there is a gross discrepancy in the predicted value as it is more than a hundred times the PNS value. As a check to ensure that the method converges towards the minimum, additional sample data in the vicinity of the predicted minimum was taken. The new sample range was chosen such that $Q_\infty \in [1.42, 1.92]$. The new response surface was generated using the new sample points as well as any existing points lying within this range. Sample data outside this region was neglected in computing the surface, as experience with the computations testing for M_d illustrate that predictive accuracy is affected by out-lying data points. The domain of interest is in the vicinity of the minimum, so it makes sense to neglect points that are likely to compromise accuracy in this region. The revised response

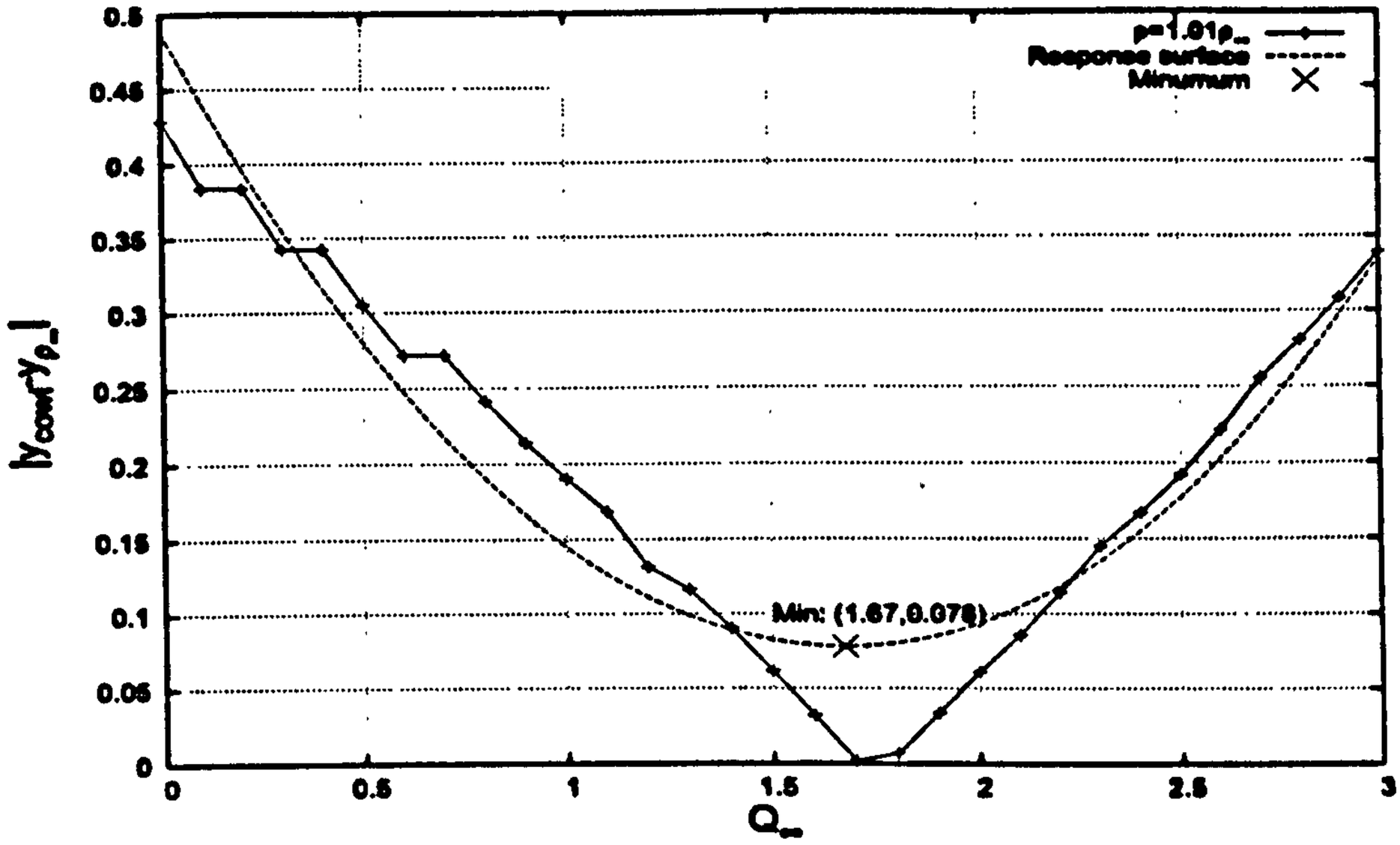

Figure 56: Objective function, as a function of Magnetic Interaction Parameter

surface, having sampled data within this new domain for Q_∞, is shown below; The revised response surface is given by the following equation,

$$|y_{cowl} - y_{\rho_\infty}| = 2.50061 \times Q_\infty^2 + 0.822763 \times Q_\infty - 2.863998 \qquad (9.4.8)$$

which predicts a minimum at $Q_\infty = 1.74$, with a value function of $0.008m$, a discrepancy of ten times that compared to the low Re_M model (which is $8.0\times10^{-4}m$). This nevertheless clearly represents a marked improvement in the agreement as is indicated graphically in figure [57]. The results indicate therefore that for a dipole in fixed position half way along the compression surface, a suitably chosen magnetic field strength is capable of reintroducing optimal working conditions, even at Mach numbers different to M_{∞_d}. For the magnetic interaction parameter $Q_\infty = 1.74$, this is equivalent to a magnetic field strength of $0.6T$. The minimum here is a global one, whose accuracy can be improved upon by making successive refinements of the domain of interest, and by increasing the number of samples there within.

In the above plot, there are certain points on the line representing the low Re_M model solution that need mentioning. In the vicinity of $Q_\infty = 1.45, 1.5$ and 1.6, there are portions on the plot that seem to suggest that the objective function is constant over these ranges. This behaviour is actually the consequence of the method used to derive the shock front location. As the sampling domain is refined, it is more likely that the grid resolution will not be fine enough to capture the changes in density that occur on an increasingly smaller scale. It is therefore important to note that in performing further detailed studies

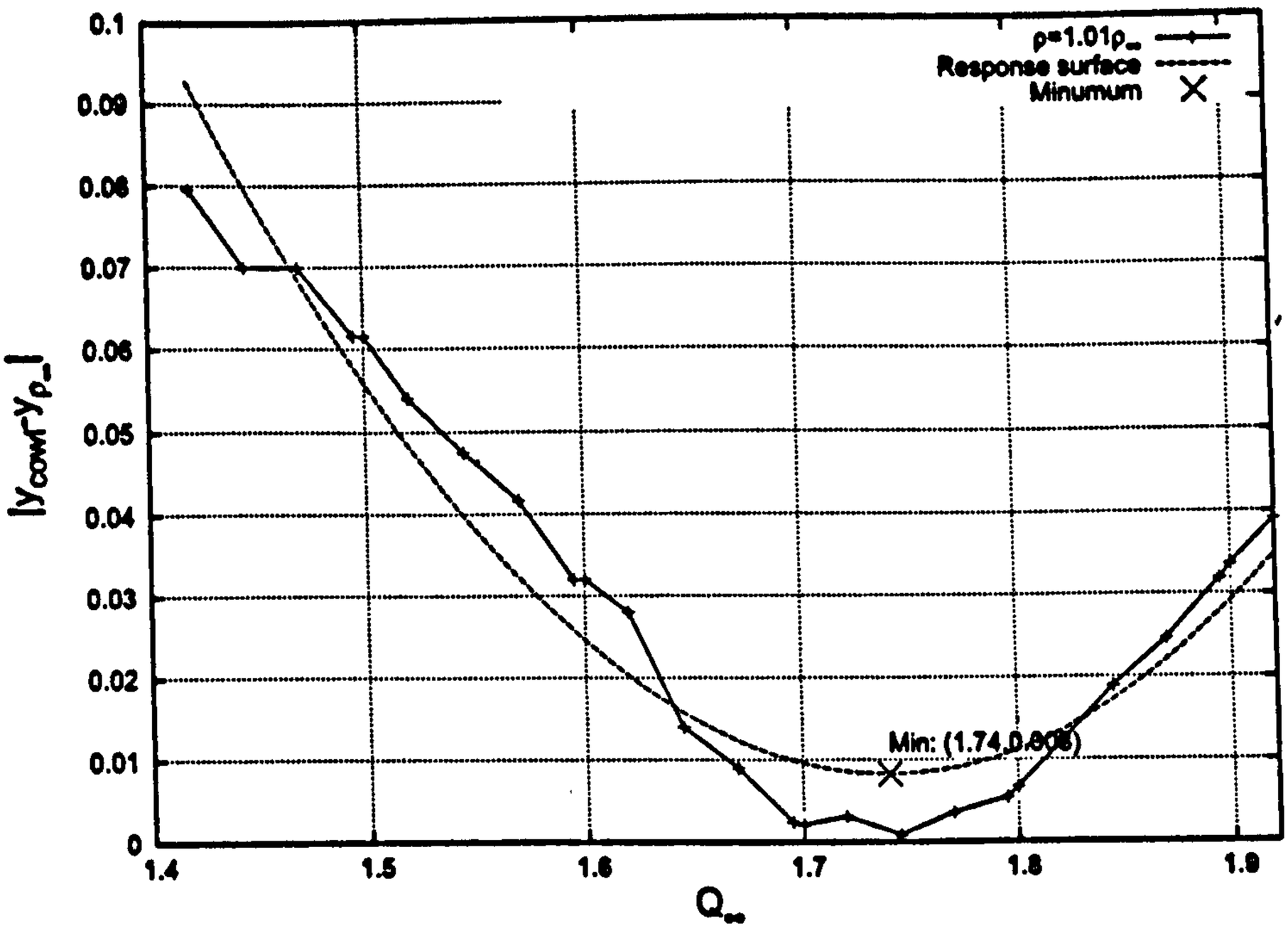

Figure 57: Objective function, after refinement of Q_∞ range

with the optimization procedure, it would be mandatory to apply additional refinement in the vicinity of the cowl lip. The process maybe repeated over an arbitrary number of iterations, depending on the accuracy required, and as future work, the ideas generated here may be extended over a wider range of Mach numbers, thereby obtaining suitable strengths under each flow condition.

9.5 Variable Dipole Location

The previous section demonstrated that a magnetic field of suitable strength is capable of ensuring optimal conditions for off design operating conditions. Applying a magnetic field however, represents a cost in generating it, which as one would expect, requires more energy, the greater its strength. This section addresses the issue of whether it is possible to achieve the same optimal condition, for a weaker field. Another key factor influencing the effects of an applied field is the location of its source. A two parameter extension study, examining the effects of both the field strength, and the dipole location is undertaken with the aim of achieving shock on lip, for the least amount of energy spent.

To try and understand the effect of dipole location on the shock front location, a series of calculations were initially performed using a dipole of fixed strength, at various locations within the isentropic compression ramp. The Mach number was fixed equal to

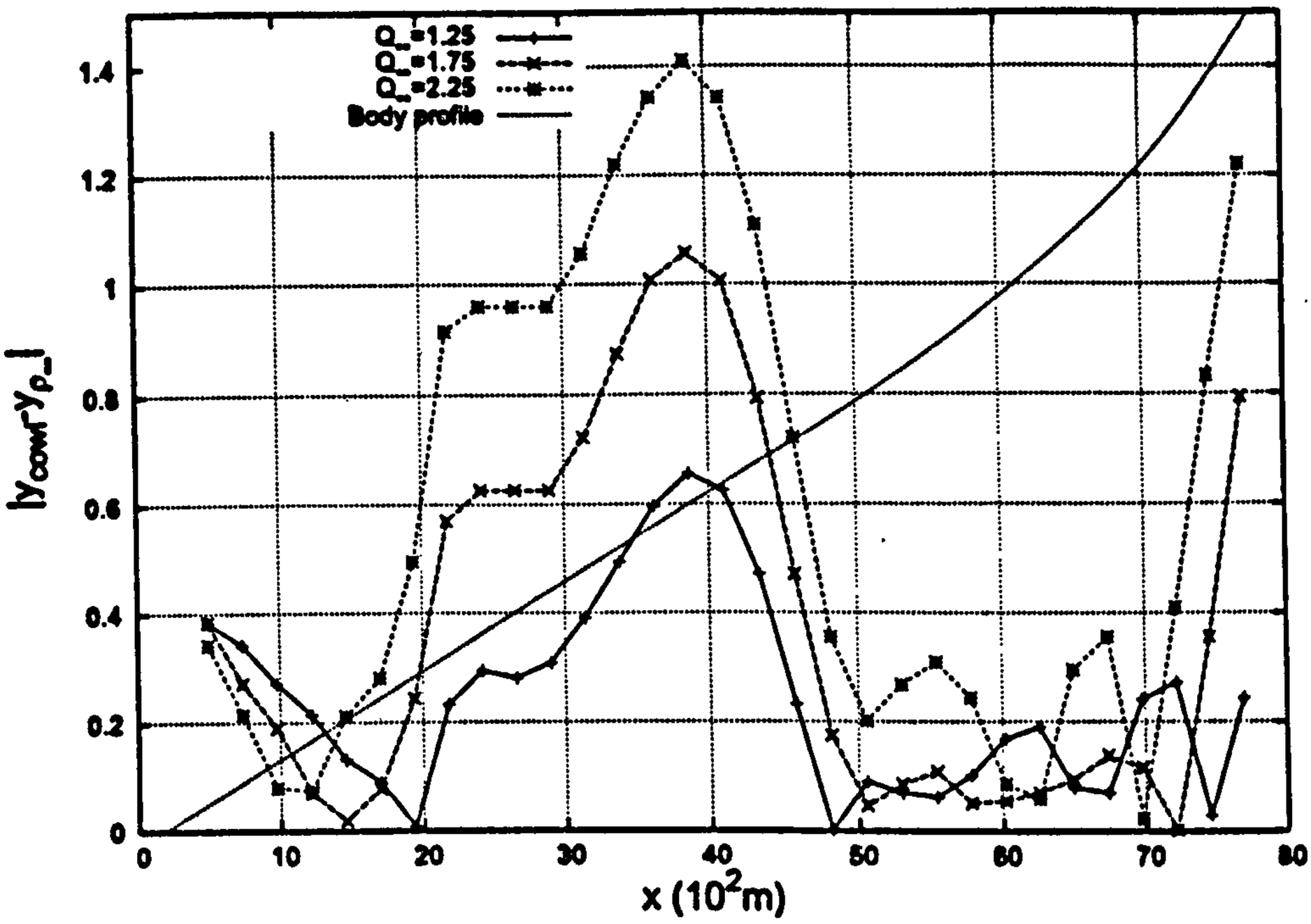

Figure 58: $|y_{cowl} - y_{\rho_{max}}|$ as a function of dipole location

6.5, as before, and magnetic interaction parameter values of $Q = 1.25, 1.75$ and 2.25 were input. Dipole positions were located $0.01m$ beneath the body surface at each streamwise position, which were chosen uniformly over the interval $x \in [0.05m, 0.77m]$ the region spanning the ramp.

Figure [58] shows the absolute shock standoff distances from the cowl, as a function of dipole locations along the body, for the three magnetic interaction parameter values. The profile of the compression ramp is superimposed to give an indication as to where the dipole positions correspond to on the ramp. The graph illustrates a peak in the objective function end of the ramp, just prior to the cowl location. For this case, the region over which the magnetic field can have influence is short, and thus there is little benefit in applying a field here.

All three profiles exhibit maxima at the centre of the compression, around $x = 0.38m$, suggesting that dipoles located at these positions slow the flow to a considerable extent that the shock is now actually located above the cowl lip. An interesting observation, is that as the dipole location is moved further downstream on the ramp surface, the shock impingement line actually approaches the cowl lip again. Possible explanations for this can be provided by examining the extent of influence of the magnetic field, at different locations.

Figure [59] represents the maximum value for the x component of the Lorentz

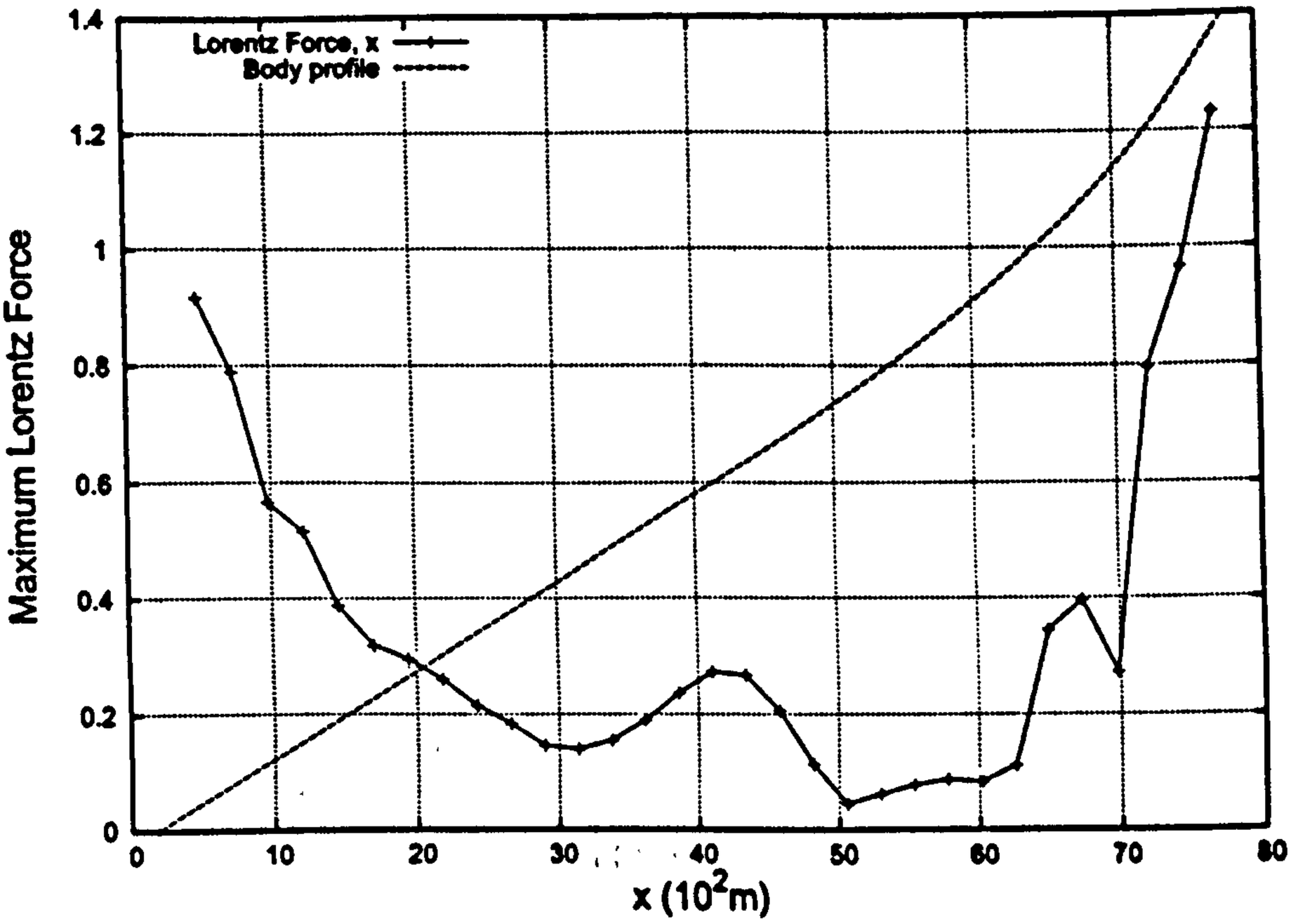

Figure 59: Max Lorentz Force as a function of dipole location

force $\mathbf{F} = \sigma(\mathbf{E} + \mathbf{v} \times \mathbf{B}) \times \mathbf{B}$, plotted against the dipole location with respect to the body. The data is taken from the case for $Q_\infty = 1.25$, though a similar trend is observed for the other two values of the magnetic interaction parameter. As discussed in section [4], for a magnetic field orientated normal to the incident flow direction, the effect of the field is to generate a Lorentz force in the direction opposite to the incident direction. Whilst the field is not entirely perpendicular to the flow, there exist regions where this is so. The underlying trend illustrates that as the dipole is shifted toward the inlet, the magnitude of the Lorentz force decreases, except in the region closest to the inlet and at the central section. The increase at the cowl end can be explained by the fact that there is a slight increase in the gradient of the body profile in this region, and consequently, more momentum is transfered in the direction normal to the wall. The Lorentz force witnesses an increase too, strong enough to push the shock above the cowl considerably. The peak near the centre section accounts for the peak witnessed in the objective function in figure [58]. What is not entirely obvious is why there are local minima in the objective function, between the mid-section and the cowl, even though the maximum Lorentz force is lower that in the region ahead of the mid section.

It turns out that the magnetic fields generated have a greater domain of influence, the further the dipole is located downstream. This is illustrated in diagram [60], where the contours for the x component of the Lorentz force are shown, for several locations.

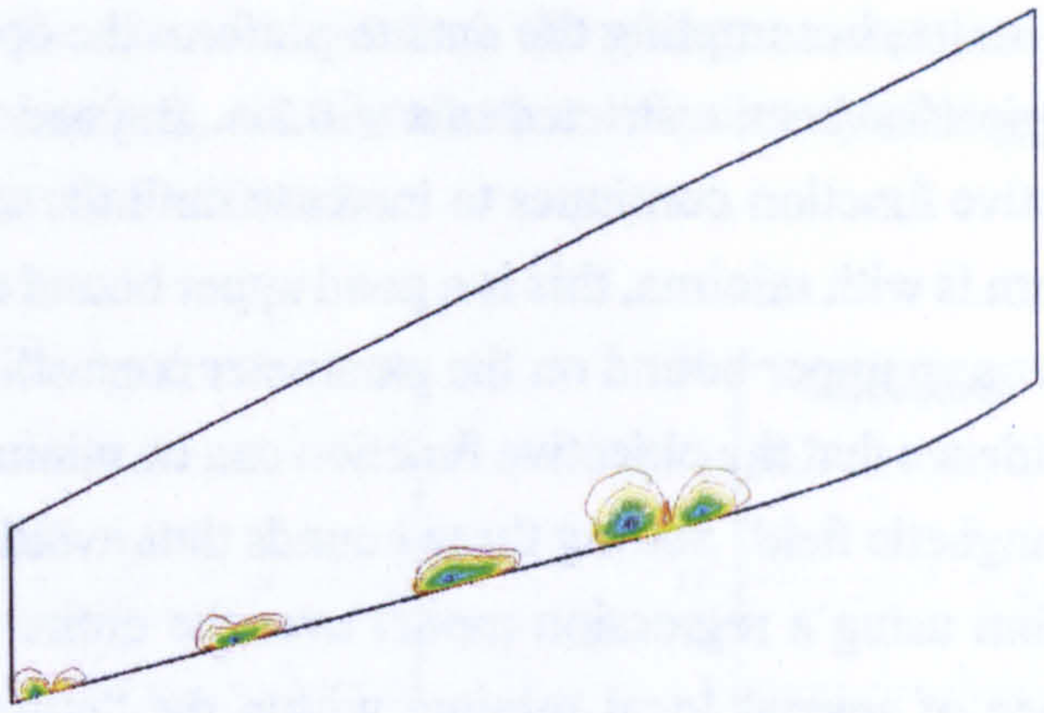

Figure 60: Lorentz force contours, Domain of influence of dipole at different locations

For each set of contours, the dipole is situated directly beneath its central region, within the body surface, and the outer line in each case represents the line $\mathbf{F}_x = 0$, so the portions within this boundary maybe considered to be the region of influence of the field. As the dipole is moved downstream, the region enclosed by this contour expands, eventually resulting in two distinct enclosures, at $X = 0.55m$. Thus, for a given magnetic field strength, the reduction in Lorentz force is compensated for by the fact that the flow is being decelerated over a wider portion over the body, which explains why local minima can occur downstream of the mid-section.

For these reasons in the region $0.45m < x < 0.77m$, the field is more effective in ensuring design operating conditions, as the objective function values are smaller than at the end and the mid section. However, the region does not seem to exhibit a discernible trend, in that the values are noisy and somewhat scattered, and the computations exhibit several local minima. In contrast, the forebody region, $0.0 < x < 0.38m$, before the peak position demonstrates a smoother trend, with a unique dipole location for each Q_∞ value.

In performing a two parameter investigation consideration must be made over the region over which to sample observation data. All three plots in figure [58] indicate that over the entire region $x \in [0.0, 0.77m]$, the function trends are anything but quadratic. An attempt therefore, to fit a quadratic regression representation through such points, would result in excessive smoothing, and the surrogate model minima will not correspond to that observed in the data. Choosing an interpolating function, such as a radial basis function would overcome this problem, but there remains the risk of the model generating artificial minima, particularly in the rear portion of the body, where the data is noisy. Indeed even with radial basis functions, one cannot avoid the issue of the optimum being highly sensitive to the starting point, within the sequential quadratic programming algorithm. Depending on whether we start at $x < 0.38m$ or $x > 0.38m$, the solutions will differ vastly.

To avoid these issues, in sampling the data to perform the optimization procedure, the dipole location region has been restricted to $x \leq 0.3m$. Beyond $x = 0.3m$, the profiles suggest that the objective function continues to increase until the mid section, and given that the primary concern is with minima, this is a good upper bound on the dipole position. $Q_\infty = 2.5$ was chosen as an upper bound on the parameter controlling the strength of the field, as there clear evidence that the objective function can be minimised for Q_∞ less than this value, a weaker magnetic field. Setting these bounds thus avoids the problem of poor data representation from using a regression model over the entire range, and the issues relating to the presence of several local minima within the "noisy" data in the region beyond the half way point on the ramp.

Using the latin hypercube sample generator, a hundred sample points were generated with $Q_\infty \in [0.0, 2.5]$ and $x_{dip} \in [0.05m, 0.3m]$. The algorithm used to generate the hypercube is as follows. The number of design variables is $n_{var} = 2$. The intervals for each design variable was divided into n_{runs} equally spaced sub-intervals, where n_{runs} denotes the number of samples to be taken, in this case one hundred. Each sub-interval was assigned an integer $\in [0, n_{runs} - 1]$, and an $n_{var} \times n_{runs}$ matrix is generated by performing random permutations of these integers. In pseudo code form;

$$\begin{aligned} &\text{for} \quad j = 1, n_{var} \\ &\quad vect = [Perm(n_{runs}) - 1] \\ &\quad DesignMatrix(i, j) = \frac{1}{2} + \frac{2 \times vect(i) + 1}{2 \times n_{runs}} \\ &\text{end for} \end{aligned}$$

where **Perm** (n_{runs}) generates a random permutation of the integers $[1, 2, \cdots, n_{runs}]$. The resultant output $DesignMatrix(i, j)$, is an $n_{runs} \times n_{var}$ array, where each column contains the values for each design variable for a particular run. Thus each column in this matrix represents a sample point in the design space to be considered by the analysis tool.

The procedure described above satisfies the conditions for a latin hypercube outlined in section [8], but given the fact that the sample point distribution relies on a stochastic permutation of integers, there can be no guarantee of the uniformity of data points. To ensure uniform coverage, the technique proposed by Audze and Englais [9] was used. Their design of experiments procedure was determined such that the quantity;

$$\sum_{i=1}^{n_{runs}} \sum_{j=1}^{n_{runs}} = \frac{1}{d_{i,j}} \tag{9.5.1}$$

where $d_{i,j}$ represents the Euclidean distance between sample points i and j. For each

sample generated by the above algorithm, the above summation was determined, and over several such generations, the distribution of points yielding the minimum [9.5.1] was chosen as optimum for uniformity.

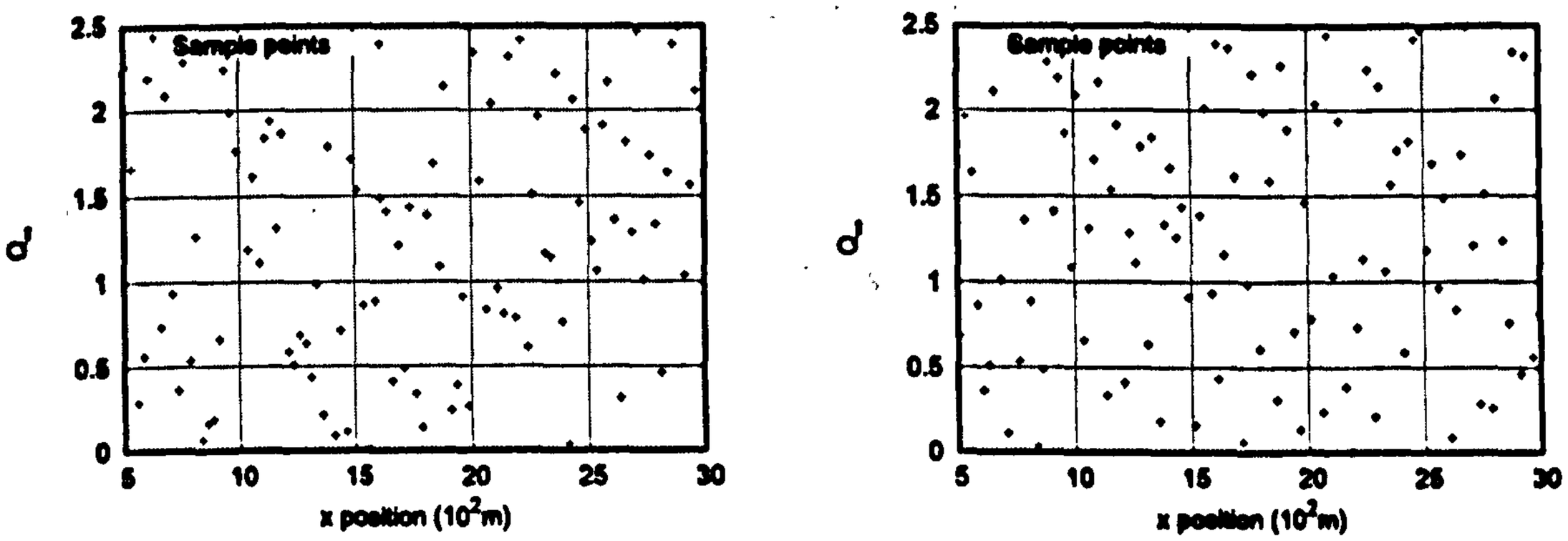

Figure 61: Sample point distribution after 1 (left) and 1000 (right) simulations

Following this procedure, a latin hypercube was generated for the case in question, over the domain $[0.0, 2.5] \times [0.05m, 0.3m]$. The distribution of sample points is illustrated in figure [61]. The figure on the left shows the scattering of points after one permutation, that on the right, after a thousand permutations, whereby the distribution yielding a smaller quantity for [9.5.1] was retained, after each permutation. Direct comparison of the two illustrates that a greater degree of uniformity is obtained having taken more samples aimed at decreasing the distance function. Although the computational time is slightly increased as a result of this procedure, only one such simulation is required to generate a design of experiments for an entire class of optimisation problems.

For a given streamwise location for the dipole origin, the y position of the dipole was fixed, to lie 0.1m beneath the surface of the ramp. One can introduce this as another design variable, but it was deemed unnecessary for the present case. The closer the dipole is located to the flow the greater its influence, which is equivalent to applying a stronger field. Since this is taken into account through the variation of Q_∞, it was not required to introduce y_{dip} as another design variable. With the sample data sets defined thus, two surrogate models have been considered to represent the objective function data.

9.6 LSQ Fit Method

With the bounds on the design space and the sample points thus defined, the PNS equations including the effects of magneto-hydrodynamic interaction, through the low magnetic Reynolds number model, has been used to obtain values for the objective function $|y_{cowl} - y_{rho\_}|$. The least squares (LSQ) polynomial regression model described in section

[8.4] is used to build a surrogate model spanning the data set. The quadratic polynomial representing the objective function is given by;

$$\begin{aligned} |\, y_{cowl} - y_{rho_\infty} \,| \;\cong\; & 1.4358 \times (10.0^{-3})x^2 + 0.1475y^2 + 2.5143 \times (10.0^{-2})xy \\ - \;\; & 6.9540 \times (10.0^{-2})x - 0.7263y + 1.1091 \end{aligned}$$

Recall that the function is fitted to the data in a least squares sense, minimising the summation of the squared error between the surface and the objective function values. The sample data, and function is represented graphically in figure [62].

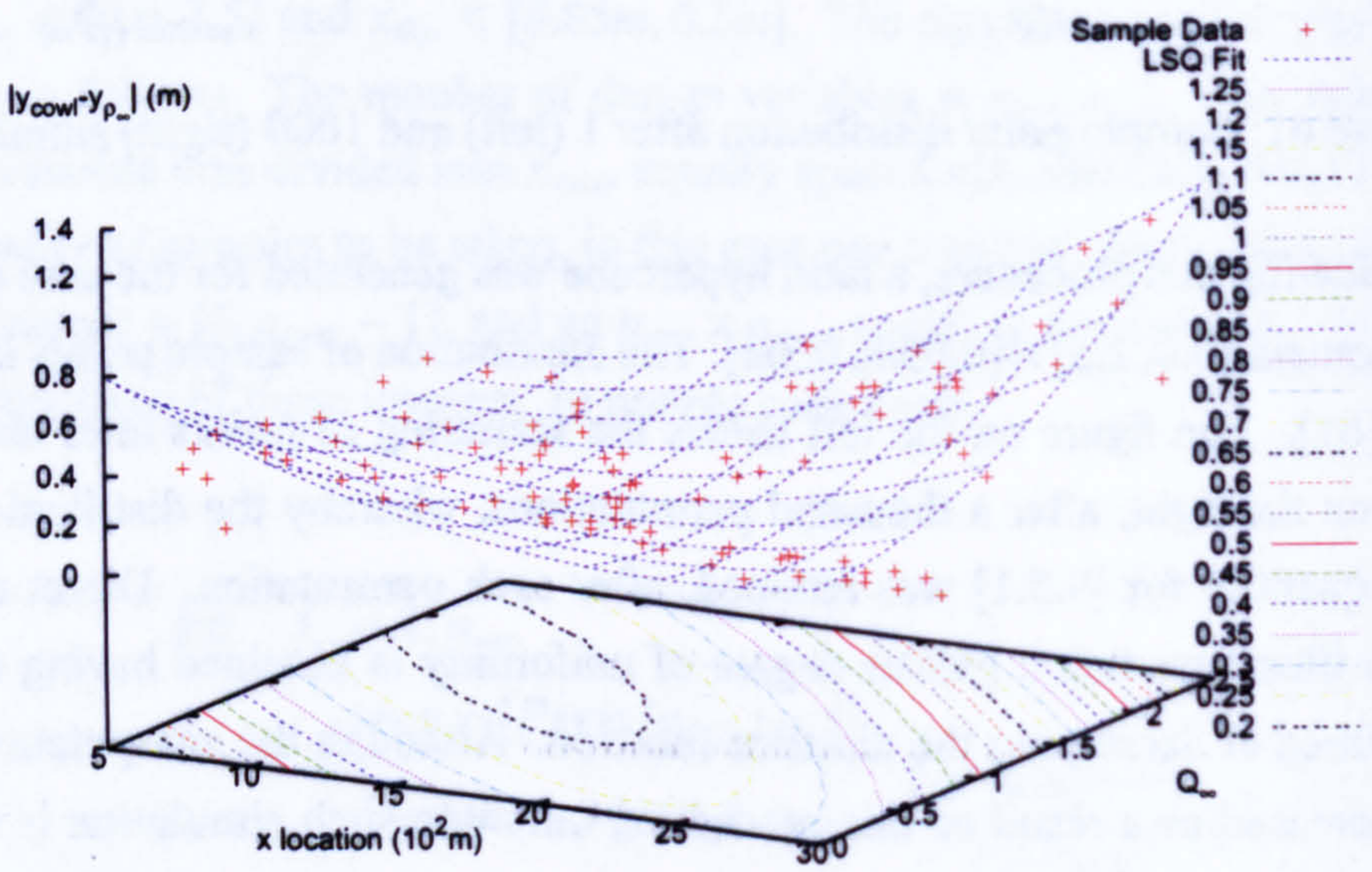

Figure 62: Sample Data and 2^{nd} order Polynomial Representation

Clearly the response surface is non-interpolant, as the diagram shows. A sequential quadratic programming module, implemented in Matlab, based on the techniques discussed in section [8.2], found the minimum objective function value to be

$$|\, y_{cowl} - y_{rho_\infty} \,|_{min} = 0.174932m \qquad (9.6.1)$$

located at

$$x = 0.104802m, \quad Q_\infty = 1.56886$$

With this prediction, the corresponding sample data is substituted into the analysis tool, to give a prediction of $0.1901m$ for the objective function, corresponding to an error of

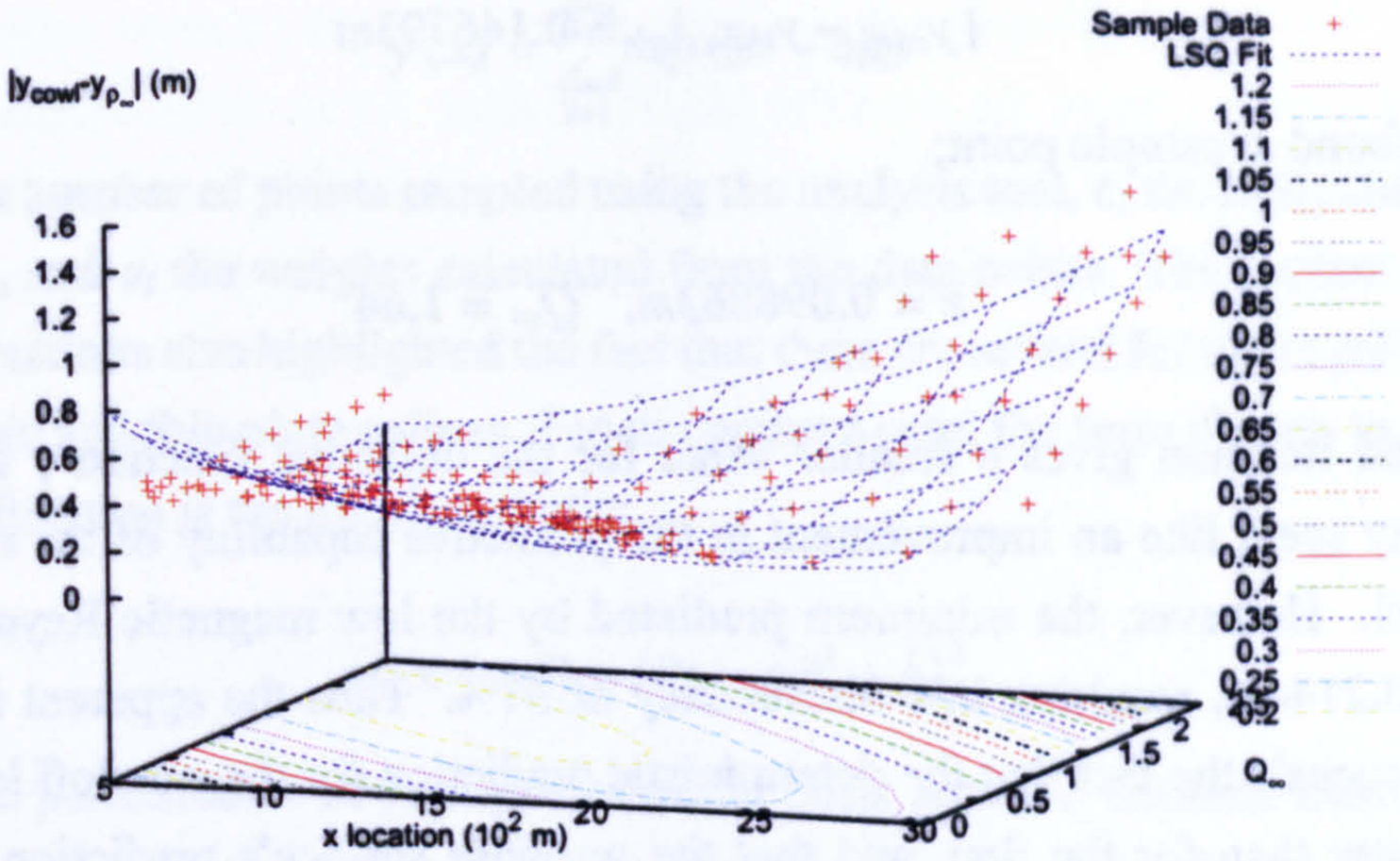

Figure 63: Sample Data and 2nd order Polynomial Representation, second iteration

8%. The objective of the current section is to return the global minimum, and thus in an analogous fashion to the one variable investigations performed in sections [9.3.2] and [9.4], additional sample points are taken in the vicinity of the predicted minimum.

Unfortunately, unlike the simple one variable investigations, it is not immediately obvious what range of values the new domain ought to cover, since the initial studies relied heavily on graphical data representation. Thus defining the bounds on the region over which to make additional samples is less formal. Nevertheless, the domain chosen was the region $\pm 0.025m$ either side of the x-location for the predicted minimum, and ± 0.25 either side of the corresponding value for the magnetic interaction parameter.

An additional twenty samples were taken over this domain, using the latin hyper-cube sampling procedure coupled with the routine to minimise the distribution function given by equation [9.5.1]. This ensured that the extended region is sampled over uniformly, and that extra weighting is provided within it when building the regression model, due to the presence of more sample points. The revised objective function is expressed as;

$$\begin{aligned} |y_{cowl} - y_{rho_\infty}| \cong\ & 9.5615 \times (10.0^{-4})x^2 + 0.1543y^2 + 1.9905 \times (10.0^{-2})xy \\ -\ & 5.1550 \times (10.0^{-2})x - 0.7028y + 0.9779 \end{aligned}$$

and represented graphically in figure [63]. SQP predicts a minimum of;

$$|y_{cowl} - y_{rho_\infty}|_{min} = 0.146793m \tag{9.6.2}$$

which is found at sample point;

$$x = 0.098863m, \quad Q_\infty = 1.64$$

The second iteration gives a smaller value for the objective function , which at first glance may seem like an improvement in the predictive capability of the revised surrogate model. However, the minimum predicted by the low magnetic Reynolds number model is $0.2144m$, resulting in a discrepancy of 31%. Thus the apparent improvement actually conceals the fact that the deterministic prediction for the standoff location is actually greater than for the first, and that the response surface's prediction has actually become worse. These issues suggest that a response surface based on a second order polynomial regression is not suitable for modelling the current domain of interest. As this second iteration demonstrates, the addition of extra samples, unlike the single variable studies, does not improve the capturing capability of the surface, due to the sample region being too large, or since the underlying function differing substantially from a quadratic representation.

Furthermore, there are a considerable number of sample points whose objective function values lie beneath both response surfaces. Of the analysis tool evaluations for example, the smallest value predicted is $0.0002m$, at $x = 0.25125m$, $Q_\infty = 1.18750$. With this information alone, it is not sufficient to guarantee that this is a global minimum, although one might expect the model to predict a minimum in the vicinity of this point. Unfortunately, the polynomial regression model, based on the evidence presented thus far does not provide approach a minimum based using an interative procedure.

To overcome this issue, and to find a better representation of the unknown representation of the objective function , Radial Basis Functions have been chosen as an alternative model. The main advantage being that its construction guarantees all sample points are interpolated through, and consequently, any minima appearing in the actual sample data will be accurately represented.

9.7 RBF fit method

As it was outlined in section [8], radial basis function (RBF) may be used as response surface construction techniques, that satisfy the property that all sample data used to construct the surface is interpolated. The general form for the objective function based on a radial basis function is expressed as;

$$\hat{\mathbf{y}}(x) = \sum_{i=1}^{N} a_i \rho(\|\mathbf{x} - \mathbf{c}_i\|) \tag{9.7.1}$$

where N is the number of points sampled using the analysis tool, $\mathbf{c}_i$ the independent sample point data, and a_i the weights calculated from the data points. The section outlining radial basis functions also highlighted the fact that there are several forms for $\rho(\cdot)$, such as Gaussian, cubic and thin plate splines. For the present case, the form chosen to represent the objective function is the multiquadratic;

$$\rho(\|\mathbf{x} - \mathbf{c}_i\|) = \left(\|\mathbf{x} - \mathbf{c}_i\|^2 + h\right)^{\beta} \tag{9.7.2}$$

The predictive performance of this type of radial basis function depends heavily on the shift parameter, h, and the exponent β. Irrespective of the values chosen for h and β, the resultant function is always an interpolant. However the extent of smoothness of radial basis functions are commonly the measure used to address their performance, and is strongly dependent on these values, which are user dependent. It is therefore necessary to estimate optimum values for these parameters, to ensure the model performs well, even on data that has not been obtained through use of the analysis tool. For the current study, the multiquadratic radial basis function has been chosen due to the fact within the literature there is a well documented optimisation procedure to determine these parameters for this type of function, in the numerous works presented by Wang [163, 165].

9.7.1 RBF Tuning Procedure

To find optimum operating parameters, generally the idea is to minimise the following risk function;

$$E(\alpha) = \frac{1}{n_{run}} \sum_{i=1}^{n_{run}} Q(x_i, y_i, \alpha) \tag{9.7.3}$$

where $Q(\mathbf{x}_i, y_i, \alpha) = y_i - \sum_{j=1}^{n_{run}} \alpha_j \rho\left(\mathbf{x}_i - \mathbf{x}_j\right)$. In this expression, y_i is the function value observed at the i-th data point and α is the vector of weights. For this class of functions however, the difference between the observed objective function, and the predicted value is zero, since the function is constructed so that it is always interpolating.

In the context of statistical learning, a good approximation to the objective function should minimise the generalisation error which takes into account the statistical distribution of $\mathbf{x}_i, y_i$ [80]. This can be done by considering $E(\alpha) = \int Q(\mathbf{x}_i, y_i, \alpha)\, dP(\mathbf{x}_i, y_i)$, where P represents the joint distribution of the sample points and the observed values. Thus E can be approximated using a large number of sample points, but this is impractical when

observations require the use of a time-intensive computational model.

The "leave one out method" is a method that allows the user to estimate the accuracy of the model without the need for additional data. As its name suggests, one of the sample points is left out, and parameters are chosen to minimise E to obtain the model for $Q(\mathbf{x}_i, y_i, \alpha_{n_{run}-1})$. The model can then be run to predict the error at the sample point removed from the dataset. Denoting the loss as a result of removing the k-th point to be, $Q(\mathbf{x}_i, y_i, \alpha_{n_{run}-1}|\mathbf{x}_k)$, the procedure is repeated n_{run} times to obtain the following estimator;

$$L(x_1, x_2, \cdots, x_{n_{run}}) = \sum_{i=1}^{n_{run}} Q(x_i, y_i, \alpha|x_i) \tag{9.7.4}$$

The mean value of the leave one out estimator approaches the mean value of E, as more sample points are taken. In practise this minimising estimator can be an expensive task, as for each sample point deleted, a new surrogate model has to be computed. The procedure by Wang demonstrates that the objective function E can be simplified for the case of multiquadratic basis functions [164].

For multi-quadratics, the error function defined as above, can be recast succinctly using the following form;

$$E = \sum_{i=1}^{n_{run}} \frac{\mathbf{c}_i}{B_{ii}} \tag{9.7.5}$$

where B_{ii} are the diagonal elements of the matrix $B = A^{-1}$. The matrix A is defined as $A_{ij} = \left(|\mathbf{x}_i - \mathbf{x}_j|^2 + h\right)^{\beta}$, and $\mathbf{c}_i$ is the vector of weights α_i, which are determined by solving $A\mathbf{c} = \mathbf{y}$, where $\mathbf{y}$ is the vector of observed objective function values. The derivation of equation [9.7.5] as the function to be minimised is not provided here, the interested reader is referred to [164]. With the aim of minimising this leave one out estimator, the shape parameters h and β are therefore sought. To this end, a gradient based search routine in method has been used to determine these quantities.

Using the original sample data obtained for the purpose of optimisation using the polynomial regression model, and the optimisation technique for the parameters above, the radial basis function has thus been computed. Given that there are approximately fifty sample points computed using the Low Magnetic Reynolds number model, the final form of the function is too long to be expressed onto this page. Instead, a graphical representation of the surface of the chosen domain is presented in figure [64];

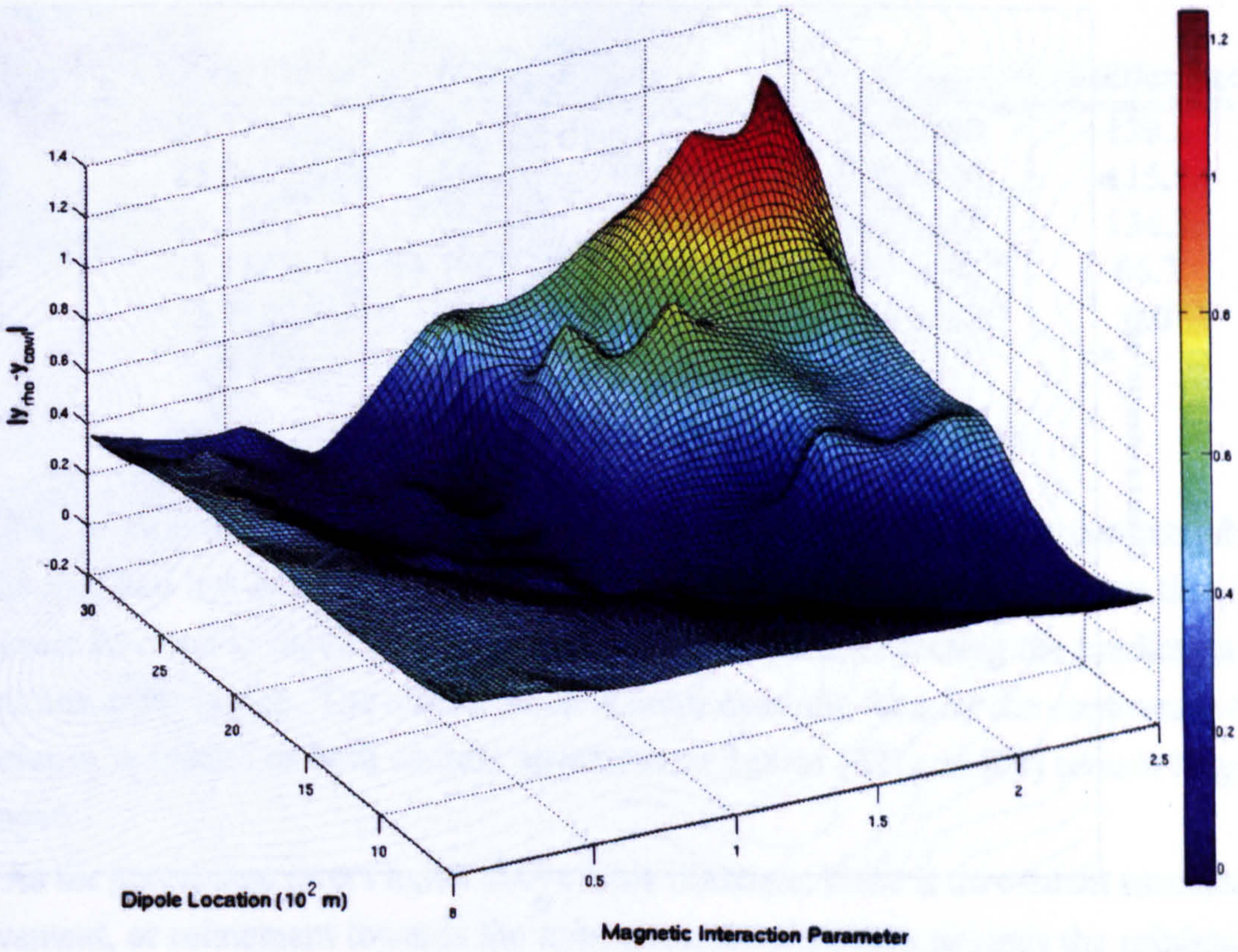

Figure 64: RBF function generated using original sample data

The complexity of the objective function is immediately apparent from the surface representation, and it is quite apparent that a simple quadratic polynomial regression surface will not suffice in adequately representing this type of trend. The contour plot illustrates that there are in fact several local minima present, as indicated by the crosses in figure [65]. The same sequential quadratic programming technique was used to obtain the minimum predicted by the function, although in view of the fact that there are several local minima present, a structured procedure was required.

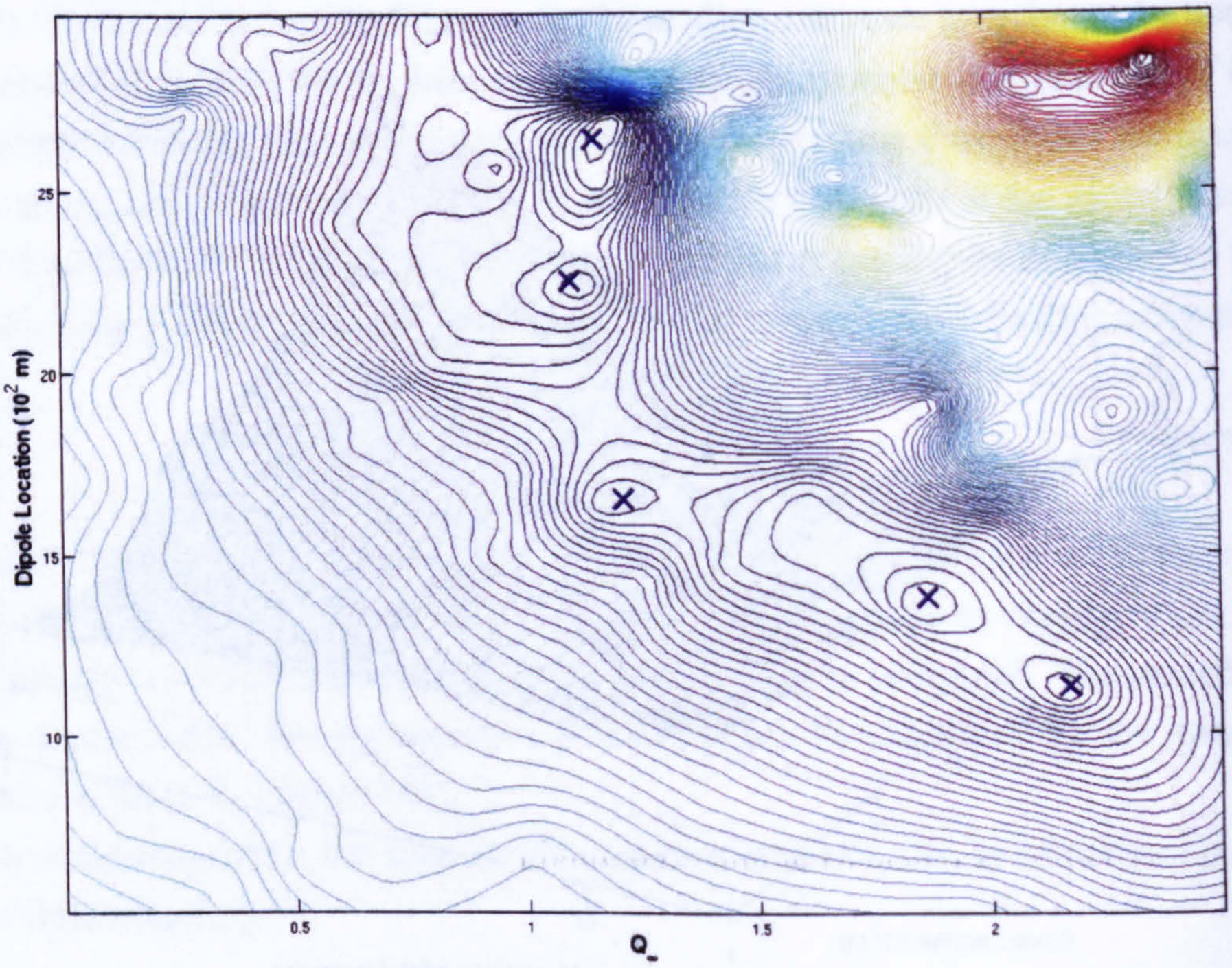

Figure 65: Objective function contours, illustrating multiple local optima

A multitude of initial points are provided to the optimisation routine, and for each one a path to an optimum is found. Of these optima, the smallest is returned as the global minimum of the surface. The set of initial points was set up on a systematic grid spanning the entire domain, thus ensuring all possible outcomes, at least within the domain, can be evaluated.

A similar approach to the iterative method used for the quadratic regression model is utilised. For every radial basis function its global minimum is predicted using the procedure above. For each prediction, the corresponding values for the dipole location, and the magnetic interaction parameter is subsequently passed into the analysis tool, for a deterministic evaluation of the objective function at the same point. Unlike the regression model however, the only extra sample point evaluated using the PNS model is that of the minimum, instead of a region encompassing the point. As radial basis functions interpolate through sample data, it is expected that the predictive accuracy will improve in the neighbourhood of the additional data points as a result of their inclusion. The new sample data point from the PNS routine is added to the sample data set, its new radial basis function computed, and the procedure is repeated. The results of the iterative process are

presented in table [9].

Iteration	x location ($10^2 m$)	Q_∞	Δ_{RBF}	Δ_{PNS}	% difference
1	26.7733	1.1923	−0.027058	0.131800	120.5
2	25.0457	1.1764	−0.0037	0.024500	115.1
3	25.1921	1.1963	−0.0072	0.021000	134.3
4	25.1187	1.1873	1.3331×10^{-4}	1.521×10^{-4}	66.7
5	25.1187	1.1873	1.521×10^{-4}	1.521×10^{-4}	0.0

Table 9: RBF and PNS predictions to objective function

The set minimum points investigated is also superimposed on the contour plots after the first and last iterations, in figure [66]. It is evident from the contours that the radial basis function is modified considerably in this region, reflecting the prediction of new minima at every step. The modification is more dynamic than for the contours in the least squares fit model, as both contour structures in figures [62] and [63] remain largely unchanged.

As the percentage errors in the above table illustrate, there is no evident successive improvement, or refinement towards the minimum, for each step towards the minimum. This type of behaviour is more evident for polynomial regression, where the region of interest can be identified. As discussed earlier, for this two-dimensional surface, ascertaining the region of interest is non-trivial, as within the data set of observed samples, there exist several local minima, which may be masking the global minimum.

Thus said, based on the sample points obtained thus far, the use of radial basis functions does at least provide the global minimum after only five iterations. Also, for each individual iteration, it is possible to argue that radial basis functions are more useful than the quadratic least squares fit, as the PNS objective function values returned from inputting the predicted minima are considerably smaller for the radial basis function , than the quadratic model.

However, it is also important to note that some of the values predicted are negative and are therefore unphysical values for a function that can never exhibit this behaviour. One must therefore exercise caution when using the model. Also, despite the smoothing as result of the parameter optimization used, the quality of a radial basis function is only truly accurate at the points sampled using the analysis tool. The surface profile is strongly dependent on the distribution of sample points, and the latin hypercube sample used, illustrated in figure [[61]], shows that there may still be regions that could be sampled more. There are local minima between where the objective function is greatest, $(x, Q_\infty) = (30.0m, 2.5)$ and the minima predicted above. Hence the graph is certainly not monotonic in this region were one might expect it to be. The appearance of unphysical optima

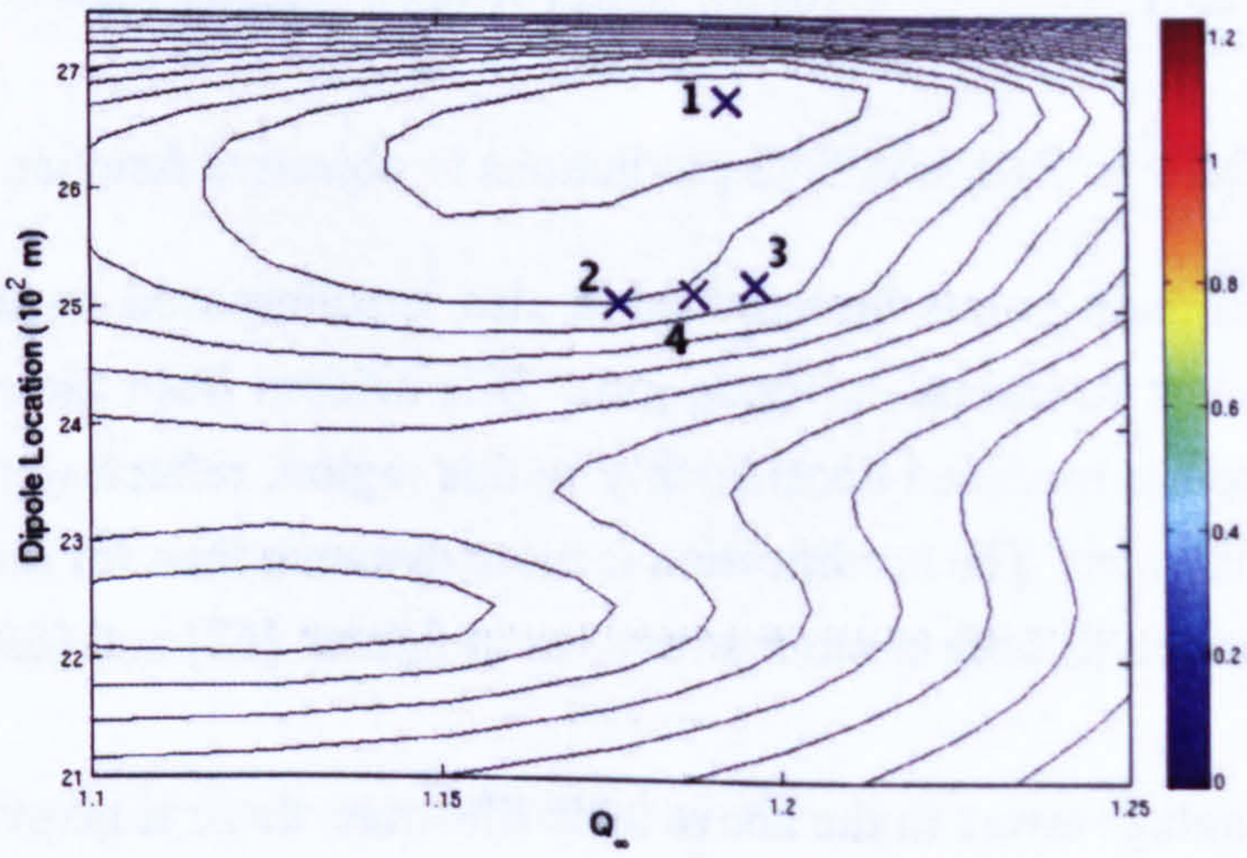

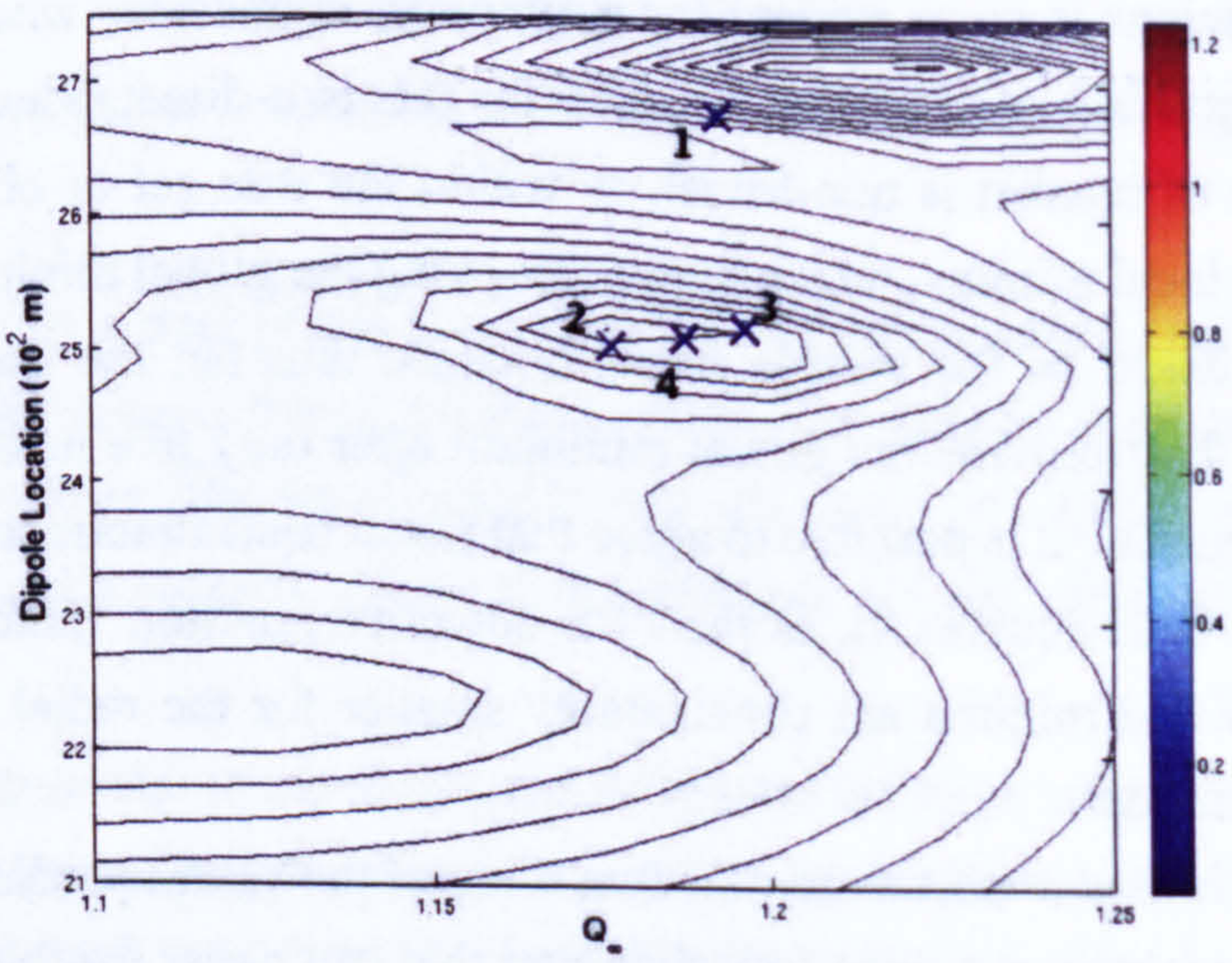

Figure 66: Contour Profiles near global minimum, after 1 (top) and 5 (bottom) iterations

is unfortunately one of the disadvantages of radial basis functions , and is documented widely in literature.

The problems associated with creating a surrogate model of this surface can be attributed to the properties of the approximation function, but it also worth noting that there are some issues relating to the observed data itself. For example the objective function can in some instances be insensitive to slight perturbations in either one of the input variables to another. To understand this, consider figure [67].

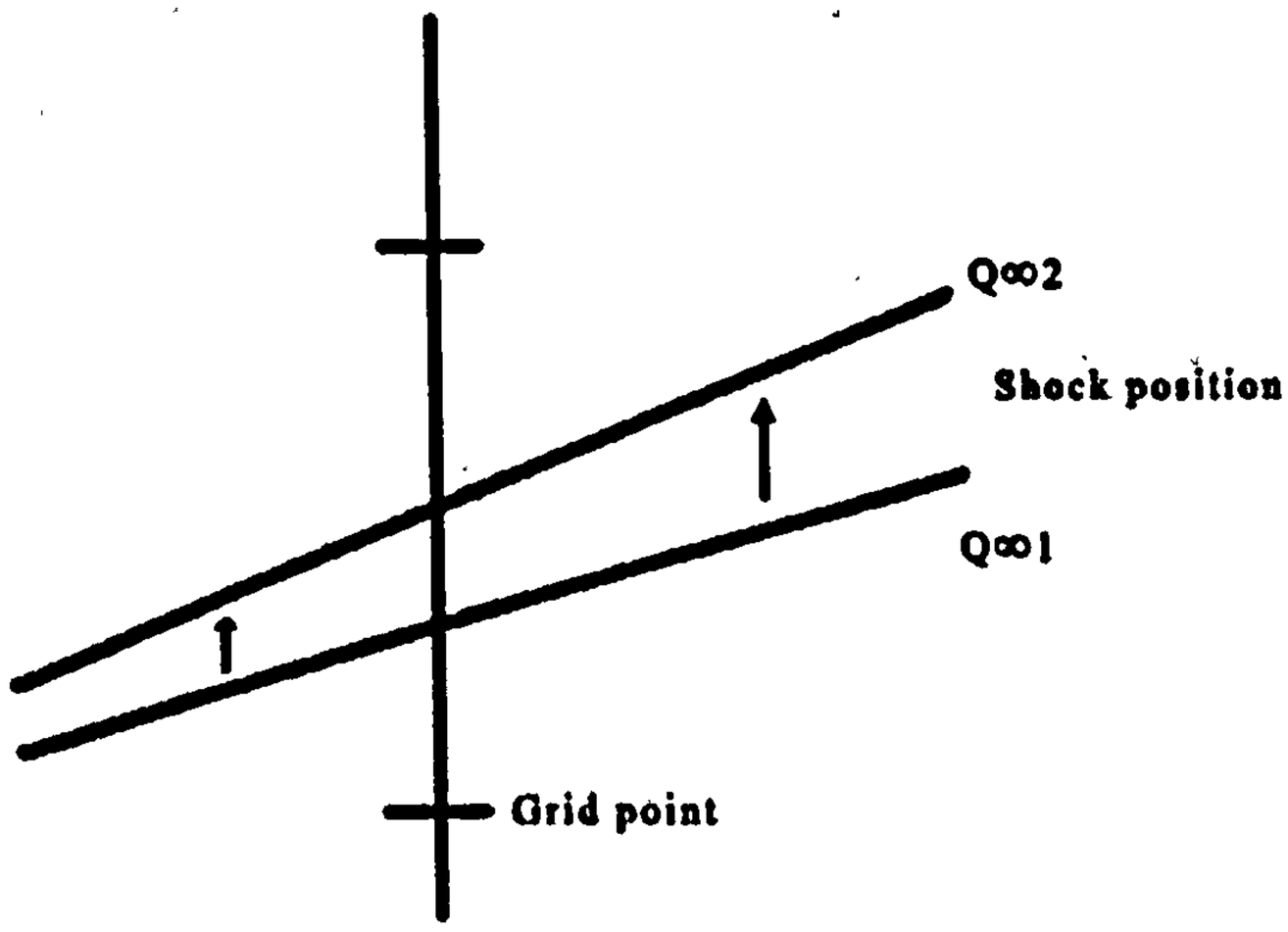

Figure 67: Effect of a small change in Q_∞

The original shock location, for a given value of magnetic interaction parameter Q_{∞_1} is taken to be the central location, between the two grid lines either side of it. Next, suppose that the magnetic interaction parameter is increased slightly, to Q_{∞_2} resulting in the effect of a decelerated flowfield. This would result in an increase in the shock angle, and a corresponding shift upward in the conical shock as shown. If however, the change in Q_∞ was so subtle that the shock position did not shift beyond the grid line above the original shock, then for all intents and purposes, the shock will remain in exactly the same position, as far as the calculation is concerned. A natural remedy to this problem would be to include additional grid points, but no matter how small the spacing, the grid is always discrete, and therefore there will always be circumstances where incremental changes of the input variables will not be accurately reflected as a change in the objective function value.

Although improvements can be made on the surface with more sample points, the radial basis function nevertheless returns a global minimum whose objective function value is in agreement with the PNS results. The minimum returns a value of $Q_\infty = 1.1873$, corresponding to a magnetic field with strength $B_0 = 0.4T$. This demonstrates the fact that the same desired effect of shock on lip can be achieved through a judicious choice of

the location of the field source. Recall that for the dipole in fixed position in section [9.4], the optimum field strength was determined to be $0.6T$. A natural extension of this study would therefore be to investigate whether a further improvement can made to this value, either through additional sampling, or via widening the design space.

9.8 Conclusions

The problem was posed as to whether the flow around a hypersonic ramjet inlet operating at off design conditions could be modified to ensure design operating conditions through the use of a magnetic field as a means of an external body force. With no experimental data to compare baseline cases in the absence of a magnetic field, the initial task of determining the optimum operating Mach number for the geometry was determined to be $M_\infty = 6.0$, having simplified the geometry to allow rapid use of the analysis tool. It is important to note that the unavailablity of comparison data makes verfication of the current section a challenging task. Thus although the optimisation algorithm returns the design Mach number stated in numerous works within the literature, due caution must be exercised when looking at results where magnetic field effects are included, as these cannot be measured against any other data source.

An off design operating condition, which in reality would lead to vehicle unstart, was chosen to investigate the influence of a magnetic field. The operating Mach number was chosen to be greater than its design value, and for a magnetic field generated by a dipole at fixed location, an optimization investigation using a quadratic least squares regression model as a surrogate form, identified an optimum magnetic field strength that would ensure the shock on lip condition.

Using the location of the magnetic field source as another design variable, it was also found that shock on lip can also be achieved for a smaller magnetic strength, if the dipole location was chosen wisely. As the generation of magnetic fields ultimately requires energy, reducing this cost is just as important as ensuring design conditions. The study revealed a counter intuitive notion that there were instances when smaller peak values for the Lorentz force generated were still sufficiently strong enough to ensure the flow decelerated to the required amount. It was discovered that not only does the peak Lorentz force play an important part in ensuring optimality, the extent of the region of influence of the field was just as important. Depending on the location of the dipole, there are positions where the influence of the field is wider than for other locations, given the same field strength, and are therefore able to decelerate the flow over a wider region.

The optimization procedures have been carried out using quadratic polynomial least squares regression models and radial basis functions as surrogate models of the objective

function. The surfaces are substituted into a SQP module for determination of various optima. For the single variable cases investigated to determine the design Mach number, and the optimal magnetic interaction parameter for a fixed dipole, the regression model proved to be adequate to isolate the required points. Although the predicted values for the objective function were found to differ compared to the observed data, the model was able to predict global minima as additional data was added to the region of interest.

The same cannot be said for the two variable test case involving variable field strengths and dipole location. Successive addition of sample points in the optimum region predicted by the regression model does not result in improved prediction capability. This can be attributed to the fact that the second order model is too simplistic to accurately identify the trends correctly. However, radial basis functions were able to predict the global optimum after several iterations. The downside is that they can result in unphysical behaviour, and as the resultant surface is more oscillatory than the regression model, the search procedure for the global minimum takes longer.

CHAPTER 10

MHD Control of Slender Body

10.1 Introduction

In this chapter a novel application of magneto-hydrodynamics on slender body aerodynamics is presented by applying the low magnetic Reynolds number model to examine the ability of magnetic fields in generating forces on slender bodies. The objective of the current section is to demonstrate the potential of magneto-hydrodynamics in generating side forces for cases that would otherwise not generate such forces. A parametric study investigating the effects of angle of incidence, streamwise dipole location and radial dipole location is performed to examine the extent of force generation under different operating conditions. Baseline test cases, in the absence of any magnetic field are included and compared to available experimental data, to provide confidence in the unmodified IMPNS solver. However, as it was outlined in the previous chapter the lack of comparative data for cases involving magneto-hydrodynamics means that caution is required when interpreting the results of applying magnetic fields to slender bodies.

10.2 Slender Body Flow Control

Interest in controlling missiles and projectiles is a subject that has received considerable interest from the aerospace research community. The primary concern is to do with accurate payload deployment, and with additional mission requirements that require highly evasive manœvres at incidence. It has been recognized for a while that axisymmetric slender bodies of revolution operating at incidence encounter cross flow separation and vortices, which at higher angles of attack result in vortex-induced yaw due to asymmetric cross flow vortex shedding [88]. Understanding the conditions under which side forces are generated have gained interest. Ericsson and Reding argue for example that asymmetric vortices are formed when the angle of incidence exceeds the total induced angle at the body tip [54]. This is not the case for supersonic flow, however, as vortex shedding emanates from the wake.

It has also been noted that geometrical asymmetries on the body itself, such as dents or imperfections on the surface are also attributable to side force generation [53]. Moskovitz et al. [108] also show that perturbations of any size that violate body symmetry

may cause flow asymmetry. Numerical simulations of Degani and Schiff [47] further identify the fact that stronger asymmetries are generated for perturbations that are located closer to the apex.

Traditional control surfaces are particularly ineffective at larger incidences, as the side forces may become especially evident. In designing and manufacturing agile combat vehicles, there may also be uncertainty in the direction of the side force , and is therefore a very important issue. This results in limiting the performance of a projectile in the worst case, although significant research has been dedicated to the exploitation of such forces, as well as in trying to limit its effects when present. Thus the interest from aerodynamicists has focused on the use of numerous control devices designed to alter the vortical structures emanating in the wake of slender bodies operating at incidence, so that this side force can be attenuated to obtain a degree of control over the yawing moment.

In one such example, Garon et al.[58] make use of MEMS devices within the nose region of a slender body for subsonic and supersonic flows. The presence of the device is shown to increase pitching moment and normal force for the subsonic case, although little change for the supersonic case is observed, apart from an increase in drag. In experimental and computational studies, Corriveau et al. have shown that flow effectors mounted in the nose region of a projectile have positive effects in generating side forces at moderate angles of incidence [33, 63, 34]. They demonstrate that the maximal side force generated, for any given angle of incidence is strongly dependent on the azimuthal location an individual deflector, as well as on its proximity to the body tip. The resultant vortex structure is modified, yielding higher pressures on the side of the body over which the deflector is placed, thus yielding side force. Using a similar technique based on deployable flow effectors, Patel et al [118] devise a closed loop control system, whereby the protuberances may be activated dynamically depending on pressure tapping readings located further downstream along the body surface.

While the above works have focused on making the most of artificially generating yaw through control devices, research has also focused on attempts to try and restrict side force generation, particularly at higher incidences. For example, Ng [115] carried out experiments to assess the effectiveness of a strake located along the nose of a slender body. For angles of attack less than 50°, the effects of its presence were not particularly noticeable, but for 50° and 60°, the strake was able to reduce vortex asymmetry. Stahl was able to show a similar effect using fins located on the leeward side of a circular cone, for subsonic flows [150]. Modi and Stewart investigated several passive flow control procedures to alleviate side force generation. This included delta strakes, porous tips and spinning tips, and were found to reduce side force from between 50% and 88%. Fisher and Cobleigh show that longitudinal boundary layer trips were able to reduce yaw at angles of

incidence greater than 60° [55], while using an altogether different approach, Roos [135] employed blowing on the nose region to suppress side force generation. Helical strips mounted over the whole length of the body [129], and the use rotating tips on the nose of the projectile coupled with strakes [101] have also gained attention.

The above research provides indication as to some of the active and passive flow control devices targeting vortex structures, that are used for the end goal of either side force generation or inhibition. As manned flight explores the potentials of hypersonic velocities, so too has the delivery mechanism for projectiles. Indeed, hypersonic flight has long been achieved through the advent of such projectiles such as inter-continental ballistic missiles. The above flow control devices face two major problems in the hypersonic regime. Firstly, it is highly likely that the protuberances introduced above will have to endure greater loads at higher velocities, and therefore be susceptible to mechanical failure. At hypersonic velocities heating also becomes an issue, and hence one is left with the additional problem of having to ensure such devices are heat tolerant throughout the flight envelope. The second is that the faster a projectile is to travel, the faster the actuation speeds must be for any given flow control device. Knight points out that the response time for a mechanical or electro-mechanical control system for high speed flows may be measured in tenths, or at smallest, in hundredths of a second [83]. This may be acceptable in the supersonic regime, but as the speed domain of future vehicles becomes greater, such actuation speeds are more than likely to become unacceptable.

Magneto-hydrodynamic systems in contrast have actuation times of the order of nanoseconds. In addition to this they have the advantage that no moving components are exposed to the external flow, and are thus better suited to the hypersonic operating environment. From identifying such benefits of magneto-hydrodynamics , and in view of the inherent control problems faced by slender bodies operating at supersonic/hypersonic velocities, it would be a natural extension to impose magnetic fields on such flow problems. Chapter 9 made use of the control properties for an over-sped ramjet intake. In this chapter, the concept is extended to the problem of trying to generate side forces, by artificially introducing asymmetries into the flow. Dipole fields typically result in axisymmetric orientations, although they may be exploited to produce asymmetries by positioning its source at different locations. The present study investigates the potential for side force generation through imposing a field to generate disturbances, in a manner similar to methods used by Patel et al. [118] and Corriveau et al. [33, 63, 34].

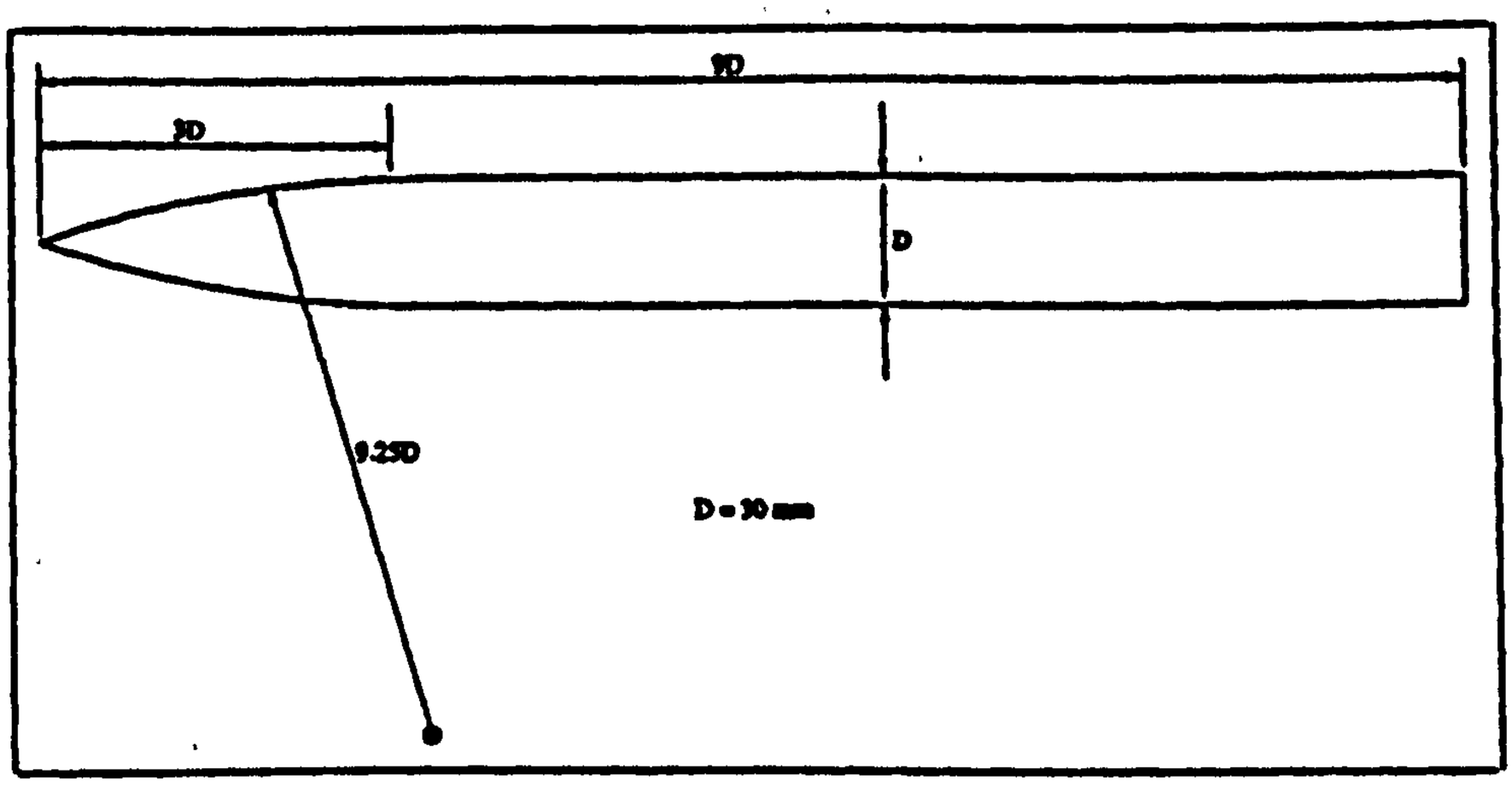

Figure 68: ONERA B1 Slender Body

10.3 Baseline Case: No Field

To obtain confidence in the baseline calculations, a series of tests have been made to compare the predictive accuracy over a slender body, in the absence of any magnetic field . The geometry to be considered is the tangent ogive slender body examined experimentally at ONERA. It has been chosen due to its relatively simple profile, with no wings or fins present. Primary interest is on the effects of magnetic interaction on the body, and it is therefore convenient to choose a body without the complexities of additional geometry. The b1 body under investigation is shown in figure [68].

The operating conditions for the baseline case are as follows; the incident Mach number has been fixed to $M_\infty = 2$, and the freestream temperature is $T_\infty = 183.33K$. The Reynolds number based on body diameter is given by $Re_\infty = 0.16 \times 10^6$. The flow is assumed to be laminar, and an adiabatic wall boundary condition is applied on the body surface. The experimental database includes sample data for turbulent calculations, however in view of the fact that this requires additional computational time, and since interest is in the interaction of the flow with the magnetic field , only laminar results are presented here.

A test case of $M_\infty = 2$ was chosen because, as the subsequent sections of the chapter will show, one is able validate the results of the IMPNS code to relevant experimental data. As the introductory sections of this chapter outlined, the current section is purely theoretical, given that there is no data to compare the effects of applying a field. Thus it is useful to compare experimental data to a baseline case, in the absence of the field, so that one can ensure confidence in the results presented later in the chapter.

10.3.1 Grid and Iterative Convergence

Examination of the predicted lift and drag coefficients, for incidences of zero and ten degrees is performed for grid and iterative studies, prior to comparison with experiment, as a necessary means of ensuring sufficient convergence in solution. The effects of changing the iterative tolerance, and the grid density on lift and drag coefficients are presented in tables [10] and [11]. Note that in the tables below, no data for side force is presented, as the flow is assumed to be symmetric about the plane $y = 0$, for the no magnetic field calculations. Thus all side force coefficient values are identically equal to zero.

Conv. Tol	C_D	C_L	Grid Level	C_D	C_L
10^{-6}	0.1389101	0.0017850	$31 \times 43 \times 23$	0.1365621	0.0035610
10^{-7}	0.1427760	0.0011626	$60 \times 85 \times 45$	0.1436124	0.0008521
10^{-8}	0.1436124	0.0008521	$123 \times 171 \times 91$	0.1466624	-0.000049

Table 10: Iterative and Grid Convergence $\alpha = 0.0°$

Conv. Tol	C_D	C_L	Grid Level	C_D	C_L
10^{-6}	0.3207150	0.9353284	$31 \times 43 \times 23$	0.3234276	0.9576335
10^{-7}	0.3298616	0.9364198	$60 \times 85 \times 45$	0.3333508	0.9360126
10^{-8}	0.3313508	0.9360126	$123 \times 171 \times 91$	0.3356595	0.9438961

Table 11: Iterative and Grid Convergence $\alpha = 10.0°$

For the zero incidence calculations, the lift coefficient value approaches zero as the convergence tolerance is decreased, and the number of grid points is increased, which is to be expected. The percentage differences in C_L values between successive tolerance and grid levels is considerable for this case however. For example, there is a 36% difference in lift coefficient values for the 10^{-7} and 10^{-8} iterative convergence tolerance levels, and an even greater difference for the two finest grids. In view of this, using lift coefficient on the zero angle of incidence case is not a good measure of the extent of convergence due to the high variability in values. At higher incidence however there is a better indication of the criterion required for sufficient tolerance. For the lift coefficient, there is a 0.1% difference between the 10^{-6} and 10^{-7} levels, and a 0.7% difference between the two finest grids, suggesting a 10^{-6} convergence criterion on a $60 \times 85 \times 45$ grid is sufficient.

Drag coefficient values are more sensitive to these parameters however, as the data indicates. At zero incidence, a 2.8% difference is observed between 10^{-6} and 10^{-7} convergence levels, and only 0.7% between 10^{-7} and 10^{-8}. A similar trend is observed for

the $\alpha = 10.0$ case; a 0.6% discrepancy in drag coefficient between 10^{-7} and 10^{-8} criteria. In terms of grid convergence there is a 2% difference for the finest two grids, for zero incidence, and at 10 degrees, comparison over the same grids returns a 0.6% difference. From this analysis, it is possible to infer that a smaller convergence criterion is required to ensure sufficient convergence. A tolerance of 10^{-7} is sufficiently small to ensure that the relative difference compared to the next level is less than one percent. The grid chosen remains the same as that inferred from analysing the lift coefficient data, as the case at 10° incidence shows little variation to the value on the finest grid.

Although the simulations in the current case do not result in any side force being generated, due to the symmetry of the problem about the $y = 0$ plane, it is nevertheless necessary to ensure that factors which may contribute to side force are sufficiently converged. To this end, circumferential pressure coefficient variations are considered at several streamwise stations, along the body surface. Analysis of the pressure coefficient profiles by comparing the convergence tolerance level indicate minimal variation between the 10^{-6} and 10^{-7} cases, further indicating that iterative convergence is achieved at the same tolerance level as for the analysis of the forces data. Figures [69(a)] to [69(d)] show the surface pressure coefficient distributions on three grids of variable density, compared to experimental data. The same grids were used as for the examinations performed on the lift and drag coefficient data, and the computations were run at an incidence of $\alpha = 10°$. Pressure coefficient data, from the windward side of the body ($\theta = 0°$) to the leeward side ($\theta = 180°$) are plotted along the surface at $x = 4D$, $x = 6D$, $x = 7D$, and $x = 8D$. All figures show that there is little variability in the pressure coefficient distribution for the three grids on the windward side, up to approximately $\theta = 70°$, although beyond this point the profiles begin to differ. The grid density in the circumferential direction has a strong impact on the solver's ability to capture cross flow separation, hence the discrepancy in profiles.

Agreement to the experimental data improves with increasing streamwise location. The most notable region of discrepancy is in capturing the primary separation point, occurring at $\theta \approx 90°$ for $x = 4D$, according to the experimental data. The graphs indicate that this point moves windward with increasing streamwise location; the parabolized Navier Stokes data demonstrates that it is able to pick up on this phenomenon, predicting the separation point accurately. The exception is for the $x = 4D$ profile however, the computed results predicting that separation takes place more towards $\theta = 100°$. In addition to the separation point, the magnitude of pressure coefficient value at separation also improves as one examines downstream data.

Prince points out that the experimental measurement error in pressure coefficient is greater towards the nose of the slender body [125]. The discrepancy observed in figure

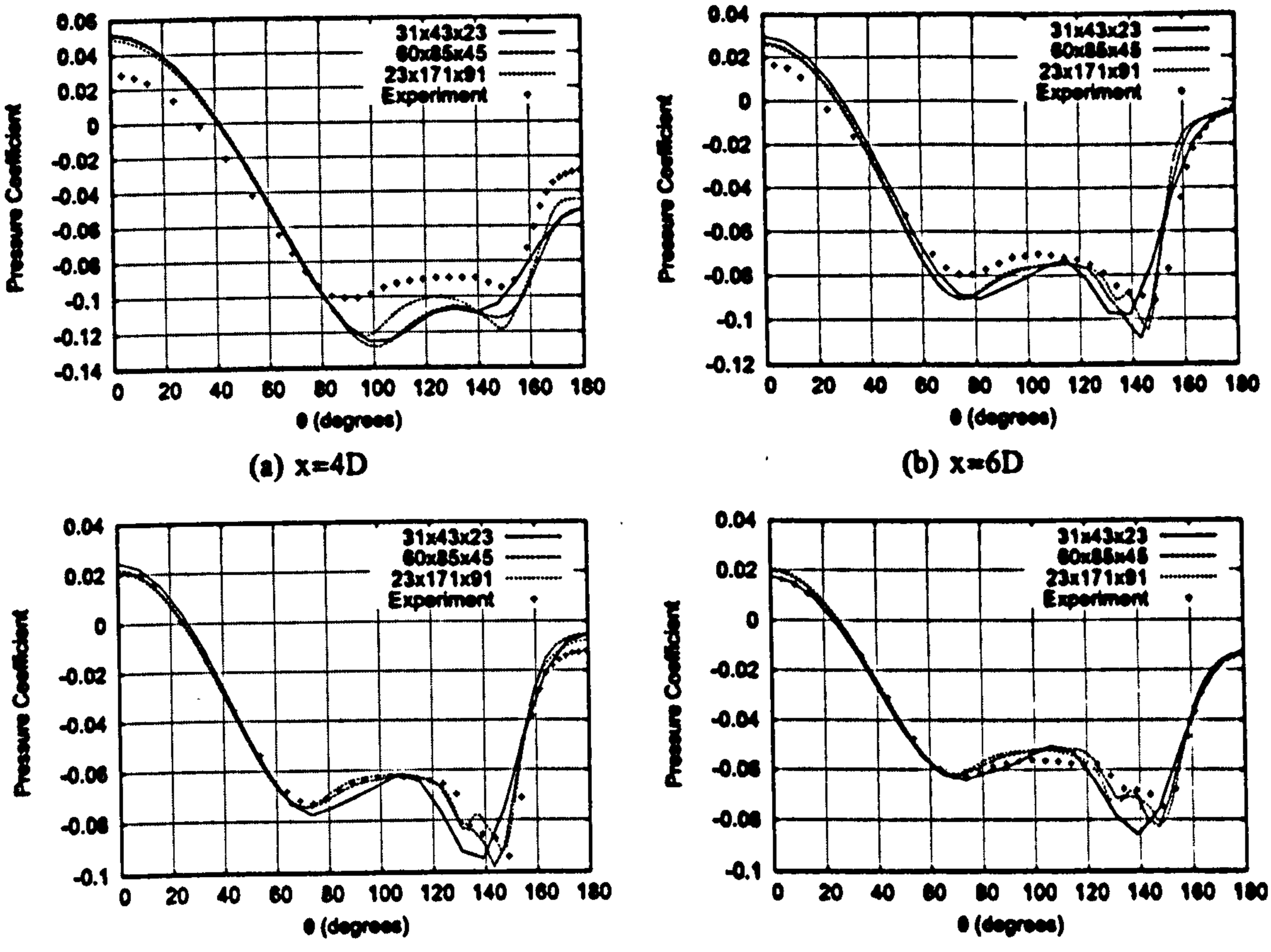

(a) x=4D

(b) x=6D

(c) x=7D

(d) x=8D

Figure 69: Circumferential Pressure Coefficient Distributions, on Three Grids

[69(a)] may be explained by the fact that over the nose area, the boundary layer displacement thickness is smaller, resulting in larger streamwise pressure gradients. Consequently there is a larger element of variability in pressure coefficient measurement, resulting in measurement uncertainty. There is limited variation between the two finest grids in the above figure, providing further evidence that the $60 \times 85 \times 45$ is sufficient in resolving the flow field adequately.

10.3.2 Comparison with Experiment

With an adequate convergence tolerance and grid density defined, the following section makes direct comparison of parabolized Navier Stokes results to the remaining experimental data presented in [11].

Circumferential and axial pressure coefficient variations are examined at angles of incidence of $\alpha = 0°, 5°, 10°, 15°$. The experimental dataset includes both laminar and turbulent calculations, but in the present instance, the concern is with the interaction of the

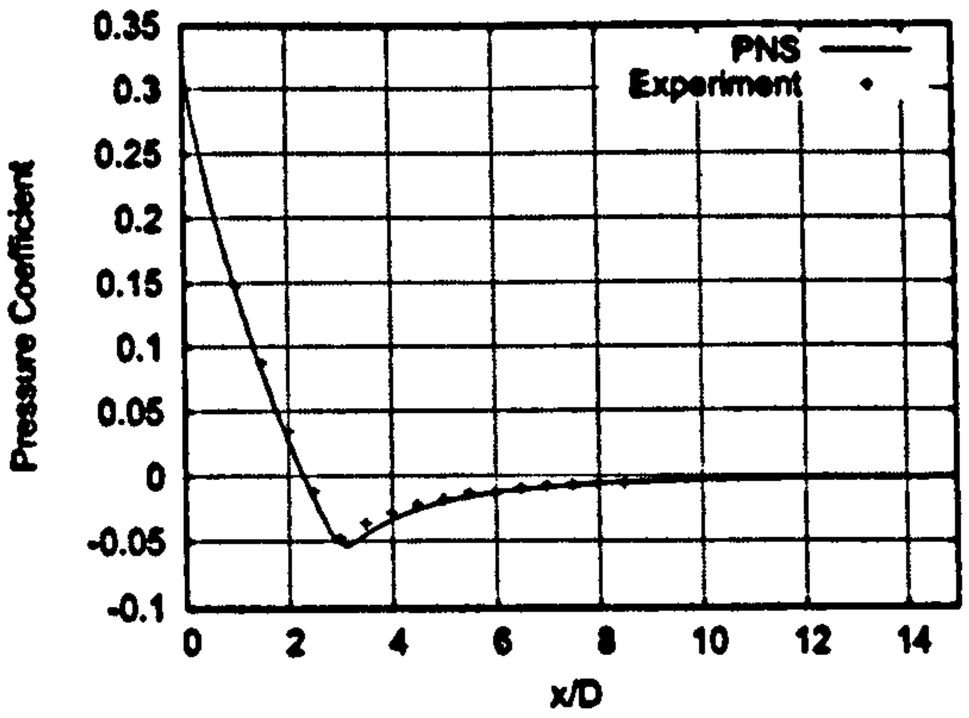

(a) $\alpha = 0°$

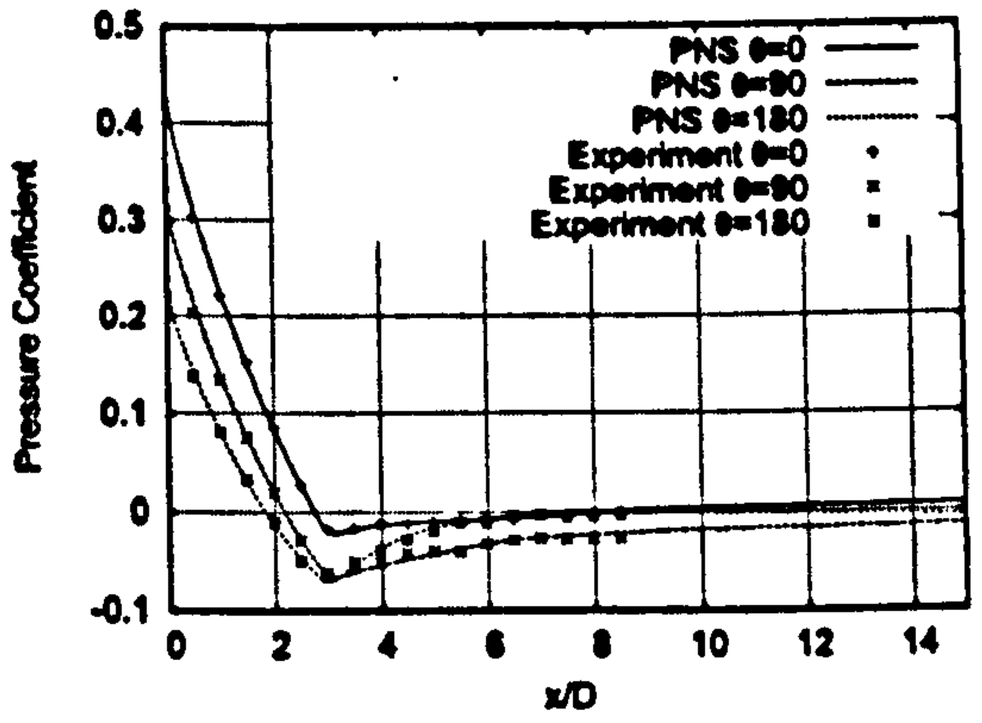

(b) $\alpha = 5°$

Figure 70: Axial Pressure Coefficient Distributions

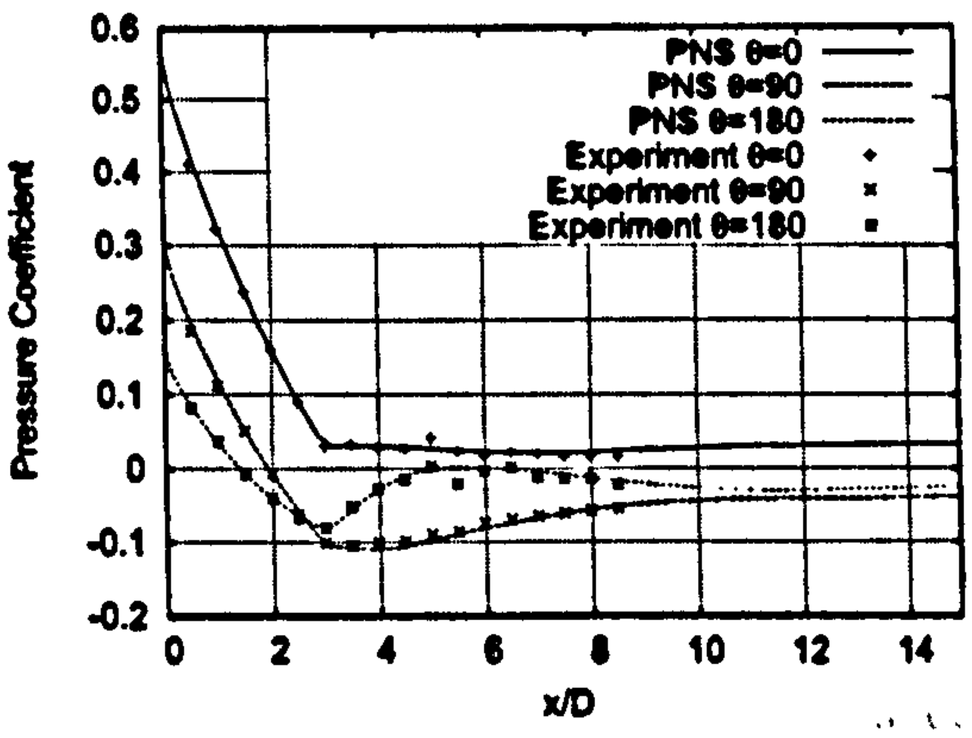

(a) $\alpha = 10°$

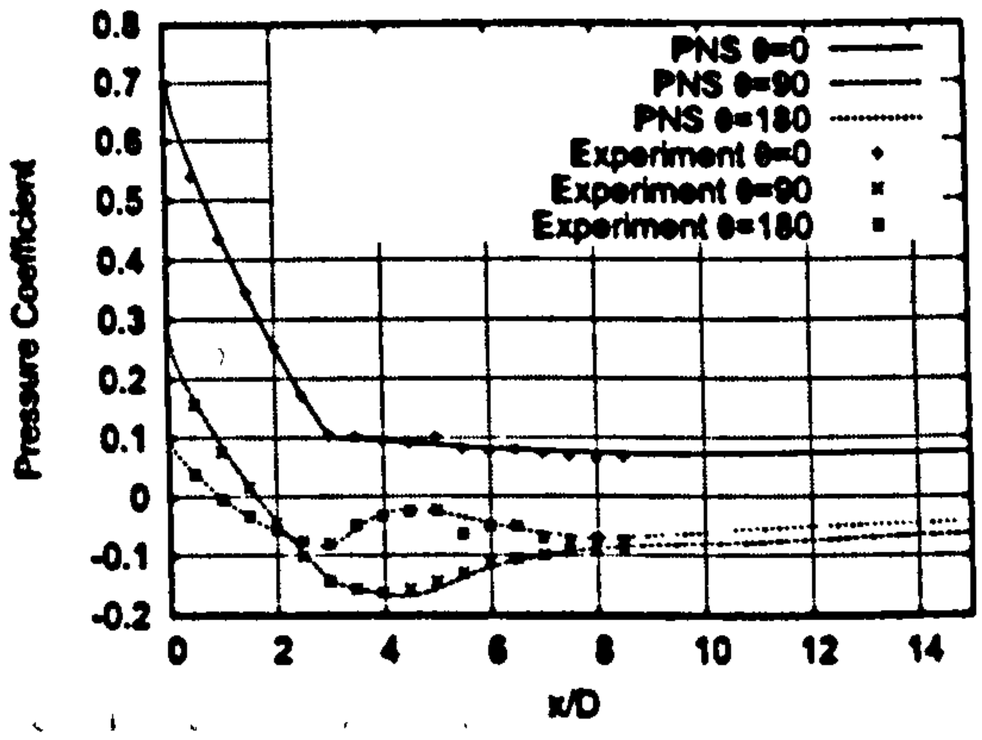

(b) $\alpha = 15°$

Figure 71: Axial Pressure Coefficient Distributions

magnetic field with flow, and therefore, to avoid further uncertainty in the modelling due to the presence of turbulence models, only comparisons to the laminar experiments are made. Figures [70] to [71] represent pressure coefficient distributions on the body surface, against axial location. Profiles for three azimuthal locations are provided, except for the zero incidence case, since the flow is axisymmetric in this circumstance. For all incidence angles, the PNS solutions show good agreement with the experimental data, for all azimuthal angles considered.

Circumferential pressure coefficient profiles for non-zero incidence calculations are presented in figures [72,73,74]. For each angle of incidence, stations $x/D = 3, 4, 6, 7, 8$ are examined.

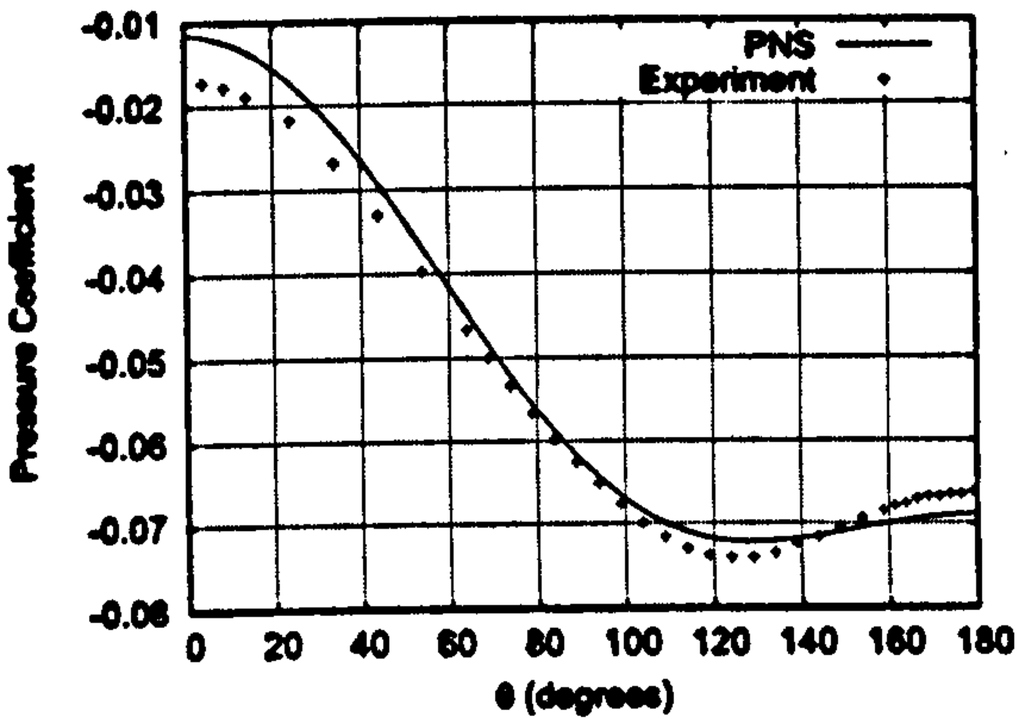

(a) $x = 3D$

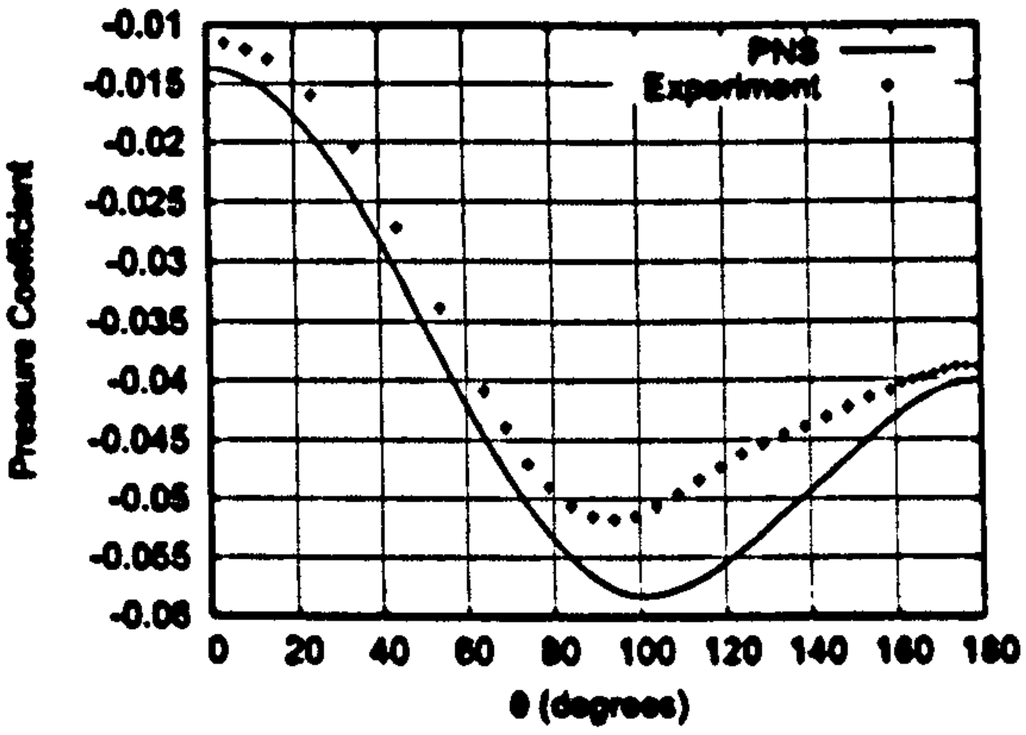

(b) $x = 4D$

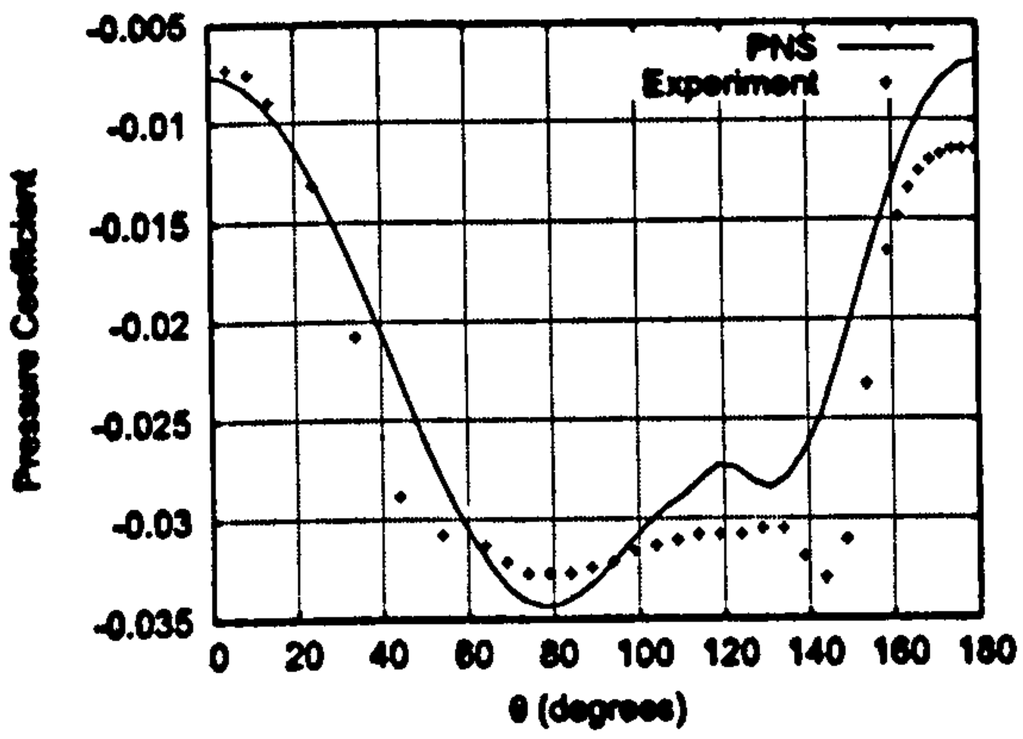

(c) $x = 6D$

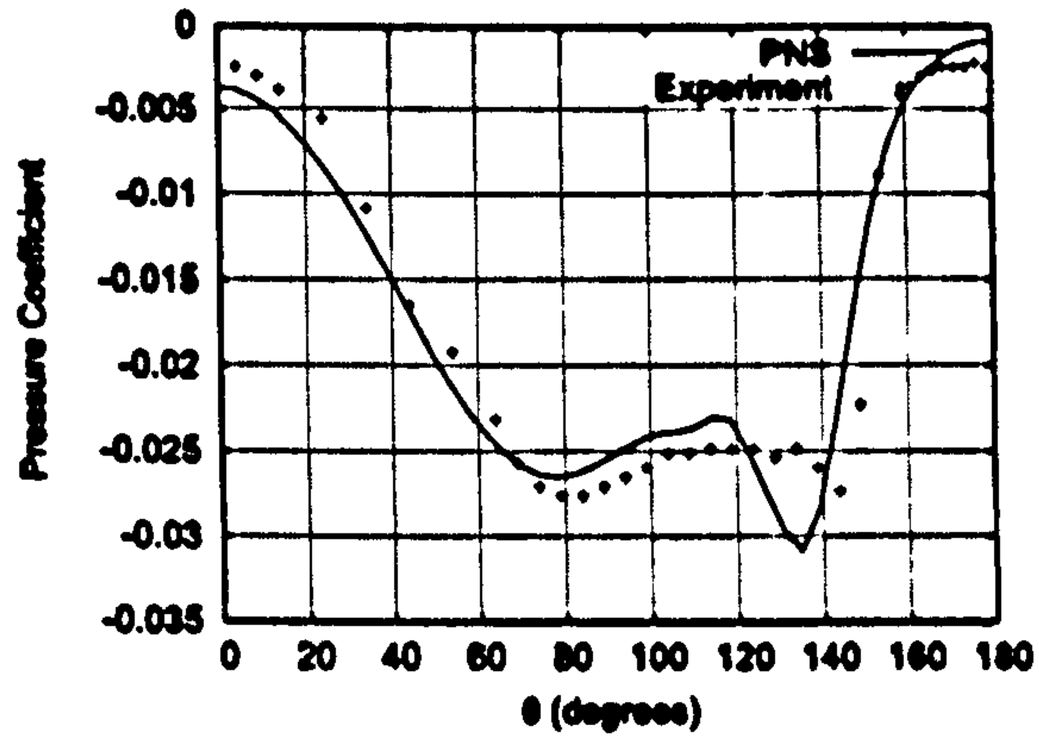

(d) $x = 7D$

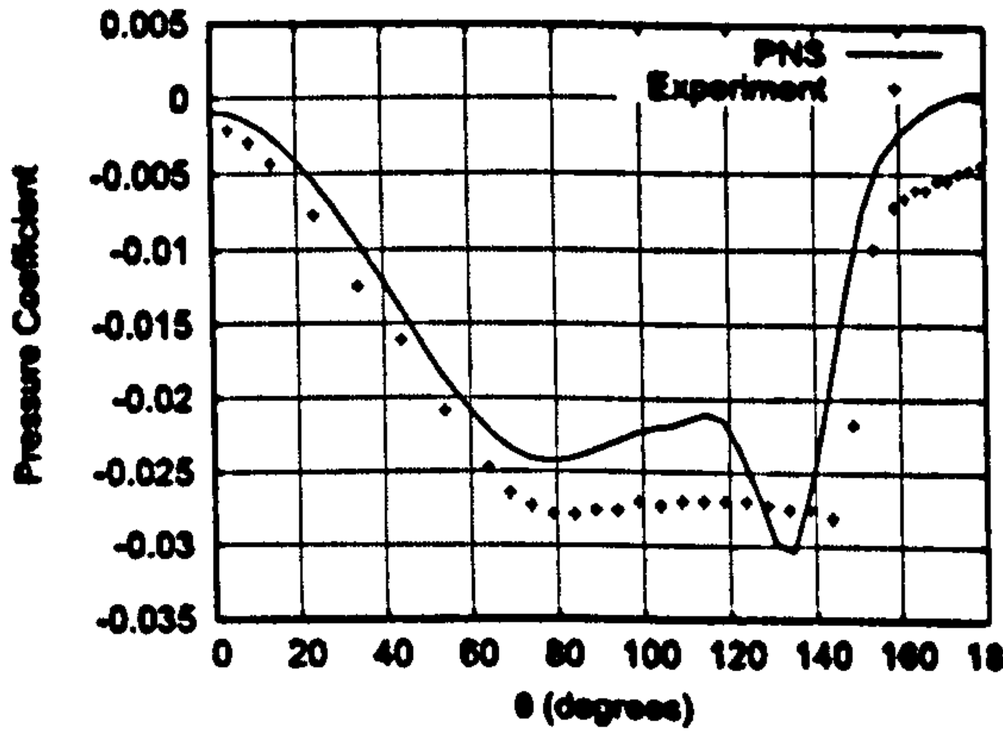

(e) $x = 8D$

Figure 72: Circumferential Pressure Coefficient Distributions, $\alpha = 5°$

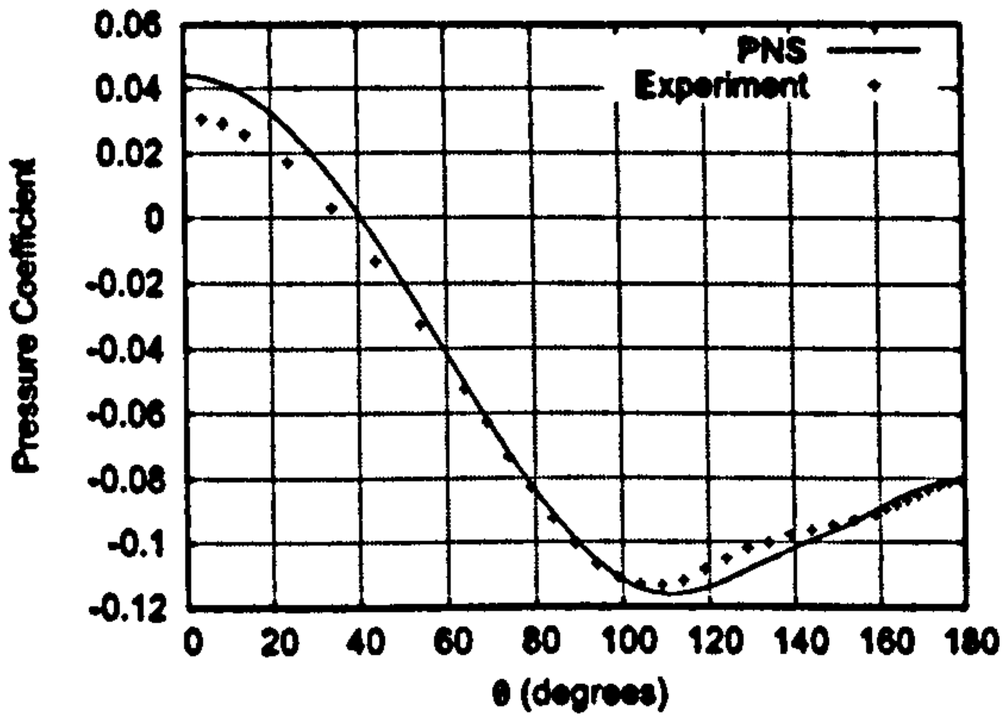

(a) $x = 3D$

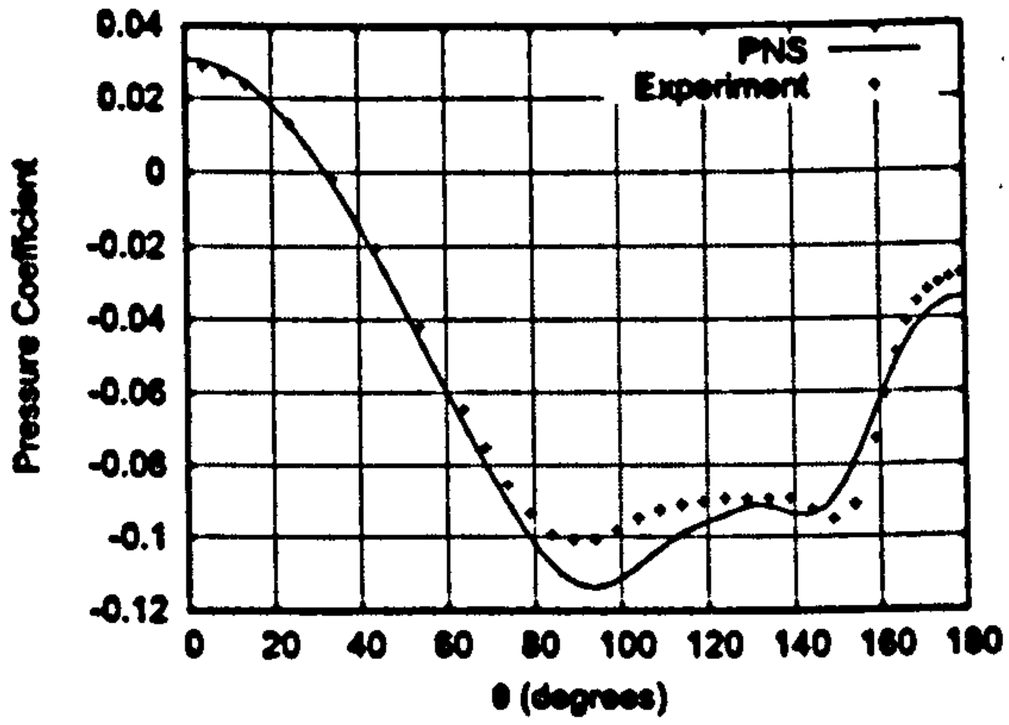

(b) $x = 4D$

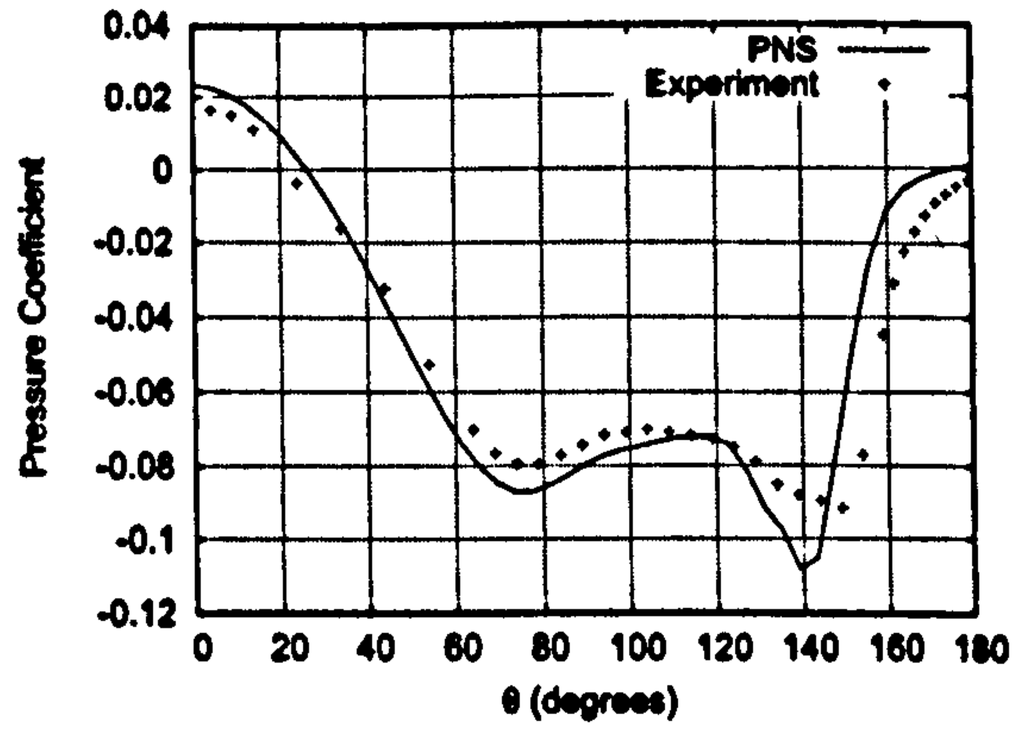

(c) $x = 6D$

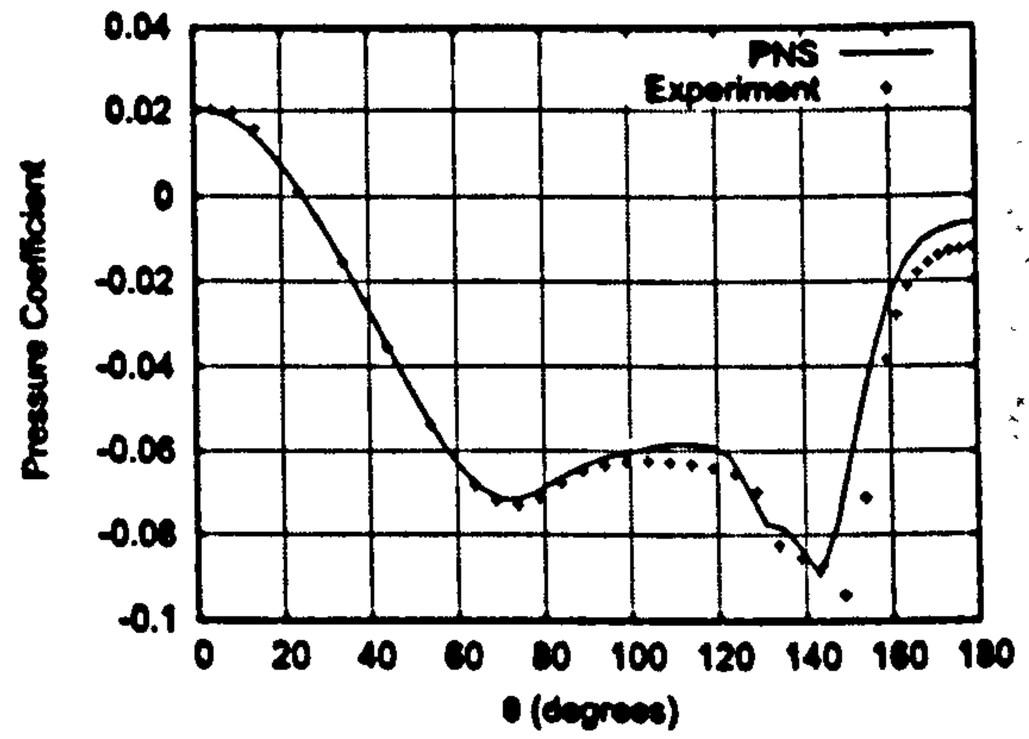

(d) $x = 7D$

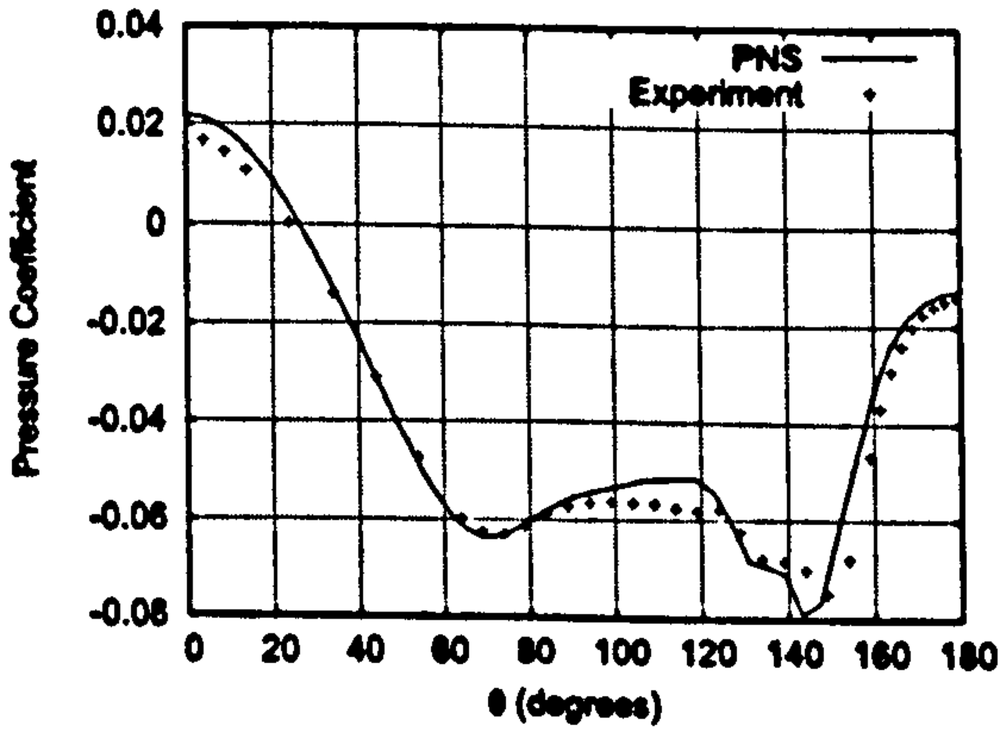

(e) $x = 8D$

Figure 73: Circumferential Pressure Coefficient Distributions, $\alpha = 10°$

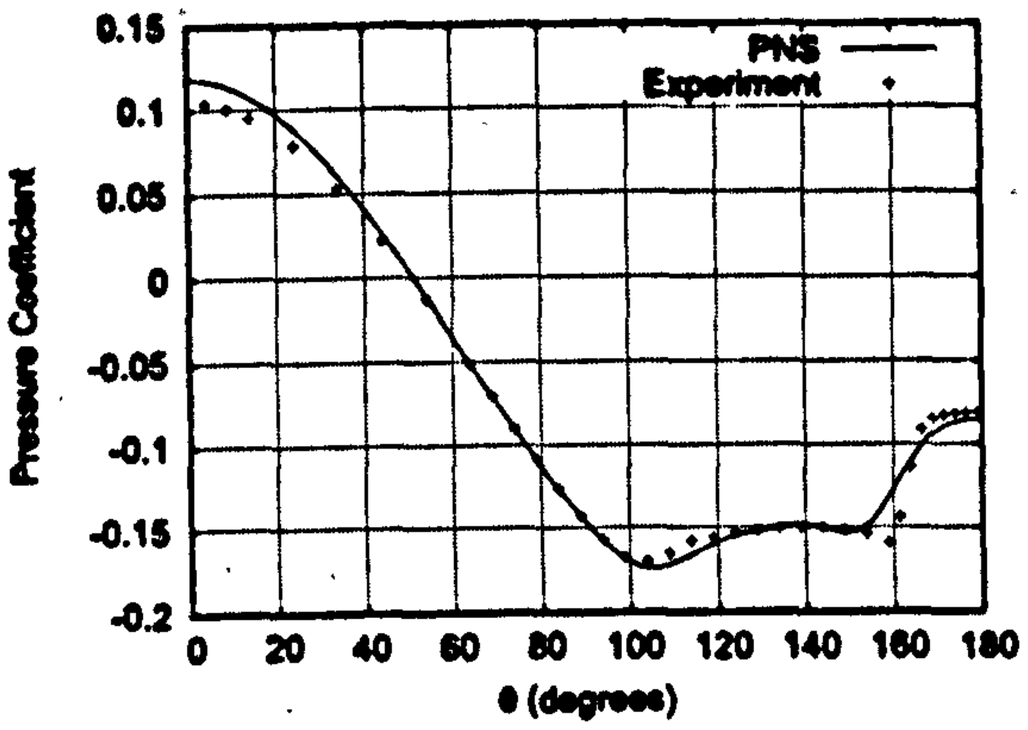

(a) $x = 3D$

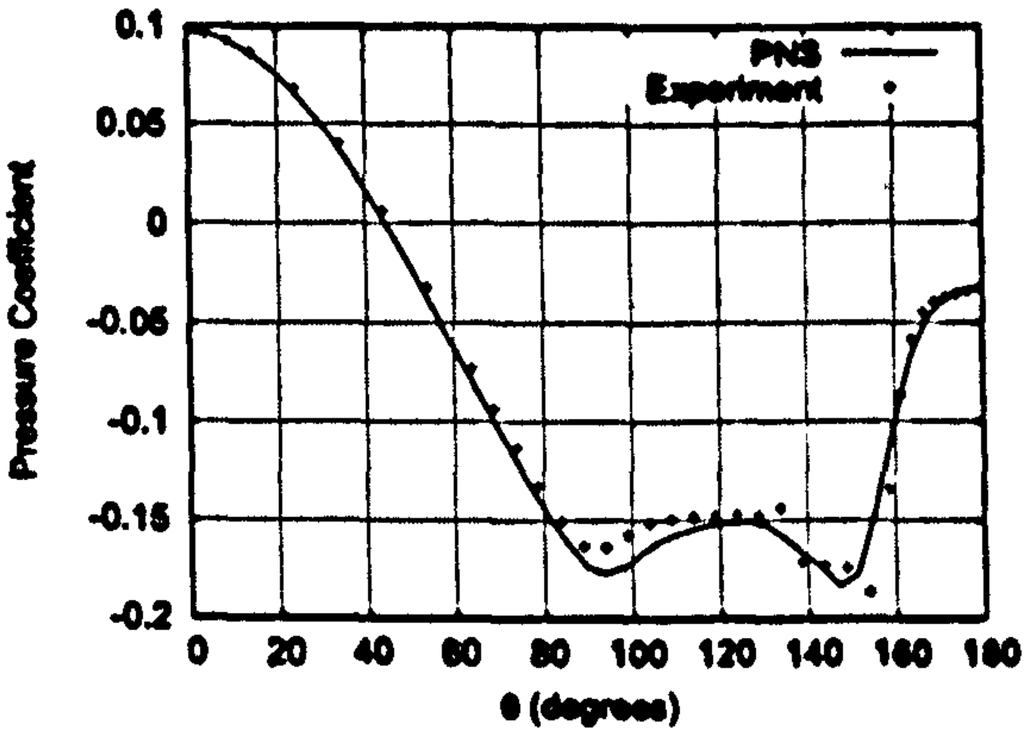

(b) $x = 4D$

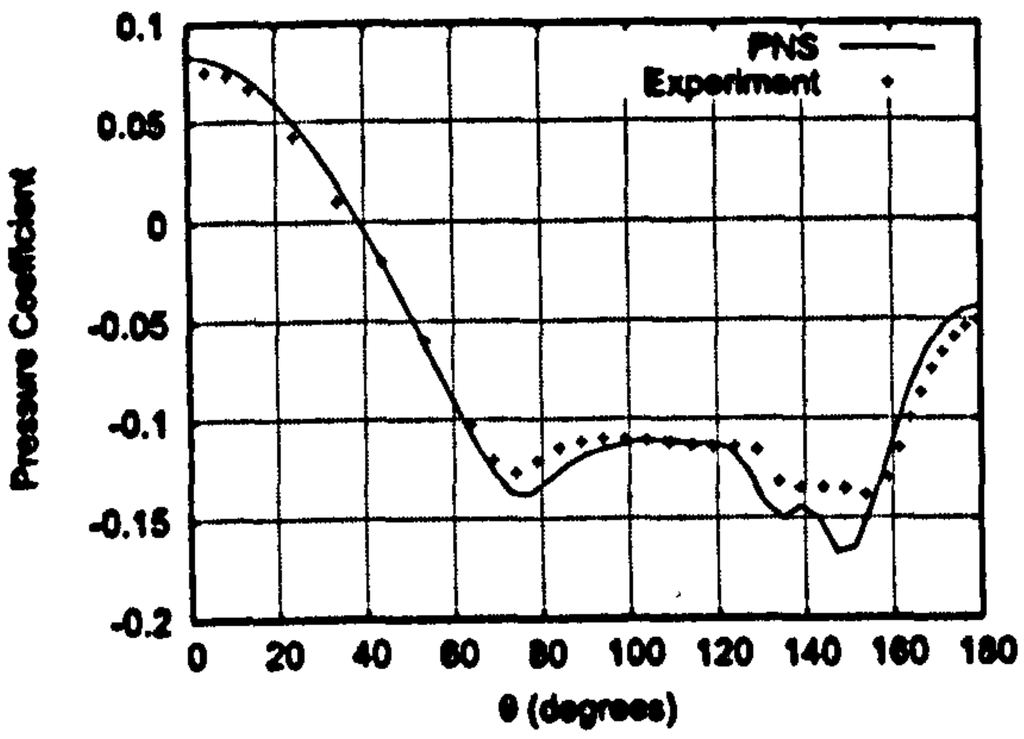

(c) $x = 6D$

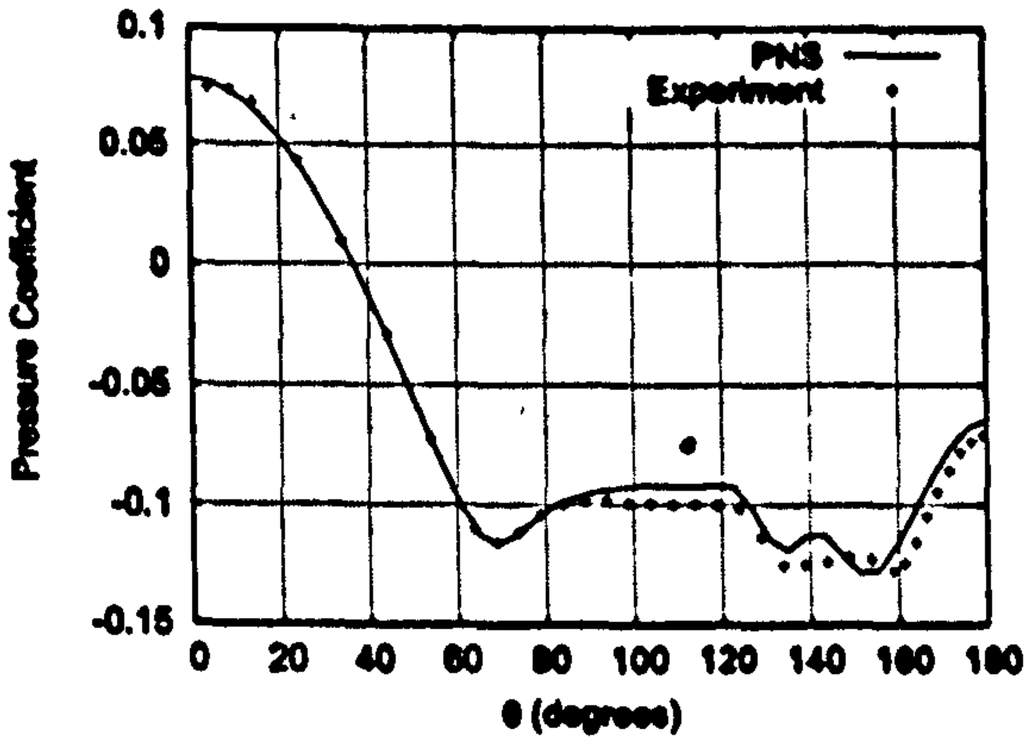

(d) $x = 7D$

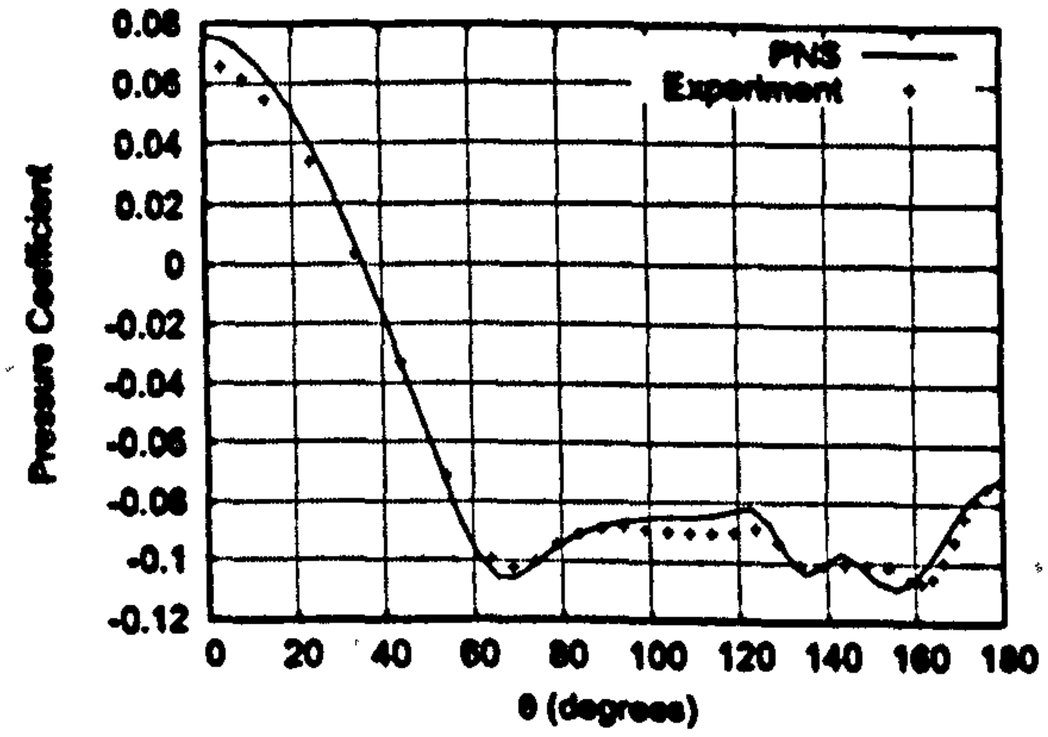

(e) $x = 8D$

Figure 74: Circumferential Pressure Coefficient Distributions, $\alpha = 15°$

From the three sets of data investigated, it is possible to conclude that in all cases, the point of primary separation is accurately predicted for all streamwise stations, although there is considerable discrepancy in the magnitude of the pressure coefficient values for the $\alpha = 5°$ case at $x = 4D$ and $8D$. Overall, agreement is worst for $\alpha = 5°$, with greater agreement at higher incidences. Although the numerical simulations are all laminar calculations, a Reynolds number of 0.16×10^6 may be large enough to induce transition naturally. It may be the case that the comparisons made in the above do not reflect identical flow conditions. Prince states that there is a mismeasurement in the circumferential angle within the experimental data [125]. The extent to which this angle was misaligned is not known, although it is a possible reason for the observed difference. An alternative explanation for the observed discrepancy for this case may be due to the fact that the vortical structures are closer to the body surface, for $\alpha = 5°$, compared to cases at higher incidence.

10.4 Application of Magnetic Field

A parametric study, investigating the influence and effectiveness of imposing a magnetic field generated from a dipole, has been undertaken. The numerical simulations up to this point have either been two-dimensional, such as in the validation exercises on the flat plate boundary layer, and the SHyFE geometry in previous chapters, or three dimensional but symmetric about a plane as the experimental comparative studies as in the previous section. In previous sections, the magnetic field imposed were relatively simplistic, in that they were either uniform fields, or dipole moments which did not exhibit any out of plane behaviour due to the nature of the problem under investigation.

In this section an attempt is made to introduce asymmetries into the field, such that one may alter the vortical structure of the flow past a slender body at incidence. The magnetic field is three dimensional in nature, and is applied to disrupt symmetry within the flow, a necessary consequence of which therefore is that a full three dimensional flow solution is required. Another complication arising due to the magnetic field is to do with its orientation. The flow is assumed to be seeded with ionising particles ahead of the missile apex, such that the magnetic field can exert influence over the flow. In contrast to the two dimensional dipoles imposed on the blunt body and the ramjet intake, there are various orientations a three dimensional dipole may take, each resulting in different Lorentz force fields, and consequently different influences on the flow. It is therefore necessary at this point to examine in detail the pertinent factors that govern the flow physics in the presence of the geometry, and to obtain an intuitive understanding of what is required from imposing the field.

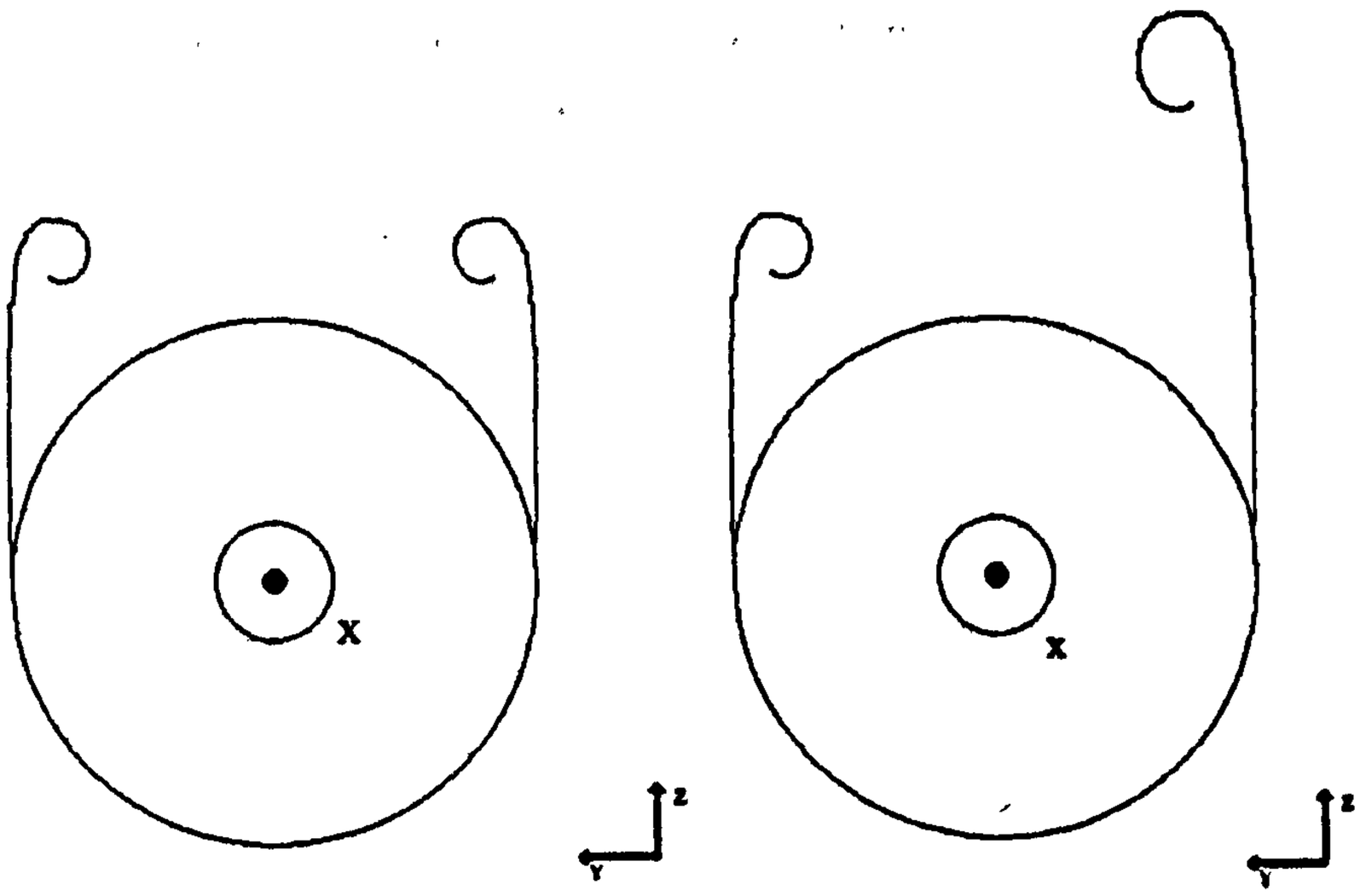

(a) Symmetric (b) Asymmetric

Figure 75: Vortex Structures for Flows at Incidence

Consider a slender body operating at moderate incidence, such as in the calculations in the previous section. In such circumstances, and under the further assumption that there are no other sources of inherent asymmetries , such as surface roughness or dents in the geometry, one would expect to see a vortex structure similar to that shown in figure [75(a)]. Cross flow separation takes place at identical locations either side of the body for a given streamwise location, and the vortices have same strength.

To generate a yawing moment, one would require the symmetry in this structure to break down, as in [75(b)], such as that associated with slender body aerodynamics at high incidences. The vortex core is associated with a low pressure coefficient region. If a vortex structure such as this is achieved, there is a pressure differential between the two surfaces, the lower pressure region being associated to the side whose vortex is closer to the geometry surface. Consequently, a side force is generated in the direction towards the vortex closer to the surface, from right to left in the diagram above.

It was shown in chapter 6, that a laminar boundary layer could separate under the influence of a magnetic field. The magnetic field was orientated in such a way as to be perpendicular to the predominant flow direction, acting to cause a deceleration in the flow and an eventual separation. Applying this concept to cross flow separation, one would require a force to act opposite to the flow direction in the cross flow plane. This would result in separation occurring at a point located closer towards the stagnation point on the windward plane in the schematic above. Thus if the force can be applied asymmetrically, it is possible to induce separation to occur earlier on one side of the body than the other, generating distorted asymmetric flow pattern. The boundary layer and SHyFE studies have shown that it is possible to use both an uniform field, as well as a dipole to decelerate

an oncoming flow. Since a uniform field is difficult to obtain in practise, one is left with trying to create a suitably orientated dipole field which generates a force field acting opposite to the flow.

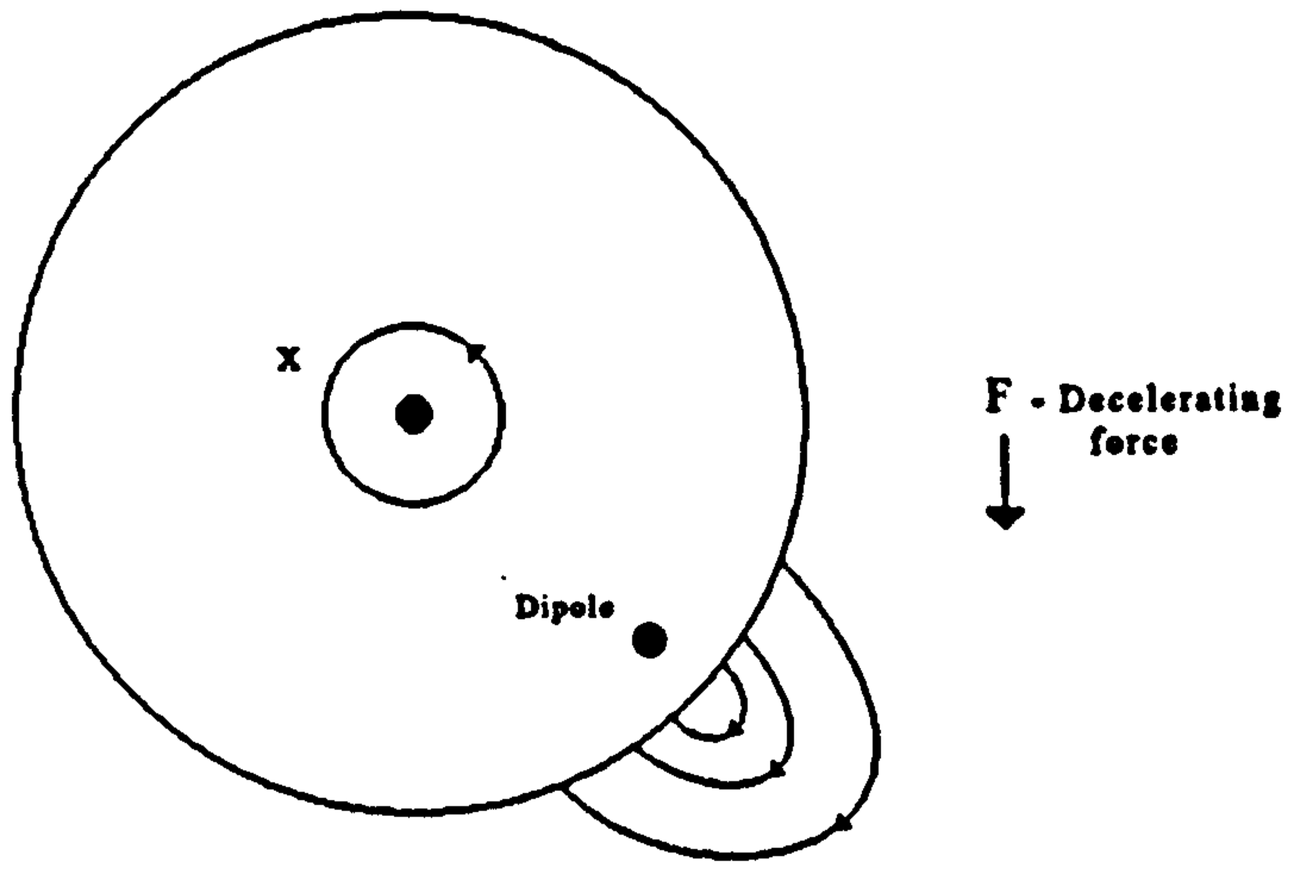

Figure 76: Magnetic Field Orientation for Slender Body

In the current investigation therefore, flow asymmetries are sought through the use of magneto-hydrodynamic interaction. Consider the orientation of the magnetic field in figure [76]. The dipole core is shown within the body, and only the magnetic field lines in the plane of the page are illustrated. It shows that given this orientation, there exist magnetic field line portions that are perpendicular to the flow, particularly in the vicinity of the body surface. This results in a Lorentz force acting opposite to the incident mean flow direction, as observed in the two aforementioned studies. As the dipole source is located off the central axis, it is guaranteed that the strength of the field to the right of it must be stronger than that on its left, and decelerating effect must be greater on the dipole side.

Recall that in 3D, the generalised equation for the magnetic field lines generated by dipole is given by the following equation;

$$\mathbf{B} = \frac{3\mathbf{m}\,(\mathbf{m}\cdot\mathbf{r}) - R^2\mathbf{m}}{R^5} \tag{10.4.1}$$

where $\mathbf{r}$ is the vector from the dipole source to a general point in space, with R its magnitude, and $\mathbf{m}$ is the vector dipole moment. To ensure that the magnetic field lines are orientated as in the above, one must choose the dipole axis to be in the y-direction. Examining the magnetic field lines in the streamwise plane at which the dipole source is located, results in a form similar to the schematic in [76]. The form of the magnetic field used for the remainder of the study is therefore given by the above equation, with $\mathbf{m} = (0, 1, 0)^T$.

10.4.1 Parameters Under Investigation

To widen the scope of the investigation, several variables were identified as being pertinent factors in the generation of side force, and formed the basis of the study, whose effects would be investigated.

As explained in the previous section, the magnetic field source was located off the centre line of the geometry, on the port side of the projectile. as the source location strongly influences the manner in which the Lorentz force is experienced by the flow, a variable dipole location was also deemed necessary as test parameter. It has been mentioned in the literature that the closer a perturbation is located to the apex of the body, the greater the asymmetry further downstream along the fuselage. It is therefore appropriate to consider these effects, thus one of the variables introduced was the streamwise location of the dipole source, located at $x = 0.5D$, $1.0D$,$1.5D$,$2.0D$, where D is the diameter of the fuselage.

The introductory section outlined that the primary separation point on a body at incidence moves windward, with increasing axial distance, and with increasing incident angle, due to an increase in skin friction coefficient and the presence of an adverse pressure gradient. To try and exert influence over this phenomenon, an additional factor introduced, coming under the umbrella of dipole location, was the effect of altering the azimuthal location for the source. For each streamwise location, the dipole source was placed at five different azimuthal locations, denoted by an angle ϕ, as shown in figure [77].

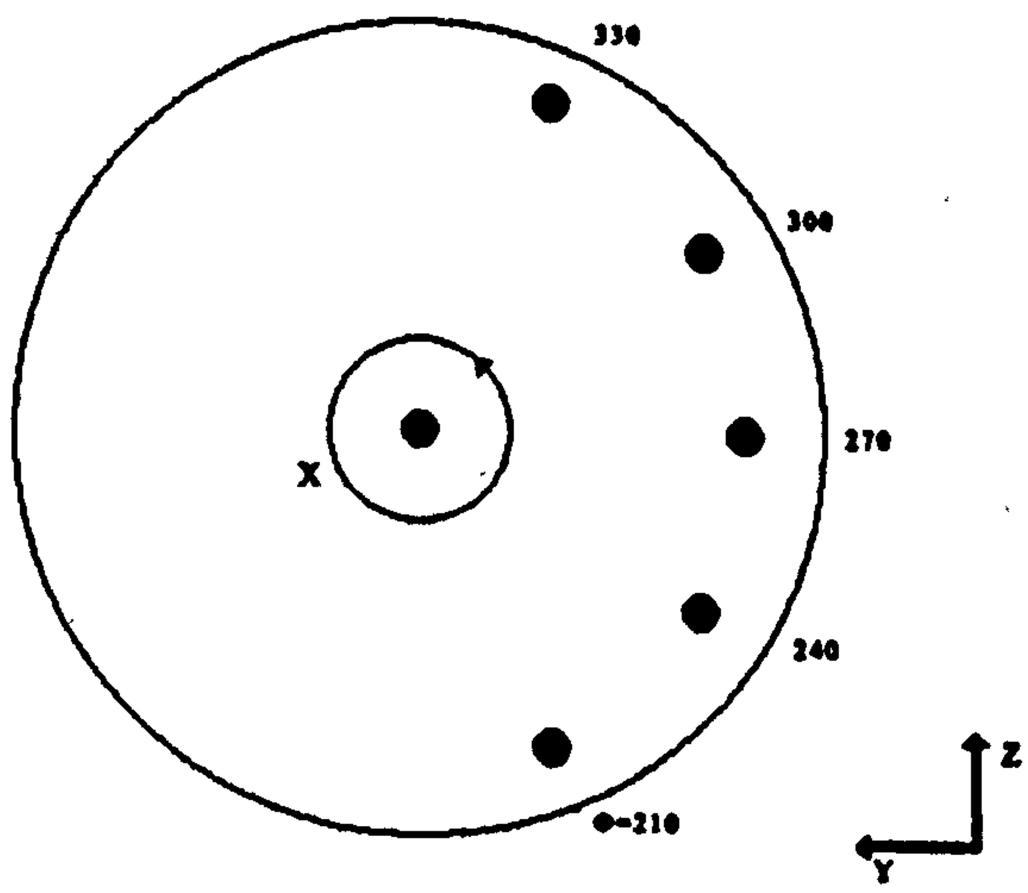

Figure 77: Azimuthal Dipole Locations for each Streamwise Station

To ensure that the dipole strength is not inadvertently altered by the choice of ϕ, and to guarantee the same magnetic field strength on the surface for all azimuthal locations, in each case, the source was placed the same radial distance away from the body surface. Measured radially from the central axis of the body, each source was placed such that

its radial distance was $0.1D$ away from the surface. From the flow conditions, under a perfect gas assumption, one can infer a value of $271.43m/s$ for the speed of sound and $4.56 \times 10^{-4} kg/m^3$ for the freestream density. The conductivity value was taken to be the same as that used for the SHyFE investigation, $100mho/m$. As the dipole sources are located in close proximity to the flow, a magnetic field strength on the order of $10^{-2}T$ was chosen. A suitable value for the magnetic interaction parameter given by equation [9.4.6] was therefore chosen to be 2.5×10^{-3}.

In addition to the above, since slender bodies typically operate at several incidences, the effects of modifying the angle of attack were also considered. To make meaningful comparisons to the test cases run in the absence of a magnetic field , a zero incidence case, in addition to $\alpha = 5°$,$10°$ and $15°$ cases were also run. The three parameters varied in the study are therefore the streamwise location of the dipole, the azimuthal angle of the dipole position, and the angle of incidence as above, each with four, five and four values respectively. A full parametric study comprising of eighty simulations was made, the results for which are presented in the following sections.

10.5 Results

10.5.1 Zero Incidence

Lateral force coefficients for the zero incidence case are shown in figure [78]. The effects of using four streamwise dipole locations, and five radial locations, ϕ, as independent variables is illustrated in the figure.

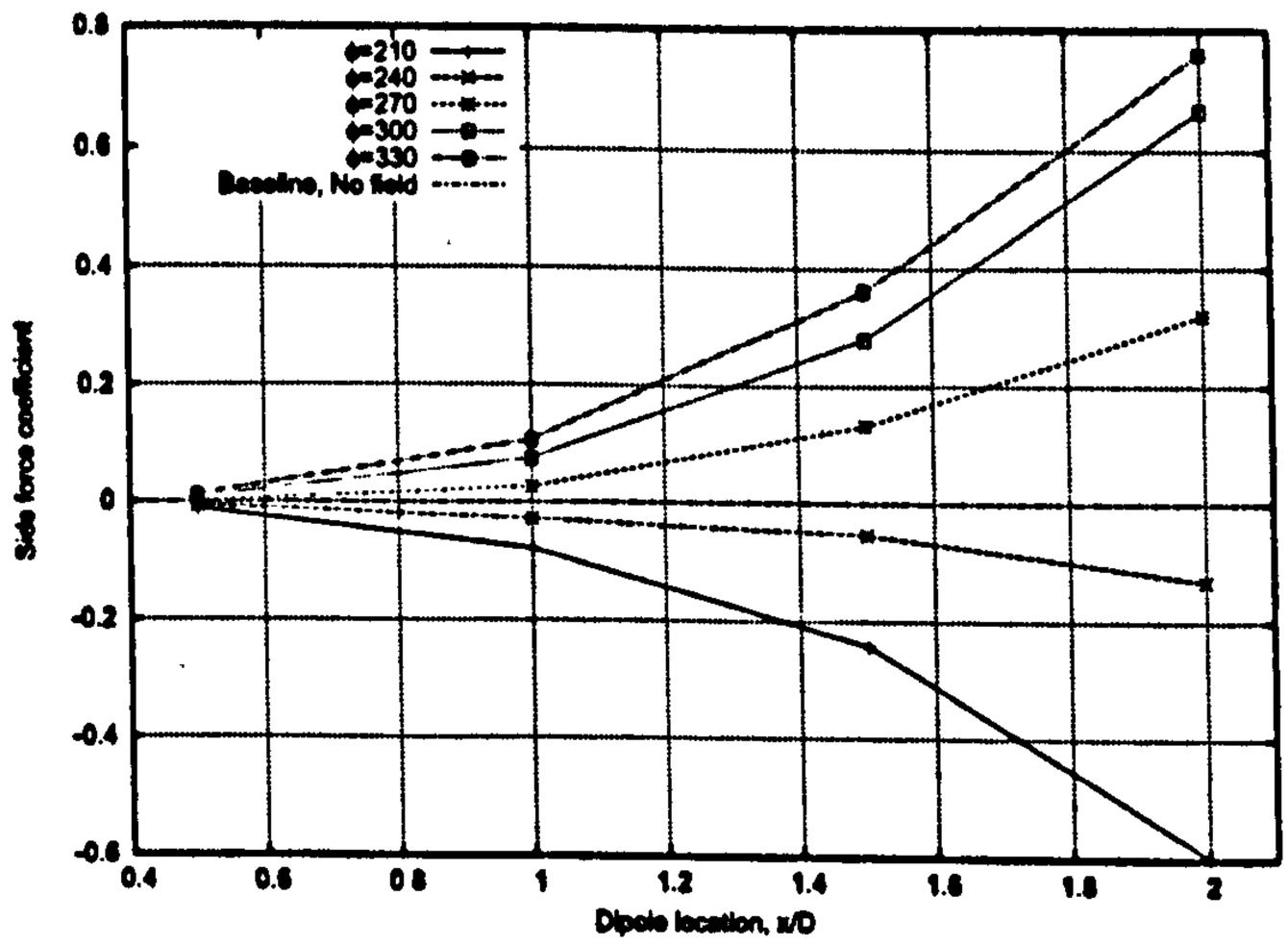

Figure 78: Side Force Coefficient, at Zero Incidence

Contrary to the initial hypothesis suggested in the previous section, the figure suggests

that side forces may be generated to act on the slender body in both directions. The previous section argued that with the field orientated as in figure [76], the flow could be decelerated so as to cause crossflow separation further towards a windward location on the body. Such an arrangement would result in separation occurring earlier on the dipole side of the body, and the ensuing vortical structure would be further away from the body surface compared to the starboard side. A consequence of this is that the force is directed in the starboard direction, due to the asymmetry in vortex structure. Another immediate observation that can be made from figure [78], which goes against an idea outlined in the previous sections, is that the effects of applying a magnetic field are not necessarily greater the closer one approaches the apex of the slender body. The figure clearly shows that the opposite seems to be true, in that for any given azimuthal dipole position the effects on side force coefficient are greater as one moves downstream.

The above plot suggests that the problem is not quite so simplistic. For a dipole located at $\phi = 210°$ and 240°, the force is directed increasingly towards the port direction, whereas for all other incidences the side force acts in the opposite direction. Furthermore, for zero incidence, the baseline case in the absence of a magnetic field does not involve any vortical structures, and it is therefore necessary to understand the causes of the above observations.

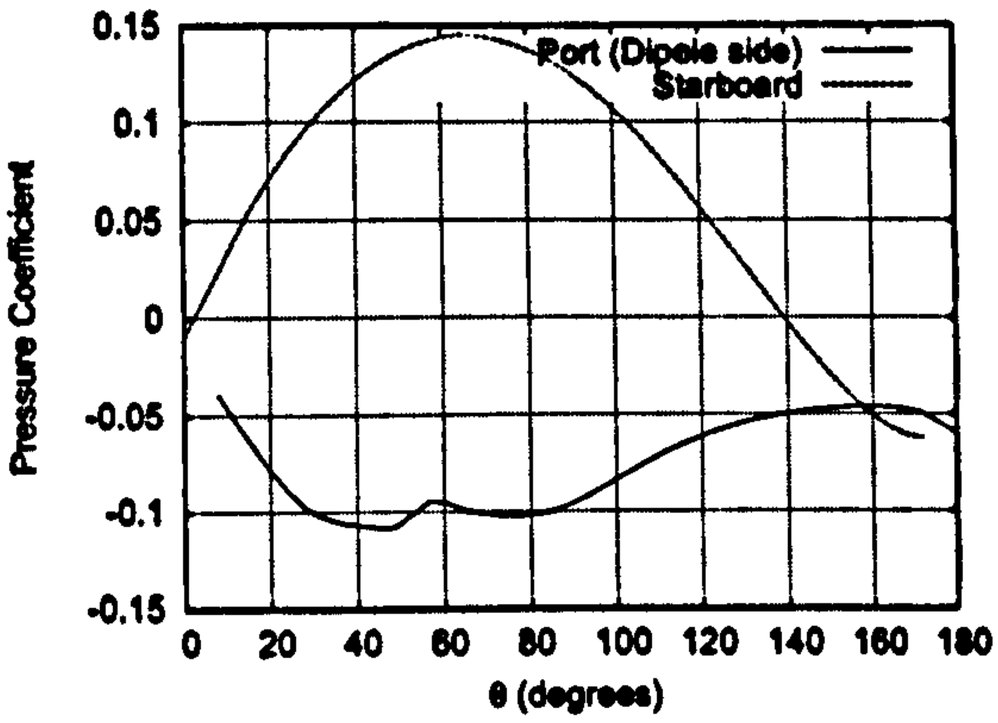

(a) $\phi = 210, x = 3.0D$

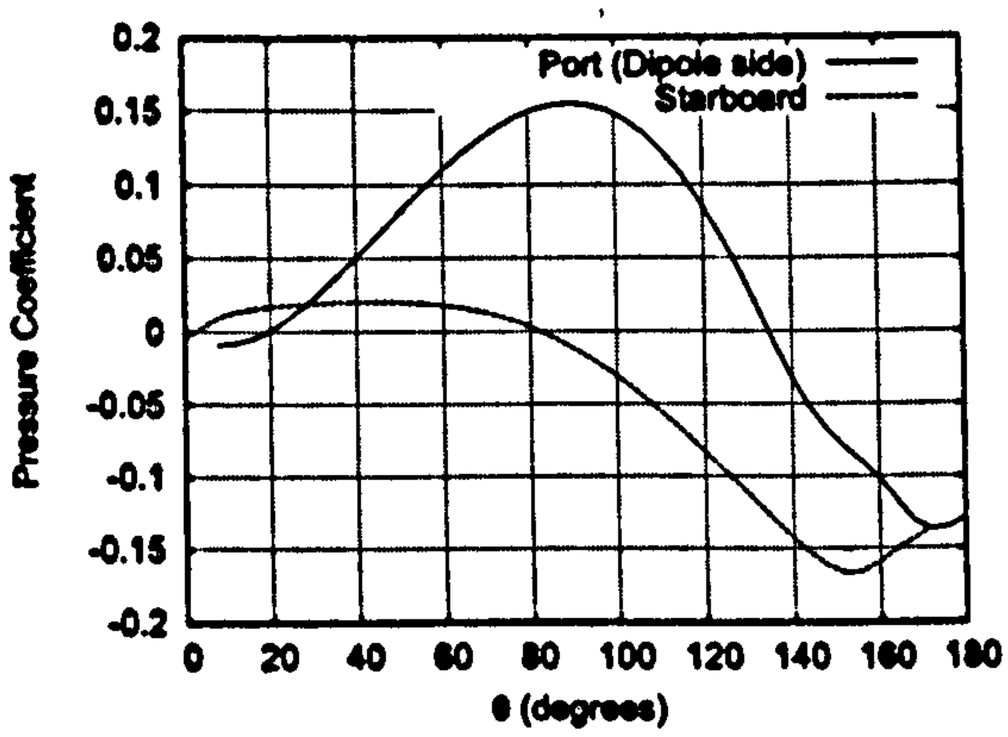

(b) $\phi = 330, x = 3.0D$

(c) $\phi = 210, x = 5.5D$

(d) $\phi = 330, x = 5.5D$

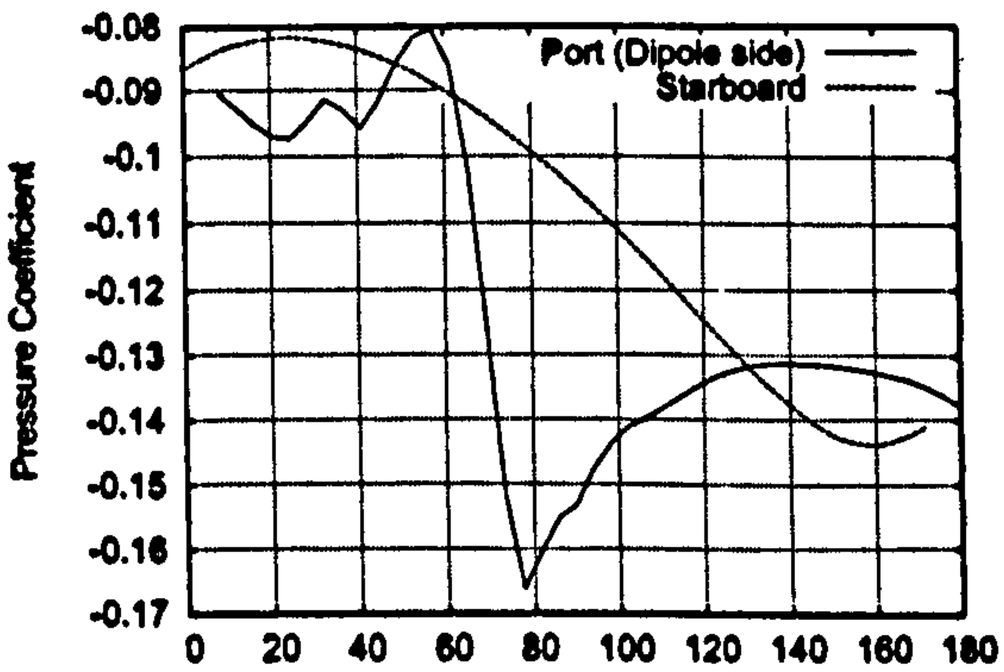

(e) $\phi = 210, x = 7.6D$

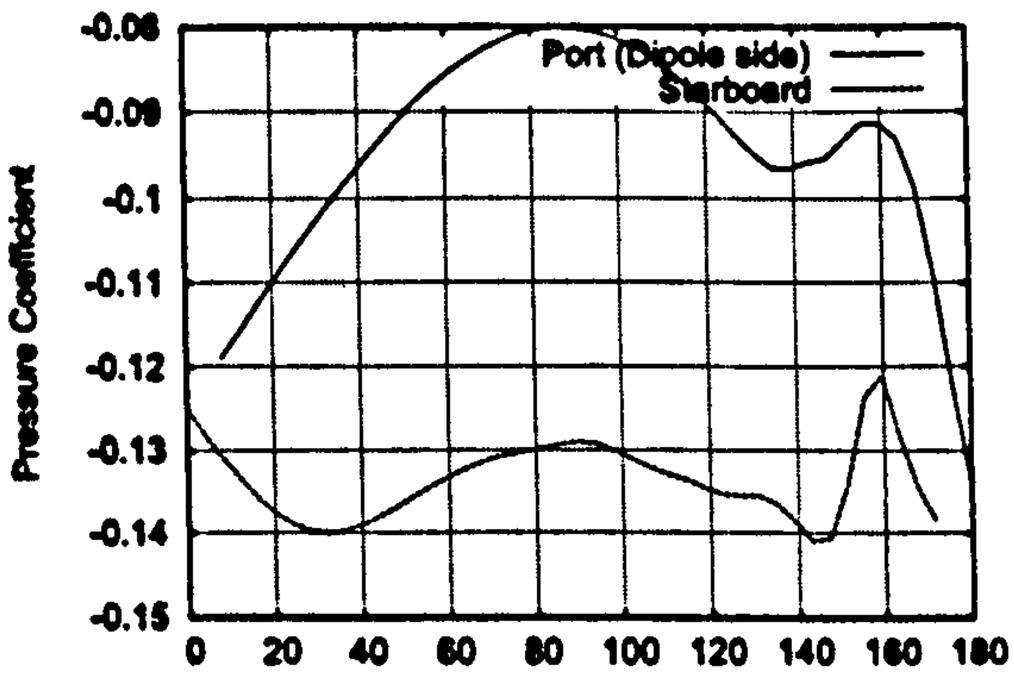

(f) $\phi = 330, x = 7.6D$

Figure 79: Circumferential Pressure Coefficient Distributions, $\alpha = 0°, x = 2.0D$

The figures in [79] show the variation of surface pressure coefficient on the port and starboard portions of the body, at several stations as indicated. On the x-axis, $\theta = 0°$ would refer to the windward location, and $\theta = 180°$ the leeward position, if the body were operating at incidence.

By considering the side force coefficient profiles in [78], only variations for the most extreme cases, in other words the case for $x = 2.0D$, at $\phi = 210°$ and $330°$ are considered. The plots on the left hand column in the above figure show that the pressure coefficient is for the most part greater on the starboard portion of the body, except for several azimuthal positions on the $x = 7.6D$ station. Thus there is a net pressure differential generating a side force acting towards the port side, in the negative y direction. For $\phi = 330°$, the converse is true. The pressure coefficient distribution is consistently greater on the port side, resulting in a net force in the positive y-direction. Thus the pressure coefficient distributions provide a convincing account of the observed behaviour in side force coefficient , and are consistent with profiles in [78].

An interesting question is to ask how the flow is disturbed by the magnetic field . The above figures show that as a result of changing the azimuthal position very slightly, the side force direction can be altered considerably. Greater insight into the behaviour can be gained by looking at the variation of vorticity magnitude across the body, as illustrated in figures [81(a)] and [??].

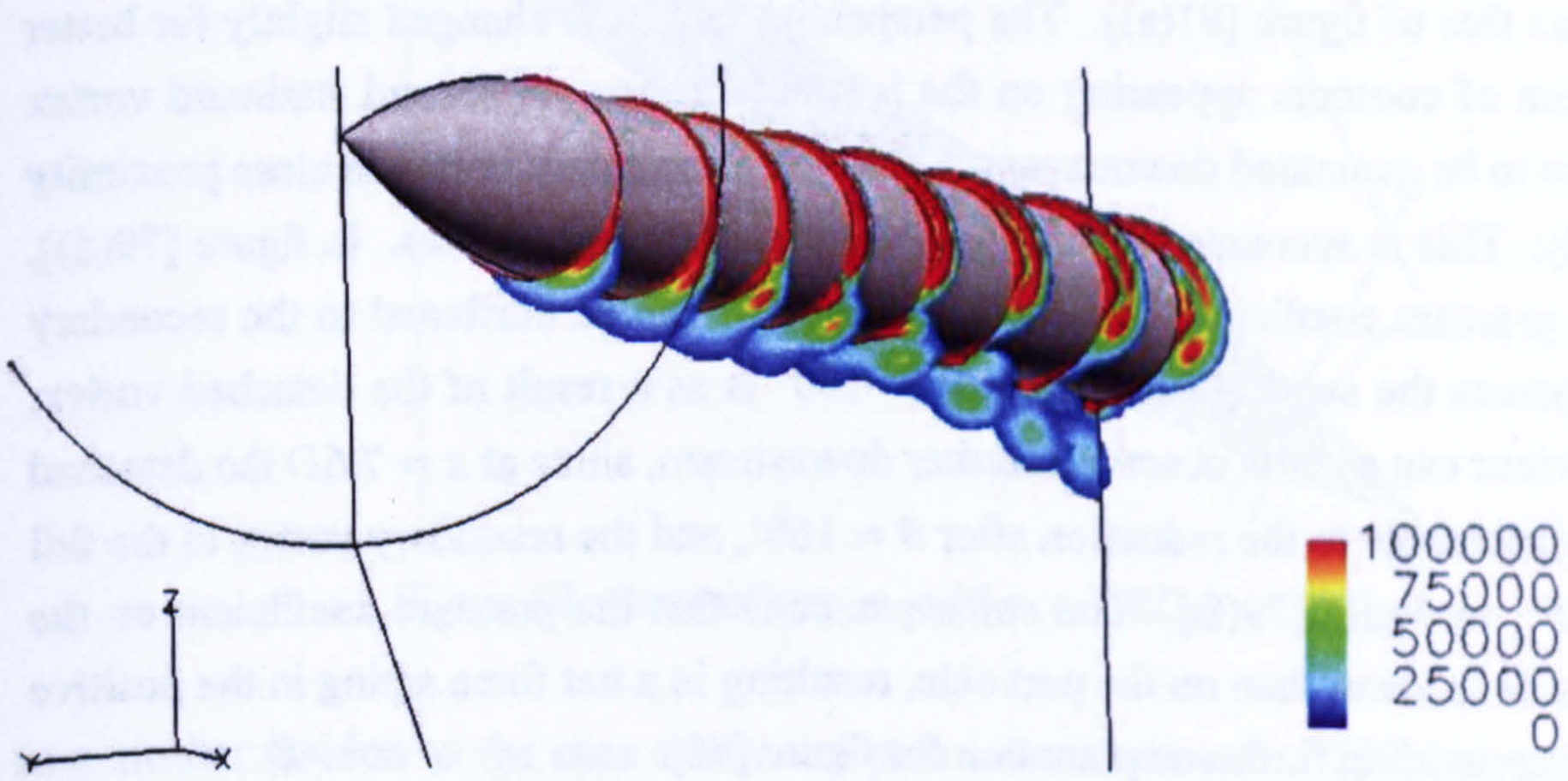

Figure 80: Vorticity Magnitude Contours, $\alpha = 0°, x = 2.0D, \phi = 210°$

For the dipole located at $\phi = 210°$, one can observe a vortex core forming on the lower portion on the dipole side (port side) of the slender body, and another further downstream, situated further up the port side. The former vortex is deflected away from the body surface, although since the latter is generated further downstream, it remains in relative proximity to the body even at the last station. Such vortex cores are associated with a region of low pressure at their centre, and serve to explain the observations in the pressure

coefficient profiles shown above. In figures [79(c)] and [79(e)] for example, one observes a sudden reduction in port side pressure coefficient at about $\theta = 60°$. Examination of figure [81(a)] confirms that such an adverse pressure gradient is due to the emergence of the secondary vortex on the port portion of the body, and also serves to explain why a side force acting in the negative y-direction is observed.

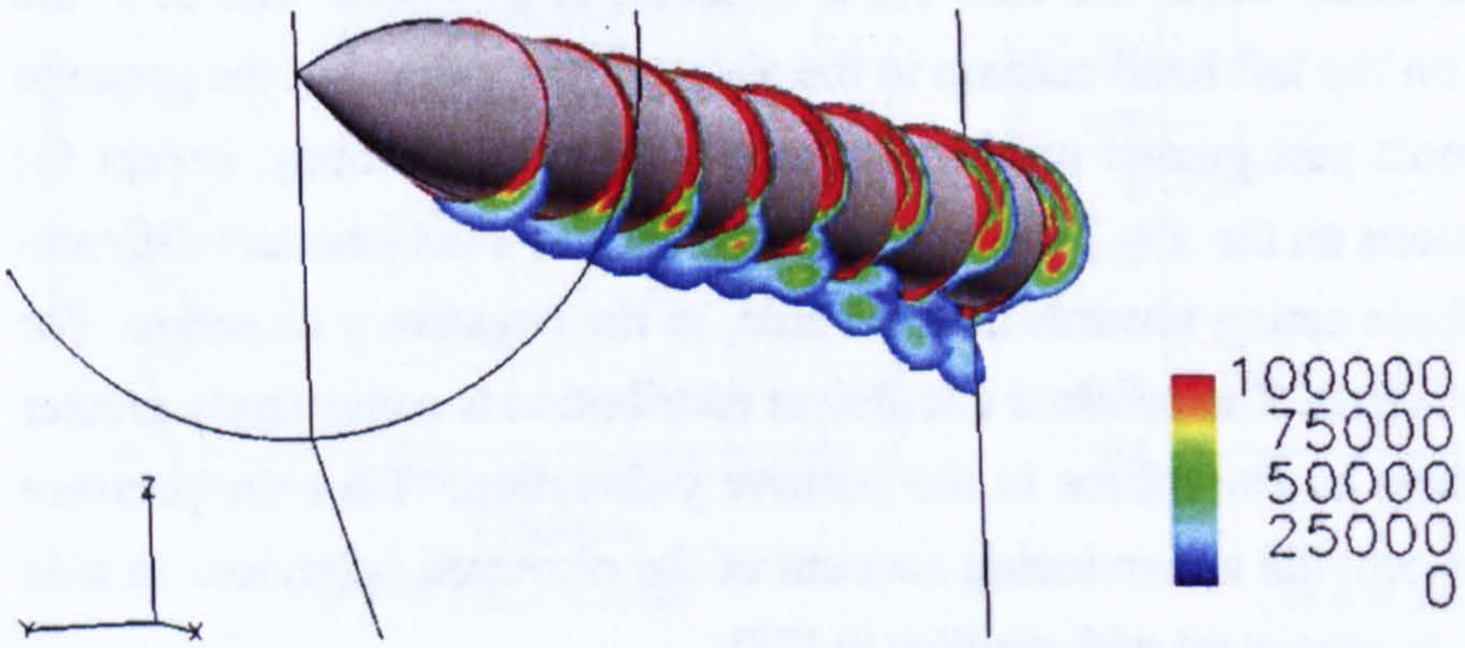

Figure 81: Vorticity Magnitude Contours, $\alpha = 0°, x = 2.0D, \phi = 330°$

In the second case, with the dipole positioned at $\phi = 330°$, figure [??] shows that vortex is generated on the starboard side, which is directed over the top of the body, directing it toward the port side. Note that the orientation of the axes in the figure is the same as that of figure [81(a)]. The perspective has been changed slightly for better visualisation of contours appearing on the leeward surface. A second starboard vortex can be seen to be generated downstream, as well as a secondary vortex in close proximity to the body. This is accounted for in the pressure coefficient profiles. In figure [79(d)], the dip in pressure coefficient occurring at $\theta = 135°$ can be attributed to the secondary vortex, whereas the subsequent drop at $\theta = 150°$ is as a result of the detached vortex. This behaviour can also be observed further downstream, since at $x = 7.6D$ the detached vortex is attributable to the reduction after $\theta = 160°$, and the secondary vortex to the fall at $\theta = 145°$, in figure [79(f)]. The consequence is that the pressure coefficient on the starboard side is lower than on the port side, resulting in a net force acting in the positive y-direction, providing further explanation for figure [78].

Exploration of the streamlines emanating from the apex of the body highlights the influence of the magnetic field on the fluid. Consider the streamline paths in figure [82], corresponding to the zero incidence case, with the dipole source situated at $x = 2.0$ and $\phi = 210°$. The streamlines emanating from the port side of the vortex are directed windward (if at incidence) side, resulting in the vortex core observed on the bottom surface in figure [81(a)]. The second vortex core, located further up on the port side, can actually be accounted for by streamlines originating from the starboard side of the missile nose. Thus, looking at the slender body front on as in the schematic in diagram [77], the

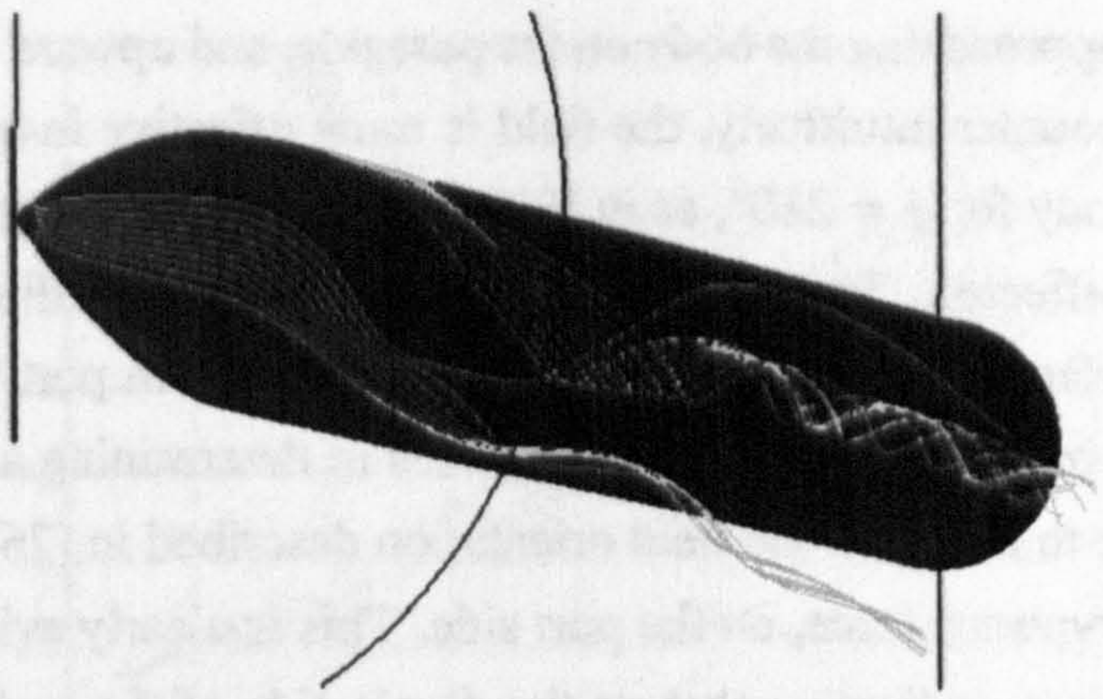

Figure 82: Streamlines, $\alpha = 0°, x = 2.0D, \phi = 210°$

magnetic field acts to redirect the flow in a "clockwise" fashion, with mass on either side separating to form the observed vorticity.

This clockwise behaviour is also confirmed in [83] below, showing the streamlines for the dipole positioned at $\phi = 330°$.

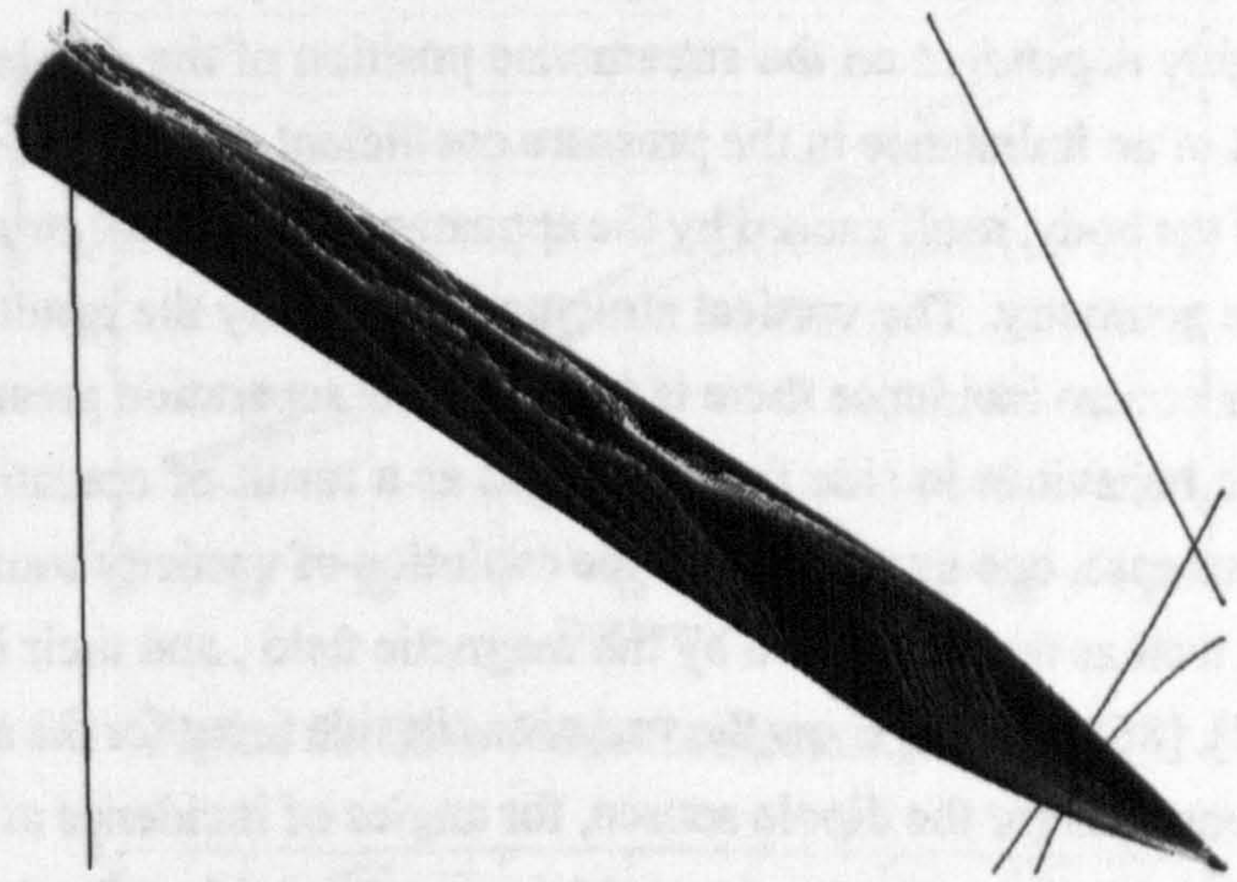

Figure 83: Streamlines, $\alpha = 0°, x = 2.0D, \phi = 330°$

In a similar fashion to the case where a dipole is located at $\phi = 210$, one can observe that the streamlines from starboard side are directed over the top of the body once again. However, the flow falls short of separating on the port side; instead the streamlines roll up into the first detached vortex observed in figure [??], which can be seen on the leeward portion. On the other hand, in the same figure, the port side streamlines are redirected downward to the extent that they form part of the vortical structures that are generated further downstream.

The above discussion of the evolution of the streamlines provides key understanding over the manner in which the magnetic field is influencing the flow. Mass is directed

downward, for flow approaching the body on the port side, and upward for that on the starboard side. Rather counter-intuitively, the field is more effective in redirecting the flow over the top of the body for $\phi = 210°$, as in [82], even though the source is furthest from where mass is most affected. The converse also holds true for the dipole source located toward the upper surface. At $\phi = 330$, mass is redirected from port to starboard under the body. Reverting back to the original hypotheses in determining a suitable magnetic field , it is instructive to note that the field orientation described in [76] does indeed generate the required downward force, on the port side. This is clearly evident in both of the above streamline figures, indicating that on the dipole side of the body, flow is directed downward.

10.5.2 Effect of Incidence

The previous subsection investigated the effects of applying a magnetic field to the slender body operating at zero incidence. It was shown that side forces could be generated in either direction depending on the azimuthal position of the dipole, and that the strength of the force was highly dependent on the streamwise position of the dipole. The generated force was a result of an imbalance in the pressure coefficient distributions on the port and starboard sides of the body, itself caused by the appearance of vortical structures at various positions over the geometry. The vortical structures are purely the result of applying the magnetic field , as at zero incidence there is no crossflow separation present. This section considers how the behaviour in side force changes as a result of operating at incidence. Unlike the previous case, one must consider the evolution of vorticity caused by operating at a incidence, as well as that generated by the magnetic field , and their interaction.

Figures [84], [85] and [86] show the variations in side force for the azimuthal angles and streamwise locations for the dipole source, for angles of incidence at 5,10 and 15 degrees respectively. A common observation, which was also evident for the zero incidence case is that as the dipole is moved downstream, the side force increases monotonically, acting to divert the slender body in the starboard direction. However, at zero incidence, it was found that for $\phi = 210°$ and $240°$, the force acted in the opposite direction, diverting the missile to the port side. The main difference in the figures below is that regardless of azimuthal location, the side force acts in the same direction. Except for several isolated cases when the angle of incidence is 15 degrees with the dipole positioned at $x = 0.5D$ or $x = 1.0D$, all simulations result in the body being directed starboard.

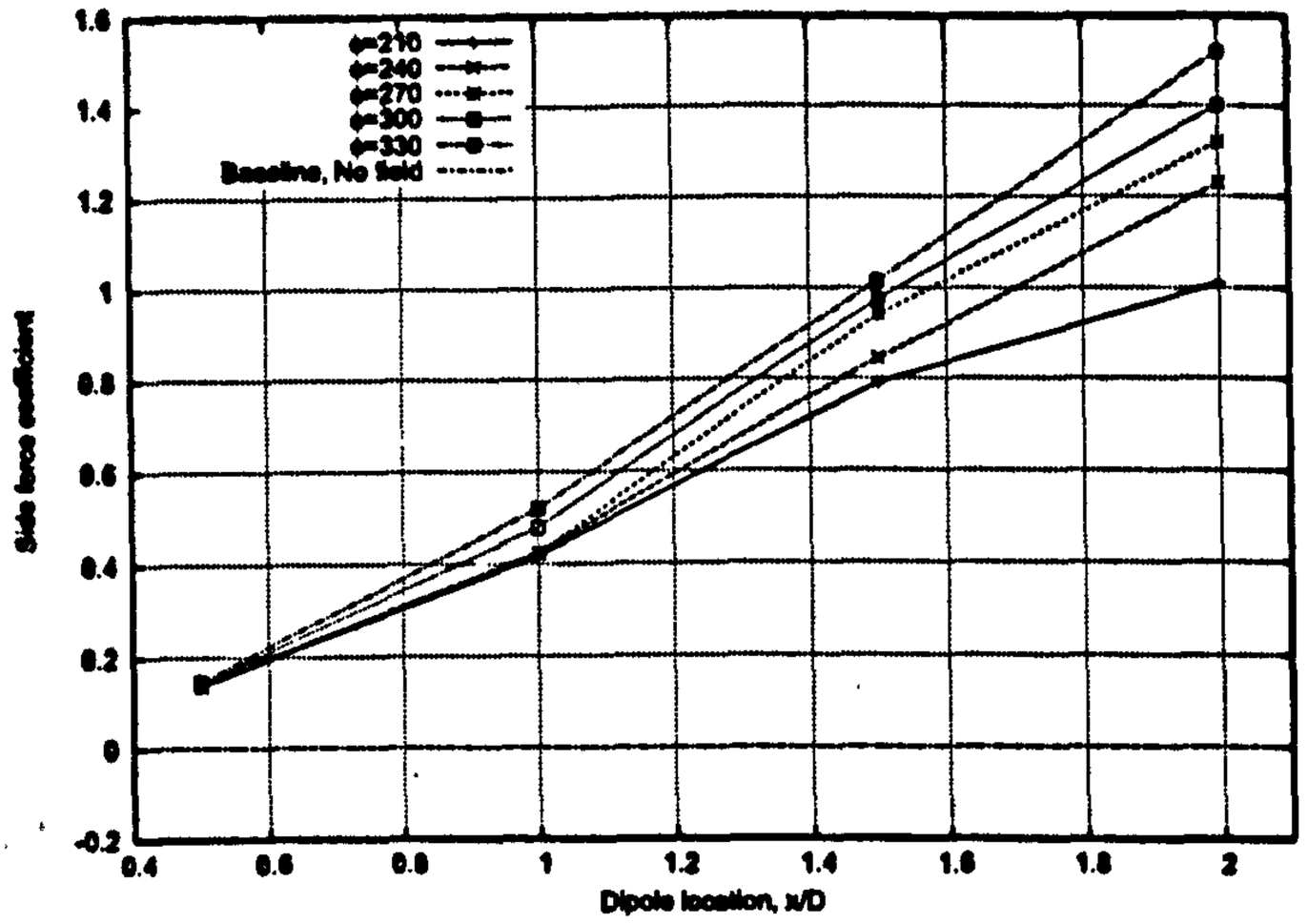

Figure 84: Side Force Coefficient, $\alpha = 5°$

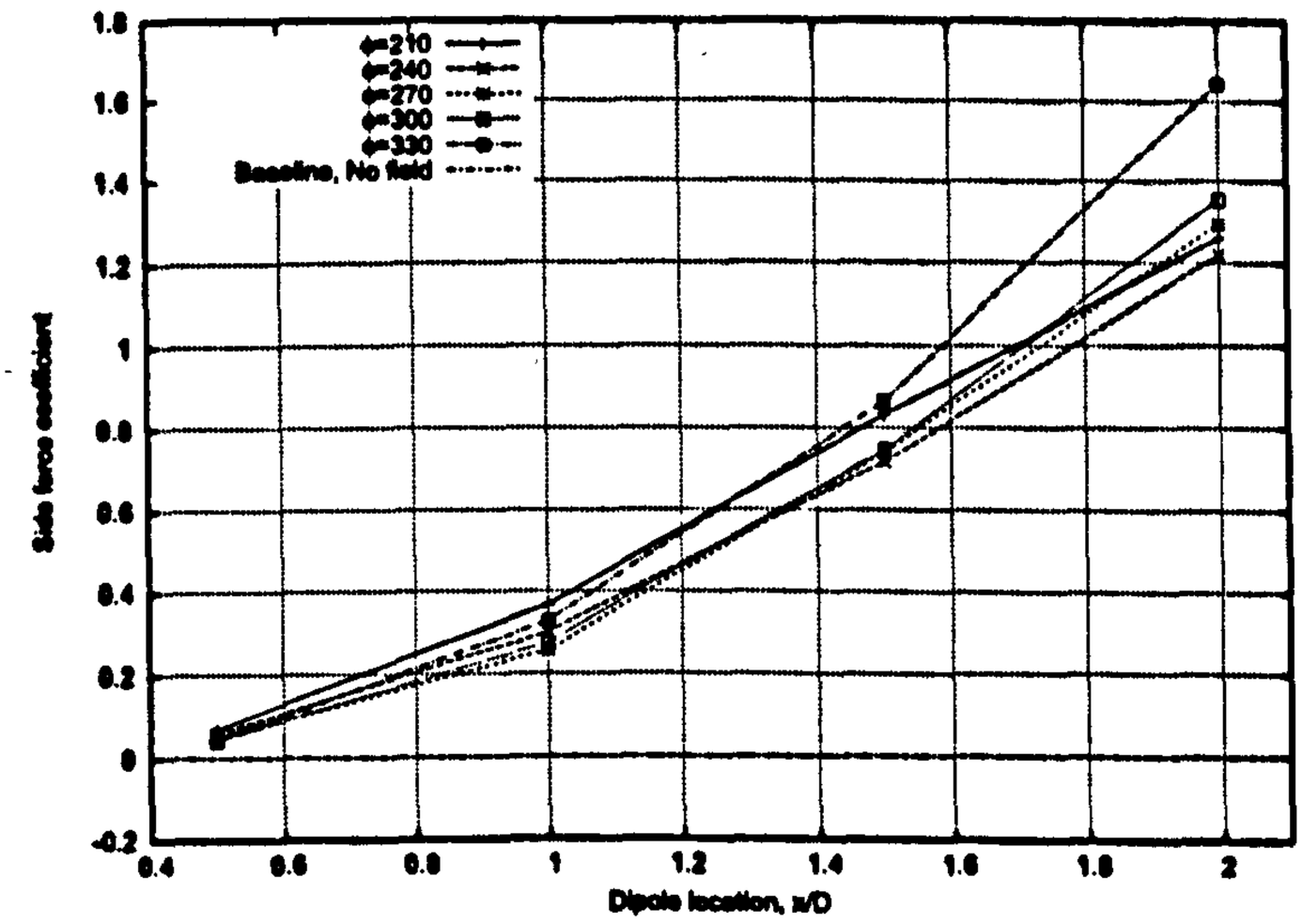

Figure 85: Side Force Coefficient, $\alpha = 10°$

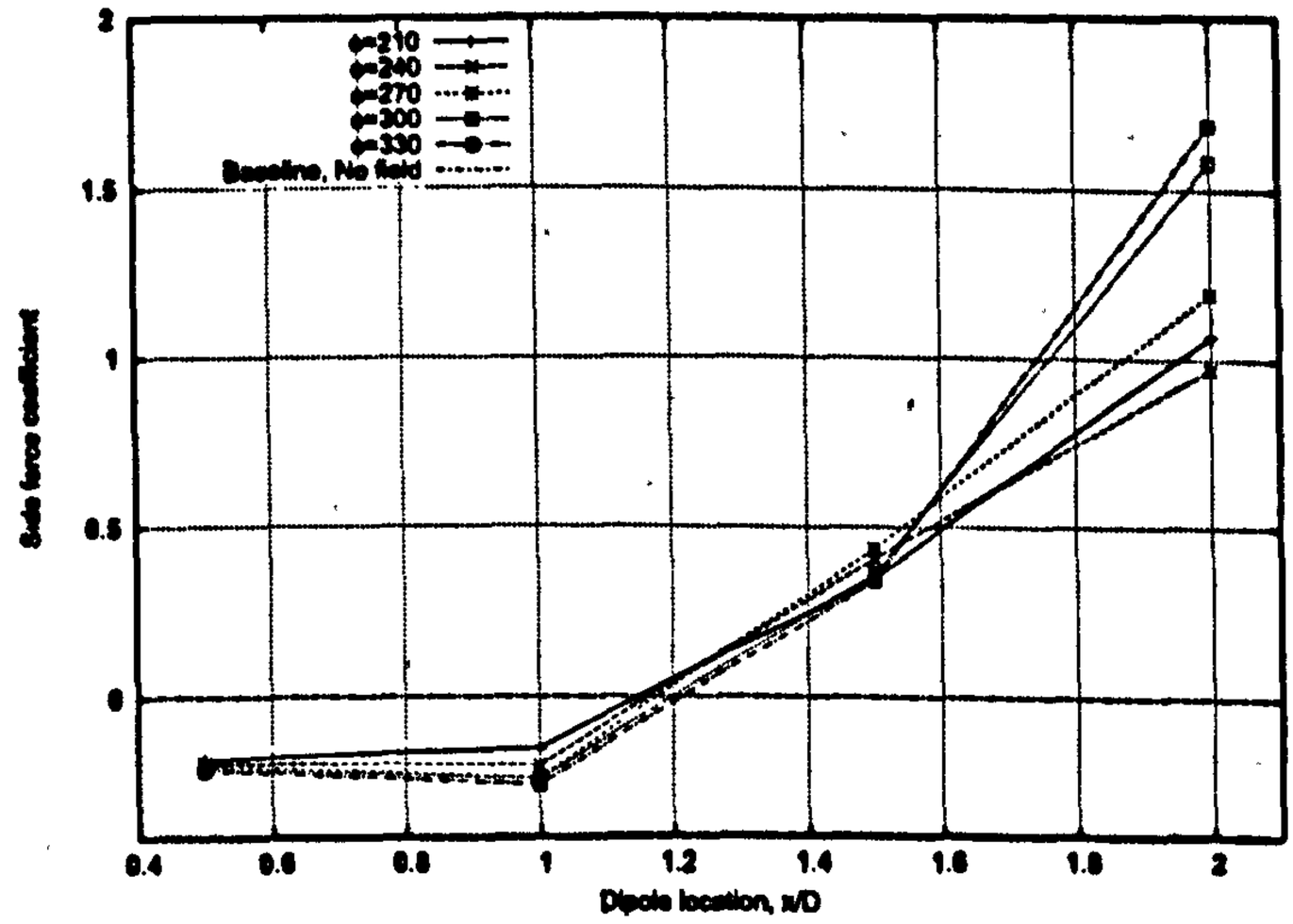

Figure 86: Side Force Coefficient, $\alpha = 15°$

Examination of the vortical structures provides an explanation for the observed variations in side force coefficient. The figures in [87] show the evolution of vorticity magnitude contours, for the slender body operating at an angle of incidence of 5 degrees, with $\phi = 330°$.

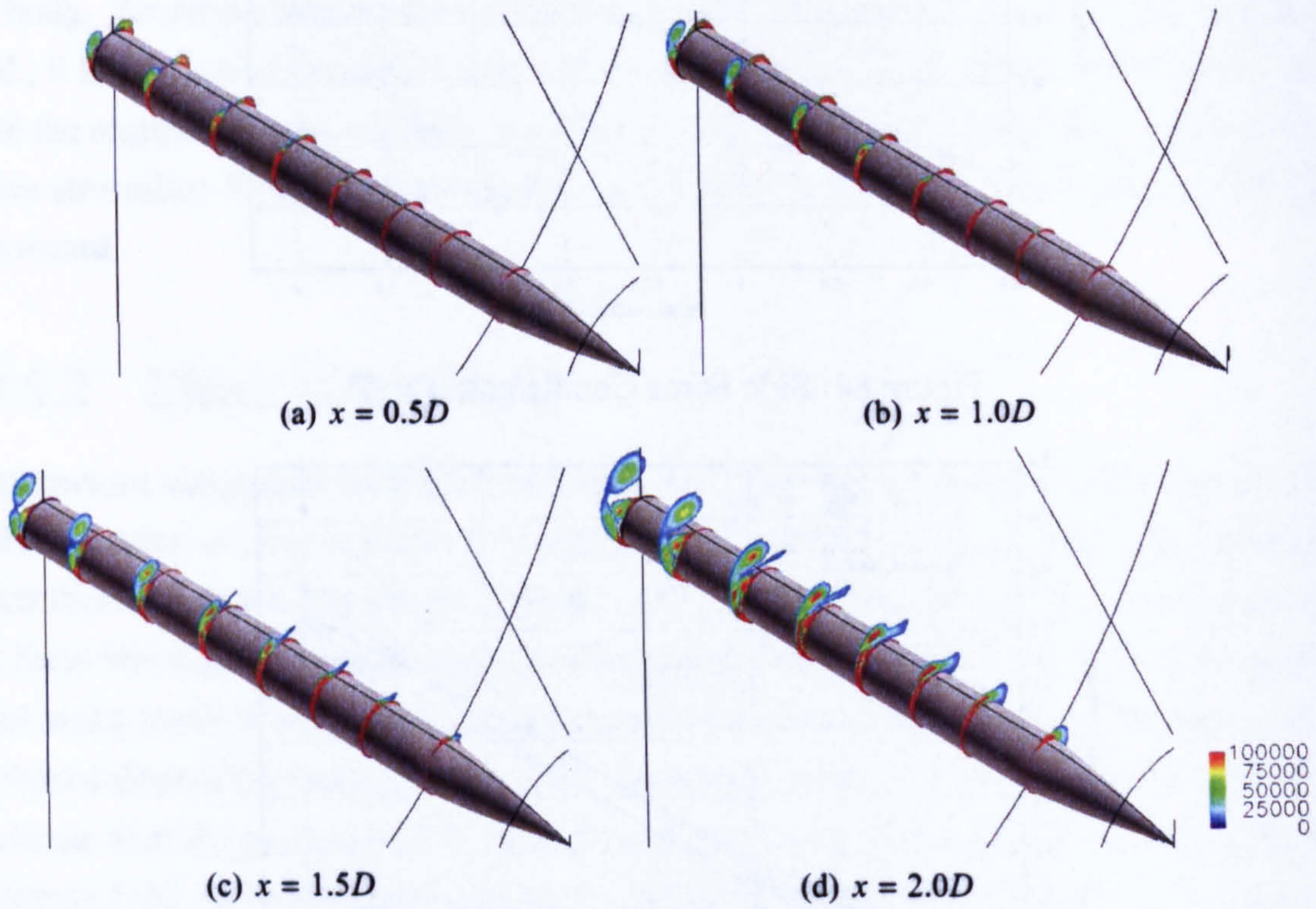

(a) $x = 0.5D$ (b) $x = 1.0D$

(c) $x = 1.5D$ (d) $x = 2.0D$

Figure 87: Vorticity Magnitude Contours, $\alpha = 5°, \phi = 330°$

For the case where the dipole is positioned at $x = 0.5D$, closest to the apex, figure [87(a)] shows that there remain some of the symmetric characteristics, as for the no field case. However, in analogy to the figure in [82], the streamlines are directed downward slightly, delaying crossflow separation on the port side. The vorticity on the starboard side is greater than that on the opposite portion of the body. This is slightly ambiguous from figure [87(a)], but is confirmed by figures [88(a)] and [88(b)], showing azimuthal pressure coefficient variation for this case. The stronger magnitude at its core is evidenced by the consistently lower surface pressure coefficient on the starboard side, hence resulting in positive side force generation.

Moving the dipole position downstream is initially characterised by the absence of a vortex appearing on the dipole side of the body. At $x = 1.0D$ for example crossflow separation occurs, resulting in a vortex core visible halfway along the fuselage of the body. As this is characterised by a low pressure region, and in the absence of an equal and opposite vortex on the port side, also results in side force acting in the positive y-direction.

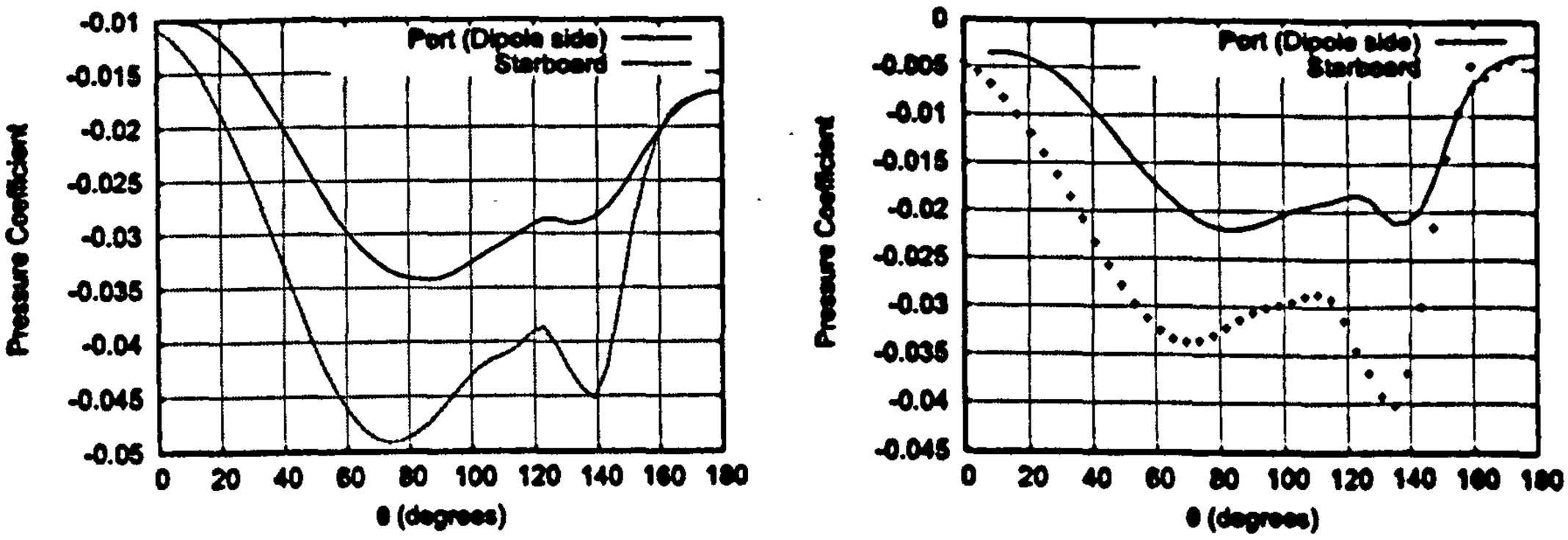

(a) Station $x = 5.5D$ (b) Station $x = 7.6D$

Figure 88: Circumferential Pressure Coefficient Distributions, $\alpha = 5°, x = 0.5D, \phi = 330°$

Further downstream at $x = 1.5D$ there is a vortex core of greater magnitude, and a suction vortex in proximity to the body, resulting in greater regions of low pressure coefficient. At $x = 2.0D$, in figure [87(d)], the crossflow separation vortex core is shown to occupy a larger region, and is directed over the top of the body. The core of the suction vortex also occupies a larger region than for $x = 1.5D$, itself detaching from the surface further downstream. Thirdly, another vortex core is shown to emanate, after the halfway position on the cylinder.

A direct comparison, demonstrating the effects of varying streamwise dipole location on the pressure coefficient distribution are shown in [89]. The effects on starboard side are self evident; an overall reduction in pressure for all azimuthal locations, consistent with the observed vortical behaviour outlined above.

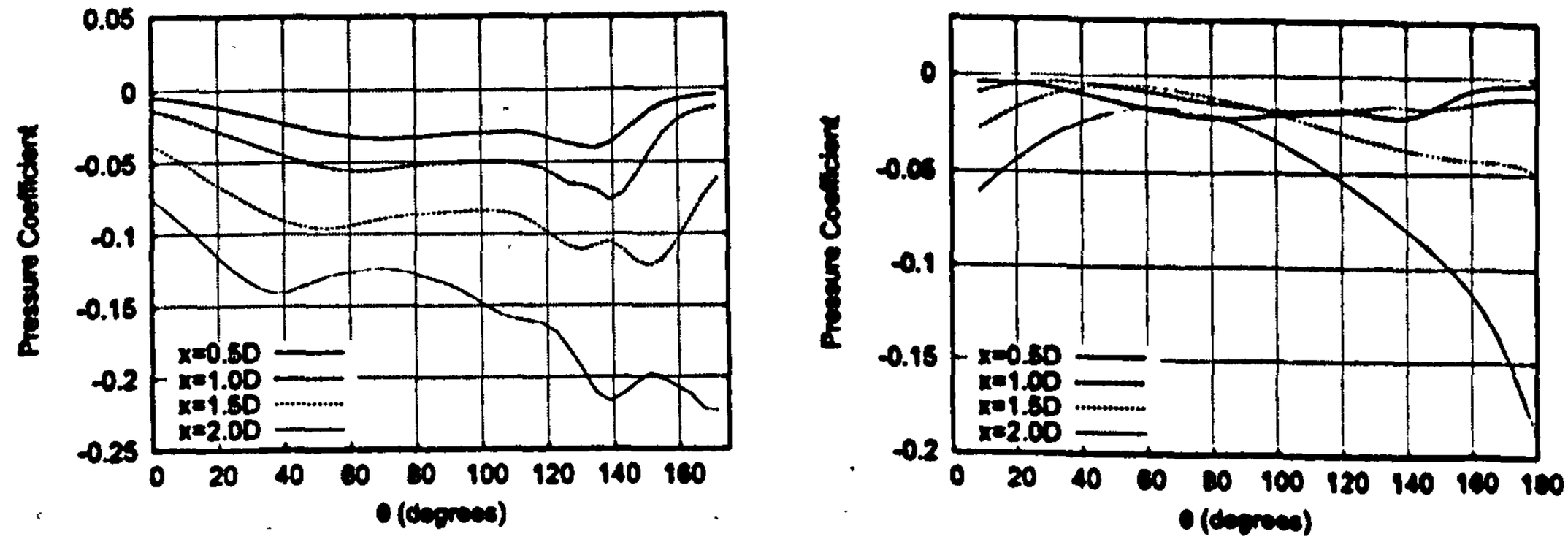

(a) Starboard Profile (b) Port Profile

Figure 89: Circumferential Pressure Coefficient Distributions, $\alpha = 5°, \phi = 330°, x = 7.6D$

The effects on the port side are not immediately obvious, but one can infer from [89(b)] that the fall in pressure coefficient around ($\theta = 120° \sim 180°$), for $x = 2.0D$ is due to the vortex on the upper portion of the body.

The vortical structures observed in [87(d)] may be explained through considering streamlines close to the surface of the body. Consider [90], showing the path of streamlines emanating from the port side of the body, from the windward face. It identifies that the vortex appearing on the upper leeward portion of the body in [87(d)] is the result of the magnetic field directing flow from the apex over the top portion of the nose. In fact, streamlines emanating from the starboard side are also directed towards its opposite side.

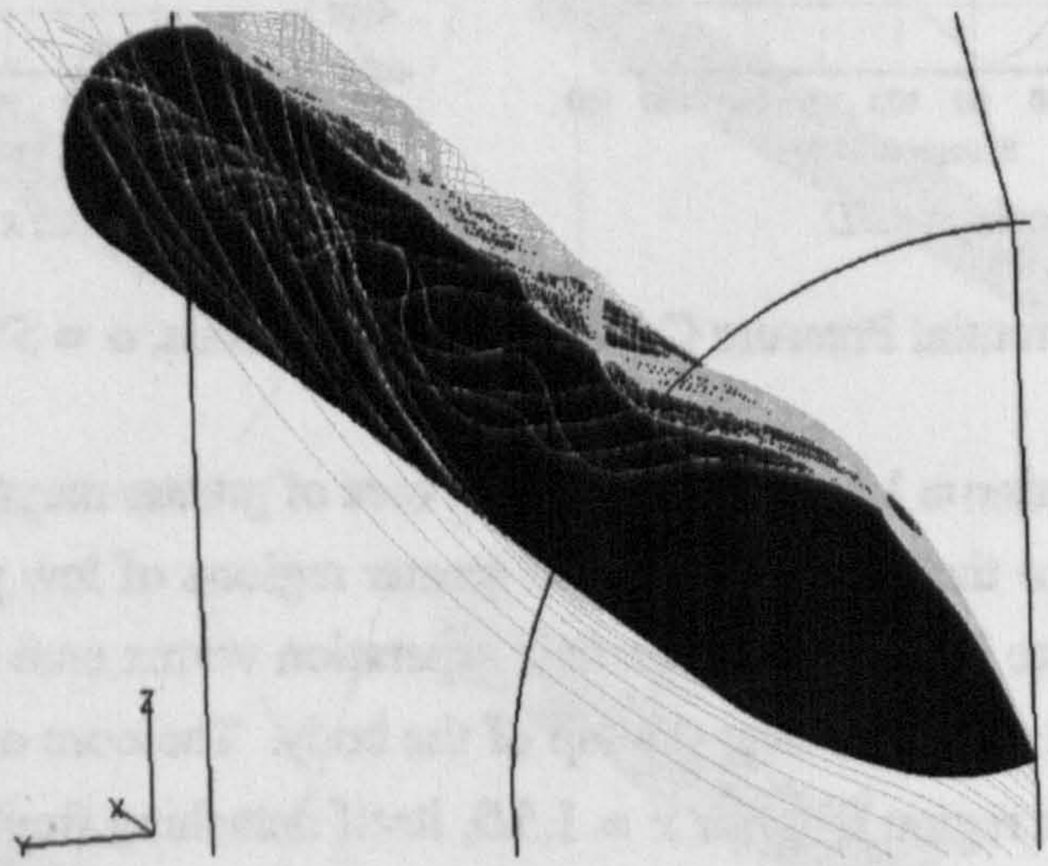

Figure 90: Streamlines, $\alpha = 5°, x = 2.0D, \phi = 330°$

The result is a shearing motion on the leeward side of the missile, culminating in the observed vorticity. Furthermore, the near wall suction vortex observed can also be accounted for by the movement of mass from port to starboard side. The third vortical structure described above, can be attributed to the effects of incidence, although it is clear that flow is also directed under the body.

At higher incidence similar trends in the vortical structures are observed, as the source is moved from the apex toward the fuselage. The figures in [91] for example, track the evolution of vorticity magnitude contours for an angle on incidence of 15 degrees, with the azimuthal location of $\phi = 330°$. At $x = 0.5D$ a certain degree of symmetry is preserved in that the vortices as a result of crossflow separation are evident. Separation occurs earlier on the starboard side however, meaning that the low pressure region at the vortex core on the port side remains closer to the body. A side force acting in in the negative y-direction ensues, and explains why in figure [86] a negative side force is encountered. As with the 5 degree incidence figures above, relocating the dipole source downstream results in the eventual absence the port-side vortex, to be replaced by regions of high vorticity at several locations on the starboard side. Thus, the side force subsequently acts to divert the body starboard, resulting in positive side force generation, as indicated in figure [86].

The effects of changing the azimuthal angle ϕ on the direction of the flow can be understood by examining the Lorentz Force field generated by imposing the magnetic

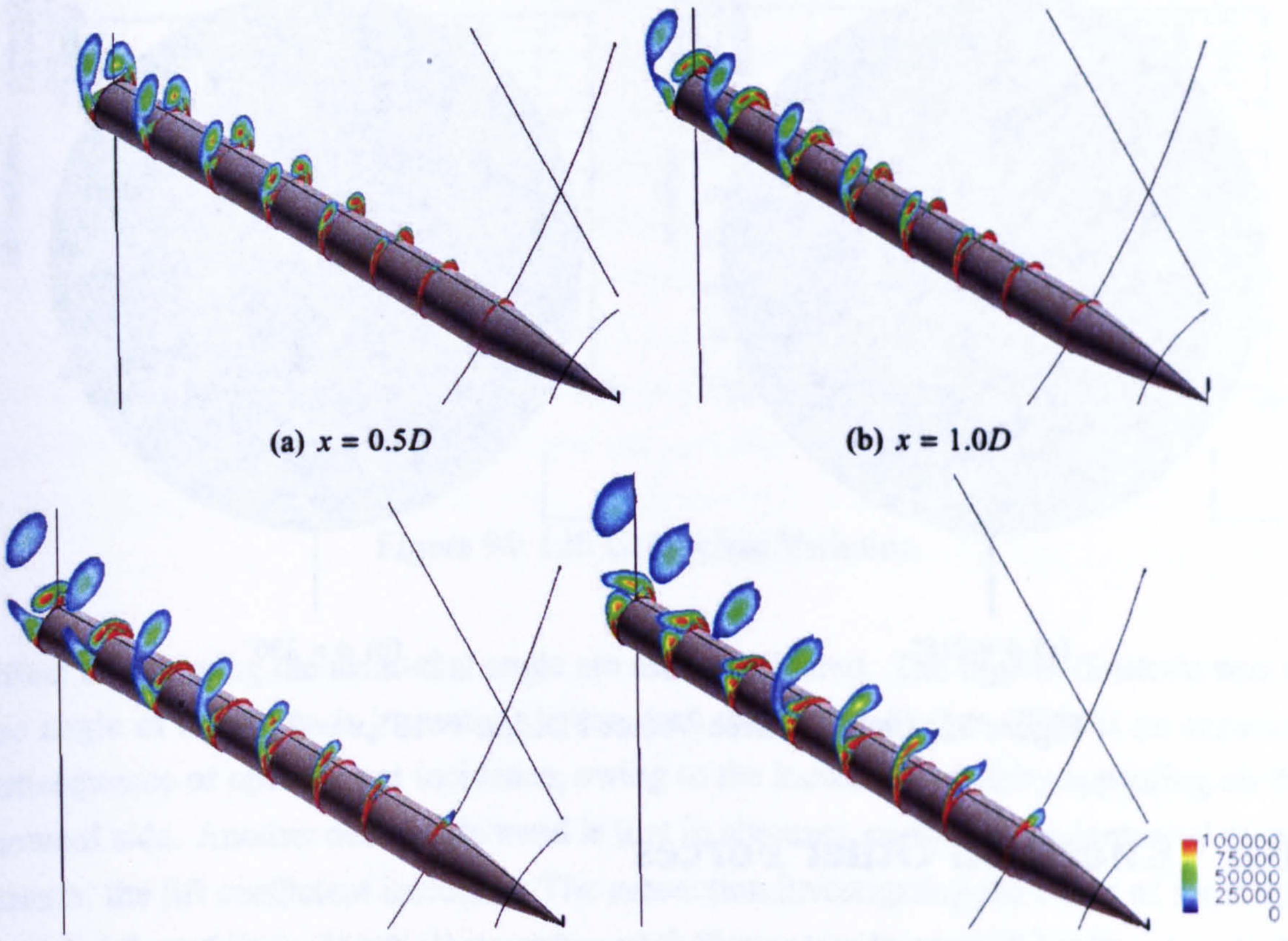

(a) $x = 0.5D$ (b) $x = 1.0D$

(c) $x = 1.5D$ (d) $x = 2.0D$

Figure 91: Vorticity Magnitude Contours, $\alpha = 15°, \phi = 330°$

field . Figure [92] illustrates the force vectors in the y-z plane, for two azimuthal angles, 210° and 330°, superimposed by the contours of the magnitude of the Lorentz force. The vector field is taken at the streamwise station where the nose and fuselage of the slender body meet. As evinced by the streamline figures above, for $\phi = 210°$ the Lorentz force acts to divert mass from the port side to starboard. The converse is also true, but the asymmetry lies in the fact that the magnitude of the vector field is greater on the right of the figure than the left. The main observable difference for the $\phi = 330°$ case is that windward-acting force vectors are present further up, towards the leeward side. There is still a force component diverting the flow over the leeward side, but to a lesser extent than for $\phi = 210°$. The figures therefore reveal consistent behaviour with figure [76] in that the force is acting windward, but particular insight is achieved by examining behaviour dependent on azimuthal dipole position.

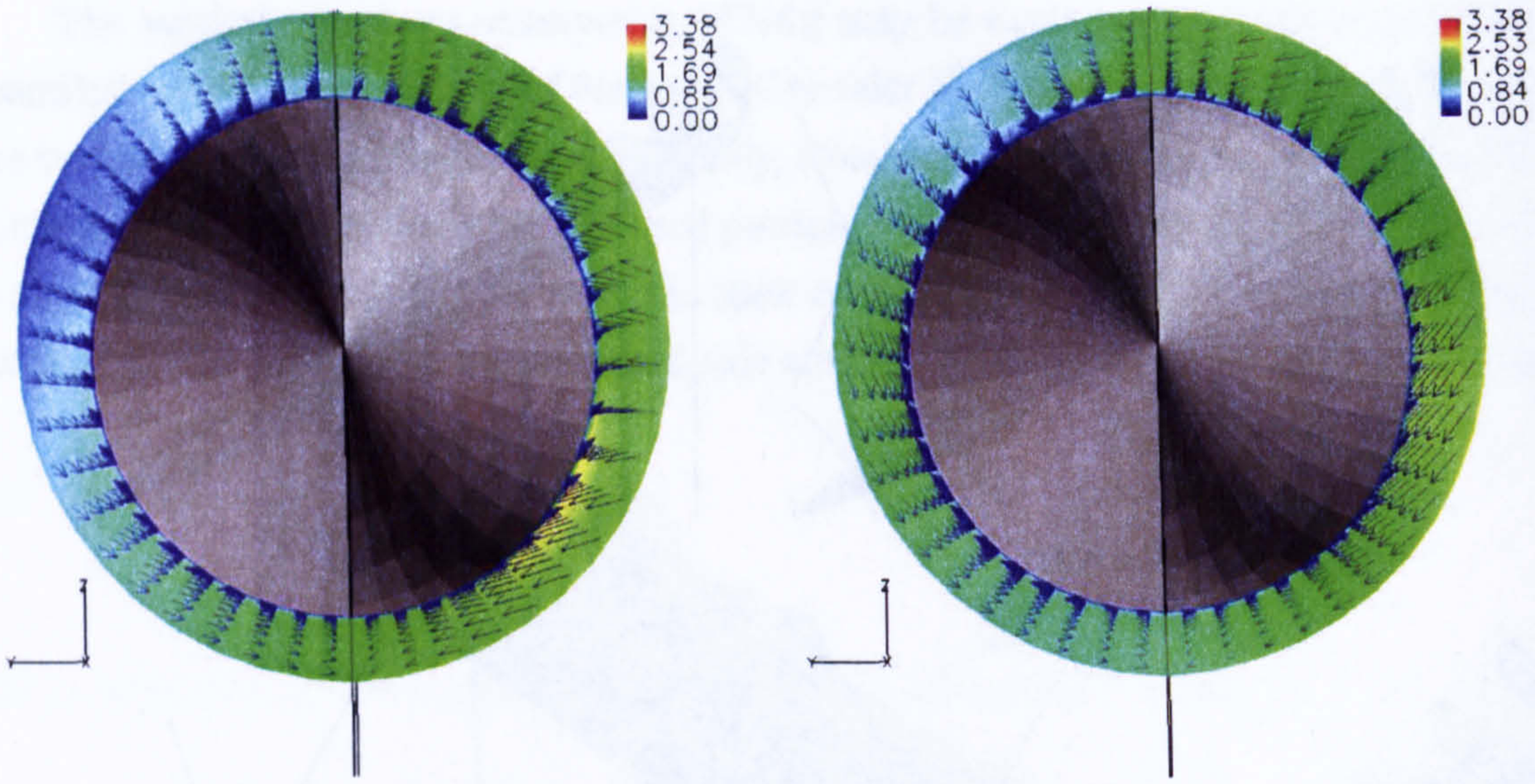

(a) $\phi = 210°$ (b) $\phi = 330°$

Figure 92: Lorentz Force Vector Field, $\alpha = 15°$,$x = 2.0D$

10.6 Effects on Other Forces

The above sections illustrate that the application of magnetic field successfully generates side force, although consideration must be made as to which direction one wishes to exert the force. Examination of side force alone does not ensure successful control however, and in this light the current section examines the consequences on other force data. The variation of lift coefficient with streamwise position of the dipole are illustrated in figures [93] and [94] .

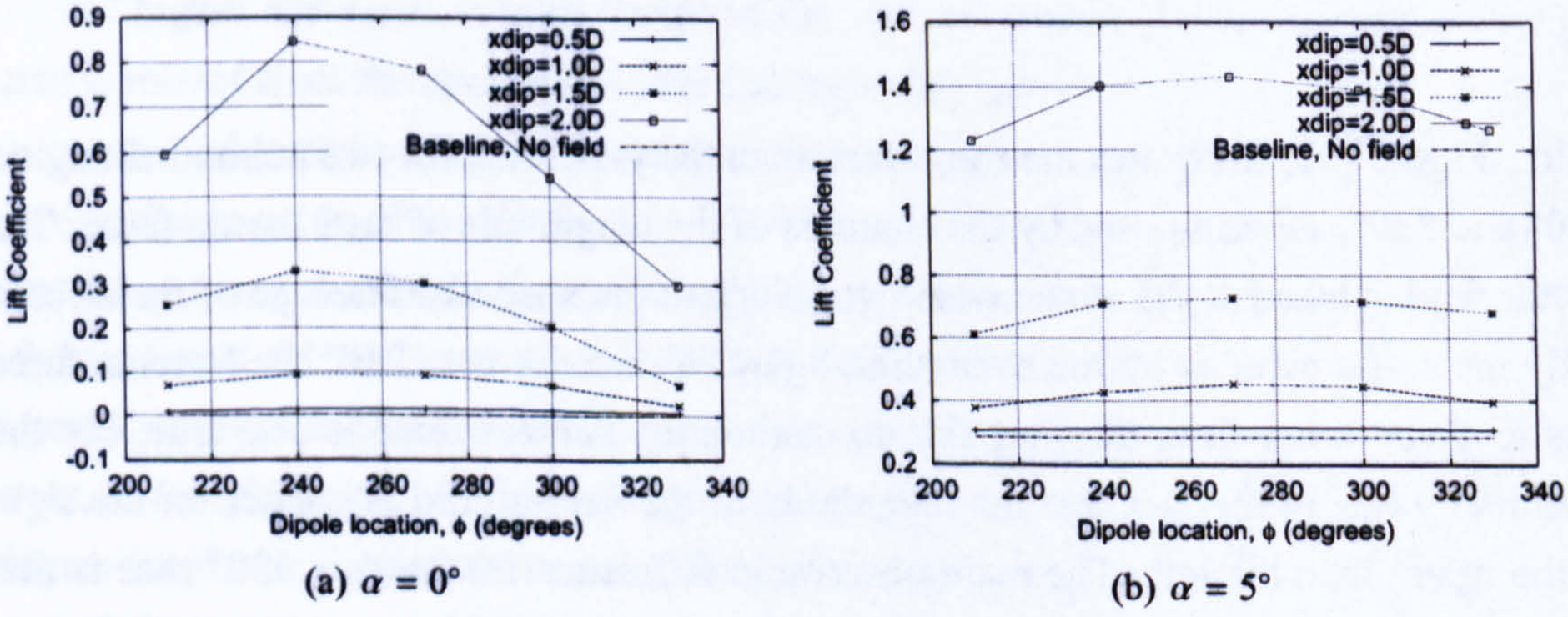

(a) $\alpha = 0°$ (b) $\alpha = 5°$

Figure 93: Lift Coefficient Variation

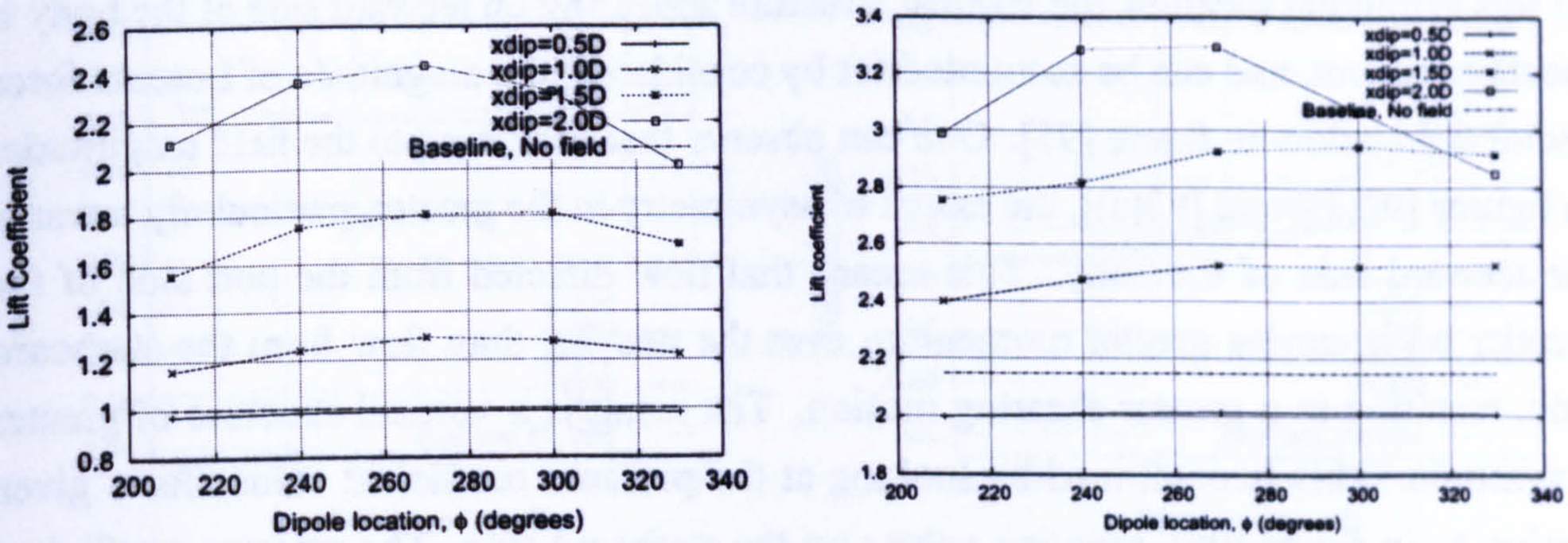

(a) $\alpha = 10°$ (b) $\alpha = 15°$

Figure 94: Lift Coefficient Variation

Effect of changing the azimuthal angle are also considered. The figures illustrate that as the angle of incidence is increased, so too does the lift coefficient. This is an expected consequence of operating at incidence, owing to the increased vorticity appearing on the leeward side. Another observable trend is that in all cases, as the source is moved downstream, the lift coefficient increases. The subsection investigating the effect of incidence revealed that additional vortical structures on the leeward side appeared as the streamwise location of the dipole was increased, resulting in a lower pressure coefficient distribution. Therefore, in addition to the port-starboard differential in pressure coefficient, the difference in pressure gradient between the leeward and windward portions of the body also increases. Since vorticity magnitude on the leeward portion increases with x-location, so too does the lift coefficient.

With the exception of the zero incidence case, the above figures identify that for any given streamwise dipole position, the peak in the lift coefficient occurs when $\phi = 270°$.

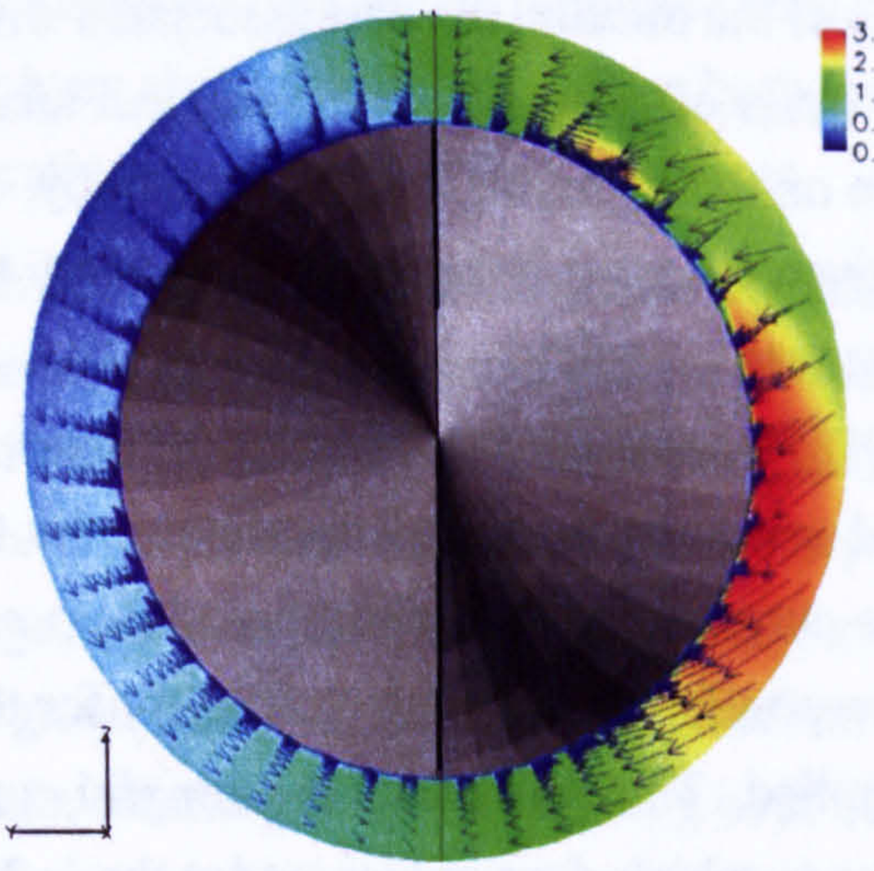

Figure 95: Lorentz Force Vector Field, $\alpha = 15°, x = 2.0D, \phi = 270°$

At this azimuthal location, the vortical structure appearing on leeward side of the body is most prominent, and can be accounted for by considering the magnitude of Lorentz force vector field below in figure [95]. One can observe that compared to the field magnitudes in figures [92(a)] and [92(a)], the extent of asymmetry in the greater, particularly towards the leeward side of the body. This means that flow directed from the port side of the slender body carries greater momentum over the missile, than flow from the starboard side, resulting in a greater shearing motion. The result is a vortical structure of greater magnitude. This is confirmed by looking at the pressure coefficient values for a given station as in figure [96], showing values on the starboard side. The pressure coefficient near $\theta = 180°$ is smallest for $\phi = 270$, confirming the magnitude of the vorticity on the upper surface is greatest for this azimuthal location.

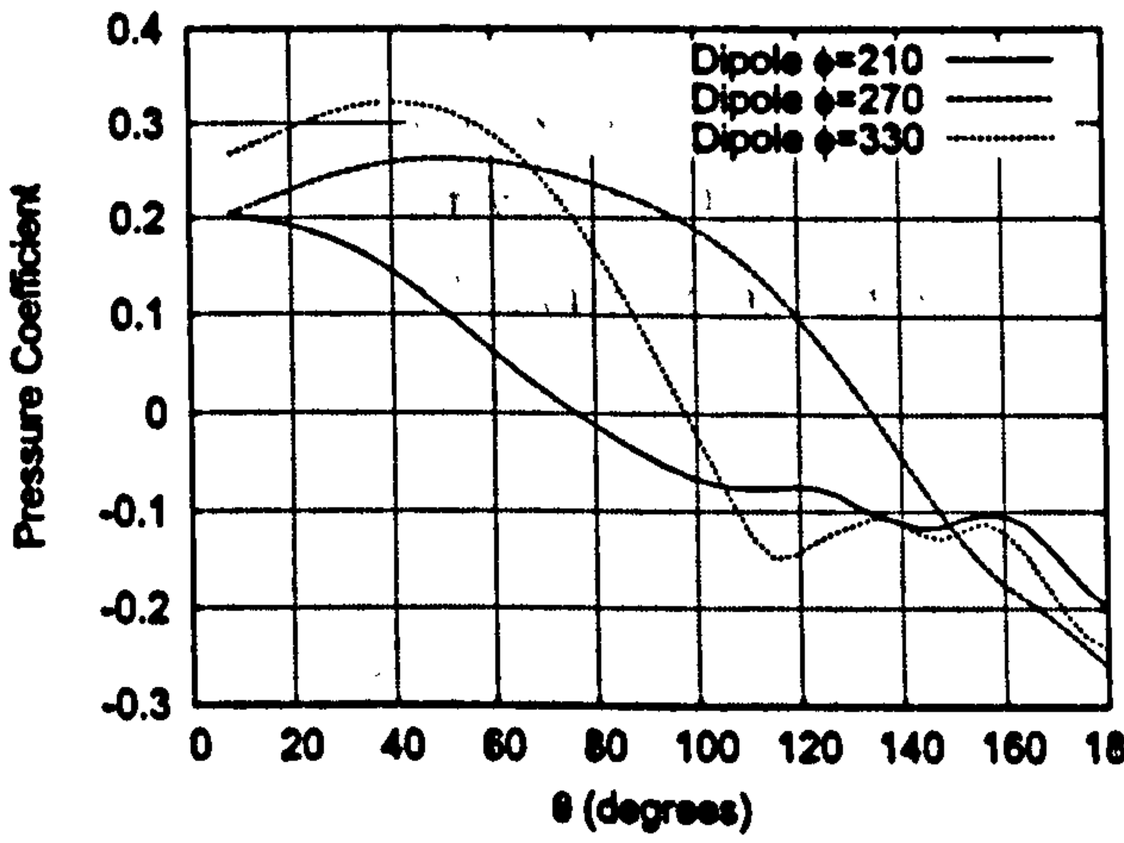

Figure 96: Circumferential Pressure Coefficient, Starboard side. $\alpha = 15°, x = 3.0D$

Any gains in terms of side force generated must be viewed in light of any potential limitations that might be imposed upon the operation of the slender body. In the context of analysing the aerodynamics of the missile, the cost associated with the generation of side force may be described in terms of the drag coefficient. An increase in drag coefficient would result in a restriction on the operating range of the body, or the requirement for a greater fuel load, for any given range. It is therefore mandatory to explore the effects on drag caused by applying the magnetic field .

Figures [97(a)] to [97(d)] represent the variation of drag coefficient as a function of streamwise position and azimuthal angle of the dipole, for the angles of incidence investigated throughout the current study. Superimposed onto each plot is the baseline drag coefficient value, corresponding to the drag coefficient for the baseline case, where the magnetic field is not applied. This provides a meaningful comparison to make, as it provides a benchmark value to which drag values under the influence of a field can be measured against.

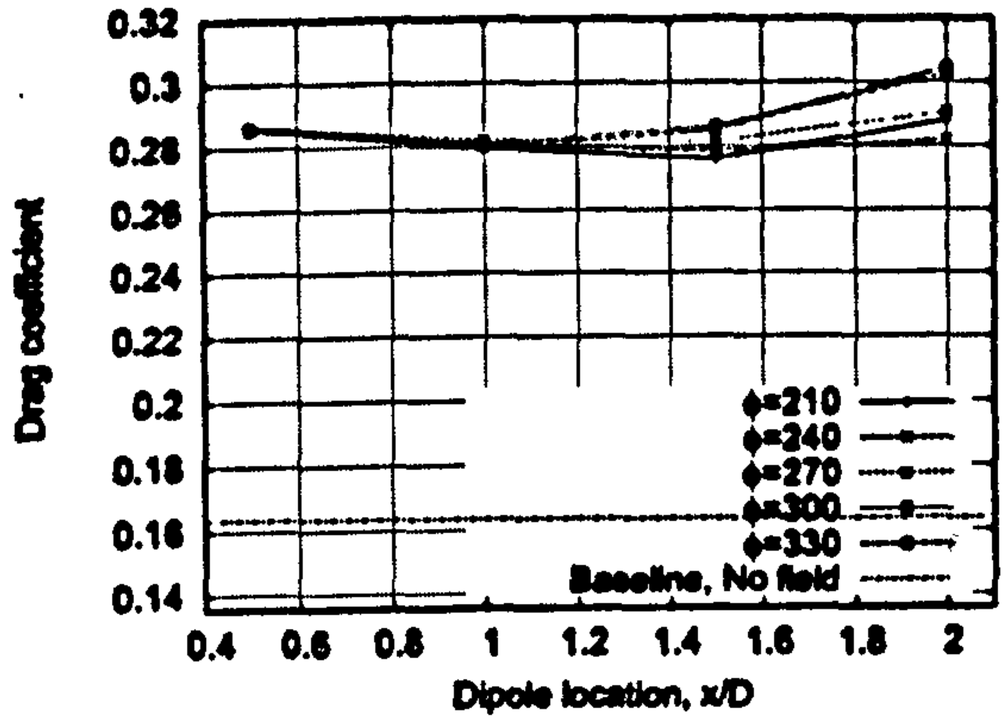

(a) $\alpha = 0°$

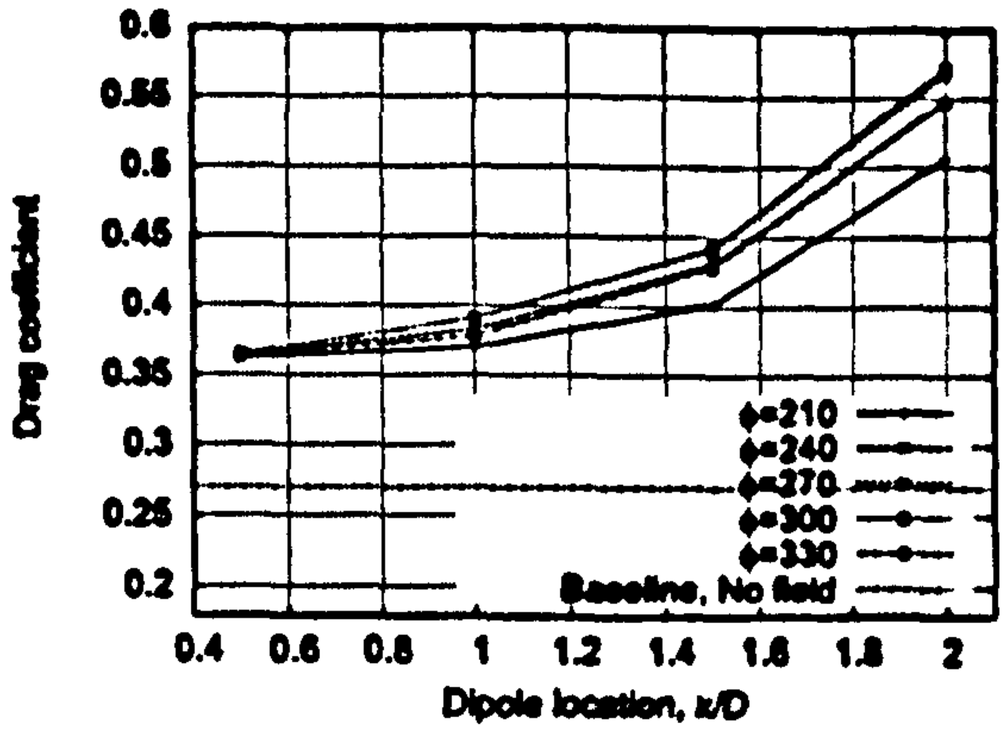

(b) $\alpha = 5°$

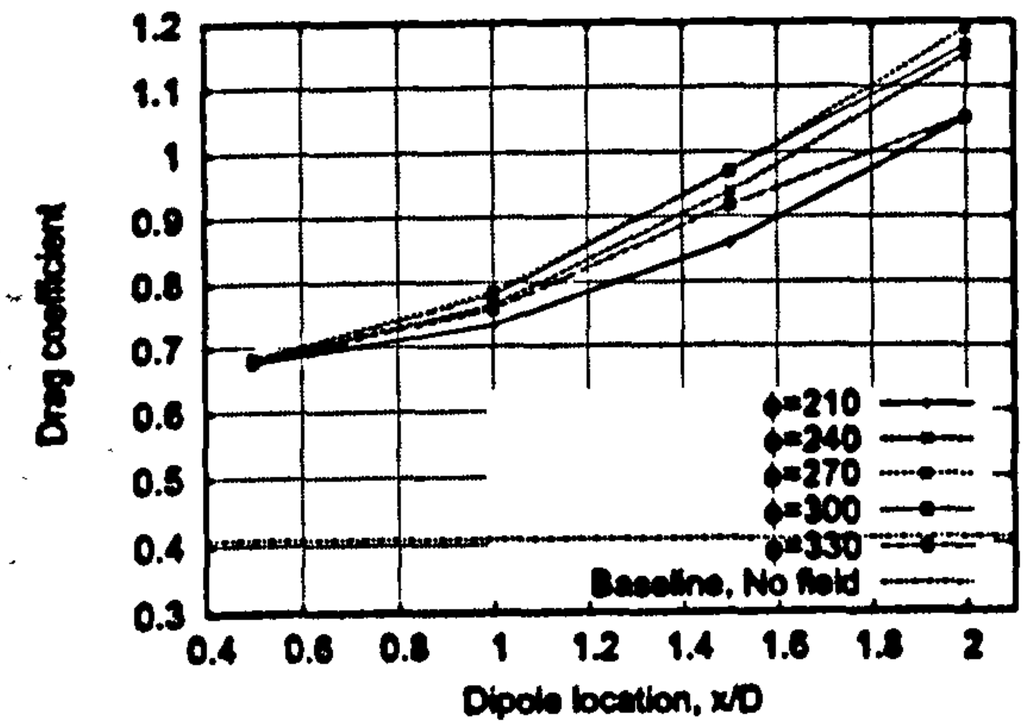

(c) $\alpha = 10°$

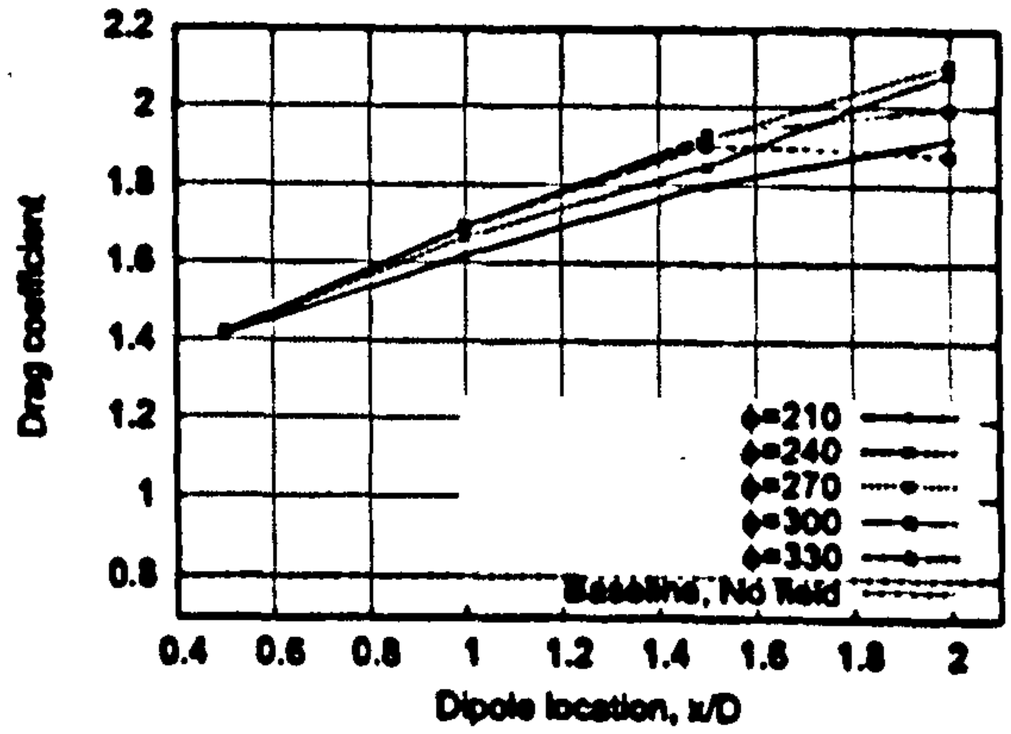

(d) $\alpha = 15°$

Figure 97: Drag Coefficient Variation

It is evident from the above figures that the magnetic field orientations result in drag coefficient values that exceed the baseline calculation value. Generally, one can conclude that drag increases with streamwise position, although there remains an exception for the zero incidence case, at $x = 1.0D$. Regardless of the position of the dipole, the drag coefficient value is greater than that for the no magnetic field case. Recall that the effect of the magnetic field has been shown to divert the flow both leeward and windward, with the consequence of generating additional vortical structures.

The effects of such vortices forming is evident in the skin friction distribution over the missile. Consider the skin friction contours, for the no magnetic field case in figure [98(a)]. In the absence of a magnetic field , the skin friction distribution is symmetric. For a dipole positioned at $x = 2.0D$, both the port and starboard profiles in figure [98] show that the skin friction is greater over the body, particularly over the fuselage. Over the nose, the skin friction is greater on both sides due to the effect of the field redirecting the flow leeward over the body, resulting in additional drag over the entire body. The regions where the skin friction is considerably greater over the fuselage, are regions where one can associate a vortex core to be not far from the surface.

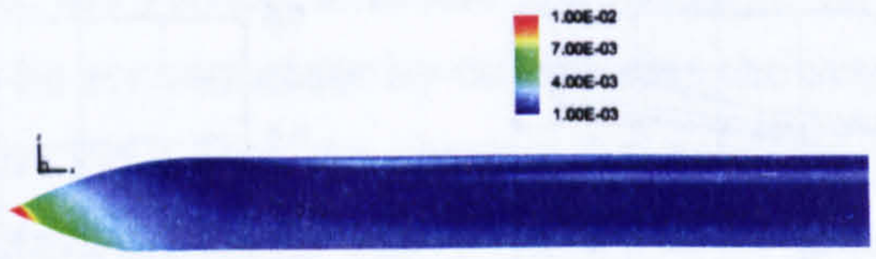

(a) No magnetic field imposed

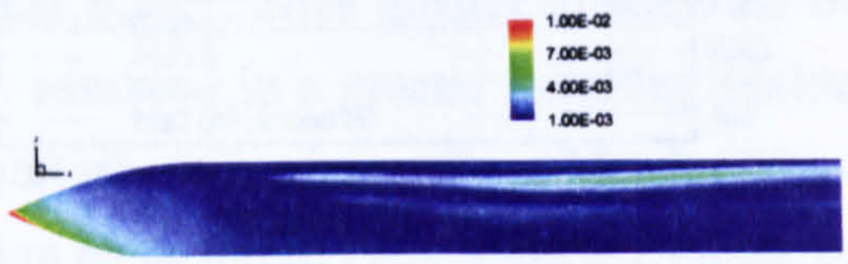

(b) Dipole at $x = 2.0D$, starboard side

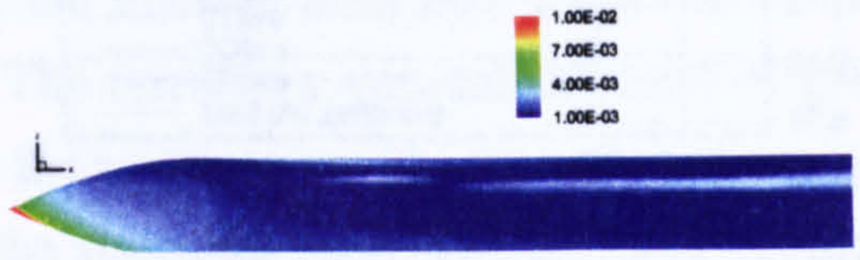

(c) Dipole at $x = 2.0D$, port side

Figure 98: Skin Friction Distributions for $\alpha = 10°$, Field applied at $\phi = 330°$

An unfortunate but necessary consequence in generating a side force therefore, is the additional drag induced by extra skin friction. As evinced in figures [81(a)],[87] and [91]. The magnetic field is capable of generating vortical structures necessary to ensure an asymmetric pressure coefficient distribution over the body, but these are precisely the flow features that result in a rise in skin friction on the body surface.

The sideforces generated due to the magnetic field therefore results in additional forces being produced in the axial and crossflow directions. As the side force intensifies due to placing the dipole further downstream, both the drag and lift coefficients also increase. The Lorentz force applied yields an asymmetric vortex structure, with greater vorticity magnitude resulting in a greater pressure coefficient difference between the leeward and windward portions of the body, causing lift. The same vortical structures also result in additional skin friction being generated, particularly on the leeward and starboard portions of the body, with the consequence of additional drag.

10.7 Stability and Comparison to Conventional Devices

So far the discussion in the present chapter has focused on the use of magneto hydrodynamics in trying to generate forces on a slender body as a means of flow control. To put such a discussion into a relevant context the following is a discussion on the main alternative methods that are available to influence forces, and a comparison of using the proposed MHD method against established techniques that are used in practise.

The most widely used control measures to date have been components such as wings, fins and canards, which are positioned strategically at various streamwise locations, and radial positions on the surface of the missile. Geometrically, these three components may often be of similar shape, but distinctions are drawn between them by the

fact that they are placed in different locations with respect to the centre of gravity of the body. Unlike an aircraft whose wings are fixed and employ elevators and rudders, canards, wings and fins on missiles are attached with hinges, for example. Thus the attachments are designed to be deflectable, and it is this feature that provides the slender body control mechanism.

An extensive amount of research has been conducted to examine the effect of employing such devices. Much of the work to date has focused around attempts to quantify the influence of using a fin or wing by performing component-only analyses, followed by examination of the slender body with wings attached. Hemsch for example estimates force and moment estimations acting on each fin, from which cross-coupling effects and influence on the slender body when attached can be determined [69]. Stallings provides a similar review, with the main emphasis on low aspect ratio wings, at high incidence angles [151]. To test the validity of missile flow prediction code "Datcom", Abney and McDaniel [1] have examined the impact of forces on slender bodies both in the presence and absence of wings, at high angles of attack.

While the emphasis on this has been on the resultant changes in side force coefficient due to adding the influence of a magnetic field, for conventional device research much of the focus has been centred around the changes in lift and drag coefficients. Thus, it is difficult to make a side by side comparison of the two control methods in terms of side force, but contrasts are made here against data that is available.

For example, in Abney and McDaniel, [1] results are compared for supersonic flows past B1 with and without the use of fin plates at the base of the projectile. The fin employed is the "T3" clipped delta planform shape, the details of which are provided in the above reference. The experiments and datcom simulations are taken such that the freestream Mach number is 0.8, with a Reynolds number of 2.3×10^6. In their work they present the following results for experimental lift coefficient data. Some of their main findings are presented within table [12] below.

Angle of Incidence	C_L without fin	C_L with fin
5	0.1	0.49
10	0.45	1.1
15	0.9	2.5

Table 12: C_L Experimental Results for B1, with and without fin, from [1]

It is clear from the above that the addition of four fins at the base of the body result in additional lift being generated, as one would expect if the body was operating at incidence.

Table [13] shows the lift coefficient results for a delta wing with several aspect

ratios (AR), operating at Mach 2.86. The data is taken from [151] and provides an idea as to the magnitude of the lift one can expect from using such a device to generate lift. The benefits to lift coefficient from using a a larger aspect ratio delta wing are evident, although Stallings also points out that increasing Mach number results in lower lift coefficients as there is a reduction in the windward-surface pressure coefficient, and also due to the loss of vortex lift on the leeward surface.

Angle of Incidence	C_L, AR=0.5	C_L, AR= 1.0	C_L, AR=2.0
5	0.06	0.1	0.105
10	0.16	0.19	0.22
15	0.23	0.28	0.34

Table 13: Delta wing Lift Coefficient, from [151]

Stallings also provides figures on the effect of using delta wings attached to a body. At a Mach number of 0.8, at 10 degrees incidence, the experimental results show that the lift coefficient increases from approximately 0.4 to 2.3 when delta wings are included in the configuration. The inclusion of strakes to the configuration increases the lift coefficient further to 2.9.

It is difficult to directly compare the results given by applying a magnetic field to the conventional device results found in the literature, as the works do not make specific reference to the impact on side force, but rather on the lift coefficient generated due to the addition of fins and wings. Nevertheless, the above discussion does provide a benchmark to which one can judge the magnitude of the impact on lift coefficient due to the magnetic field .

Examining figures [93] and [94] shows that as one would expect even in the absence of the field, lift coefficient is an increasing function of incidence. Secondly specific figures also show that as the field source is moved downstream, lift coefficient increases. Comparing the effects on lift coefficient between the baseline case and the cases where the dipole is positioned at $xdip = 2.0D$, in the most extreme case, one can observe an increase of more than double in the lift coefficient. This is observed for the case where $\alpha = 10°$, $\phi = 270$. The above discussions on the works by Abney and McDaniel [1], and Stallings [151] also show a more than double increase in lift coefficient due to the additions of fins and wings respectively. Given these figures one might conclude that the resultant change due to the magnetic field is not excessive.

However, one must reiterate here that the purpose of applying the magnetic field is to try and introduce side forces that might alter and control the flight trajectory of the body. Figures 84, 85 and 86 illustrate that such an introduction is indeed possible,

but this discussion highlights that there are some unintentional consequences as regards lift. There are two causes of the additional lift. The first is due to the body operating at incidence. The second is due to the low pressure regions being created on the leeward side of the body. This magnetic field acts to redirect the flow, resulting in extra vorticity. The increase in lift can at most be a twofold increase, thus further analyses are required to try and alleviate the control mechanism of this consequence. This could be in the form of restricting the dipole position to be in close proximity to the body apex, or to use a weaker magnetic field.

The above discussion therefore suggests that the changes to the lift coefficient are of the same magnitude as if one were to attach conventional flow control devices such a fins or wings to the slender body. This unintentional consequence of imposing a field is thus a restriction in making use of MHD as a flow control mechanism, although to assess its use thoroughly one must also investigate the stability characteristics of a body under the influence of the field. As the calculations in this chapter have examined the effect of angle of incidence, longitudinal stability is considered here.

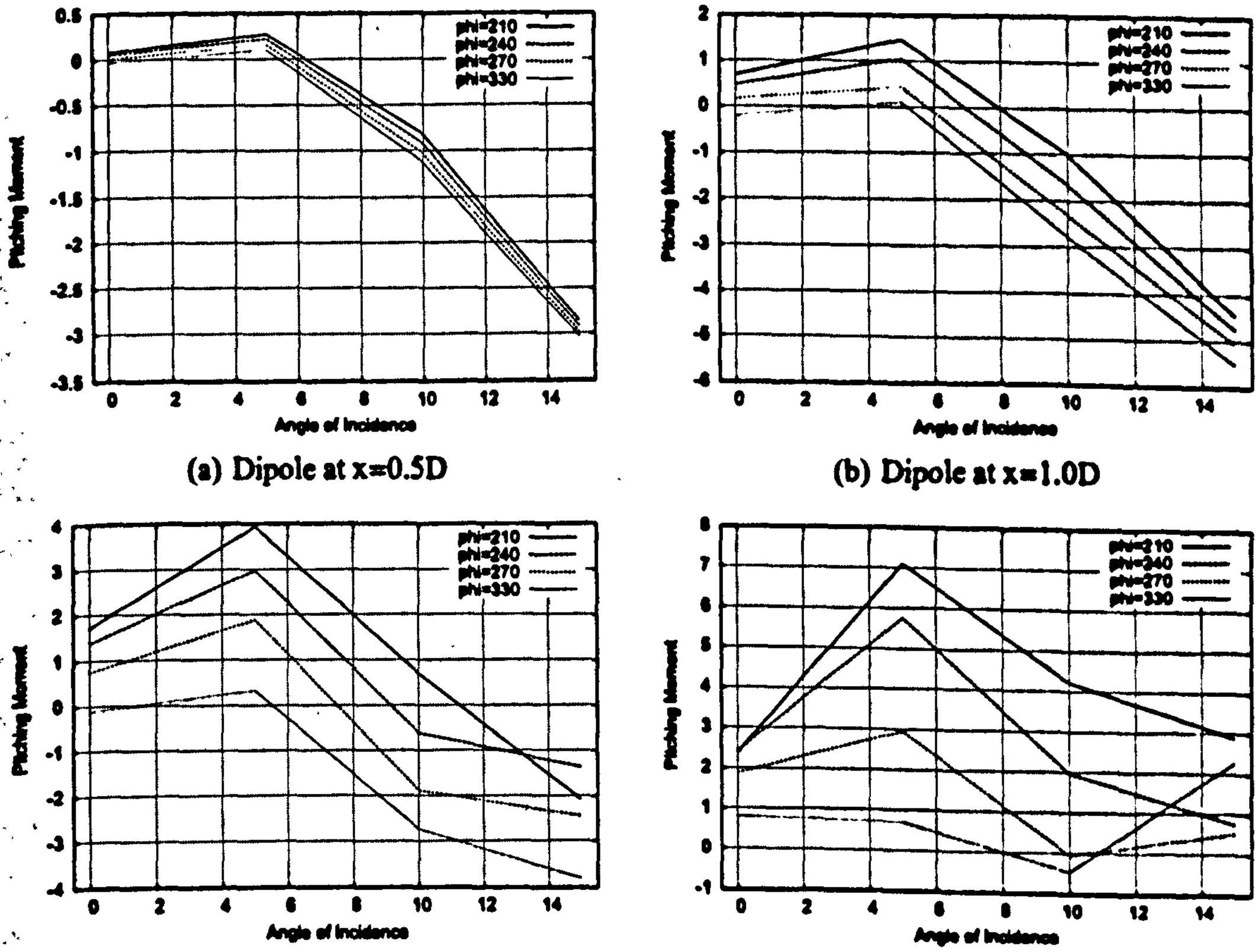

(a) Dipole at x=0.5D

(b) Dipole at x=1.0D

(c) Dipole at x=1.5D

(d) Dipole at x= 2.0D

Figure 99: Pitching Moment Coefficient, as a function of Angle of Incidence

Figures 99(a) to 99(d) show the variation of pitching moment coefficient with respect to angle of incidence ,for a dipole placed at each of the four streamwise locations and 5 radial positions. The moment is taken about the centre of gravity of the body. A body is defined to be longitudinally stable if the derivative of the pitching moment with respect to α is negative, and as the figures show, this is generally true for most cases except where the angle of incidence is between zero and five degrees. It is therefore possible to conclude that the pitching moment acts to restore stability outside the zero to five degrees incidence range. Within this range, the body is longitudinally unstable, therefore caution is needed in operating in this domain.

From the above figure, it can therefore be concluded that the imposition of the magnetic field does not disturb the longitudinal stability of the slender body, except for when the angle of incidence is between zero and 5 degrees. As far as yaw and rolling moments are concerned, the current calculations do not involve simulations with non zero side-slip or roll angle, so no discussions can be made as to the stability of the aircraft with respect to these moments. Future work therefore must address this issue by examination of the field effects under the influence of side slip and and roll.

10.8 Engineering aspects of MHD control

When considering the present test case, it is important to note the flow conditions associated with the problem. Given that the incidient Mach number is 2, and the freestream temperature is 183.33 Kelvin, it would be wrong to assume that the flow would become ionised naturally in the presence of the body. In chapter 2 it was stated that temperatures in excess of 9000K were needed for Oxygen and Nitrogen to ionize.

At a low incident Mach number such as in this case, an artificial ionization mechanism, such as those discussed in chapter 4, would be needed to seed the flow with electrons. It is therefore mandatory to examine the costs and penalties of these configurations and compare them with conventional control devices.

In the work of Shang [144], the ionization of air using glow discharge is considered to be most efficient given that only the valency electrons, that is the outer shell electrons are removed. The ionization potential to remove an electron from an air mixture is given by the ionization potentials of the specific components. The ionization potentials for N_2 and O_2 are 15.6 and 12.1 electron Volts (eV) respectively, where as alkali metals have lower ionization potentials. Cesium for example has an ionization potential of 3.9eV. Thus seeding materials such as potassium or sodium are favourable.

Glow discharge generation can be achieved using radio frequency generation or direct current discharge, both of which can generate a uniform plasma. At pressures from

above 2 torr Shang reports that radio frequency can generate a plasma with power up to 100W with a modest operational cost, where as direct current discharge consumes about 1kW for the equivalent plasma. Thus the operational costs for ionizing the flowfield may be regarded as relatively small amount in terms of power consumed.

As for the weight penalty, in a separate work Steeves et al approximate the weight of a system to generate magnetic field to be on the order of 100kg [152]. This might seem like a prohibitively expensive cost penalty when considering a slender body such as in the present case, but it is important to note that in Steeves work, the vehicle in question is an atmospheric reentry vehicle. The extent of the weight penalty really needs to be addressed in terms of the missile for which its use is intended, thus one cannot make a single statement as to whether such a system would be prohibitive. Air to air missiles on one hand are typically on the order of about 100kg, thus such as system would be unfeasible, although some air to surface missiles can be several thousand kilograms. Intercontinental missiles are on the order of several tens of thousands of kilograms, and are therefore a more suitable candidate.

It should also be mentioned that Shreeve et al [152] state that a 110kg magnetic system was able to extract 0.6MW of power over a period of 1000 seconds. For a case involving atmospheric reentry the extent of ionization of the flowfield is likely to be a lot greater than that for the case where seeding particles are generated by some of the aforementioned systems. However, given that there the flow is ionized, it is conceivable that the magnetic system may be used to extract power and supply the seeding mechanisms. What is unclear at present however, is how the weight of the magnetic system might change, depending on the extent of ionization. At low ionization levels, one would expect that a stronger field would be required for control, in turn necessitating a larger system. Thus some exploratory work for the weight penalty, given the extent of seeding is also necessary.

10.9 Conclusions

A novel application of magneto-hydrodynamic flow control, applied to slender body aerodynamics has been studied. The results have shown that flow may be redirected over the missile, to return side forces in both directions, depending on the position of the dipole source.

The chapter began with the aim of trying to apply a controlling mechanism for a supersonic slender body flow, through the application of a magnetic field . The objective was to be able to generate a side force by introducing artificial asymmetries into the flow. The use of magneto-hydrodynamics provides a distinct advantage over conventional

mechanical flow control devices, as it allows flow to be enacted upon at a distance, and the actuation times are considerably faster.

To ensure accuracy of the original model in the absence of the low magnetic Reynolds number model , iterative and convergence studies have been performed, and an extensive comparison to experimental pressure coefficient distribution data has been made. Comparisons to axial pressure coefficient distributions revealed excellent agreement at all incidences, for all azimuthal positions. With regard to circumferential pressure distributions on the surface, the parabolized Navier Stokes model returned good agreement in terms of capturing the primary separation location for all angles of incidence considered. However, accuracy in resolving the magnitude of the pressure coefficient showed some discrepancy, most notably for the $\alpha = 5°$ case. Laminar simulations have been performed, although the discrepancy in the above calculations may be the result of transition to turbulence in the experiment, in view of the fact that the operating Reynolds number is relatively large.

A parametric study, investigating the effects of an asymmetrically positioned dipole was performed. Earlier sections revealed that magnetic field lines directed normally to the incident flow direction result in a decelerating effect. The creation of an asymmetric vortical structure depended upon being able to decelerate the flow in the crossflow plane, and therefore a dipole field was chosen such that vector dipole moment was parallel to the y-vector. The study considered the effects of streamwise position, azimuthal location, and angle of incidence on the forces generated on the body.

At zero incidence, simulations revealed that it is possible to generate side forces acting in both directions, depending on the azimuthal position of the magnetic field source. For dipoles positioned in the windward region (in relation to slender body flows at incidence), the side force generated acted to divert the body in the port direction, and dipoles positioned in the leeward region resulted in forces acting starboard. The magnitude of the side force was shown to be highly dependent on the streamwise position of the source. This result remained true for flows at incidence, although the side force in the majority of cases resulted in a force acting starboard, regardless of the choice of ϕ. The direction and extent of force created could be understood by examination of the vortical structures generated. The magnetic field redirected flow both over and under the nose region of the body, causing the eventual suppression of the port side vortex as the source was moved downstream, as well as the creation of additional structures on the leeward and starboard areas. Since the cores of such vortical structures are associated with low pressure, this resulted in differentials in pressure coefficient on the surface, and hence the generation of side force .

The same vortical structures also resulted in additional lift and drag for the missile. Not only is there an imbalance in pressure coefficient between the port and starboard

sides, the additional structures also result in greater imbalance between the windward and leeward pressure coefficient distributions, and thus greater lift. Greater skin friction coefficient could also be identified on the body surface, within regions beneath the vortical structures, a contributing factor to the observed increase in drag coefficient.

In the works by Corriveau et al [33, 63, 34], side force is generated through the use of micro flow effectors protruding from the surface of the missile nose. They were able to generate side force coefficients of up to approximately 0.6, depending on the angle of incidence, with minimal consequences on the lift and drag coefficient. The current study demonstrated that larger side force coefficients may be generated, at the expense of extra lift and drag. To try and limit the effects on these force coefficients, it may be worth investigating the effects of field strength as well as the radial position of the source. In some circumstances, crossflow separation may be minimised on the dipole side, resulting in asymmetry purely as a consequence of vortex cores of differing strength. In other cases however, the port side vortex was shown to disappear completely, resulting in considerable asymmetry. It may be possible to limit such situations through the use of weaker magnetic fields, and hence its investigation is warranted as further work.

Conclusions and Future Work

A research programme was initiated to evaluate the potential of magneto-hydrodynamics as a viable flow control device for supersonic and hypersonic vehicles. The initial objective was to develop and implement magneto-hydrodynamic models into an existing solver, and to obtain an understanding of the effects of applying magneto-hydrodynamics to practical supersonic and hypersonic flow problems. Models accounting for magneto-hydrodynamic effects have been developed and implemented into a three dimensional parabolized Navier Stokes solver. The models investigated were the following;

- The simplified magneto-hydrodynamic model, accounting for the coupled interaction between a flow field and magnetic field, for a single species gas.

- The low magnetic Reynolds number model , suited to circumstances where the magnetic Reynolds number is negligible, corresponding to cases where the magnetic field may influence the flow, but not vice versa.

The models were verified and validated, whereupon they have been used to study the effects of magneto-hydrodynamics on two and three dimensional flows of interest.

- **PNS and MHD model Validation and Verification**

Throughout the thesis, constant reference was made to assessing the predictive reliability of the IMPNS parabolized Navier Stokes solver in dealing with problems of interest. In the absence of experimental data for magneto-hydrodynamic problems to which comparisons could be made, ensuring accuracy of the baseline solver was paramount. To this end several observations can be made;

- In verifying the low magnetic Reynolds number model , comparisons of shock stand off distance profiles without any magnetic field showed good agreement with analytical and experimental data. At higher Mach numbers there was some difference with Van Dyke's simulations, possibly caused by choice of geometry.

- Good agreement with theoretical results in the prediction of an optimal parameter for the axisymmetric power law body was also achieved.

- Prior to investigating the effects of applying a magnetic field to flow past a slender body, an extensive analysis going beyond prior comparisons, was undertaken to

compare numerical simulations to experimental data. Axial pressure coefficient distributions showed excellent agreement for all conditions investigated.

- Circumferential distributions also indicated that the points of primary separation were accurately captured.

- At low incidence however, there was a degree of discrepancy in the magnitude of the pressure coefficients for circumferential distributions. This could be attributed to possible natural transition to turbulence in the experiments, or data mismeasurement.

The simplified magneto-hydrodynamic model has been used to examine flow through a compression-expansion channel. In light of the fact that the model was unable to return a converged solution, a novel verification procedure has been applied to the magnetic induction equations.

- The method of manufactured solutions identified specific errors in the implementation of the modified source term and boundary conditions, for the equations governing the magnetic field.

- The modifications as result of analysing the code using the method of manufacture solutions resulted in iterative convergence and robustness for the induction equation solver.

Despite the improvement however, the full solver accounting for field-flow interactions could not provide convergence. Necessary future work therefore, will be in the investigation of alternative numerical solution procedures for the simplified magneto-hydrodynamic equations. Satisfying the $\nabla \cdot \mathbf{B} = 0$ condition was addressed by adding Powell's source term to the governing equations, and subsequently re-writing the term to appear in the form of convective derivatives in the original equations. Furthermore, a decoupled algorithm, whereby flow and magnetic field solution variables are updated independently of each other had been used. In light of this, an alternative would be to employ a coupled algorithm, using a flux evaluation scheme that takes into account the variations in both sets of variables simultaneously.

The low magnetic Reynolds number model was used to gain further understanding as to how different types of magnetic field orientation affect a flow field. Excellent agreement was made in validating the implementation against other numerical results, and an uniformly distributed field was shown generate a more effective Lorentz force to decelerate incident flow for a blunt body geometry. Whilst impractical to achieve uniformity in practise, this provided valuable understanding as to the form of magnetic fields required

for subsequent studies.

SHyFE Optimisation Study

One of the areas identified in the literature that require investigation was in combining magneto-hydrodynamic models into an optimisation framework for practical bodies of interest. A novel optimisation study on a ramjet intake was therefore initiated to investigate the possibility of rectifying an off design condition.

- Using a response surface based optimisation technique with a least squares polynomial regression model, an optimal magnetic field strength was identified to ensure shock on lip condition, for a dipole with fixed position.

- A further study, investigating the combined effects of magnetic field strength, and a variable dipole position, revealed that the same condition could be achieved with a weaker field, if one chose a suitable magnetic field source location.

- For cases where trends in the objective function are relatively simple, or where the domain of interest is relatively small, the least squares regression model was appropriate due to its simple formulation and speed with which a gradient based search could be performed.

- The least squares regression model was found to be inappropriate for a multivariate optimisation problem, as there was no improvement in the search for the optimum, for the variable dipole location study.

- Due to their interpolating nature, radial basis functions were shown to be more effective, although some optimum values proved to be physically untenable. Updating such values with the analysis code dealt with such issues, and despite the extra time needed in the optimum search procedure, the radial basis functions proved to be more effective in obtaining the global optimum over the data.

Extending the SHyFE geometry to a full three dimensional body would provide greater understanding of some of the other complex issues related to shock impingement control. For example, a three dimensional intake operating at incidence could result in spillage in some regions, as well as unstart in other areas. Finding an optimal field that would satisfy impingement over the entire lip therefore poses a significant challenge, but one that would result in considerable efficiency gains for the intake.

Slender Body Flow Control

In a novel application of magneto-hydrodynamics , it was also shown that a magnetic field

may be successfully applied to flows past a slender body to induce side forces, thereby improving manoeuvrability of missiles.

- The direction and extent of the side force was found to be dependent on angle of incidence of the body, as well as the streamwise position and azimuthal location of the dipole source.

- At zero incidence, side forces were shown to be generated in both directions, depending on the azimuthal location of the dipole. Sources placed in the lower quadrant diverted the body in the port direction, and sources in the upper portion directed the missile starboard.

- At incidence, greater side forces could be generated due to the fact that there is already vorticity present in the flow due to naturally occurring structures in the absence of the field. These may exploited by enhancing or subduing the structures to create greater asymmetries.

- Regardless of incidence, it was found that moving the source downstream resulted in greater side force generation.

- As the side forces generated were due to low pressure regions within the vortex cores, the application of a field also resulted in changes to increases in the lift and drag coefficient.

Other studies involving the use of flow effectors have shown that it is possible to induce side forces with minimal side effects on the lift and drag coefficient. Consequently, further work is needed to achieve this outcome. The side forces generated were typically greater than those generated through the use of effectors, suggesting that the field imposed may have been excessively strong. Whilst the underlying influence of the field has been investigated and understood, it is not clear at present what effect changing the field strength would have. A natural extension therefore would be to introduce magnetic field strength as an additional design parameter. The study also only considered one magnetic field orientation, based on previous revelations concerning the nature of field/flow interaction. There may be more suitable orientations, depending on the incidence, for example. Furthermore, in light of the optimisation study performed for the SHyFE intake, it would be constructive to perform a similar analysis for the slender body. Searching for the largest side force generated given the above variables as the design space, as an example.

General

Use of the low magnetic Reynolds number model required the assumption that the flow field is ionised some how. For reentry problems, due to the high temperatures, ionisation would be a naturally occurring phenomenon, but in the current investigations, the flow was assumed to be seeded artificially. The simplified magneto-hydrodynamic model was also limited in that it modelled a single species gas. Therefore to make simulations more physically realistic, some effort could be spent as future work in the development of multi-species model that would capture the effects of ionisation. Such an implementation would allow experimental verification of numerical simulations, as many of the experimental test cases performed have involved artificial ionisation techniques.

BIBLIOGRAPHY

[1] E.J. Abney and M.A. McDaniel. AIAA-2005-5086: High angle of attack aerodynamic predictions using missile datcom. In *AIAA Applied Aerodynamics Conference*, 2005.

[2] M.C. Adams. Determination of shapes of boattail bodies of revolution for minimum wave drag. NACA-TN-2550. Technical report, NACA, 1951.

[3] R.K. Agarwal, K.Y. Yun, and R. Balakrishnan. Beyond navier stokes: Burnett equations for flows in the continuum transition regime. *Physics of Fluids*, 13:3061–3085, 2001.

[4] J. Ahn, H.J. Kim, D.H. Lee, and O. Rho. Response surface method for airfoil design in transonic flow. *Journal of Aircraft*, 38:231–238, 2001.

[5] H.J. Allen and A.J. Eggars. A study of the motion and aerodynamic heating of ballistic missiles entering the earth's atmosphere at high supersonic speeds. naca report 1381. Technical report, NACA, 1958.

[6] D.A. Anderson, J.C. Tannehill, and R.H. Pletcher. *Computational Fluid Mechanics and Heat Transfer*. Routledge, 1984.

[7] J.D. Anderson. *Hypersonic and High Temperature Gas Dynamics*. AIAA, 2000.

[8] J.D. Anderson. *Modern Compressible Flow: With Historical Perspective*. McGraw-Hill, 2004.

[9] P. Audze and V. Eglais. New approach to planning out of experiments. *Problems of Dynamics and Strength*, 35:104–107, 1977.

[10] J. Augustinus, K.A. Hoffmann, and S. Harada. Effect of magnetic field on the structure of high speed flows. *Journal of Spacecraft and Rockets*, 35(5):639–646, 1998.

[11] D. Barberis. Supersonic vortex flow around a missile body. AR 303. Technical report, AGARD, 1994.

[12] S.B. Batdorf. Alleviation of the sonic boom by thermal means. *Journal of Aircraft*, 9:150, 1972.

[13] M.C. Biggs. *Towards Global Optimization*, chapter :Constrained Minimization Using Recursive Quadratic Programming. North-Holland, 1975.

[14] T.J. Birch, W.S. Helliwell, S.A. Prince, G.M. Simpson, and D.K. Ludlow. AIAA-2002-4512: IMPNS: A space marching solver for predicting the aerodynamic characteristics of high speed missiles. In *AIAA Atmospheric Flight Mechanics Conference and Exhibit, 2002*, 2002.

[15] T.J. Birch, S.A. Prince, D.K. Ludlow, and N. Qin. AIAA-2001-1753: The application of a parabolised navier stokes solver to some hypersonic flow problems. In *International Space Planes and Hypersonic Systems and Technologies Conference, 10th*, 2001.

[16] V. Bityurin, V. Velikodny, A. Klimov, S. Leonov, and V. Potebnya. AIAA-1999-3533: Interaction of shock waves with a pulse electrical discharge. In *AIAA Plasmadynamics and Lasers Conference, 30th*, 1999.

[17] S. Boon and R. Hillier. AIAA-2006-3036: Mach 6 hypersonic inlet flow analysis at incidence. In *36th AIAA Fluid Dynamics Conference and Exhibit, San Francisco*, 2006.

[18] G.E. Box and Draper. *Empirical model-building and response surfaces*. Wiley, 1987.

[19] I.D. Boyd, G. Chen, and G.V. Candler. Predicting failure of the continuum fluid equations in transitional hypersonic flows. *Physics of Fluids*, 7:210–218, 1995.

[20] M. Brio and C.C. Wu. An upwind differencing scheme for the equations of ideal magnetohydrodynamics. *Journal of Computational Physics*, 75(2):400–422, 1988.

[21] D. Burnett. The distribution of velocities in a slightly non-uniform gas. *Proceedings of the London Mathematics. Society*, 39:385–430, 1935.

[22] W.B. Bush. Magnetohydrodynamic hypersonic flow past a blunt body. *Journal of Aerospace Sciences*, 25 (11):685–690, 1958.

[23] T. Cain and C. Walton. AIAA-2003-7030: The sustained hypersonic flight experiment. In *12th AIAA International Space Planes and Hypersonic Systems and Technologies*, 2003.

[24] A.B. Cambel. *Plasma Physics and Magnetofluidmechanics*. McGraw-Hill, 1963.

[25] F. Cheng, X. Zhong, S. Gogineni, and R.L. Kimmel. AIAA-2002-0351: Effect of applied magnetic field on the instability of mach 4.5 boundary layer over a flat plate. In *AIAA Aerospace Sciences Meeting and Exhibit, 40th*, 2002.

[26] H.K. Cheng, S.Y. Chen, R. Mobley, and C.R. Huber. The viscous hypersonic slender-body problem: A numerical approach based on a system of composite equations: RM-6193-PR. Technical report, Rand, 1970.

[27] H.K. Cheng and G. Emanuel. Perspective on hypersonic equilibrium flow. *AIAA Journal*, V33 N3:385–400, 1995.

[28] S. Cheung, P. Aaronson, and T. Edwards. Cfd optimization of a theoretical minimum-drag body. *Journal of Aircraft*, V32N1:193–198, 1995.

[29] S.Y. Chou and D. Baganoff. Kinetic fluxvector splitting for the navierstokes equations. *Jounral of Computational Physics*, V130 N2:217–230, 1997.

[30] H.S. Chung and J.J. Alonso. AIAA-2000-4754: Comparison of approximation models with merit functions for design optimization. In *Symposium on Multidisciplinary Analysis and Optimization*, 2000.

[31] J.D. Cole. Newtonian flow theory for slender bodies. *Journal of the Aerospace Sciences*, V24N6:448–455, 1957.

[32] T.C. Corke, B. Mertz, and Matel M.P. AIAA-2006-1208: Plasma flow control optimized airfoil. In *44th AIAA Aerospace Sciences Meeting and Exhibit*, 2006.

[33] D. Corriveau, N. Hamel, and F. Wong. AIAA-2006-3000: Side force generation mechanism for a missile with nose-mounted micro-structures. In *24th AIAA Applied Aerodynamics Conference*, 2006.

[34] D. Corriveau, N. Hamel, and F. Wong. AIAA-2007-273: Force and moment measurements on a generic finned missile with nose-mounted micro-structures. In *45th AIAA Aerospace Sciences Meeting and Exhibit*, 2007.

[35] R. Cosner, W. Oberkampf, C. Rumsey, C. Rahaim, and T. Shih. AIAA-2005-568: Aiaa committee on standards for computational fluid dynamics: Status and plans. In *43rd AIAA Aerospace Sciences Meeting and Exhibit*, 2005.

[36] R.N. Cox and L.F. Crabtree. *Elements of Hypersonic Aerodynamics*. English Universities Press, 1965.

[37] S.C. Crow and Bergmeier G.G. Active sonic boom control. *Journal of Fluid Mechanics*, 325:1–28, 1996.

[38] G. Dadd, R. Owen, J. Hodges, and K. Atkinson. AIAA-2006-7926: The sustained hypersonic flight experiment. In *14th AIAA/AHI Space Planes and Hypersonic Systems and Technologies Conference,*, 2006.

[39] W. Dai and P.R. Woodward. Extension of the piecewise parabolic method to multidimensional ideal magnetohydrodynamics. *Journal of Computational Physics*, 115(2):485–514, 12 1994.

[40] W. Dai and P.R. Woodward. A simple riemann solver and high-order godunov schemes for hyperbolic conservation laws. *Journal of Computational Physics*, 121(1):51–65, 10 1995.

[41] D D'Ambrosio and D Giordano. AIAA-2004-2165: Electromagnetic fluid dynamics for aerospace applications. part 1: Classification and critical review of physical models. In *35th AIAA Plasmadynamics and Lasers Conference, Portland, Oregon*. AIAA, June 2004.

[42] D. D'Ambrosio and M. Pandolfi. AIAA-2004-2164: An upwind numerical method for the prediction of ideal mhd high speed flows. In *35th AIAA Plasmadynamics and Lasers Conference*, 2004.

[43] D D'Ambrosio, M Pandolfi, and Giordano D. AIAA-2004-2362: Electromagnetic fluid dynamics for aerospace applications. part 2: Numerical simulations using different physical models. In *45th Aerospace Sciences Meeting and Exhibit, Reno, Nevada*. AIAA, June 2004.

[44] H. Damevin, J. Dietiker, and Hoffmann K.A. AIAA-2000-0451: Hypersonic flow computations with magnetic field. In *38th Aerospace Sciences Meeting and Exhibit, Reno, Nevada*, 2000.

[45] H. Damevin, K.A. Hoffmann, and J. Dietiker. AIAA-1999-3611: Numerical simulation of hypersonic mhd applications. In *AIAA Plasmadynamics and Lasers Conference, 30th*, 1999.

[46] P. Deb and R. Agarwal. AIAA-2000-0449: Numerical study of compressible viscous mhd equations with a bi-temperature model for supersonic blunt body flows. In *Aerospace Sciences Meeting and Exhibit, 38th*, 01 2000.

[47] D. Degani and L. B. Schiff. AIAA-1989-340: Numerical simulation of the effect of spatial disturbances on vortex asymmetry. In *Aerospace Sciences Meeting, 27th*, 1989.

[48] J. Dietiker and K.A. Hoffmann. AIAA-2001-2737: Numerical simulation of turbulent magnetohydrodynamic flows. In *Plasmadynamics and Lasers Conference, 32nd*, 2001.

[49] J. Dietiker and K.A. Hoffmann. AIAA-2002-0130: Boundary layer control in magnetohydrodynamic flows. In *AIAA Aerospace Sciences Meeting and Exhibit*, 2002.

[50] J. Dietiker and K.A. Hoffmann. Numerical simulation of magnetohydrodynamic flows. *Journal of Spacecraft and Rockets*, 41(4):592–602, 2004.

[51] A. J. Jr. Eggers, M. M. Resnikoff, and D. H. Dennis. NACA-TR-1306: Bodies of revolution having minimum drag at high supersonic airspeeds. Technical report, NACA, 1955.

[52] W.C. Engelund, D.C. Stanley, M. McMillian, and R. Unal. AIAA-1993-3967: Aerodynamic configuration design using response surface methodology analysis. In *Aircraft Design, Systems and Operations Meeting*, 1993.

[53] L. E. ERICSSON. AIAA-1990-2835: Unsteady flow separation on slender bodies at high angles of attack. In *Atmospheric Flight Mechanics Conference*, 1990.

[54] L. E. ERICSSON and J. P READING. AIAA-1985-1797: Aerodynamic effects of asymmetric vortex shedding from slender bodies. In *Atmospheric Flight Mechanics Conference*, 1985.

[55] D.F. Fisher and B.R. Cobleigh. NASA-TM-4595: Controlling forebody asymmetries in flight-experience with boundary layer transition strips. Technical report, NASA, 1994.

[56] D.V. Gaitonde and J. Poggie. AIAA-2000-2326: Simulation of magnetogasdynamic flow control techniques. In *Fluids 2000 Conference and Exhibit,*, 2000.

[57] Y. Ganiev, V. Gordeev, A. Krasilnikov, V. Lagutin, V. Otmennikov, and A. Panasenko. Aerodynamic drag reduction by plasma and hot-gas injection. *Journal of Thermophysics and Heat Transfer*, 14:10–17, 2000.

[58] K. Garon, G. Abate, and W. Hathaway. AIAA-2003-1242: Free-flight testing of generic missile with mems protuberances. In *41st Aerospace Sciences Meeting and Exhibit*, 2003.

[59] D. Giordano. AIAA-2002-2165: Hypersonic flow governing equations with electromagnetic fields. In *33rd Plasmadynamics and Lasers Conference*, 05 2002.

[60] A. Giunta, S. Wojtkiewicz, and M. Eldred. AIAA-2003-649: Overview of modern design of experiments methods for computational simulations. In *41st Aerospace Sciences Meeting and Exhibit*, 2003.

[61] J. Goodman and P. Ireland. AIAA-2006-8071: Thermal modelling for the sustained hypersonic flight experiment. In *14th AIAA/AHI Space Planes and Hypersonic Systems and Technologies Conference*, 2006.

[62] P. Hajela. Non-gradient methods in mdo - status and potential. *Journal of Aircraft*, 36:255–265, 1999.

[63] N. Hamel, D. Corriveau, and F. Wong. AIAA-2005-4968: Numerical investigation on the leeside vortex manipulation of a generic missile. In *23rd AIAA Applied Aerodynamics Conference*, 2005.

[64] S.P. Han. A globally convergent method for nonlinear programming. *Journal of Optimization Theory and Applications*, 22:297–309, 1977.

[65] S. Harada, K.A. Hoffmann, and J. Augustinus. AIAA-1998-0981: Development of a modified runge-kutta scheme with tvd limiters for the ideal two-dimensional mhd equations. In *Aerospace Sciences Meeting and Exhibit, 36th*, 01 1998.

[66] R.L. Hardy. Multiquadratic equations of topography and other irregular surfaces. *Journal of Geophysical Research*, 76:1905–1915, 1971.

[67] Jr. Harris, R. V. and E. J. Landrum. Drag characteristics of low drag bodies of revolution at mach numbers from 0.6 to 4.0. NASA-TN-D-3163. Technical report, NASA, 1965.

[68] J.K. Harvey and M.A. Gallis. Review of code validation studies in high speed low density flows. *Journal of Spacecraft and Rockets*, V37 N1:8–20, 2000.

[69] M.J. Hemsch. *Tactical Missile Aerodynamics*, chapter :Component Build Up Method for Engineering Analysis of Missiles at Low to High angles of Attack. AIAA, 1992.

[70] K. Hida. An approximate study on the detached shock wave in front of a circular cylinder and a sphere. *Journal of Physics Society of Japan*, V8N6:740–745, 1953.

[71] K.A. Hoffmann, H. Damevin, and J. Dietiker. AIAA-2000-2259: Numerical simulation of hypersonic magnetohydrodynamic flows. In *AIAA Plasmadynamics and Lasers Conference, 31st*, 2000.

[72] http://en.wikipedia.org/wiki/Yamato_1 March 2007.

[73] http://www-pao.ksc.nasa.gov/nasafact/tps.htm February 1989.

[74] M.F. Hussain, R.R. Barton, and S.B. Joshi. Metamodeling: Radial basis functions, versus polynomials. *European Journal of Operational Research*, 138:142–154, 2002.

[75] R. Jin, W. Chen, and T.W. Simpson. Comparative studies of metamodeling techniques under multiple modeling criteria. *Structural and Multidisciplinary Optimization*, 23:1–13, 2001.

[76] B.R. Jones, Crossley; W.A., and A.S. Lyrintzis. Aerodynamic and aeroacoustic optimization of rotorcraft airfoils via a parallel genetic algorithm. *Journal of Aircraft*, 37:1088–1096, 2000.

[77] H Kato, J.C Tannehill, and Mehta U.B. AIAA-2002-0202: Computation of magnetohydrodynamic flows using an iterative pns algorithm. In *40th Aerospace Sciences Meeting and Exhibit, Reno, Nevada*, 01 2002.

[78] H Kato, J.C Tannehill, and Mehta U.B. AIAA-2003-0326: Numerical simulation of turbulent mhd flows using an iterative pns algorithm. In *41st Aerospace Sciences Meeting and Exhibit, Reno, Nevada*, 2003.

[79] T. Kawamura. On the detached shock wave in front of a body moving at speeds greater that the speed of sound. *Uni of Kyoto College Science*, 26:207–232, 1950.

[80] A. Keane and P. Nair. *Computation Approaches for Aerospace Design*. Wiley, 2005.

[81] O. Khan, K. Hoffmann, and J. Dietiker. Numerical study of magnetogasdynamic high speed flows over blunt bodies. In *44th AIAA Aerospace Sciences Meeting and Exhibit*, 2006.

[82] J. Kline. Microwave plasma-electron beam interactions for hypersonic flow control. paper 3b06. In *IEEE Conference on Plasma Science, 2000*, 2000.

[83] D. Knight. AIAA-2004-1191: Survey of magnetogasdynamic local flow control at high speeds. In *42nd AIAA Aerospace Sciences Meeting and Exhibit*, 01 2004.

[84] A. L. Kuranov, A. V. Korabelnicov, V. V. Kichinskiy, and E. G. Sheiken. AIAA-2001-1915: Fundamental techniques of the "ajax" concept - modern state of research. In *International Space Planes and Hypersonic Systems and Technologies Conference, 10th*, 2001.

[85] E. V. Laitone and O. Pardee. NACA RMA7110: Location of detached shock wave in front of a body moving at supersonic speeds. Technical report, NACA, 1947.

[86] C.J. Lee. Unique determination of solutions to the burnett solutions. *AIAA Journal*, V32 N5:985–990, 1994.

[87] J. Lee and W.H. Mason. Development of an efficient inverse method for supersonic and hypersonic body design. *JOURNAL OF SPACECRAFT AND ROCKETS*, V31N3:400–405, 1994.

[88] W. Letko. NACA-TN-2911: A low-speed experimental study of the directional characteristics of a sharp-nosed fuselage though a large angle-of-attack range at zero angle of sideslip. Technical report, NACA, 2953.

[89] M.S. Liou. A sequel to ausm: Ausm+. *Journal of Computational Physics*, 129:364–382, 1996.

[90] J.L. Liu. Intelligent genetic algorithm and its application to aerodynamic optimization of airplanes. *AIAA Journal*, 43:530–538, 2005.

[91] D.K. Ludlow. IMPNS theory guide: Coa report NFP-0112. Technical report, Cranfield University, 2001.

[92] D.K. Ludlow. IMPNS user guide: Coa report NFP-0112. Technical report, Cranfield University, 2001.

[93] P.S. Lykoudis. The newtonian approximation in magnetic hypersonic stagnation point flow. *Journal of Aerospace Sciences*, 28 (7):541–546, 1961.

[94] R.W. MacCormack. AIAA-1999-3609: An upwind conservation form method for magneto-fluid dynamics. In *AIAA Plasmadynamics and Lasers Conference, 30th*, 1999.

[95] R.W. MacCormack. AIAA-2001-0195: A conservation form method for magneto-fluid dynamics. In *Aerospace Sciences Meeting and Exhibit, 39th*, 01 2001.

[96] R.W. MacCormack. AIAA 2005-559: Aerodynamic flow calculations with strong magnetic induction and diffusion. In *43rd AIAA Aerospace Sciences Meeting and Exhibit*, 2005.

[97] R.W. MacCormack. AIAA 2006-970: Simulation of hypersonic flow with strong magnetic field interaction. In *44th AIAA Aerospace Sciences Meeting and Exhibit*, 2006.

[98] S.O. Macheret, M.N. Schneider, and Candler G.V. AIAA-2004-1024: Modelling of mhd power generation on board entry vehicles. In *42nd AIAA Aerospace Sciences Meeting and Exhibit*, 01 2004.

[99] S.O. Macheret, M.N. Schneider, and R. Miles. Magnetohydrodynamic control of hypersonic flows and scramjet inlets using electron beam ionization. *AIAA Journal*, 40:74–81, 2002.

[100] W.H. Mason and J. Lee. Minimum-drag axisymmetric bodies in the supersonic/hypersonic flow regimes. *JOURNAL OF SPACECRAFT AND ROCKETS*, V31N3:406–413, 1994.

[101] R. D. Maynes and G. A. Gebert. Rotating nose tip effects on slender body aerodynamics at high angles of attac. *JOURNAL OF SPACECRAFT AND ROCKETS*, V32 N6:944–950, 1995.

[102] D.B. McDonald, W.J. Grantham, W.L. Tabor, and M.J. Murphy. AIAA-2000-4776: Response surface model development for global/local optimization using radial basis functions. In *AIAA/USAF/NASA/ISSMO Symposium on Multidisciplinary Analysis and Optimization*, 2000.

[103] M. D. McKay, W.J. Conover, and R.J. Beckman. A comparison of three methods for selecting values of input variables in the analysis of output from a computer code. *Technometrics*, 21:239–245, 1979.

[104] A. Miele. *Theory of Optimum Aerodynamic Shapes*. Academic, 1965.

[105] R. Miles, S. Macharet, L. Martinelli, R. Murray, M. Schneider, and Y. Ionikh. AIAA-2001-3062: Plasma control of shock waves in aerodynamics and sonic boom mitigation. In *32nd AIAA Plasmadynamics Conference*, 2001.

[106] R. B. Miles. AIAA-2000-2324: Flow control by energy addition into high-speed air. In *Fluids 2000 Conference and Exhibit*, 2000.

[107] J.H. Miller, J.C. Tannehill, S.L. Lawrence, and T.A. Edwards. Parabolized navier-stokes code for hypersonic flows in thermo-chemical equilibrium or nonequilibrium. *Computers and Fluids*, 27(2):199–215, 1998.

[108] C. A. Moskovitz, F. R. Dejarnette, and R.M. Hall. AIAA-1988-483: Effects of surface perturbations on the asymmetric vortex flow over a slender body. In *Aerospace Sciences Meeting, 26th*, 1988.

[109] A Mullur and A. Messac. AIAA-2004-4573: Extended radial basis functions: More flexible and effective metamodeling. In *10th AIAA/ISSMO Multidisciplinary Analysis and Optimization Conference*, 2004.

[110] R. Myers and D. Montgomery. *Response Surface Methodology*. Wiley, 1995.

[111] H.T. Nagamatsu, R.E. Jr. Sheer, and J.R. Schmid. High temperature rarefied hypersonic flow over a flat plate. *ARS Journal*, 31:902–910, 1961.

[112] Narasimha. Relaminarization - mhd and otherwise. *Progress in Astronautics and Aeronautics*, 84:30–52, 1983.

[113] R. Narducci, B. Grossman, and R. T. Haftka. AIAA-1994-96: Sensitivity algorithms for an inverse design problem involving a shock wave. In *Aerospace Sciences Meeting and Exhibit,*, 1993.

[114] C. Nelson and C. Roy. AIAA-2004-1104: Verification of the wind-us cfd code using the method of manufactured solutions. In *42nd AIAA Aerospace Sciences Meeting and Exhibit,*, 2004.

[115] T. Ng. Effect of a single strake on the forebody vortex asymmetry. *Journal of Aircraft*, V27 N9:844–846, 1997.

[116] S. Osher and F. Solomon. Upwind difference schemes for hyperbolic systems of conservation laws. *Mathematics of Computation*, 38:339–374, 1982.

[117] C. Park, D. W. Bogdanoff, and U.B. Mehta. AIAA 2001-792: Performance of a nonequilibrium mhd-bypass scramjet. In *Aerospace Sciences Meeting and Exhibit, 39th*, 2001.

[118] M.P. Patel, C.P. Tilmann, and T. Ng. Closed-loop missile yaw control via manipulation of forebody flow asymmetrics. *Journal of Spacecraft and Rockets*, V41 N3:436–443, 2005.

[119] J. Poggie. AIAA-2006-1007: Plasma-based control of shock-wave / boundary-layer interaction. In *44th AIAA Aerospace Sciences Meeting and Exhibit*, 2006.

[120] J. Poggie and D. Gaitonde. Magnetic control of flow past a blunt body: Numerical validation and exploration. *Physics of Fluids*, 14:1720–1731, 2002.

[121] J. Poggie and D.V. Gaitonde. AIAA-2001-0196: Computational studies of magnetic control in hypersonic flow. In *Aerospace Sciences Meeting and Exhibit, 39th*, 01 2001.

[122] K.G. Powell, P.L. Roe, T.J. Linde, T. Gombosi, and D. De Zeeuw. A solution-adaptive upwind scheme for ideal magnetohydrodynamics. *Journal of Computational Physics*, 154:284–309, 1999.

[123] K.G. Powell, P.L. Roe, R.S. Myong, T. Gombosi, and D. De Zeeuw. Aiaa-1995-1704 an upwind scheme for magnetohydrodynamics. In *AIAA Computational Fluid Dynamics Conference, 12th*, 1995.

[124] M.J.D. Powell. *Numerical Analysis, Lecture Notes in Mathematics*, chapter A Fast Algorithm for Nonlinearly Constrained Optimization, page 144. Springer, 1978.

[125] S.A. Prince. *The aerodynamics of high speed aerial weapons*. PhD thesis, Cranfield University, 1999.

[126] S.A. Prince and M.J. Williams. AIAA-2001-4066: Application of a parabolized navier-stokes solver to some problems in hypersonic propulsion aerodynamics. In *AIAA Atmospheric Flight Mechanics Conference and Exhibit,2001*, 2001.

[127] N. Qin and D.K. Ludlow. Computational prediction of pitch damping for supersonic blunt cones. *Journal of Spacecraft and Rockets*, 35:849–851, 1998.

[128] N. Qin, D.K. Ludlow, S.T. Shaw, J.A. Edwards, and A. Dupuis. Calculation of pitch damping coefficients for a flared projectile. *Journal of Spacecraft and Rockets*, 34:566–568, 1997.

[129] D.M. Rao. Side-force alleviation on slender, pointed forebodies at high angles of attack. *Journal of Aircraft*, V16 N11:763–768, 1997.

[130] Oliver R.E. An experimental investigation of flow over simple blunt bodies at a nominal mach number of 5.8. *Journal of Aerospace Sciences*, 23, 1956.

[131] E.L. Resler and W.R. Sears. The prospects of magneto-aerodynamics. *J. Aeronaut. Sci.*, 25:235–247, 1958.

[132] P. Roache. Code verification by the method of manufactured solutions. *Journal of Fluids Engineering*, 124:4–10, 2002.

[133] P.J. Roache and S. Steinberg. Symbolic manipulation and computational fluid dynamics. *AIAA*, 22:1390–1394, 1984.

[134] J.F. Rodriguez and L.T. Renaud, J.E.and Watson. Convergence of trust region augmented lagrangian methods using variable fidelity approximation data. *Journal of Mechanical Design*, 120:58–66, 1998.

[135] F.W. Roos. AIAA-1996-543: Microblowing for high-angle-of-attack vortex flow control on a fighter aircraft. In *Aerospace Sciences Meeting and Exhibit, 34th*, 1996.

[136] V.J. Rossow. NACA TN 3971: On flow of electrically conducting fluids over a flat plate in the presence of a transverse magnetic. Technical report, NACA, 1957.

[137] J. Roth, D. Sherman, and S. Wilkinson. Electrohydrodynamic flow control with a glow-discharge surface plasma. *AIAA Journal*, 38:1166–1172, 2000.

[138] C.J. Roy. Review of code and solution verification procedures for computational simulation. *Journal of Computational Physics*, 205:131, 2006.

[139] S. Rudman and S.G. Rubin. Hypersonic viscous flow over slender bodies with sharp leading edges. *AIAA Journal*, 6(10):1883–1889, 10 1968.

[140] J. Sacks, S. B. Schiller, and W. J Welch. Design of computer experiments. *Technometrics*, 31:41–47, 1989.

[141] M.N. Schneider, S.O. Macheret, and R. Miles. AIAA-2003-170: Comparative analysis of mhd and plasma methods of scramjet inlet control. In *41st Aerospace Sciences Meeting and Exhibit,*, 2003.

[142] J. Shang, J. Hayes, and K. Wurtzler. AIAA-2000-2325: Jet-spike bifurcation in high-speed flows. In *Fluids 2000 Conference and Exhibit*, 2000.

[143] J. S. Shang, B. Ganguly, R. Umstattd, J. Hayes, M. Arman, and P. Bletzinger. AIAA-2000-447: Developing a facility for magneto-aerodynamic experiments. In *Aerospace Sciences Meeting and Exhibit, 38th*, 2000.

[144] J.S. Shang. Recent research in magneto-aerodynamics. *Journal of Applied Mechanics*, 37:1–20, 2001.

[145] E.G. Sheikin and A.L. Kuranov. AIAA-2005-3223: Scramjet with mhd controlled inlet. In *AIAA/CIRA 13th International Space Planes and Hypersonics Systems and Technologies Conference*, 2005.

[146] J.A. Shercliff. *A Textbook of Magnetohydrodynamics*. Pergamon, 1965.

[147] T.W Simpson. ICASE 1998-206935: Comparison of response surface and kriging models in the multidisciplinary design of the aerospike nozzle. Technical report, ICASE, 1998.

[148] T.W. Simpson and W. Lin, D.K.and Chen. Sampling strategies for computer experiments: Design and analysis. *International Journal of Reliability and Applications*, 2:209–240, 2002.

[149] T.W. Simpson, J.D. Poplinski, P. N. Koch, and J.K. Allen. Metamodels for computer-based engineering design: Survey and recommendations. *Engineering with Computers*, 17:129–150, 2001.

[150] W. Stahl. AIAA-1989-3372: Suppression of asymmetry of the vortex flow behind a circular cone at high incidence. In *Atmospheric Flight Mechanics Symposium*, 1989.

[151] R.L. Stallings. *Tactical Missile Aerodynamics*, chapter :Low Aspect Ratio Wings at High Angles of Attack. AIAA, 1992.

[152] C. Steeves, H. Wadley, R. Miles, and A. Evans. A magnetohydrodynamic power panel for space reentry vehicles. *Journal of Applied Mechanics*, 74:57–64, 2007.

[153] J.L. Steger and R.F. Warming. Flux vector splitting of the inviscid gasdynamic equations with application to finite difference methods. *Journal of Computational Physics*, 40:263–293, 1981.

[154] W.S. Sutton and A. Sherman. *Engineering Magnetohydrodynamics*. McGraw-Hill, 1965.

[155] J.C. Tannehill, P.E. Buelow, J.O. Ielvats, and S.L. Lawrence. Three - dimensional upwind parabolised navier stokes code for real gas flows. *Journal of Spacecraft and Rockets*, 27(2):150–159, 1990.

[156] E.F. Toro. *Riemann Solvers and Numerical Methods for Fluid Dynamic*. Springer, 2006.

[157] R. Unal, R. Lepsch, and M. McMillin. AIAA-1998-4759: Response surface model building and multidisciplinary optimization using d-optimal designs. In *AIAA/USAF/NASA/ISSMO Symposium on Multidisciplinary Analysis and Optimization*, 1998.

[158] G.A. Updike, J.S. Shang, and D.V. Gaitonde. AIAA-2005-0164: Hypersonic separated flow control using magneto-aerodynamic interaction. In *43rd AIAA Aerospace Sciences Meeting and Exhibit*, 2005.

[159] M. D. Van Dyke and H. D. Gordon. NASA Rep 1: Supersonic flow past a family of blunt axisymmetric bodies. Technical report, NASA, 1959.

[160] B. Van Leer. Towards the ultimate conservative difference scheme. *Journal of Computational Physics*, 32:101–136, 1979.

[161] Y.C. Vigneron, J.C. Tannehill, and J.V. Rakich. AIAA-1978-1137: Calculation of supersonic viscous flows over delta wings with sharp subsonic leading edges. In *AIAA Fluid and PlasmaDynamics Conference, 1978*, 1978.

[162] R.E. Walpole and R.H. Myers. *Probability and statistics for engineers and scientists*. Prentice-Hall, 2002.

[163] B.P. Wang. AIAA-2002-1344: Parameter optimization in radial basis function response surface approximations. In *43rd AIAA/ASME/ASCE/AHS/ASC Structures, Structural Dynamics, and Materials Conference*, 2002.

[164] B.P. Wang. Parameter optimization in multiquadric response surface approximations. *Structural and Multidisciplinary Optimization*, V26, N3-4:219–223, 2004.

[165] B.P. Wang and A. Apte. AIAA-2006-1814: Topology optimization using hyper radial basis function network. In *47th AIAA/ASME/ASCE/AHS/ASC Structures, Structural Dynamics, and Materials Conference*, 2006.

[166] K. Xu. NASA/CR-1998-208747: Gas kinetic theory based flux splitting method for idean magnetohydrodynamics. Technical report, NASA, 1998.

APPENDIX A

Component Testing

The following section provides an overview of the technique used to confirm correct implementation of the additional magnetic field field terms appearing in the parabolized Navier Stokes equations, as a result of the magneto-hydrodynamic assumption. Section [5.3] illustrates the form of the additional terms arising in the momentum and energy equations.

Using Gauss' divergence theorem, from equation [5.3.2], we know that;

$$\delta V\,[\nabla . A]_{AVE} = \sum_{l=1}^{6} A_l \cdot n_l \qquad \text{(A.0.1)}$$

In the above equation A is any one of the vectors given by equations [5.3.1] [5.3.3] and [5.3.4], and n the unit normal for each cell interface. Any finite volume formulation discretises space into finite spaces, but the derivatives that appear in the term $\nabla \cdot A$ are taken in an infinitesimal limit. The subroutine to determine these terms therefore constructs a small volume, and approximates it the value at a particular point to be the average value over the entire volume.

The subroutine calculates the sum using the approach outlined in section [5.3]. For each A_l, its value on each cell interface is approximated using an average of the adjacent cell values, and n_l are known quantities from the cell geometry. To test the implementation, the magnetic field variables are chosen to be the following;

$$B = \begin{bmatrix} cos(x) \\ sin(y) \\ cos(z) \end{bmatrix} \qquad \text{(A.0.2)}$$

and the velocity vector is;

$$u = \begin{bmatrix} 1 \\ 1 \\ 1 \end{bmatrix} \qquad \text{(A.0.3)}$$

which results in the following;

$$\nabla \cdot A_u = cos(x)sin(x) - cos(x)sin(y) + cos(x)sin(z) \quad \text{(A.0.4)}$$

$$\nabla \cdot A_v = sin(y)sin(x) - sin(y)cos(y) + sin(y)sin(z) \quad \text{(A.0.5)}$$

$$\nabla \cdot A_w = cos(z)sin(x) - cos(z)cos(y) + cos(z)sin(z) \quad \text{(A.0.6)}$$

$$\nabla \cdot A_E = [sin(x) - cos(y) + sin(z)][cos(x) + sin(y) + cos(z)] \quad \text{(A.0.7)}$$

A test point of $\mathbf{x}_0 = (1.5, 1.5, 1.5)$ is chosen, and a cell length l is also identified. A simple Cartesian grid was chosen as the test domain, and as such the values for B in the adjacent cells (1-6) are computed by considering points $\pm l$ in the x, y, z directions from $\mathbf{x}_0$ respectively. With the cell centre positions defined as such, the cell normals are given by

$$n_\xi = (l^2, 0, 0) \quad \text{(A.0.8)}$$

$$n_\eta = (0, l^2, 0) \quad \text{(A.0.9)}$$

$$n_\zeta = (0, 0, l^2) \quad \text{(A.0.10)}$$

The analytic expressions are computed using the expressions in [A.0.7], at $\mathbf{x}_0$, and for several values of l, the values based numerical implementation of the finite volume form are presented below;

Term	Analytic Value	$l = 0.1$	$l = 0.01$	$l = 0.001$
A_u	0.1361163	0.1355380	0.1361091	0.1361025
A_v	1.919433	1.916587	1.919405	1.919448
A_w	0.1361163	0.1355380	0.1361091	0.1361025
A_E	2.191665	2.187663	2.191627	2.191663

Table 14: Table of sample data for Regression coefficients

The above data indicates that as $l \rightarrow 0$, the numerical values approach the analytical values, confirming that the finite volume implementation used to determine the contributions from terms [5.3.1] [5.3.3] and [5.3.4] in the parabolized Navier Stokes equations is correct.